Hybrid quantum well polariton optomechanics

Romain de Oliveira

Université Paris Cité - CNRS

Ecole doctorale EDPIF 564

Laboratoire Matériaux et Phénomènes Quantiques

Hybrid Quantum Well Polariton Optomechanics

Par Romain De Oliveira

Thèse de doctorat de Physique

Dirigée par Ivan Favero

Présentée et soutenue publiquement le 21/04/2022

Devant un jury composé de :

Emmanuelle Deleporte, Professeure, ENS Paris-Saclay Laboratoire LUMIN, Rapporteure et Examinatrice. Yannick Dumeige, Professeur, CNRS Institut FOTON, Rapporteur et Examinateur. Rémy Braive, Maître de conférence, CNRS C2N, Examinateur. Jean-Philippe Poizat, Directeur de recherche, CNRS Institut Néel, Président du jury. Jacqueline Bloch, Directrice de recherche, CNRS C2N, Membre Invitée, Cristiano Ciuti, Professeur, Université de Paris Laboratoire MPQ, Membre Invité. Ivan Favero, Directeur de recherche, CNRS Laboratoire MPQ.

Titre : **Optomécanique hybrides avec polaritons à puits quantiques**

Résumé : L'optomécanique hybride est un domaine de recherche au carrefour de l'optique, de l'électrodynamique quantique et des micro-dispositifs mécaniques. Ce travail de thèse porte sur la conception, la fabrication et la mesure de résonateurs optomécaniques hybrides : des disques en arséniure de gallium (GaAs). Ces résonateurs forment une trinité: ils possèdent des modes mécaniques à haute fréquence (GHz), des modes optiques de galerie à haut facteur de qualité, et des modes excitoniques associés à l'intégration de structures à puits quantiques multiples en arséniure de gallium/indium (InGaAs) dans le plan du disque. Le confinement dans un volume sub-micronique des modes optiques et excitoniques aboutit à une situation de couplage fort exciton-photon. Le système accueille alors des quasi-particules hybrides lumière-matière : les polaritons, qui partagent à la fois les propriétés des excitons et des photons. Dans un tel résonateur, les mécanismes de couplage optomécanique usuels sont complétés par des effets mécaniques médiés par les porteurs de charge. En raison de l'importance du couplage exciton-phonon, les interactions polariton-phonon peuvent largement surpasser le couplage optomécanique. Nous présentons un modèle théorique construit pour décrire ce système à trois pôles (photon-phonon-exciton) et estimons la force du couplage optomécanique effectif dans notre architecture de type disque. Nous présentons les développements technologiques et de conception qui nous ont permis la réalisation d'expériences avec ces résonateurs. Nous analysons les sources de dissipation optique, mécanique et excitonique. Nous présentons des expériences optiques démontrant la génération de polaritons dans notre structure, en accord avec un modèle de Hopfield exprimé exactement pour les résonateurs en disque à modes de galerie. Enfin, nous exposons les premières expériences optomécaniques réalisées sur la plateforme hybride. Nous terminons la discussion par une prospective.

Mots clefs : Optomécanique, polariton de cavité, couplage fort, mode de galerie, cavité optique, mode de respiration, puit quantique, exciton, potentiel de déformation, cryogénie, couplage evanescent, guide d'onde, photonique intégrée, GaAs, InGaAs, nanofabrication, auto-oscillation.

Title: **Hybrid Quantum Well Polariton Optomechanics**

Abstract: Hybrid optomechanics is a field of research at the crossroads of optics, quantum electrodynamics, and mechanical micro-devices. This thesis deals with the design, fabrication, and measurement of hybrid optomechanical resonators: gallium arsenide (GaAs) disks. These resonators form a trinity: they have high frequency (GHz) mechanical modes, high-quality optical whispering gallery modes (WGMs), and excitonic modes associated with the integration of gallium/indium arsenide (InGaAs) multiple quantum well structures in the disk plane. The confinement in a sub-micron volume of the optical and excitonic modes results in a situation of strong exciton-photon coupling. The system thereupon hosts light-matter hybrid quasiparticles: polaritons, which share both exciton and photon properties. In such a resonator, the usual optomechanical coupling mechanisms are complemented by mechanical effects mediated by charge carriers. Owing to the large exciton-phonon coupling, polariton-phonon interactions can greatly outperform optomechanical coupling. We present a theoretical model constructed to describe this tripartite (photon-phonon-exciton) system and estimate the strength of the effective optomechanical coupling in our disk architecture. We present the technological and design developments that have allowed us to perform experiments with these resonators. We analyze sources of optical, mechanical, and excitonic dissipation. We present optical experiments demonstrating the generation of polaritons in our structure, in agreement with a Hopfield model expressed exactly for gallery mode disk resonators. Finally, we present the first optomechanical experiments performed on the hybrid platform. We conclude the discussion with a perspective.

Keywords: Optomechanics, cavity polariton, strong coupling, whispering gallery mode, optical cavity, radial breathing mode, quantum well, exciton, deformation potential, cryogenics, evanescent coupling, waveguide, integrated photonics, GaAs, InGaAs, nanofabrication, self-oscillation

Contents

List of Figures

List of Tables

Abstract

Hybrid optomechanics is a field of research at the crossroads of optics, quantum electrodynamics, and mechanical micro-devices. This thesis deals with the design, fabrication, and measurement of hybrid optomechanical resonators: gallium arsenide (GaAs) disks. These resonators form a trinity: they have high frequency (GHz) mechanical modes, high-quality optical whispering gallery modes (WGMs), and excitonic modes associated with the integration of gallium/indium arsenide (InGaAs) multiple quantum well structures in the disk plane. The confinement in a sub-micron volume of the optical and excitonic modes results in a situation of strong exciton-photon coupling. The system thereupon hosts light-matter hybrid quasiparticles: polaritons, which share both exciton and photon properties. In such a resonator, the usual optomechanical coupling mechanisms are complemented by mechanical effects mediated by charge carriers. Owing to the large exciton-phonon coupling, polariton-phonon interactions can greatly outperform optomechanical coupling. We present a theoretical model constructed to describe this tripartite (photon-phonon-exciton) system and estimate the strength of the effective optomechanical coupling in our disk architecture. We present the technological and design developments that have allowed us to perform experiments with these resonators. We analyze sources of optical, mechanical, and excitonic dissipation. We present optical experiments demonstrating the generation of polaritons in our structure, in agreement with a Hopfield model expressed exactly for gallery mode disk resonators. Finally, we present the first optomechanical experiments performed on the hybrid platform. We conclude the discussion with a perspective.

Résumé en français

L'optomécanique hybride est un domaine de recherche au carrefour de l'optique, de l'électrodynamique quantique et des micro-dispositifs mécaniques. Ce travail de thèse porte sur la conception, la fabrication et la mesure de résonateurs optomécaniques hybrides : des disques en arséniure de gallium (GaAs). Ces résonateurs forment une trinité : ils possèdent des modes mécaniques à haute fréquence (GHz), des modes optiques de galerie à haut facteur de qualité, et des modes excitoniques associés à l'intégration de structures à puits quantiques multiples en arséniure de gallium/indium (InGaAs) dans le plan du disque. Le confinement dans un volume sub-micronique des modes optiques et excitoniques aboutit à une situation de couplage fort exciton-photon. Le système accueille alors des quasi-particules hybrides lumière-matière : les polaritons, qui partagent à la fois les propriétés des excitons et des photons. Dans un tel résonateur, les mécanismes de couplage optomécanique usuels sont complétés par des effets mécaniques médiés par les porteurs de charge. En raison de l'importance du couplage exciton-phonon, les interactions polariton-phonon peuvent largement surpasser le couplage optomécanique. Nous présentons un modèle théorique construit pour décrire ce système à trois pôles (photon-phonon-exciton) et estimons la force du couplage optomécanique effectif dans notre architecture de type disque. Nous présentons les développements technologiques et de conception qui nous ont permis la réalisation d'expériences avec ces résonateurs. Nous analysons les sources de dissipation optique, mécanique et excitonique. Nous présentons des expériences optiques démontrant la génération de polaritons dans notre structure, en accord avec un modèle de Hopfield exprimé exactement pour les résonateurs en disque à modes de galerie. Enfin, nous exposons les premières expériences optomécaniques réalisées sur la plateforme hybride. Nous terminons la discussion par une prospective.

Introduction

During the last decades, the development of information and communication technology (ICT) has drastically changed our world. Data transfer, digital support, inviolable encrypted communications, ultra-performing and efficient computing are a few examples of the challenges the XXIst century has to overcome. One envisioned solution to face these challenges is the development of quantum technologies, associated with the ability to control physical systems at the nanoscale. The interest in quantum technologies goes now beyond the borders of the academic world, leading to major financial investments in the private and public sector [1–9].

Optomechanics, i.e. the study of the interaction between an electromagnetic field and the mechanical degrees of freedom of a physical system, represents a sub-field of quantum technologies, which inherits the assets of micro-electromechanical systems (MEMS) and photonic devices [10, 11]. Optomechanics is thus an hybrid technology. Hybridization [12–14], thanks to the combination of various information carriers (photons, phonons, or electrons), can marshal the strengths of each system to gain in versatility and performance. Optomechanical systems exist in a large variety of forms, masses, and physical parameters as illustrated by figure I and table I. Thanks to the development and progress of nano-fabrication techniques, optomechanics has recently given rise to considerable applications such as:

- Force and mass sensing [15, 16], in association with AFM techniques [17, 18] for biological applications [19–21].
- Quantum information: mechanical resonators in their quantum fundamental ground state [22, 23] act as transducers between optical photons and radiofrequency. Different schemes involving quantum entanglement [24, 25], superposition [26] or teleportation [27] have been designed and tested.
- Optical manipulation like wavelength conversion [28] or delays lines [29].
- Gravitational interferometry [30], notably enabled by a deep understanding of the impacts and limits induced by the optical measurement inside an interferometer [31].

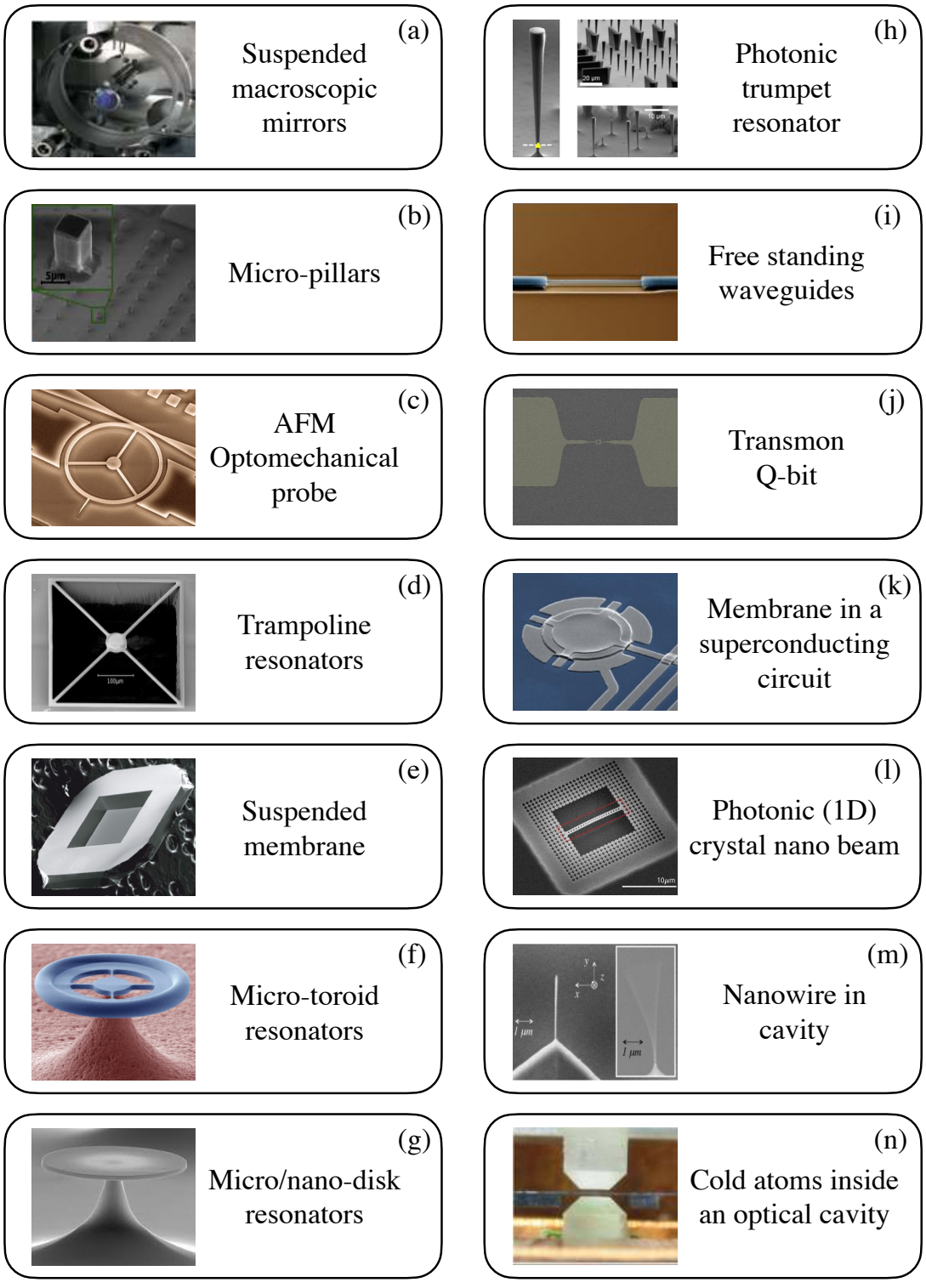

Figure I – Experimental implementations of optomechanical systems. Pictures are taken from: (a) [32] - (b) [33] - (c) [18] - (d) [34] - (e) [35] - (f) [36] - (g) [37] - (h) [38] - (i) [39] - (j) [40] - (k) [41] - (l) [42] - (m) [43] - (n) [44].

	$\Omega_m/2\pi$ [Hz]	m [kg]	$\Gamma_m/2\pi$ [Hz]	$Q_m f_m$ [Hz]	$\kappa_c/2\pi$ [Hz]	κ_c/Ω_m	g_0 [Hz]
Atomic gas [45]	$4.2 \cdot 10^4$	$1 \cdot 10^{-22}$	$1 \cdot 10^3$	$1.7 \cdot 10^6$	$6.6 \cdot 10^5$	15.7	$6 \cdot 10^5$
Si Photonic crystal [46]	$3.9 \cdot 10^9$	$3.1 \cdot 10^{-16}$	$3.9 \cdot 10^4$	$3.9 \cdot 10^{14}$	$5 \cdot 10^8$	0.13	$9 \cdot 10^5$
SiN membrane [35]	$1.3 \cdot 10^4$	$4 \cdot 10^{-11}$	0.12	$1.5 \cdot 10^{11}$	$5 \cdot 10^5$	3.7	$5 \cdot 10^1$
Sapphire transducer [47]	10^3	1.85	$2.5 \cdot 10^{-6}$	$4.1 \cdot 10^{10}$	275	0.9	$1.2 \cdot 10^{-3}$
GaAs disk [37]	$0.5 \cdot 10^9$	$1 \cdot 10^{-12}$	$0.5 \cdot 10^6$	$0.5 \cdot 10^{13}$	$1 \cdot 10^9$	2	$1 \cdot 10^6$

Table I – Optomechanical system experimental parameters for a variety of system. $f_m = \Omega_m/2\pi$ mechanical frequency, m mass, Γ_m mechanical dissipation rate, Q_m mechanical quality factor, κ_c optical dissipation rate, g_0 optomechanical coupling constant, see section 1.3 for further details

To push the hybridization beyond optics and mechanics, optomechanical devices can be coupled to another third degree of freedom, forming an *hybrid optomechanical system*. This extra degree of freedom can take the form of a true or artificial two-level atom, or of an atomic assemble. A zoo of hybrid optomechanical system is already available in the literature [10, 38, 48–59] .

In this thesis we focus our attention on hybrid optomechanical systems composed of a mechanical oscillator interacting with an electromagnetic field and with an electronic degree of freedom in a semiconductor, hence forming an opto-electro-mechanical resonator (see figure II (b)). Our device, schematically presented in figure II (a), consists in a GaAs *active* optomechanical disk resonator embedding a quantum-well structure. It possesses some specificities:

- Because of the peculiar disk shape, optical and mechanical modes of the resonator have an azimuthal symmetry. The Whispering Gallery Modes (WGMs), combine ultra-high quality factor and small mode volume, which has led to realizations in microlasers [60], sensing [61, 62], non-linear quantum optics [63, 64], cavity quantum electrodynamics [65] and optomechanics [37, 66]. The mechanical modes, in particular, the Radial Breathing Modes (RBMs), enable ultra-high frequencies (GHz) and strong coupling to WGMs [67].

- In contrast to previous work of our team, the material constituting the disk embeds a hetero-structure constituted of multiple quantum wells (MQW). This *active* material can support well-controlled excitons (electron-hole pairs). Excitons can be strongly coupled to the resonator photons, a regime where new quasi-particles emerge: exciton-polaritons [68].

Ever since the pioneering work of Hopfield in 1958 [69] on bulk semiconductors, the research on polaritons has grown a lot. The vivid progress in the fabrication of epitaxial heterostructures, from 2D to 0D, has enabled the study of polaritons in a large variety of systems [68, 70, 71]. Due to strong Coulomb interactions, polaritons exhibit large $\chi^{(3)}$

resonant nonlinearities that entail nonlinear optical phenomena such as parametric amplification [72] and oscillation [73]. Alternatively, polaritons exhibit bosonic behavior at low densities. Under peculiar conditions, they can accumulate in the lowest energy state, forming a Bose-Einstein condensate (BEC) [74–76]. Polariton interactions also lead to fascinating effects such as superfluidity [77] or the generation of vortices [78].

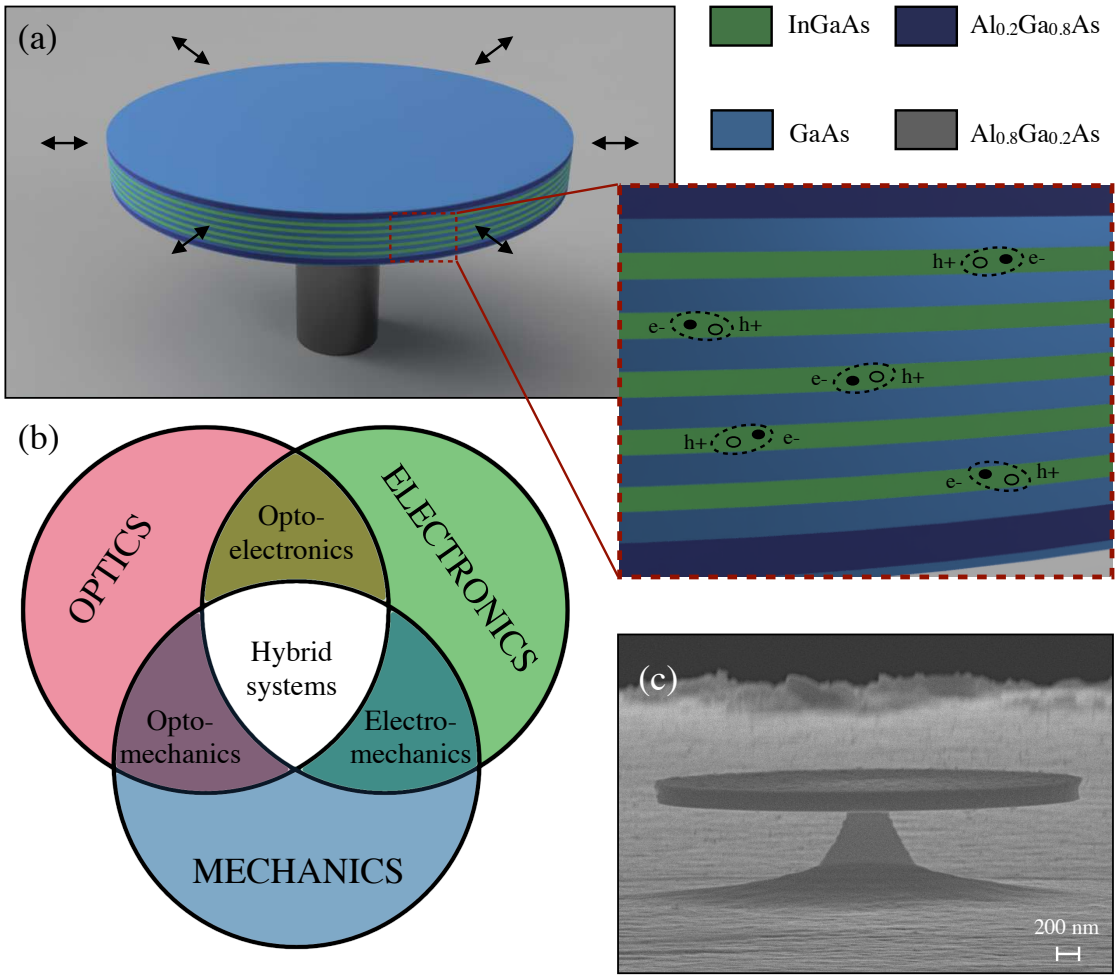

Figure II – (a) Sketch of an hybrid GaAs disk optomechanical resonator. The disk, composed of a stack of different GaAs alloy layers, is both an optical resonator supporting WGMs and a mechanical resonator sustaining different mechanical modes such as RBMs, (radial expansion/contraction modes). In this thesis, it becomes as well an excitonic resonator, and the exciton will couple to both WGMs and RBMs. An AlGaAs pedestal (dark grey) isolates the disk from the sample substrate. The inset provides a closer look at the hetero-structure, illustrating as well locations of excitons in the device. (b) Diagram of a hybrid system as considered in this thesis. (c) SEM micrograph of an isolated hybrid disk of this thesis. Magnification $\simeq$ 20.7K.

Coupling polaritons to the mechanical motion of a micro/nanofabricated device broadens the scope of possibilities. The first application is to take advantage of the hybrid light-

matter nature of excitations in the semiconductor resonators to enhance optomechanical interactions. Indeed the excitonic component is highly sensitive to strain fields via the deformation potential [79, 80] which is large in the considered III-V materials. A second prospect is to use the polariton condensate to act on the mechanical degree of freedom [81,82] or inversely use the mechanical device to probe the peculiar dynamics of the condensate.

Outline of the thesis

Chapter 1 is dedicated to the theoretical framework of optomechanics and polaritons. It introduces the tools required to describe a generic hybrid optomechanical system, pinpointing the new phenomena emerging from such architecture. This chapter establishes the basic conceptual frame that will be needed to describe future QW-polariton optomechanical realizations. **Chapter 2** presents in great detail all the important parameters at play in the hybrid GaAs disk resonator of this thesis: optical, mechanical, and excitonic modes, as well as their mutual interactions ,are not only described but also modeled. As a result of models developed along this thesis, quantitative optomechanical, electromechanical, and optoelectrical coupling are computed and discussed. **Chapter 3** gives a close look at experimental techniques and constraints on the design of the sample. It includes a description of the waveguide/disk evanescent coupling, with emphasis on dissipation mechanisms (optics, mechanical, excitonic). A discussion of the MQW structure is provided, as well as a detailed presentation of our clean-room fabrication techniques. **Chapter 4** is dedicated to the observation of polaritons in our platform, associated with an analysis based on an original model for WGM quantum-well excitons, developed in this thesis. Polariton lasing is also reported and discussed. **Chapter 5** finally presents the first optomechanical experiments carried out on our hybrid system, discussing achievements and limitations. It opens on different perspectives for the future.

Chapter 1

Quantum-well hybrid optomechanics: concepts and tools

Summary: This chapter presents the conceptual tools needed to describe a quantum-well hybrid optomechanical system. We start by introducing the standard optomechanical formalism, then move to the description of quantum-well cavity exciton-polaritons. Finally, we illustrate the different coupling Hamiltonians governing the hybrid tripartite system (photon-phonon-exciton).

1.1 Optomechanics

This part presents the models employed to describe the interaction between light and mechanical motion: how optical and mechanical modes couple together and how they can

exchange energy [10, 11].

1.1.1 Hamiltonian description for a closed system

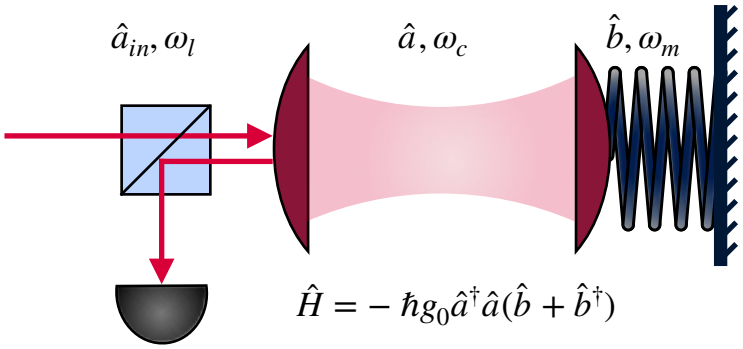

Figure 1.1 – Archetypal optomechanical resonator : Laser driven Fabry-Pérot cavity with a fixed and a free spring-mounted mirror

Figure 1.1 represents the archetypal optomechanical system. The optical cavity is a Fabry-Pérot cavity, with optical frequency ω_c, photon annihilation (creation) $\hat{a}$ ($\hat{a}^\dagger$) operator, and one mirror of the cavity is free to move (compliant). This mirror, with mass m, behaves like a harmonic mechanical oscillator with a mechanical frequency ω_m and a phonon annihilation (creation) $\hat{b}$ ($\hat{b}^\dagger$) operator. Both photonic ($\hat{a}, \hat{a}^\dagger$) and phononic operators ($\hat{b}, \hat{b}^\dagger$) obey the bosonic commutation relation $\left[\hat{a}, \hat{a}^\dagger\right] = 1$. In the absence of any optomechanical interaction, the Hamiltonian of the system is:

$$\hat{H} = \hbar\omega_c \hat{a}^\dagger \hat{a} + \hbar\omega_m \hat{b}^\dagger \hat{b} \tag{1.1}$$

Where does the optomechanical interaction come from? We assume first that the mechanical system (moving mirror) is at an equilibrium position. When light enters the optical cavity, satisfying the cavity resonance condition, photo-induced forces like radiation pressure displace the mirror. If the position of the mirror is modified, the same is true for the cavity resonance condition. The circulating power inside the cavity therefore decreases, and the optical forces exerted on the mirror as well, until the mirror reaches a new equilibrium position, where the optical force balances the restoring force of the spring. If the displacement $\hat{x}$ is small enough, the cavity resonance frequency is modulated by the mechanical displacement:

$$\omega_c(\hat{x}) \simeq \omega_c(0) + \hat{x}\frac{\partial \omega_c}{\partial \hat{x}} \simeq \omega_c(0) - g_{om}\hat{x} \tag{1.2}$$

where $\hat{x} = x_{\mathrm{ZPF}}(\hat{b} + \hat{b}^\dagger)$, with the amplitude of the mechanical zero point fluctuations $x_{\mathrm{ZPF}} = \sqrt{\frac{\hbar}{2m\omega_m}}$ and $g_{om} = -\frac{\partial \omega_c}{\partial \hat{x}}$ the optical frequency pull parameter. From now on $\omega_c(0)$ is noted ω_c. For a Fabry-Pérot cavity, g_{om} is given by $g_{om} = \omega_c/L$, where L is the cavity length.

A seminal work of Law for a Fabry-Pérot cavity did establish the lowest order interaction Hamiltonian of the optomechanical system [83, 84], in the case of a single optical and single mechanical mode:

$$\begin{aligned}\hat{H} &= \hbar\omega_c\hat{a}^\dagger\hat{a} + \hbar\omega_m\hat{b}^\dagger\hat{b} - \hbar g_0\hat{a}^\dagger\hat{a}(\hat{b}^\dagger + \hat{b}) \\ \hat{H} &= \hbar\omega_c\hat{a}^\dagger\hat{a} + \hbar\omega_m\hat{b}^\dagger\hat{b} + \hat{H}_{cm}\end{aligned} \tag{1.3}$$

with $g_0 = x_{\mathrm{ZPF}} \cdot g_{om}$, the vacuum (or single-photon) optomechanical coupling, corresponding to the optical frequency shift associated with the zero-point motion of the mechanical oscillator. While originally established for a Fabry-Pérot cavity the Hamiltonian (1.3) is quite general and can be applied to any system where the optical resonance frequency is linearly shifted by a mechanical motion.

The conservative optical force is taken as the derivative of the interaction energy $\hat{H}_{cm}$ with respect to the displacement:

$$\hat{F} = -\frac{\partial\hat{H}_{cm}}{\partial\hat{x}} = \frac{\hbar g_0}{x_{ZPF}}\hat{a}^\dagger\hat{a} = \hbar g_{om}\hat{n} \tag{1.4}$$

This force is proportional to the number of photons inside the cavity $\hat{n} = \hat{a}^\dagger\hat{a}$.

1.1.2 Modeling the environment

A real physical system is not isolated but coupled to an environment, in our case the field inside the cavity is coupled to an electromagnetic environment, while the mobile mirror is coupled to a support via an anchor point. These couplings are responsible for the optical and mechanical damping, and for the various noises (vacuum, thermal...). To depict this in a cavity optomechanical system, a good starting point is the input-output formalism [85–88] where the external environment is modeled as a bath of harmonic modes.

1.1.2.1 Optical bath

The optical environment is represented by a bath of photons, described by a continuum of independent harmonic oscillators governed by the following Hamiltonian:

$$\hat{H}_{\text{O-bath}} = \hbar\int \omega\hat{A}^\dagger(\omega)\hat{A}(\omega)d\omega \tag{1.5}$$

where the bath creation $\hat{A}^\dagger(\omega)$ and annihilation $\hat{A}(\omega)$ operators obey the commutation relation $\left[\hat{A}(\omega'), \hat{A}^\dagger(\omega)\right] = \delta(\omega - \omega')$. We assume that only modes close to the resonance frequency ω_c can be excited out from the vacuum, and the interaction between the system and the bath to be of a Jaynes-Cummings form:

$$\hat{H}_{\text{O-bath,int}} = -j\hbar\int d\omega\sqrt{\kappa(\omega)}\left[\hat{a}^\dagger\hat{A}(\omega) - \hat{A}^\dagger(\omega)\hat{a}\right] \tag{1.6}$$

where $\sqrt{\kappa(\omega)}$ represents the strength of the interaction, such that the total optical Hamiltonian is:

$$\hat{H}_{\text{opt}} = \hbar\omega_c \hat{a}^\dagger \hat{a} + \int d\omega \left[\hbar\omega \hat{A}^\dagger(\omega)\hat{A}(\omega) - j\hbar\sqrt{\kappa(\omega)}\left(\hat{a}^\dagger \hat{A}(\omega) - \hat{A}^\dagger(\omega)\hat{a}\right)\right] \tag{1.7}$$

1.1.2.2 Mechanical bath

Similarly we can define a phononic bath in interaction with the mechanical mode where each bath mode is coupled by a coupling coefficient $\sqrt{\Gamma(\omega)}$:

$$\hat{H}_{\text{M-bath}} = \hbar \int \omega \hat{B}^\dagger(\omega)\hat{B}(\omega)d\omega \tag{1.8}$$

$$\hat{H}_{\text{M-bath,int}} = -j\hbar \int d\omega \sqrt{\Gamma(\omega)}\left[\hat{b}^\dagger \hat{B}(\omega) - \hat{B}^\dagger(\omega)\hat{b}\right] \tag{1.9}$$

With this second bath defined, the total mechanical Hamiltonian is therefore:

$$\hat{H}_{\text{mec}} = \hbar\omega_m \hat{b}^\dagger \hat{b} + \int d\omega \left[\hbar\omega \hat{B}^\dagger(\omega)\hat{B}(\omega) - j\hbar\sqrt{\Gamma(\omega)}\left(\hat{b}^\dagger \hat{B}(\omega) - \hat{B}^\dagger(\omega)\hat{b}\right)\right] \tag{1.10}$$

1.1.2.3 Drive Hamiltonian

We consider now the action of the external pump laser, populating the laser mode $\omega = \omega_l$ [1] with a coherent state $|\alpha_l(t)\rangle$, that obeys $\hat{A}_l|\hat{\alpha}_l(t)\rangle = \alpha_l(t)|\hat{\alpha}_l(t)\rangle$ where $\alpha_l(t) = \alpha_{\text{ext}}\exp(-j\omega_l t)$. This mode is coupled to the cavity mode with a constant $\sqrt{\kappa(\omega_l)} = \sqrt{\kappa_{\text{ext}}}$. We apply a unitary transformation defined by the following displacement operator $\hat{D}^\dagger[\alpha_l(t)] = \exp\left[-\alpha_l(t)\hat{A}_l^\dagger + \alpha_l^*(t)\hat{A}_l\right]$, which keeps the mechanical Hamiltonian (1.10) and the interraction Hamiltonian $\hat{H}_{cm}$ unchanged and transforms the total optical Hamiltonian (1.7) into [2] [89]:

$$\begin{aligned}\hat{H}^D_{\text{opt}} &= \hat{D}^\dagger[\alpha_l(t)]\hat{H}_{opt}\hat{D}[\alpha_l(t)] + j\hbar\frac{\partial\hat{D}^\dagger[\alpha_l(t)]}{\partial t}\hat{D}[\alpha_l(t)] \\ &= \hbar\omega_c\hat{a}^\dagger\hat{a} + j\hbar\sqrt{\kappa_{\text{ext}}}\alpha_{\text{ext}}\left[\hat{a}e^{j\omega_l t} - \hat{a}^\dagger e^{-j\omega_l t}\right] \\ &+ \int d\omega \left[\hbar\omega\hat{A}^\dagger(\omega)\hat{A}(\omega) - j\hbar\sqrt{\kappa(\omega)}\left(\hat{a}^\dagger\hat{A}(\omega) - \hat{A}^\dagger(\omega)\hat{a}\right)\right]\end{aligned} \tag{1.11}$$

1. We consider a pure monochromatic excitation and hence neglect phase noise

2. Up to a scalar constant that we have not expressed here. The new Schrödinger equation is $\hat{H}^D_{opt}|\Psi\rangle = j\hbar\partial_t|\Psi\rangle$, with $|\Psi\rangle = \hat{D}^\dagger[\alpha_l(t)]|\Phi\rangle$ and $|\Phi\rangle$ a Hilbert vector before displacement solution of $\hat{H}_{opt}|\Phi\rangle = j\hbar\partial_t|\Phi\rangle$

We finally use a rotating wave approximation $\left(\hat{U} = \exp\left(-j\omega_l \hat{a}^\dagger \hat{a} t\right)\right)$ to recenter the dynamics of the optical degrees of freedom close to the exciting laser frequency ω_l [3]:

$$\begin{aligned}\hat{H}_{\text{opt}}^{UD} &= \hat{U}^\dagger \hat{H}_{\text{opt}}^{D} \hat{U} + j\hbar \frac{\partial \hat{U}^\dagger}{\partial t} \hat{U} \\ &= -\hbar\Delta \hat{a}^\dagger \hat{a} + j\hbar\sqrt{\kappa_{\text{ext}}}\alpha_{\text{ext}}\left[\hat{a} - \hat{a}^\dagger\right] \\ &+ \int d\omega \left[\hbar\omega \hat{A}^\dagger(\omega)\hat{A}(\omega) - j\hbar\sqrt{\kappa(\omega)}\left(\hat{a}^\dagger \hat{A}(\omega) e^{j\omega_l t} - \hat{A}^\dagger(\omega)\hat{a} e^{-j\omega_l t}\right)\right]\end{aligned} \tag{1.12}$$

where $\Delta = \omega_l - \omega_c$, is the laser detuning with respect to the cavity mode [4].

After those transformations the total optomechanical Hamiltonian of the system now reads:

$$\begin{aligned}\hat{H}_{\text{tot}} =& \hat{H}_{\text{opt}}^{UD} + \hat{H}_{\text{mec}} + \hat{H}_{cm} \\ \hat{H}_{\text{tot}} =& -\hbar\Delta \hat{a}^\dagger \hat{a} + \hbar\omega_m \hat{b}^\dagger \hat{b} - \hbar g_0 \hat{a}^\dagger \hat{a}(\hat{b}^\dagger + \hat{b}) + j\hbar\sqrt{\kappa_{\text{ext}}}\alpha_{\text{ext}}\left[\hat{a} - \hat{a}^\dagger\right] \\ &+ \int d\omega \left[\hbar\omega \hat{A}^\dagger(\omega)\hat{A}(\omega) - j\hbar\sqrt{\kappa(\omega)}\left(\hat{a}^\dagger \hat{A}(\omega) e^{j\omega_l t} - \hat{A}^\dagger(\omega)\hat{a} e^{-j\omega_l t}\right)\right] \\ &+ \int d\omega \left[\hbar\omega \hat{B}^\dagger(\omega)\hat{B}(\omega) - j\hbar\sqrt{\Gamma(\omega)}\left(\hat{b}^\dagger \hat{B}(\omega) - \hat{B}^\dagger(\omega)\hat{b}\right)\right]\end{aligned} \tag{1.13}$$

1.2 Dynamic optomechanical equations

1.2.1 Quantum Langevin equations

After having performed the transformation $\hat{U}\hat{D}$, we next perform a Heisenberg transformation ($\tilde{o} = \hat{V}^\dagger \hat{o} \hat{V}$ where $\hat{o}$ is an arbitrary operator and $d\hat{V}/dt = -j\hat{H}_{\text{tot}}\hat{V}/\hbar$) in order to derive the evolution equations for both photon and phonon annihilation operators in the Heisenberg picture [5] [90]:

$$\begin{aligned}\dot{\hat{a}} = \frac{d\hat{a}}{dt} &= \frac{j}{\hbar}\left[\hat{H}_{\text{tot}}, \hat{a}\right] = j\Delta\hat{a} + jg_0\hat{a}(\hat{b}^\dagger + \hat{b}) + \sqrt{\kappa_{\text{ext}}}\alpha_{\text{ext}} + \int d\omega \sqrt{\kappa(\omega)}\hat{A}(\omega)e^{j\omega_l t} \\ \dot{\hat{b}} = \frac{d\hat{b}}{dt} &= \frac{j}{\hbar}\left[\hat{H}_{\text{tot}}, \hat{b}\right] = -j\omega_m\hat{b} + jg_0\hat{a}^\dagger\hat{a} + \int d\omega \sqrt{\Gamma(\omega)}\hat{B}(\omega)\end{aligned} \tag{1.14}$$

The dynamics of the optical and mechanical fields are intrinsically coupled to the dynamics of the baths.

3. This transformation also does not impact $\hat{H}_{mec}$ and $\hat{H}_{cm}$

4. At that stage, $\hat{a}$ and $\hat{A}$ are the original field operators, and do not depend on time while $\hat{H}_{opt}^{UD}$ do.

5. From now on, the operators that appear in the equations are in the Heisenberg representation, to avoid making the expression more cumbersome, we kept the same notation.

To get rid of the two integral terms in equation (1.14) we must compute explicitly their dynamics. The method to do so is expressed in appendix A.2. We obtain consequently the Langevin equation for the optomechanical system [6]:

$$\begin{aligned}\dot{\hat{a}} &= (j\Delta - \frac{\kappa_c}{2})\hat{a} + jg_0\hat{a}(\hat{b}^\dagger + \hat{b}) + \sqrt{\kappa_{\text{ext}}}\alpha_{\text{ext}} + \sqrt{\kappa_c}\hat{a}_{\text{in}} \\ \dot{\hat{b}} &= -(j\omega_m + \frac{\Gamma_m}{2})\hat{b} + jg_0\hat{a}^\dagger\hat{a} + \sqrt{\Gamma_m}\hat{b}_{\text{in}}\end{aligned} \tag{1.15}$$

where $\hat{a}_{\text{in}}$ and $\hat{b}_{\text{in}}$ are operators representing the noise generated by the environment interacting with the optomechanical system and can be considered as Langevin forces. Using the first Markov approximation, these noises are delta-correlated in time and their expected values follow the Planck distribution (see appendix A.3).

1.2.2 Linearized equations

We will now work in the *weak coupling regime*, where $g_0 \ll \kappa_c$. Indeed, all the optomechanical interactions are fundamentally non linear (presence of a quadratic term in photons operators in the Hamiltonian (1.3)), but when $g_0 \ll \kappa_c$ linearization of the equations (1.15) is a good approximation. A more detailed discussion about the "quantumness" factor in optomechanical interactions defined by g_0/κ_c is provided in [91].

The laser driving results in the displacement of both the optical and mechanical degrees of freedom, since the average photon number inside the cavity exerts a static force on the mechanical resonator leading to a new mechanical equilibrium position. A displacement transformation can therefore be applied: $\hat{a} \to \alpha + \delta\hat{a}$, $\hat{b} \to \beta + \delta\hat{b}$, where α and β are strictly speaking complex numbers that we take real, without loss of generality in the case of a single cavity, $\alpha = \sqrt{N_{cav}}$ the mean coherent state amplitude inside the cavity. $\delta\hat{a}$ and $\delta\hat{b}$ are operators that represent the fluctuations of the optical and mechanical fields around their mean values. The quantum Langevin equations are rewritten as:

$$\alpha = \frac{\sqrt{\kappa_{\text{ext}}}\alpha_{\text{ext}}}{j\Delta' - \kappa_c/2} \tag{1.16}$$

$$\beta = \frac{g_0 N_{cav}}{\omega_m + j\Gamma_m/2} \tag{1.17}$$

$$\delta\dot{\hat{a}} = (j\Delta + \frac{\kappa_c}{2})\delta\hat{a} + jg_0\alpha(\delta\hat{b}^\dagger + \delta\hat{b}) + jg_0\delta\hat{a}(\delta\hat{b}^\dagger + \delta\hat{b}) + \sqrt{\kappa_c}\hat{a}_{\text{in}} \tag{1.18}$$

$$\delta\dot{\hat{b}} = -(j\omega_m + \frac{\Gamma_m}{2})\delta\hat{b} + jg_0\alpha(\delta\hat{a}^\dagger + \delta\hat{a}) + jg_0\delta\hat{a}^\dagger\delta\hat{a} + \sqrt{\Gamma_m}\hat{b}_{\text{in}} \tag{1.19}$$

with $\Delta' = \Delta + 2g_0\beta = \Delta + g_{om}\langle\hat{x}\rangle$ the shifted cavity detuning.

6. In this set of equations we could have distinguished for the input fields κ_{ext} and κ_{in}, the first one being associated with the external incoming laser coupling and the second one to all the other loss processes which go undetected, the amplitude experience decay at a rate $\kappa_c = \kappa_{\text{ext}} + \kappa_{\text{in}}$

For strong driving conditions terms that are not driven can be safely neglected ($jg_0\delta\hat{a}(\delta\hat{b}^\dagger + \delta\hat{b})$ in eq. (1.18) and $jg_0\delta\hat{a}^\dagger\delta\hat{a}$ in eq. (1.19)) leading to Langevin equations for $\delta\hat{a}$ and $\delta\hat{b}$ corresponding to an effective linearized optomechanical Hamiltonian (in the absence of dissipation)

$$\hat{H} = -\hbar\Delta\delta\hat{a}^\dagger\delta\hat{a} + \hbar\omega_m\delta\hat{b}^\dagger\delta\hat{b} - \hbar G(\delta\hat{a}^\dagger + \delta\hat{a})(\delta\hat{b}^\dagger + \delta\hat{b}) \tag{1.20}$$

where $G = g_0\sqrt{N_{cav}}$ represents the enhanced coupling parameter. (1.20) is an Hamiltonian coupling linearly two harmonic oscillators $\delta\hat{a}$ and $\delta\hat{b}$, each of them being on top coupled to a dissipative bath at a rate κ_c and Γ_m respectively. Given the symmetry of the problem, it is natural to expect that the energy exchange between the two oscillators will be quantified by the adimensionnal parameter $G^2/\Gamma_m\kappa_c = g_0^2 N_{cav/\Gamma_m\kappa_c}$, ratio between the interaction strength and the loss of both oscillators.

For illustrative purpose, we detail here how this parameter indeed emerges as central in the phenomena of side-band cooling and amplification of mechanical motion.

1.2.3 The optomechanical cooperativity, cooling and amplification

Three important regimes can be singled-out in the interaction Hamiltonian (1.20) [7] [10, 92–94]:

$$\begin{aligned}
\Delta = -\omega_m &\Longrightarrow \hat{H} = -\hbar G(\delta\hat{a}^\dagger\delta\hat{b} + \delta\hat{a}\delta\hat{b}^\dagger) \\
\Delta = \omega_m &\Longrightarrow \hat{H} = -\hbar G(\delta\hat{a}^\dagger\delta\hat{b}^\dagger + \delta\hat{a}\delta\hat{b}) \\
\Delta = 0 &\Longrightarrow \hat{H} = -\hbar G(\delta\hat{a}^\dagger + \delta\hat{a})(\delta\hat{b}e^{-j\omega_m t} + \delta\hat{b}^\dagger e^{j\omega_m t})
\end{aligned} \tag{1.21}$$

When the driving laser is red-detuned from the cavity by precisely the mechanical frequency ($\Delta = -\omega_m$, see figure 1.2-(a)), the elementary process where an incident laser photon at ω_l absorbs a phonon before leaving the system at $\omega_c = \omega_l + \omega_m$ is resonantly enhanced by the presence of the cavity, leading to a reduction of the phonon population (cooling) [95–97]. Conversely, for a blue-detuning at precisely the mechanical frequency ($\Delta = \omega_m$, see figure 1.2-(c)), the symmetric process where an incident photon at ω_l emits a phonon at ω_m before leaving the system at $\omega_l - \omega_m$ is resonantly favored. Phonons are generated into the mechanical mode in a coherent fashion, this is the regime of optomechanical amplification of motion [98]. In the case where the driving is exactly on resonance with the cavity ($\Delta = 0$, see figure 1.2-(b)), the two previous processes have the same weight, there is no exchange of energy between the two oscillators, this configuration can be used to read out the mechanical motion.

7. These equations are obtained by applying a rotating wave approximation $\hat{U} = \exp\left(-j\Delta\delta\hat{a}^\dagger\delta\hat{a}t + j\omega_m\delta\hat{b}^\dagger\delta\hat{b}t\right)$ onto the Hamiltionian (1.20)

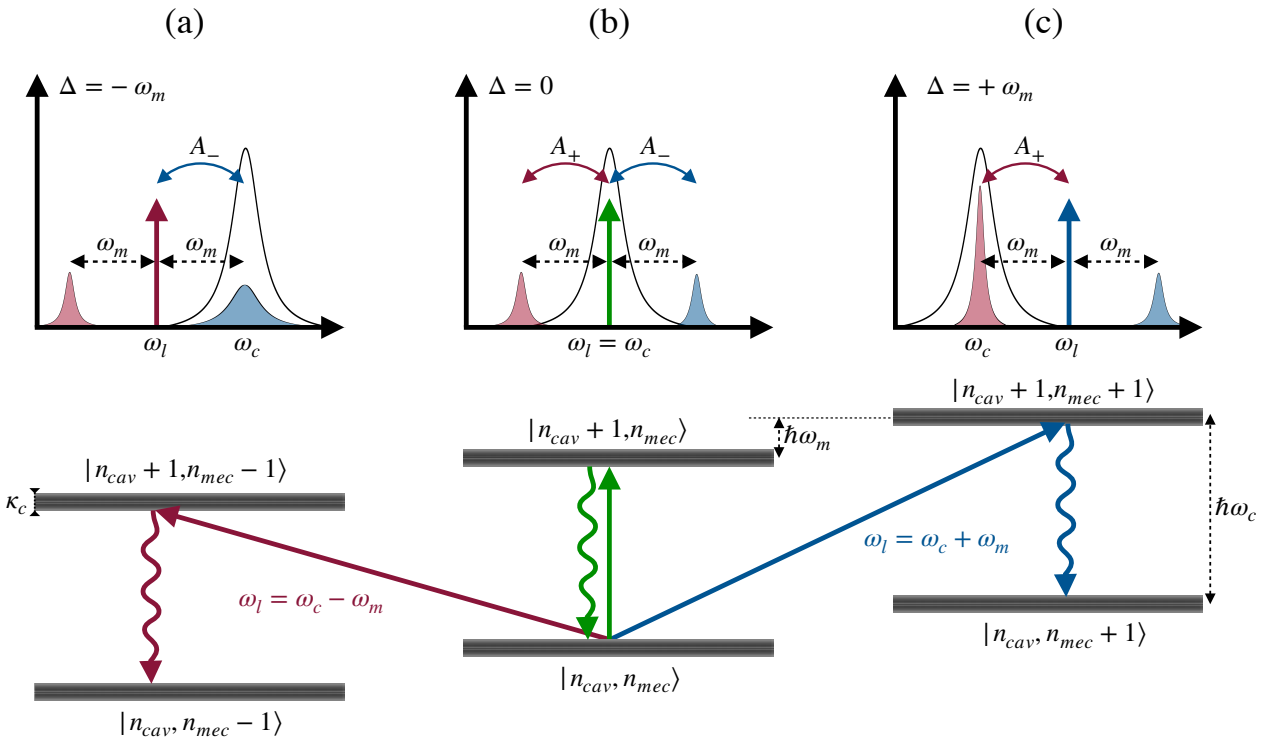

Figure 1.2 – (a) Anti-Stokes (b) In-cavity and (c) Stokes scattering process represented here in the regime ($\omega_m > \kappa_c$). Top panels: scattering picture. The black Lorentzian represents the optical cavity mode, the blue Lorentzian the anti-Stokes peak, and the red one the Stokes peak. A_+ and A_- represent here the Stokes and anti-Stokes cavity photon scattering rates. Bottom panels: transition diagram representing the three schemes (cooling, readout, amplification). n_{cav} and n_{mec} represent respectively the number of photons and phonons. An appropriate detuning lead to the selection of one of these three processes

Let us formalize these phenomena with dynamic equations. The fourier transform of eq. (1.18) and (1.19) under strong driving conditions gives (we drop the shifted index $'$ and write $\Delta' = \Delta$ thereafter):

$$\delta\hat{a}[\omega] = \frac{jG(\delta\hat{b}^\dagger[\omega] + \delta\hat{b}[\omega]) + \sqrt{\kappa_c}\hat{a}_{\text{in}}[\omega]}{-j(\omega + \Delta) + \frac{\kappa_c}{2}} = \frac{jG(\delta\hat{b}^\dagger[\omega] + \delta\hat{b}[\omega]) + \sqrt{\kappa_c}\hat{a}_{\text{in}}[\omega]}{\chi_c^{-1}[\omega]} \tag{1.22}$$

$$\delta\hat{b}[\omega] = \frac{jG(\delta\hat{a}^\dagger[\omega] + \delta\hat{a}[\omega]) + \sqrt{\Gamma_m}\hat{b}_{\text{in}}[\omega]}{j(\omega_m - \omega) + \frac{\Gamma_m}{2}} = \frac{jG(\delta\hat{a}^\dagger[\omega] + \delta\hat{a}[\omega]) + \sqrt{\Gamma_m}\hat{b}_{\text{in}}[\omega]}{\chi_m^{-1}[\omega]} \tag{1.23}$$

where $\chi_c^{-1}[\omega]$ and $\chi_m^{-1}[\omega]$ are the optical and mechanical response functions.

Injecting eq. (1.22) and its conjugate into eq. (1.23) leads after some algebraic manipulations to the expression [8]:

$$\delta\hat{b}[\omega] = \chi_m'^{-1}[\omega]\left(\sqrt{\Gamma_m}\hat{b}_{\rm in}[\omega] + \frac{jG}{\chi_c^{-1}[\omega]}\sqrt{\kappa_c}\hat{a}_{\rm in}[\omega] + \frac{jG}{\bar{\chi}_c^{-1}[-\omega]}\sqrt{\kappa_c}\hat{a}_{\rm in}^{\dagger}[\omega]\right) \tag{1.24}$$

with $\chi_m'^{-1} = j(\omega_m' - \omega) + \frac{\Gamma_m'}{2}$ where the mechanical frequency and dissipation rate have been modified by the optomechanical interaction: $\omega_m' = \omega_m + \delta\omega_m$, $\Gamma_m' = \Gamma_m + \Gamma_{om}$. These modifications are given by:

$$\begin{aligned}
\delta\omega_m[\omega] &= G^2\,\mathrm{Im}\left(\chi_c[\omega] - \bar{\chi}_c[-\omega]\right) \\
\delta\omega_m &\simeq G^2\left[\frac{\Delta+\omega_m}{(\Delta+\omega_m)^2 + \left(\frac{\kappa_c}{2}\right)^2} + \frac{\Delta-\omega_m}{(\Delta-\omega_m)^2 + \left(\frac{\kappa_c}{2}\right)^2}\right] \qquad (1.25)\\
\Gamma_{om}[\omega] &= 2G^2\,\mathrm{Re}\left(\chi_c[\omega] - \bar{\chi}_c[-\omega]\right) \\
\Gamma_{om} &\simeq G^2\left[\frac{\kappa_c}{(\Delta+\omega_m)^2 + \left(\frac{\kappa_c}{2}\right)^2} - \frac{\kappa_c}{(\Delta-\omega_m)^2 + \left(\frac{\kappa_c}{2}\right)^2}\right] \qquad (1.26)
\end{aligned}$$

For $\omega = \omega_m$, a valid approximation when $\mid \omega_m - \omega \mid \lesssim \Gamma_m \ll \kappa_c$.

We will not discuss in detail the modification of the mechanical frequency by the optomechanical interaction (the *optical-spring* effect captured by equation (1.25) and illustrated in figure 1.3 (b)) and rather discuss the optomechanical modification of the mechanical dissipation Γ_{om} (equation (1.26) and figure 1.3 (a)).

Depending on the sign of Δ, Γ_{om} can be a damping or anti-damping of the mechanical motion. Red pumping the cavity ($\Delta = -\omega_m$) leads to an attenuation of the mechanical vibrations ($\Gamma_{om} > 0$). For $\omega_m \gg \kappa_c$ and $\Delta = -\omega_m$, Γ_{om} takes the simple form $\frac{4G^2}{\kappa_c}$. In such case the mechanical resonator is connected to two different baths: a thermal bath of temperature T (rate of dissipation Γ_m) and an optical bath of low effective temperature (rate of dissipation Γ_{om}). At equilibrium, this translates into a mean population in the mechanical mode of $\frac{\Gamma_m}{\Gamma_m+\Gamma_{om}}\bar{n}_{th}^{mec}$, with $\bar{n}_{th}^{mec} \simeq {}^{k_bT}/_{\hbar\omega_m}$ the thermal occupation of the mechanical mode (see appendix A.3). The parameter $\Gamma_{om}/\Gamma_m = 4G^2/(\Gamma_m\kappa_c) = 4g_0^2N_{cav}/\Gamma_m\kappa_c$ appears as a quantification of the ability to reduce the mechanical population by optomechanical sideband cooling [9].

Blue-detuned pumping of the cavity ($\Delta = \omega_m$) leads in contrast to an amplification (anti-damping) of the mechanical motion ($\Gamma_{om} < 0$). When this amplification balances the

8. To obtain this result we have dropped terms proportional to $\chi_m[\omega]\delta\hat{b}$ since $\delta\hat{b}$ is strongly peaked around $\omega = -\omega_m$ and $\chi_m[\omega]$ peaked at $\omega = \omega_m$. Their product is therefore negligible especially for narrow bandwidth resonators $\omega_m/\Gamma_m \gg 1$.

9. This reasoning neglects the back-action of the optical force (no temperature for the photon bath). For a further introduction to the phenemenon of optomechanical cooling we invite the reader to check the appendix A.4

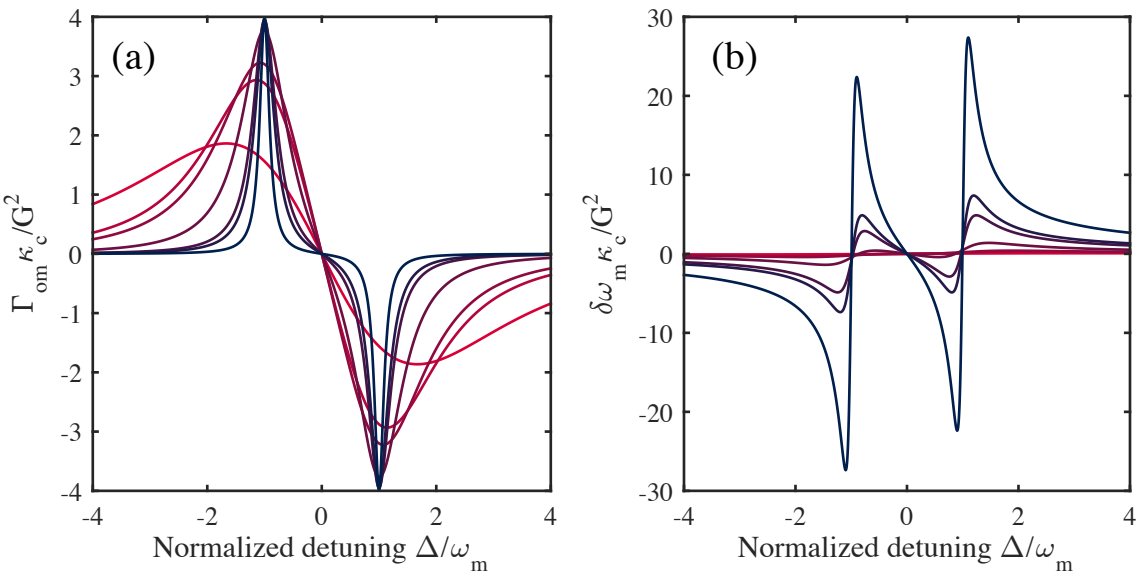

Figure 1.3 – (a) Optomechanical damping and (b) optical spring effect as a function of the detuning Δ/ω_m. Cooling/heating is maximal at $\Delta/\omega_m = \pm 1$. The color code corresponds to different values of the ω_m/κ_c ratio. From red to blue this ratio is equal to [0.2, 0.4, 0.5, 1, 2, 2.5, 5]

natural damping of the system ($\Gamma_{om} = -\Gamma_m$), the mechanical motion is "sustained" and adopts a coherent sinusoidal trajectory equivalent to a mechanical laser. The threshold to reach this regime (when $\omega_m \gg \kappa_c$) is $4g_0^2 N_{cav}/\Gamma_m \kappa_c = 1$, pinpointing again the central role of this adimensional parameter.

This parameter is called optomechanical cooperativity C, and has a broad significance in most of the applications of linearized optomechanics such as optomechanical induced transparency [99, 100] or measurements at the standard quantum limit (radiation pressure shot-noise) [10].

1.3 Optomechanical parameters of interest

Mechanical resonator: A higher mechanical frequency ω_m facilitates observation of quantum effects, most naturally accessible when $\hbar\omega_m \geq k_B T$. The mechanical quality factor $Q_m = \omega_m/\Gamma_m$ quantifies the level of decoupling of the mechanical mode from its environment. The "$Q_m \cdot f_m$" product ($f_m = \omega_m/2\pi$) is in practice often the quantity to optimize, and parametrizes the number of independent quantum operations that can be performed before decoherence sets-in. The increase of f_m is most generally achieved by decreasing the size and the effective mass of the resonator. High Q_m are obtained by working on the different loss channels such as clamping losses, viscous losses, or intrinsic losses usually reduced by cooling down the system to cryogenic temperatures [101].

Optical resonator: Working at optical and telecom wavelengths, the optical resonant frequency ω_c is fixed, and efforts are mostly focused on enhancing the optical quality factor $Q_{opt} = \omega_c/\kappa_c$, usually by mitigating the scattering and absorption in the device materials.

Optomechanical coupling: The strength of the optomechanical interaction characterized by g_0 is central especially as it is squared in the cooperativity. A coherent driving of the cavity can effectively increase the interaction ($G = g_0\sqrt{N_{cav}}$). By increasing G we can reach different coupling regimes such as: strong coupling ($\kappa_c, \Gamma_m, \ll G \ll \omega_m, \Delta$) where Rabi oscillations between the two eigenstates occurs [36, 102, 103] or ultrastrong coupling ($\kappa_c, \Gamma_m, \ll G \lesssim \omega_m \ll \Delta$) where the interaction strength becomes of the order of the eigenfrequencies [104].

During the past years, extensive work and progress have been made by the optomechanical community to push the boundaries of these figures of merit. In our group, optical quality factor up to $5 \cdot 10^6$ [105] has been reached, notably by improving the nanofabrication process. The use of mechanical shield [106] has considerably enhanced the "$Q_m \cdot f_m$" product. Regarding the parameter g_0, the value has somewhat saturated for several years around a few MHz, like observed in nanoscale optomechanical disk and crystals. The fabrication of ultimately small disks would allow pushing this value but at the cost of an increase in both optical and mechanical dissipation.

This thesis aims at opening a new path to boost g_0 to further levels by using a hybrid system, without changing drastically the overall design of the device.

1.4 Hybrid optomechanics with quantum-well cavity polaritons

Hybrid optomechanics is the sub-field of optomechanics where an extra quantum object (a third degree of freedom) is added to the optomechanical resonator. This new object is coupled either to the mechanics, to the optical field, or both. It can be a two-level system such as an atom or artificial atoms [49–51] (NV-center [56, 57], quantum dot [38, 58], superconducting Q-bit [13, 55]), a cold gas or atomic condensate [45, 48, 52–54], or any other controlled systems of interest [59]. Here we will focus on hybrid systems that involve cavity polaritons formed on quantum well excitons [107, 108]. Before introducing the new hybrid Hamiltonian we will briefly present the cavity polariton formalism based on the Hopfield model [69].

1.4.1 Hopfield model for cavity polaritons

1.4.1.1 Closed-system Hamiltonian

Since the pioneering work of Purcell [109], it is known that the emission probability of a two-level atom is enhanced when placed at the antinode of a standing electromagnetic wave inside a Fabry-Pérot cavity. If the coupling between these two entities is strong enough, i.e.

if the energy exchange is faster than the decay rate of each entity, the new eigenmodes of the coupled system can be described as linear superpositions of the atomic and cavity degrees of freedom: this is the strong coupling regime of cavity-QED.

If many identical atoms are employed instead of one, an atomic excitation can be delocalized in the ensemble. If the ensemble is large, many atomic excitations can be accommodated without interfering: a collective mode can be populated in a quasi-harmonic manner and the associated operator becomes quasi-bosonic in the limit of a large ensemble: this is the Holstein-Primakoff transform [110]. In a semiconductor quantum-well, we will see in the next chapter how bosonic operators $\hat{d}$ and $\hat{d}^\dagger$ can there as well describe the collective mode associated to the fundamental exciton trapped within the well. The light-matter coupling Hamiltonian for such quantum-well exciton coupled to a cavity mode $\hat{a}$ is given by [10]:

$$\hat{H}_{cx} = \hbar\omega_c \hat{a}^\dagger \hat{a} + \hbar\omega_x \hat{d}^\dagger \hat{d} + \frac{\hbar\Omega_R}{2}\left(\hat{a}^\dagger \hat{d} + \hat{a}\hat{d}^\dagger\right) \tag{1.27}$$

where $\hbar\Omega_R/2$ is the coupling energy and Ω_R the Rabi splitting. The Hamiltonian (1.27) can be diagonalized (for $\hat{d}$ operators bosonic) thanks to the Hopfield (unitary) transformation:

$$\hat{H}_{cx} = E_u \hat{p}_u^\dagger \hat{p}_u + E_l \hat{p}_l^\dagger \hat{p}_l \tag{1.28}$$

where the two new eigenstates of the system called Upper Polariton (UP) and Lower Polariton (LP) have their eigenenergy:

$$E_{u/l} = \frac{1}{2}\left(E_c + E_x \pm \hbar\sqrt{\delta^2 + \Omega_R^2}\right) = \frac{1}{2}\left(\hbar\omega_c + \hbar\omega_x \pm \hbar\sqrt{\delta^2 + \Omega_R^2}\right) \tag{1.29}$$

with $\hbar\delta = E_c - E_x = \hbar\omega_c - \hbar\omega_x$ the cavity-exciton detuning. The corresponding bosonic operators are given by:

$$\begin{bmatrix}\hat{p}_l \\ \hat{p}_u\end{bmatrix} = \begin{bmatrix}-C & X \\ X & C\end{bmatrix}\begin{bmatrix}\hat{a} \\ \hat{d}\end{bmatrix}, \quad X^2 = \frac{1}{2}\left(1 + \frac{\delta}{\sqrt{\delta^2 + \Omega_R^2}}\right), \quad C^2 = \frac{1}{2}\left(1 - \frac{\delta}{\sqrt{\delta^2 + \Omega_R^2}}\right) \tag{1.30}$$

where X and C are the (positive) real Hopfield coefficients [69] that represent respectively the excitonic and photonic fractions of the polariton particle. $X^2 + C^2 = 1$ and at zero detuning ($\delta = 0$) $X^2 = C^2 = 1/2$.

The eigenenergies of the polaritonic system exhibit characteristic anti-crossing behavior in analogy with two classical coupled oscillators as illustrated in figure 1.4. When the cavity-exciton detuning is null the energy splitting between the lower and upper branch is exactly Ω_R.

10. This is the simplest form for the polariton Hamiltonian, we did not take into account the energy dispersion of the exciton or cavity and we have considered pure spin states. Second-order terms describing non-linear effects are also omitted.

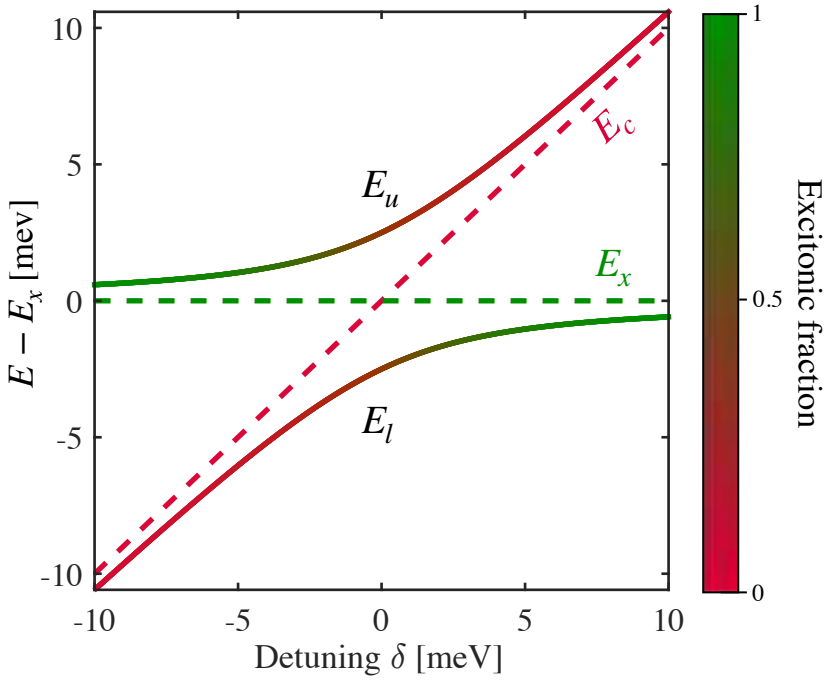

Figure 1.4 – UP and LP eigenenergy as a function of the cavity-exciton detuning δ. The color map corresponds to the excitonic fraction (X). Ω_R=5 meV

1.4.1.2 Strong coupling criterion for a dissipative system

Just like for two coupled classical oscillators [111, 112], we can insert relaxation phenomena that confer to both exciton and photon a finite lifetime. The Langevin equations of the coupled systems in the absence of any forces are [11]:

$$\dot{\hat{a}} = -\left(j\omega_c + \frac{\kappa_c}{2}\right)\hat{a} - j\frac{\Omega_R}{2}\hat{d} \tag{1.31}$$

$$\dot{\hat{d}} = -\left(j\omega_x + \frac{\kappa_x}{2}\right)\hat{d} - j\frac{\Omega_R}{2}\hat{a} \tag{1.32}$$

where κ_c, κ_x are respectively the cavity photon and exciton decay rates. Inserting the ansatz $\hat{a}/\hat{d} = \hat{a}_0/\hat{d}_0 e^{-j\omega t}$, and writing the equations in matrix form we get:

$$\begin{bmatrix} \omega - \omega_c + j\frac{\kappa_c}{2} & -\frac{\Omega_R}{2} \\ \frac{\Omega_R}{2} & \omega - \omega_x + j\frac{\kappa_x}{2} \end{bmatrix} \begin{bmatrix} \hat{a}_0 \\ \hat{d}_0 \end{bmatrix} = \begin{bmatrix} 0 \\ 0 \end{bmatrix} \tag{1.33}$$

The corresponding determinant is:

$$(\omega - \omega_c + j\frac{\kappa_c}{2})(\omega - \omega_x + j\frac{\kappa_x}{2}) = \frac{\Omega_R^2}{4} \tag{1.34}$$

11. To obtain this set of equations we employ the same method used on eqs. (1.14) and (1.15), with the Hamiltonian $\hat{H}_{cx}$. The Langevin forces have been neglected and a thermal bath has been used to model the exciton relaxation, $\hat{H}_{X-bath} = \hbar\int \omega \hat{D}^\dagger(\omega)\hat{D}(\omega)d\omega$ and $\hat{H}_{X-bath,int} = j\hbar\int d\omega\sqrt{\kappa(\omega)}\left[\hat{d}^\dagger\hat{D}(\omega) - \hat{D}^\dagger(\omega)\hat{d}\right]$ (see appendix A.2.)

The new eigenenergies are therefore given by:

$$\begin{aligned}\tilde{E}_{u/l} &= \frac{E_c + E_x}{2} - j\hbar\frac{\kappa_c + \kappa_x}{2} \pm \frac{\hbar}{2}\sqrt{\left(\delta - j(\kappa_c - \kappa_x)\right)^2 + \Omega_R^2} \\ &= \frac{\hbar\tilde{\omega}}{2} \pm \frac{\hbar}{2}\sqrt{\tilde{\delta}^2 + \Omega_R^2}\end{aligned} \tag{1.35}$$

with $\tilde{\omega} = \omega_c + \omega_x - j(\kappa_c + \kappa_x)$ the average complex angular frequency of the states and $\tilde{\delta} = \delta - j(\kappa_c - \kappa_x)$ the effective complex detuning for the exciton-cavity couple.

Figure 1.5-(a) and (b) exhibit the real and imaginary part of $\omega_{l/u} = E_{u/l}/\hbar$ as a function of the Rabi splitting Ω_R for a zero cavity-exciton detuning. For $\delta = 0$, when $\Omega_R <\mid \kappa_c - \kappa_x \mid$ the square root in (1.35) is purely imaginary and the coupling term is not impacting the real part of the eigenfrequencies: it is the weak coupling regime. On the other hand, when $\delta = 0$ and $\Omega_R >\mid \kappa_c - \kappa_x \mid$ we enter in the strong coupling regime, where energy exchange between the cavity and the exciton occurs, and two new hybrid eigenstates emerge. The situation $\Omega_R =\mid \kappa_c - \kappa_x \mid$ marks the difference between the two regimes.

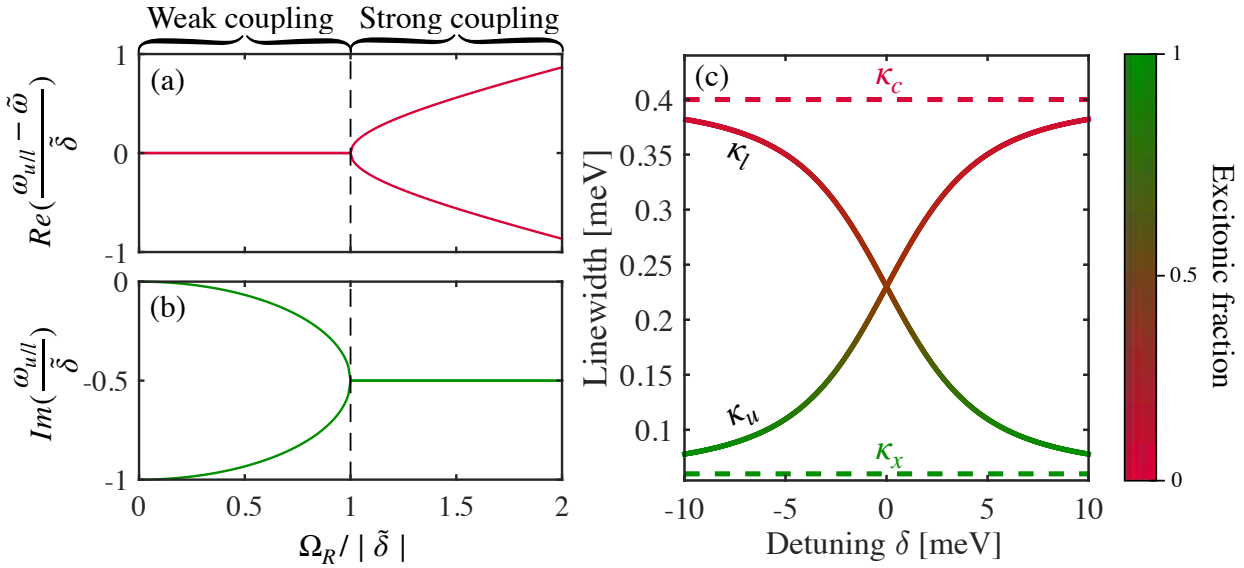

Figure 1.5 – (a) Real and (b) imaginary part of the eigenenergies $\omega_{u/l}$ as a function of the Rabi splitting Ω_R for a zero cavity-exciton detuning. Parameters are $\omega_c/\kappa_c = 10^4$, $\kappa_x = 0$. (c) UP and LP linewidth ($\hbar\kappa_{u/l}$) as a function of δ. The color map corresponds to the excitonic fraction (X). Ω_R=5 meV, κ_c=0.4 meV, κ_x=0.06 meV

In the strong coupling regime the decay rates of the lower and upper branch are given by $\kappa_{l/u} = -\,\mathrm{Im}\left\{\tilde{E}_{l/u}/\hbar\right\}$:

$$\kappa_l = X^2\kappa_x + C^2\kappa_c \tag{1.36}$$

$$\kappa_u = C^2\kappa_x + X^2\kappa_c \tag{1.37}$$

Their variations with the cavity-exciton detuning δ are plotted in figure 1.5-(c).

1.4.2 Tripartite system: Photon, exciton, phonon

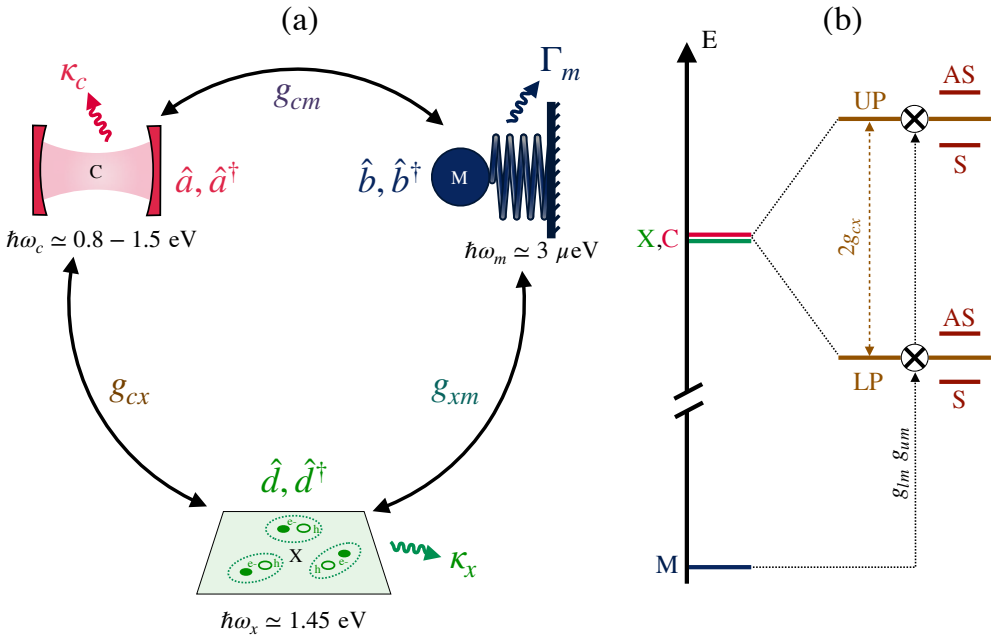

Figure 1.6 – (a) - Sketch of the tripartite system. The system is composed of a resonator supporting both an optical cavity resonance (C) and a mechanical resonance (M) at frequency ω_c and ω_m. A quantum well QW, inserted inside the resonator, hosts exciton (X) at frequency ω_x. Photons, phonons and excitons can be considered as bosons characterized by annihilation/creation operators $(\hat{a}, \hat{a}^\dagger)$,$(\hat{b}, \hat{b}^\dagger)$ and $(\hat{d}, \hat{d}^\dagger)$. κ_c, Γ_m and κ_x are the associated decay rates. (b) Energy diagram: strong coupling induces a Rabi splitting $\Omega_R = 2g_{cx}$ between the normal modes of the cavity/exciton, generating two polariton branches UP and LP. The interaction of the mechanical mode with the polariton modes via the polariton-mechanical coupling g_{lm} and g_{um} is generating Stokes (S) and anti-Stokes (AS) sidebands

Hamiltonian description: We start this section by writing down the Hamiltonian of the tripartite system (photon-exciton-phonon), illustrated in figure 1.6-(a) [113]:

$$\begin{aligned}\hat{H} &= \hat{H}_0 + \hat{H}_{int} \\ &= \hbar\omega_c \hat{a}^\dagger\hat{a} + \hbar\omega_x \hat{d}^\dagger\hat{d} + \hbar\omega_m \hat{b}^\dagger\hat{b} + \hbar g_{cx}(\hat{a}^\dagger\hat{d} + \hat{a}\hat{d}^\dagger) - \hbar g_{xm}\hat{d}^\dagger\hat{d}(\hat{b}^\dagger + \hat{b}) \\ &\qquad - \hbar g_{cm}\hat{a}^\dagger\hat{a}(\hat{b}^\dagger + \hat{b})\end{aligned} \tag{1.38}$$

where $g_{cx} = \Omega_R/2$ and $g_{cm} = g_0$, and where g_{xm} is the electromechanical coupling parametrizing the interaction between the exciton and the phonon (detailed on section 2.6). This Hamiltonian can be split into two different parts $\hat{H}_0$ and $\hat{H}_{int}$ corresponding respectively to the bare energies of the three coupled systems, and their mutual interactions. The

first term in $\hat{H}_{int}$ describes the Rabi exciton-cavity interaction, while the two others govern the modulation of the cavity and exciton resonances by the mechanical motion.

In the strong coupling regime ($g_{cx}^2 > (\kappa_c - \kappa_x)^2/4$) we can rewrite this Hamiltonian in the polariton basis introduced in eq. (1.30), after some algebra:

$$\begin{aligned}
\hat{H} &= \hat{H}_m + \hat{H}_l + \hat{H}_u + \hat{H}_{lum} \\
\hat{H}_m &= \hbar\omega_m \hat{b}^\dagger \hat{b} \\
\hat{H}_l &= \hbar\omega_l \hat{p}_l^\dagger \hat{p}_l - \hbar g_{lm} \hat{p}_l^\dagger \hat{p}_l (\hat{b}^\dagger + \hat{b}) \\
\hat{H}_u &= \hbar\omega_u \hat{p}_u^\dagger \hat{p}_u - \hbar g_{um} \hat{p}_u^\dagger \hat{p}_u (\hat{b}^\dagger + \hat{b}) \\
\hat{H}_{lum} &= -\hbar g_{lum} (\hat{p}_u^\dagger \hat{p}_l + \hat{p}_u \hat{p}_l^\dagger)(\hat{b}^\dagger + \hat{b})
\end{aligned} \tag{1.39}$$

with $g_{lm} = X^2 g_{xm} + C^2 g_{cm}$, $g_{um} = C^2 g_{xm} + X^2 g_{cm}$ and $g_{lum} = XC(g_{xm} - g_{cm})$. $\hat{H}_l$ and $\hat{H}_u$ look precisely like a canonical optomechanical Hamiltonian, where the cavity photon mode has been replaced by a polariton mode and where the optomechanical coupling g_{cm} has been replaced by g_{lm} or g_{um}. $\hat{H}_{lum}$ corresponds to phonon-accompanied scattering processes between the two polariton branches.

- If the energy splitting between the UP and LP is close to the mechanical energy, $2g_{cx} \simeq \omega_m$, the Hamiltonian $\hat{H}_{lum}$ will contain resonant terms corresponding to transitions between the UP and LP branch assisted by the emission or absorption of one phonon. This scenario is highly unlikely in our system since the mechanical frequency of the resonator is typically around the gigahertz while the Rabi splitting is around ten terahertz.

- In consequence for quasi-resonant laser driving of the system close to one of the polariton modes $\eta = u, l$ the Hamiltonian (1.39) reduces to:

  $$\hat{H} = \hbar\omega_m \hat{b}^\dagger \hat{b} + \hbar\omega_\eta \hat{p}_\eta^\dagger \hat{p}_\eta - \hbar g_{\eta m} \hat{p}_\eta^\dagger \hat{p}_\eta (\hat{b}^\dagger + \hat{b}) \tag{1.40}$$

  In this configuration, the system obeys the laws of optomechanics with photons in the resonator simply replaced by polaritons. The coupling of the polaritons with the mechanical motion, g_{lm} or g_{um}, is a sum of the optomechanical and electromechanical couplings, weighted by the excitonic and photonic fractions of the polariton. This coupling will for example amongst others, generate Stockes and anti-Stokes sidebands, as represented in figure 1.6 (b) similar to those illustrated in figure 1.2.

In conclusion, the emergence of polaritons does modify the strength of the effective optomechanical interaction within the resonator. In this thesis, we are investigating devices fabricated out of III-V semiconductors, where the deformation potential is strong and can give rise to electromechanical couplings that are 10 to 1000 times larger than state-of-the-art optomechanical couplings. In concrete devices, this may ultimately lead to an enhancement of the effective optomechanical interaction g by a factor of 10 to 100 (as represented in figure

1.7 (a)). Our experimental efforts will constitute first steps toward observing this effect.

On top of the g coupling factor, one should also look at how dissipation is affected when polaritons emerge. This is overall well quantified by the cooperativity introduced earlier in canonical optomechanical equations $C = \frac{4g^2 N_{cav}}{\Gamma_m \kappa_c}$, which we will take at the single-particle level C_0, considering that an experimentalist would employ as many polaritons in the resonator as he/she would do with the photons. The ratio between the single-polariton cooperativity and the single-photon cooperativity is given by:

$$\frac{C_0^{lm}}{C_0} = \frac{\left(X^2 \frac{g_{xm}}{g_{cm}} + C^2\right)^2}{X^2 \frac{\kappa_x}{\kappa_c} + C^2}, \qquad \frac{C_0^{um}}{C_0} = \frac{\left(C^2 \frac{g_{xm}}{g_{cm}} + X^2\right)^2}{C^2 \frac{\kappa_x}{\kappa_c} + X^2} \tag{1.41}$$

The variations of those two ratios are represented in figure 1.7 (b). For the LP we see that an enhancement of the cooperativity/optomechanical coupling is achieved as soon as the excitonic fraction X start to increase, with a visible outcome for positive detuning ($X^2 > 0.5$), where the polariton will tend to have more an excitonic character. A similar observation holds for the UP, with the cavity fraction C and when the detuning is negative ($C^2 > 0.5$).

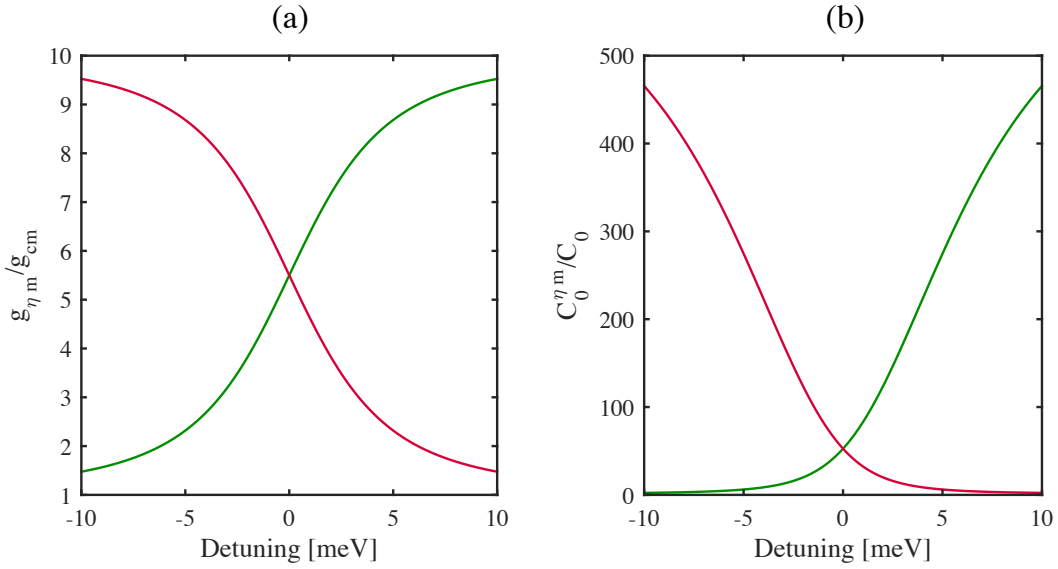

Figure 1.7 – Optomechanical coupling (a) and cooperativity (b) enhancement as a function of the cavity-exciton detuning δ. $\eta = l/u$ - Green curves LP, red curves UP. $\Omega_R = 5$ meV, κ_c =0.4 meV, $\kappa_x = 0.06$ meV, $g_{xm}/g_{cm} = 10$

We see that there are multiple challenges on the way to observe these effects of polaritonic enhancement in optomechanical resonators. One should first control a platform where the three degrees of freedom; photon, exciton, phonon; are controlled on the same footing, and strongly interact with one another. At the same time the photon dissipation, the exciton broadening, and the mechanical damping should all be mitigated and kept to a minimal

amount. Finally, experiments should combine optomechanical techniques with spectroscopy methods typical of polaritonics. The next chapter will present our efforts in such a direction.

Chapter 2

Hybrid quantum well optomechanical disk resonators in GaAs

Summary : In this chapter, we describe thoroughly the optical (section 2.1), mechanical (section 2.2) and excitonic modes (section 2.3) of our GaAs disk resonator embeddingMQW hetero-structures. We introduce new models, developed along this thesis, that enable full calculation of the strength of their mutual interactions (sections 2.4, 2.5 and 2.6). While WGM resonators per se are well-known photonic objects, at the beginning of this thesis, there was no rigorous theory describing their interaction with an embedded quantum-well at the quantum level. The same was true of the interaction between QW excitons and mechanical vibrations of a disk. The development of these theories along this thesis has been an important ingredient of its advances, leading us to a quantitative analysis of the generic parameters of hybrid quantum-well optomechanics introduced in the previous chapter.

2.1 Electromagnetic modes of a dielectric disk : Whispering Gallery Modes

2.1.1 General discussion

In this discussion, a microdisk refers to a piece of semiconductor shaped like a disk with a μm-scale radius R and a thickness h comparable to $\frac{\lambda}{n}$, where n is the refractive index of the material, with a value usually close to 3 for III-V semiconductors. Such a structure supports confined electromagnetic modes located close to the periphery of the disk called Whispering Gallery Modes (WGMs) [1]. Their analysis starts with Maxwell equations without source terms :

$$\boldsymbol{\nabla}.(\varepsilon \boldsymbol{E}) = 0 \tag{2.1}$$
$$\boldsymbol{\nabla}.(\mu_0 \boldsymbol{H}) = 0 \tag{2.2}$$
$$\boldsymbol{\nabla} \times \boldsymbol{E} = -j\omega\mu_0 \boldsymbol{H} \tag{2.3}$$
$$\boldsymbol{\nabla} \times \boldsymbol{H} = j\omega\varepsilon \boldsymbol{E} \tag{2.4}$$

where $\varepsilon = \varepsilon_0 n^2$ is the dielectric permittivity of the material, considered here as non magnetic ($\mu = \mu_0$). A combination of these equations in Fourier space leads to the well known Helmoltz equation :

$$\boldsymbol{\Delta F} + \frac{n^2\omega^2}{c^2}\boldsymbol{F} = 0 \tag{2.5}$$

where $\boldsymbol{F}$ represents either the electric ($\boldsymbol{E}$) or magnetic field ($\boldsymbol{H}$) . The use of cylindrical coordinates (r, θ, z) is natural in a disk. The Laplacian operator in cylindrical coordinates is given by :

1. This atypical name is because WGMs were first discovered in the context of sound waves. In 1877 [114] Lord Rayleigh mentioned the term for the first time in an attempt to describe the peculiar acoustic of St-Paul cathedral's dome in London, where two persons can have a conversation by whispering along the dome regardless of the distance between them. The optical counterpart was studied later in a large variety of structures such as droplets, spheres, and of course disk.

$$\Delta F(r,\theta,z) = \begin{pmatrix} \left(\frac{\partial^2}{\partial r^2} + \frac{1}{r}\frac{\partial}{\partial r} + \frac{1}{r^2}\frac{\partial^2}{\partial \theta^2} + \frac{\partial^2}{\partial z^2}\right) F_r - \frac{F_r}{r^2} - \frac{2}{r^2}\frac{\partial F_\theta}{\partial \theta} \\ \left(\frac{\partial^2}{\partial r^2} + \frac{1}{r}\frac{\partial}{\partial r} + \frac{1}{r^2}\frac{\partial^2}{\partial \theta^2} + \frac{\partial^2}{\partial z^2}\right) F_\theta - \frac{F_\theta}{r^2} + \frac{2}{r^2}\frac{\partial F_r}{\partial \theta} \\ \left(\frac{\partial^2}{\partial r^2} + \frac{1}{r}\frac{\partial}{\partial r} + \frac{1}{r^2}\frac{\partial^2}{\partial \theta^2} + \frac{\partial^2}{\partial z^2}\right) F_z \end{pmatrix} \tag{2.6}$$

Inside a disk resonator of this thesis, the thickness is smaller than the radius ($h \ll R$ in our system $h/R \simeq 0.1$). It seems reasonable decouple the electromagnetic field variations along z from those along r and θ. However, even considering this last statement to hold true, there are no rigorous analytical solutions for the electromagnetic field in a such problem. Numerical simulations (FEM, FDTD) or the effective index approach, can be independently used to appreciatively obtain the spatial distribution of the electromagnetic modes. We develop here the second option that consists in transforming the dimensionality of the 3D problem into 2D+1. In the vertical z-direction, due to the step-index, the system will be treated as an infinite slab waveguide whose eigenwaves are categorized into two different groups: TE (transverse electric) modes, and TM (transverse magnetic) modes. Each group comes with its own "effective refractive index" n_{eff}, which corresponds to the refractive index "seen" by the TE or TM field in the 2D disk. Once that is accomplished we study the propagation of the electromagnetic field in the plane of the disk and consider this time the step-index in the radial direction [2]. This 2D+1 effective index method represents admittedly an approximation relying on strong assumptions, but it enables a useful analytic formulation of the electromagnetic field.

2.1.2 Modes in a slab waveguide

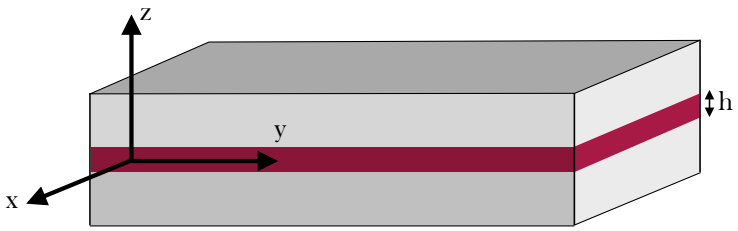

Figure 2.1 – Geometry of a slab waveguide. The structure is infinite in the x and y direction, the waveguide is formed by a semiconductor layer (red) with a refractive index $n = 3.5$ surrounded by vacuum $n = 1$ (gray).

We consider an infinite slab waveguide like in figure 2.1. Choosing a mode propagating in the y-direction, and invariant in x-direction, the nonzero components of the electromagnetic field can be written $\boldsymbol{F}(\boldsymbol{r}) = \boldsymbol{F}(x,z)e^{j(\omega t - \beta y)}$, with $\boldsymbol{F}_{TE} = (E_x, H_y, H_z)$ and $\boldsymbol{F}_{TM} = (E_y, E_z, H_x)$ for TE and TM polarization. Keeping the component in the plane of the slab and transverse to the propagation direction, the wave equation is :

2. In cylindrical coordinates for the 2D WGMs: TM modes - $(E_z, H_r, H_\theta \neq (0,0,0))$, TE modes - $(H_z, E_r, E_\theta \neq (0,0,0))$.

$$\frac{\partial^2}{\partial z^2}F_x(z) + (k_0^2 n(z)^2 - \beta^2)F_x(z) = 0 \tag{2.7}$$

with $k_0 = \omega\sqrt{\mu_0\varepsilon_0} = \frac{2\pi}{\lambda}$ the propagation constant in vacuum and $\beta = k_0 n_{\text{eff}}$ the propagation constant along the y-axis. We consider a symmetric slab of height h surrounded by vacuum, so $n(z) = n$ for $|z| \leq \frac{h}{2}$ and $n(z) = 1$ for $|z| > \frac{h}{2}$. We are interested in the guided modes of the slab. We use the ansatz of an oscillating field in the slab and exponentially decaying fields in the surroundings:

$$F_x(z) = A_\sigma e^{\gamma_z z} \quad \text{for } z < -\frac{h}{2} \tag{2.8}$$

$$F_x(z) = B_\sigma e^{jk_z z} + C_\sigma e^{-jk_z z} \quad \text{for } -\frac{h}{2} \leq z \leq \frac{h}{2} \tag{2.9}$$

$$F_x(z) = D_\sigma e^{-\gamma_z z} \quad \text{for } z > \frac{h}{2} \tag{2.10}$$

with $k_z = \sqrt{n^2 k_0^2 - \beta^2}$ and $\gamma_z = \sqrt{\beta^2 - k_0^2}$. $A_\sigma, B_\sigma, C_\sigma$ and D_σ are constants with σ the polarization TE or TM . The waveguide is symmetric, leading to identify two types of solutions: even and odd modes. In the case of vertically even modes the field is written as:

$$F_x(z) = A_\sigma e^{\gamma_z(z+\frac{h}{2})} \quad \text{for } z < -\frac{h}{2} \tag{2.11}$$

$$F_x(z) = B_\sigma \cos k_z z \quad \text{for } -\frac{h}{2} \leq z \leq \frac{h}{2} \tag{2.12}$$

$$F_x(z) = A_\sigma e^{-\gamma_z(z-\frac{h}{2})} \quad \text{for } z > \frac{h}{2} \tag{2.13}$$

For odd modes, the field is given by :

$$F_x(z) = -A_\sigma e^{\gamma_z(z+\frac{h}{2})} \quad \text{for } z < -\frac{h}{2} \tag{2.14}$$

$$F_x(z) = B_\sigma \sin k_z z \quad \text{for } -\frac{h}{2} \leq z \leq \frac{h}{2} \tag{2.15}$$

$$F_x(z) = A_\sigma e^{-\gamma_z(z-\frac{h}{2})} \quad \text{for } z > \frac{h}{2} \tag{2.16}$$

We focus now on TE modes, whose tangential component of the electric field (i.e. E_x) must be continue at $z = \pm\frac{h}{2}$ thus :

$$A_{TE} = B_{TE} \cos\frac{k_z h}{2} \quad \text{for even modes} \tag{2.17}$$

$$A_{TE} = B_{TE} \sin\frac{k_z h}{2} \quad \text{for odd modes} \tag{2.18}$$

The tangential component of the magnetic field (H_y) must also be continue at $z = \pm\frac{h}{2}$:

$$A_{TE}\gamma_z = B_{TE}k_z \sin\frac{k_z h}{2} \quad \text{for even modes} \tag{2.19}$$

$$-A_{TE}\gamma_z = B_{TE}k_z \cos\frac{k_z h}{2} \quad \text{for odd modes} \tag{2.20}$$

By assembling the previous relations, we obtain characteristic equations:

$$\frac{\gamma_z h}{2} = \frac{k_z h}{2}\tan\frac{k_z h}{2} \quad \text{for even modes} \tag{2.21}$$

$$-\frac{\gamma_z h}{2} = \frac{k_z h}{2}\cot\frac{k_z h}{2} \quad \text{for odd modes} \tag{2.22}$$

Certain specific values of γ_z and k_z can satisfy these equations, i.e. the guide only supports a discrete set of modes. These equations cannot be solved analytically in a close-form, and are rather treated with a numerical solver. [3]

For TM modes the procedure is the same, and yields:

$$\frac{\gamma_z h}{2} = \frac{1}{n^2}\frac{k_z h}{2}\tan\frac{k_z h}{2} \quad \text{for even modes} \tag{2.25}$$

$$-\frac{\gamma_z h}{2} = \frac{1}{n^2}\frac{k_z h}{2}\cot\frac{k_z h}{2} \quad \text{for even modes} \tag{2.26}$$

The effective indices calculated for the first modes of a slab of interest for us are plotted in figure 2.2-(a). Given the thickness of our disk, 200 nm, it seems reasonable to take into account only the first symmetric (even) TE and TM mode, as shown in figure 2.2 (b)).

3. However one can also remark that:

$$\begin{aligned}\left(\frac{\gamma_z h}{2}\right)^2 + \left(\frac{k_z h}{2}\right)^2 &= \frac{(\beta^2 - k_0^2)h^2}{4} + \frac{(k_0^2 n^2 - \beta^2)h^2}{4} \\ &= (n^2-1)\left(\frac{k_0 h}{2}\right)^2 \\ &= \mathcal{R}^2\end{aligned} \tag{2.23}$$

which describes a circle in the plane (γ_z, k_z). The solutions of the above characteristic equations are the intersections of the circle with the tangents and cotangents of the expressions (**??**) and (2.22). By increasing the thickness h or the step-index n, the number N of guided modes increases, obeying the relation:

$$N \leq \frac{2h}{\lambda}\sqrt{n^2-1} \tag{2.24}$$

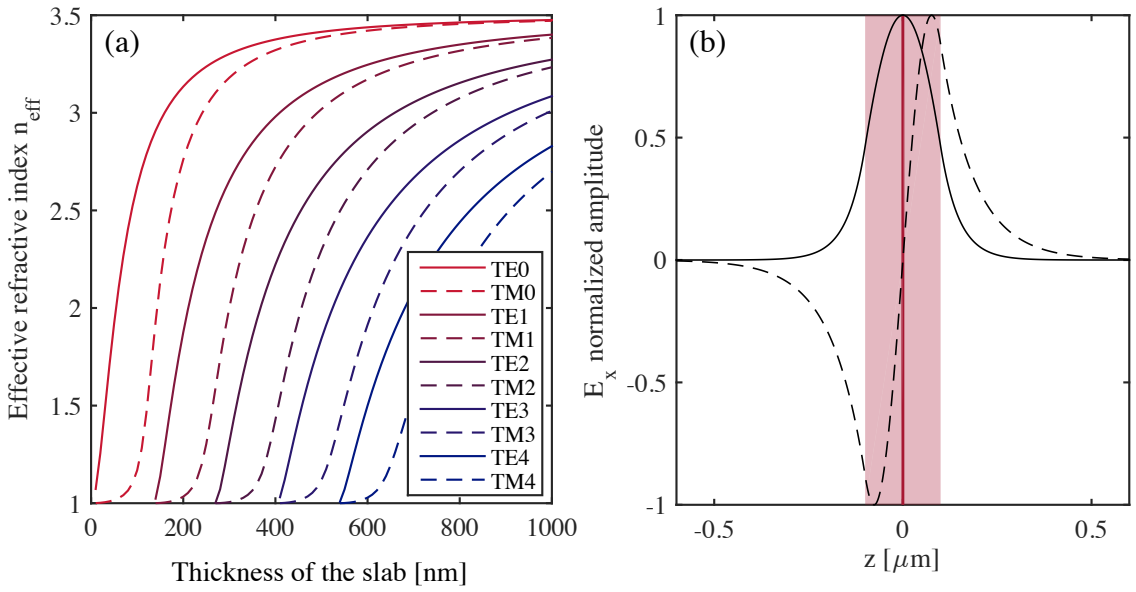

Figure 2.2 – (a) Effective index for the first five modes TE and TM, as a function the of slab thickness h. $\lambda = 900$ nm and n=3.5. (b) First two TE modes, TE0 (solid dark) and TE1 (dashed dark) for a 200nm thick slab, $\lambda = 900$ nm. The light red region represents the slab waveguide and the dark red line indicate a centered position for a quantum well.

Effective length, area, and volume of an electromagnetic mode: The effective mode length, area, volume are intrinsic characteristics of an electromagnetic mode defined through the ratio between the energy stored within the mode and the maximum energy density. For the 3D case of a volume, it is expressed as [4]:

$$\begin{aligned} V_{\text{eff}} &= \frac{1}{M} \iiint \frac{\varepsilon(\boldsymbol{r})}{2}|E(\boldsymbol{r})|^2 + \frac{\mu_0}{2}|H(\boldsymbol{r})|^2 d^3\boldsymbol{r} \\ M &= \max\left(\frac{\varepsilon(\boldsymbol{r})}{2}|E(\boldsymbol{r})|^2 + \frac{\mu_0}{2}|H(\boldsymbol{r})|^2\right) \end{aligned} \tag{2.27}$$

Mode volume is a piece of precious information, it appears in a large variety of physical parameters such as the lasing threshold or the Purcell Factor. Energy losses by diffraction and diffusion are usually assumed to be negligible so that the contribution of the electric field and the magnetic field to the energy density is equal (energy conservation law) :

$$\iiint \left\langle \frac{\varepsilon(\boldsymbol{r})}{2}|E(\boldsymbol{r})|^2 d(\boldsymbol{r}) \right\rangle = \iiint \left\langle \frac{\mu_0}{2}|H(\boldsymbol{r})|^2 d(\boldsymbol{r}) \right\rangle \tag{2.28}$$

4. The definition of the mode volume is an open question: it depends on the physical problem studied and different expressions can be found in the literature. Integrating over the entire space can sometimes leads to a diverging integral, but this issue is mostly ignored and overcome by integrating over a finite integration domain. Several other definitions independent of the computing volume are available for this calculation [115], however, the corrections obtained thanks to these methods are relatively small, especially for modes with a high-quality factor.

with $\langle ... \rangle$ the temporal mean value, we therefore obtain [116] :

$$V_{\text{eff}} = \frac{1}{M} \iiint \left\langle \varepsilon(\boldsymbol{r}) |E(\boldsymbol{r})|^2 \right\rangle d^3\boldsymbol{r}, \quad M = \max \left\langle \varepsilon(\boldsymbol{r}) |E(\boldsymbol{r})|^2 \right\rangle \tag{2.29}$$

This definition is independent of the chosen field normalization coefficient.

In the case of the slab waveguide, one single dimension (z) is relevant, and the meaningful notion is that of an effective length :

$$L_{\text{eff}} = \frac{1}{M} \int_{-\infty}^{+\infty} dz \left\langle \varepsilon(z) |E(z)|^2 \right\rangle, M = \max \left\langle \varepsilon(z) |E(z)|^2 \right\rangle \tag{2.30}$$

As an example, of analytic expression, for the first even TE mode (TE_0), we get:

$$\begin{aligned} L_{\text{eff}} =& \frac{1}{M} \int_{-\infty}^{\frac{-h}{2}} dz \varepsilon_0 \cos\left(k_z \frac{h}{2}\right)^2 e^{2\gamma_z \left(z + \frac{h}{2}\right)} + \frac{1}{M} \int_{\frac{-h}{2}}^{\frac{h}{2}} dz \varepsilon \cos\left(k_z\right)^2 \\ &+ \frac{1}{M} \int_{\frac{h}{2}}^{\infty} dz \varepsilon_0 \cos\left(k_z \frac{h}{2}\right)^2 e^{-2\gamma_z \left(z - \frac{h}{2}\right)} \\ L_{\text{eff}} =& \frac{1}{M} \left[\frac{\varepsilon}{2k_z} \sin\left(k_z h\right) + \frac{\varepsilon_0}{\gamma_z} \cos\left(k_z \frac{h}{2}\right)^2 \right] \end{aligned} \tag{2.31}$$

With a wavelength $\lambda = 900$ nm, and a thickness $h = 200$ nm, the effective length is $L_{\text{eff}} = 138.67$ nm, with the effective index $n_{\text{eff}} = 3.1341$.

2.1.3 Whispering Gallery Modes

In the previous section, we obtained an effective index for the slab and calculated the dependence of the field in the z-direction. We consider now the effect of the radial confinement in the disk. Looking at the Laplacian in cylindrical coordinate (2.6), we notice that the only independent component is F_z. A separation of variables can be performed $F_z(r, \theta, z) = F_{z,\parallel}(r, \theta) F_{z,\perp}(z) = \Psi(r)\Lambda(\theta)X(z)$, where $F_{z,\parallel}$ is the field imposed by the radial confinement (in the plane of the disk) while $F_{z,\perp}$ is the field pattern imposed by the vertical confinement, calculated in the prior section 2.1.2. Inserting this ansatz in (2.6) leads to :

$$\begin{cases} \frac{d^2}{d\theta^2}\Lambda(\theta) + m^2\Lambda(\theta) = 0 \\ \frac{d^2}{dz^2}X(z) + \frac{\omega^2}{c^2}\left(n^2 - n_{\text{eff}}^2\right)X(z) = 0 \\ \left(\frac{d^2}{dr^2} + \frac{1}{r}\frac{d}{dr}\right)\Psi(r) + \left(\frac{n_{\text{eff}}^2\omega^2}{c^2} - \frac{m^2}{r^2}\right)\Psi(r) = 0 \end{cases} \tag{2.32}$$

The first equation is solved analytically $\Lambda(\theta) = Ae^{-jm\theta}$, where $m \in \mathbb{Z}$ is called the azimuthal number. The second equation is that of a slab waveguide solved previously. Posing $u = (\omega/c)n_{\text{eff}}r$, the third equation reads :

$$(u^2 \frac{\partial^2}{\partial u^2} + u \frac{\partial}{\partial u})\Psi(r) + (u^2 - m^2)\Psi(r) = 0 \tag{2.33}$$

If u is a complex number, the resonance frequencies ω possess an imaginary part. The time dependence of solutions is $e^{j\omega t}$. We pose $\omega = \omega_0 + j\kappa$ with $\kappa > 0$ to avoid divergence. The solutions of (2.33) are Bessel and Hankel functions of the first and second kind ($J_m(u)$, $Y_m(u)$, $H_m^{(1)}(u)$, $H_m^{(2)}(u)$). The field must be null at $r = 0$ ($u = 0$) in the disk, for both polarizations. Outside of the disk, the field should decrease toward zero. The first condition is only verified by the Bessel function of the first kind and the second by the Hankel function of the second kind. Hence:

$$\Psi(r) = \begin{cases} N_\sigma J_m(k n_{\text{eff}} r) & \text{for } r \leq R \\ N_\sigma B H_m^{(2)}(kr) & \text{for } r > R \end{cases} \tag{2.34}$$

with $n_{\text{eff}} \simeq 1$ in vacuum ($r > R$). N^σ is a normalization constant and $B = J_m(k n_{\text{eff}} R)/H_m^{(2)}(kR)$. The tangential components of the electric and magnetic field must be continuous at the interface (H_z, E_θ for TE polarization; and E_z, H_θ for TM polarization). We thus obtain to the following characteristic equations :

$$\begin{aligned} n_{\text{eff}}^{\text{TM}} \frac{\dot{J}_m(k n_{\text{eff}}^{\text{TM}} R)}{J_m(k n_{\text{eff}}^{\text{TM}} R)} &= \frac{\dot{H}_m^{(2)}(kR)}{H_m^{(2)}(kR)} \qquad \text{for TM modes} \\ \frac{\dot{J}_m(k n_{\text{eff}}^{TE} R)}{J_m(k n_{\text{eff}}^{TE} R)} &= n_{\text{eff}}^{TE} \frac{\dot{H}_m^{(2)}(kR)}{H_m^{(2)}(kR)} \qquad \text{for TE modes} \end{aligned} \tag{2.35}$$

For a m number, several solutions $k_{m,p}$ of equations (2.35) can exist: they are labeled thanks to a radial number p. The azimuthal number m represents the number of field oscillations around the disk, while its sign indicates if the phase propagation is "clockwise" ($m > 0$) or "counter-clockwise" ($m < 0$). The radial number p corresponds to the number of lobes of the field in the radial direction. The other components of the field are obtained through [5]:

$$\text{TM modes} \quad \begin{cases} H_r = \frac{m}{\omega\mu_0 r} E_z \\ H_\theta = \frac{-j}{\omega\mu_0} \frac{\partial E_z}{\partial r} \end{cases} \qquad \text{TE modes} \quad \begin{cases} E_r = \frac{-m}{\omega\varepsilon_0 \varepsilon_{\text{eff}}^{TE} r} H_z \\ E_\theta = \frac{j}{\omega\varepsilon_0 \varepsilon_{\text{eff}}^{(TE)}} \frac{\partial H_z}{\partial r} \end{cases} \tag{2.38}$$

and are represented in figure 2.3.

5. In a more detailed version for $r < R$:

$$\text{TM modes} \quad \begin{cases} H_r = \frac{N_{m,p}^{\text{TM}} m}{\omega\mu_0 r} J_m(\beta_{m,p} r) e^{-jm\theta} \\ H_\theta = -\frac{N_{m,p}^{\text{TM}} j}{\omega\mu_0} \left[\frac{m}{r} J_m(\beta_{m,p} r) - \beta_{m,p} J_{m+1}(\beta_{m,p} r)\right] e^{-jm\theta} \end{cases} \tag{2.36}$$

$$\text{TE modes} \quad \begin{cases} E_r = -\frac{N_{m,p}^{\text{TE}} m}{\omega\varepsilon_0 \varepsilon_{\text{eff}}^{(TE)} r} J_m(\beta_{m,p} r) e^{-jm\theta} \\ E_\theta = \frac{N_{m,p}^{\text{TE}} j}{\omega\varepsilon_0 \varepsilon_{\text{eff}}^{(TE)}} \left[\frac{m}{r} J_m(\beta_{m,p} r) - \beta_{m,p} J_{m+1}(\beta_{m,p} r)\right] e^{-jm\theta} \end{cases} \tag{2.37}$$

with $\beta_{m,p} = k_{m,p} n_{\text{eff}}^\sigma$.

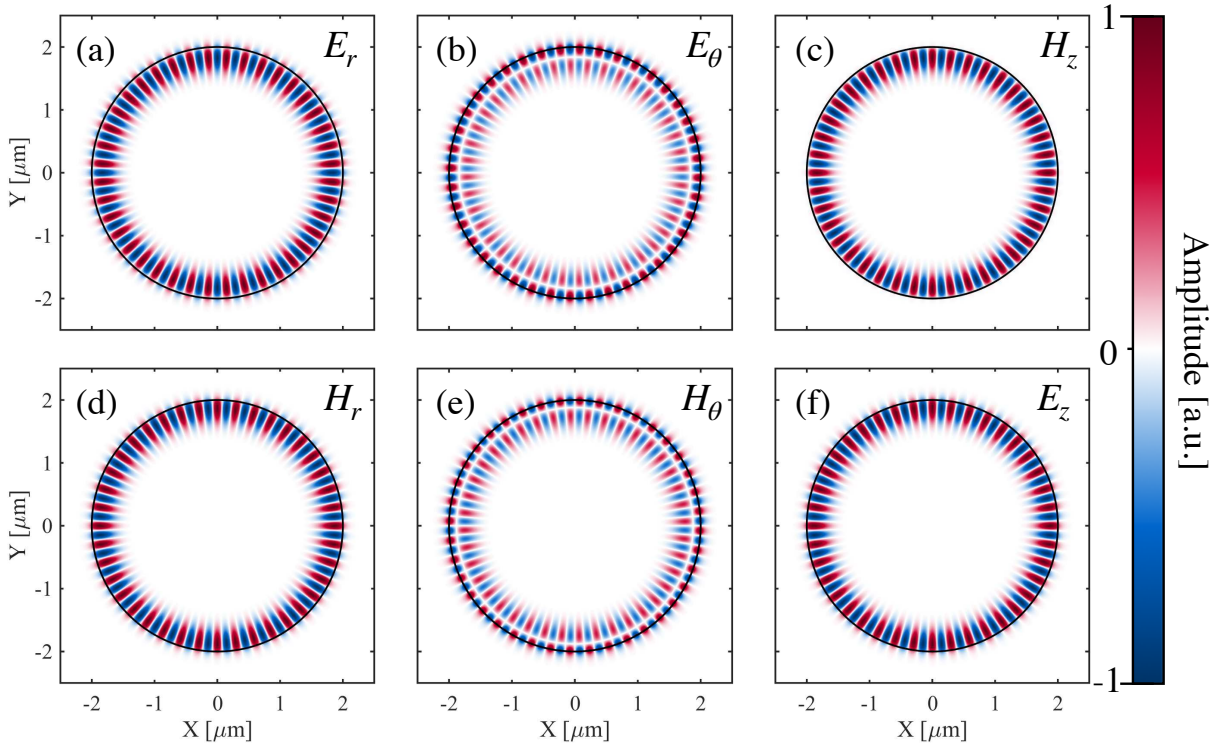

Figure 2.3 – Components of the electromagnetic field (real part) for a WGM $m = 40$ and $p = 1$ - (a)-(b)-(c) TE mode λ_c= 851.97 nm - $n_{\text{eff}}^{\text{TE}} \simeq 3.3$ - (d)-(e)-(f) TM mode λ_c= 855.59 nm. $n_{\text{eff}}^{\text{TE}} \simeq 3.1$

We will later make use of a compact notation involving circularly polarized components of the electromagnetic field: the normalized complex vectors $\boldsymbol{E}_+$ and $\boldsymbol{E}_-$ defined by:

$$\boldsymbol{E}_\pm = E_\pm \frac{(\boldsymbol{x} \mp j\boldsymbol{y})}{\sqrt{2}} e^{j\omega t} \tag{2.39}$$

where $E_\pm = |E_\pm| e^{j\delta_\pm}$ is a complex-valued scalar quantity. Introducing the short-hand basis:

$$\boldsymbol{v}_+ = \frac{\boldsymbol{x} - j\boldsymbol{y}}{\sqrt{2}} = \frac{e^{-j\theta}}{\sqrt{2}}(\boldsymbol{r} - j\boldsymbol{\theta}) = \boldsymbol{v}_-^* \qquad \boldsymbol{v}_- = \frac{\boldsymbol{x} + j\boldsymbol{y}}{\sqrt{2}} = \frac{e^{j\theta}}{\sqrt{2}}(\boldsymbol{r} + j\boldsymbol{\theta}) = \boldsymbol{v}_+^* \tag{2.40}$$

one can write any electromagnetic field as a linear superposition:

$$\boldsymbol{E} = E_x\boldsymbol{x} + E_y\boldsymbol{x} + E_z\boldsymbol{z} = E_r\boldsymbol{r} + E_\theta\boldsymbol{\theta} + E_z\boldsymbol{z} = E_+\boldsymbol{v}_+ + E_-\boldsymbol{v}_- + E_z\boldsymbol{z} \tag{2.41}$$

From the transfer matrices,

$$\begin{bmatrix} \boldsymbol{v}_+ \\ \boldsymbol{v}_- \\ \boldsymbol{z} \end{bmatrix} = \frac{1}{\sqrt{2}} \begin{pmatrix} 1 & -j & 0 \\ 1 & j & 0 \\ 0 & 0 & 1 \end{pmatrix} \begin{bmatrix} \boldsymbol{x} \\ \boldsymbol{y} \\ \boldsymbol{z} \end{bmatrix} \quad , \quad \begin{bmatrix} \boldsymbol{v}_+ \\ \boldsymbol{v}_- \\ \boldsymbol{z} \end{bmatrix} = \frac{1}{\sqrt{2}} \begin{pmatrix} e^{-j\theta} & -je^{-j\theta} & 0 \\ e^{j\theta} & je^{j\theta} & 0 \\ 0 & 0 & 1 \end{pmatrix} \begin{bmatrix} \boldsymbol{r} \\ \boldsymbol{\theta} \\ \boldsymbol{z} \end{bmatrix} \tag{2.42}$$

we can deduce the following relations:

$$E_{\pm} = \frac{(E_x \pm jE_y)}{\sqrt{2}} = e^{\pm j\theta}\frac{(E_r \pm jE_\theta)}{\sqrt{2}} \tag{2.43}$$

For the WGMs we obtain (for $r < R$):

$$E_r \pm jE_\theta = -\frac{N^{\mathrm{TE}}_{m,p}\beta_{m,p}}{\omega\varepsilon_0\varepsilon_{\mathrm{eff}}}J_{m\mp1}(\beta_{m,p}r)e^{-jm\theta} \tag{2.44}$$

$$H_r \pm jH_\theta = \frac{N^{\mathrm{TM}}_{m,p}\beta_{m,p}}{\omega\mu_0}J_{m\mp1}(\beta_{m,p}r)e^{-jm\theta} \tag{2.45}$$

which gives the following expression for the circularly polarized electric field (for $r < R$):

$$\boldsymbol{E}_{\pm} = -\frac{N^{\mathrm{TE}}_{m,p}\beta_{m,p}}{\sqrt{2}\omega\varepsilon_0\varepsilon_{\mathrm{eff}}}J_{m\mp1}(\beta_{m,p}r)e^{-j(m\mp1)\theta}\boldsymbol{v}_{\pm} \tag{2.46}$$

,which are represented in figure 2.4.

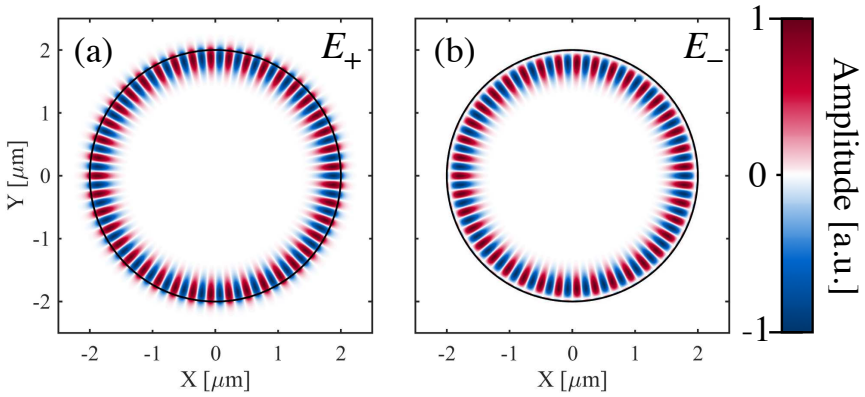

Figure 2.4 – Circularly polarized components of the electromagnetic field (real part) for a TE WGM ($m = 40$ and $p = 1$) at λ_c= 851.97 nm. $n^{\mathrm{TE}}_{\mathrm{eff}} \simeq 3.3$.

We compute the effective area of such mode confined in the 2D disk:

$$A_{\mathrm{eff}} = \frac{1}{M}\iint rdrd\theta\left\langle\varepsilon(r)|E(r,\theta)|^2\right\rangle, \quad M = \max\left\langle\varepsilon(r)|E(r,\theta)|^2\right\rangle \tag{2.47}$$

Using the basis of circularly polarized fields, we obtain :

$$
\begin{aligned}
A_{\text{eff}}^{m,p} &= \frac{1}{M}\int_0^{2\pi}\int_0^{\infty} r dr d\theta \varepsilon_0 \varepsilon_{\text{eff}}^{(\text{TE})} \left[E_+ E_+^* + E_- E_-^*\right] \\
&= \frac{2\pi}{M}\int_0^{R} r dr \left(\varepsilon_0 \varepsilon_{\text{eff}}^{(\text{TE})} \left(\frac{N_{m,p}^{\text{TE}} \beta_{m,p}}{\omega \varepsilon_0 \varepsilon_{\text{eff}}^{(\text{TE})}\sqrt{2}}\right)^2 \left[J_{m+1}^2(\beta_{m,p} r) + J_{m-1}^2(\beta_{m,p} r)\right]\right) \\
&+ \frac{2\pi}{M}\int_R^{\infty} r dr \left(\varepsilon_0 \left(\frac{N_{m,p}^{\text{TE}} B k_{m,p}}{\omega \varepsilon_0 \sqrt{2}}\right)^2 \left[H_{m+1}^2(k_{m,p} r) + H_{m-1}^2(k_{m,p} r)\right]\right)
\end{aligned}
\tag{2.48}
$$

Similar results can be obtained using the cylindrical basis, since $E_+E_+^* + E_-E_-^* = E_r E_r^* + E_\theta E_\theta^*$. The expression of $A_{\text{eff}}^{m,p}$ does eventually not depend on the normalization coefficient $N_{m,p}^{\text{TE}}\beta_{m,p}$ which appears in M as well. Using this formula for a TE mode with $m = 41$ and $p = 1$, we find an effective area $A_{\text{eff}} = 2.654\ \mu m^2$ for a disk of radius $R = 2\ \mu$m, $n_{\text{eff}}^{\text{TE}} = 3.26$.

2D+1 WGMs

The full 3D spatial distribution of the electromagnetic field can now be expressed, by multiplying the slab waveguide vertical variation (section 2.1.2) by the in-plane variations within the 2D disk (section 2.1.3): we get for $r < R$,

$$
\begin{aligned}
\boldsymbol{E}_{m,p}^{\text{TE}} &= \left[\boldsymbol{E}_+(r,\theta) + \boldsymbol{E}_-(r,\theta)\right] E_x(z) = \boldsymbol{E}_{m,p}(r,\theta) E_x(z) \\
&= E_{0-m,p}^{(\text{TE})} E_x(z) \left[J_{m-1}(\beta_{m,p} r) e^{-j(m-1)\theta} \boldsymbol{v}_+ + J_{m+1}(\beta_{m,p} r) e^{-j(m+1)\theta} \boldsymbol{v}_-\right]
\end{aligned}
\tag{2.49}
$$

$$
\begin{aligned}
\boldsymbol{E}_{m,p}^{\text{TM}} &= \boldsymbol{E_z}(r,\theta) E_z(z) = -\frac{1}{j\omega\varepsilon_0\varepsilon_r}\frac{\partial H_x}{\partial y}\boldsymbol{E_z}(r,\theta) \\
&= E_{0-m,p}^{(\text{TM})} J_m(\beta_{m,p} r) e^{im\theta} H_x(z) \boldsymbol{z}
\end{aligned}
\tag{2.50}
$$

where the normalization factors introduced in previous relations (A_σ,B_σ,$N_{m,p}^\sigma$...) have been merged into a single coefficient $E_{0-m,p}^\sigma$. Figure 2.5 provides a comparative view of the electric field distribution in the disk, obtained either with our (2D+1) analytic model or with 2D-axisymmetric FEM-simulations. The profile is almost identical: a small difference remains in the predicted frequency of the mode (0.09 % error).

Using the expression (2.49) the effective (3D) volume in the TE case takes this form :

$$
\begin{aligned}
V_{\text{eff}} &= \frac{1}{M}\iiint \left\langle \varepsilon(\boldsymbol{r}) |E(\boldsymbol{r})|^2 \right\rangle d\boldsymbol{V}, \quad M = \max\left\langle \varepsilon(\boldsymbol{r}) |E(\boldsymbol{r})|^2 \right\rangle \\
&= \frac{1}{2M}\int_{-\infty}^{+\infty}\int_0^{2\pi}\int_0^{+\infty} r dr d\theta dz \varepsilon_0 \varepsilon_r(r,z) \left[E_+ E_+^*(r,\theta) + E_- E_-^*(r,\theta)\right] |E_x(z)|^2
\end{aligned}
\tag{2.51}
$$

where the permittivity $\varepsilon_r(r,z)$ is described by the following function :

$$
\varepsilon_r(r,z) = 1 + (\varepsilon_r - 1) \times \Pi\left(\frac{z}{h}\right) \times \tilde{H}(r - R) \tag{2.52}
$$

with

$$\Pi(z) = \begin{cases} 1 & \text{for} \quad -\frac{1}{2} \leq z \leq \frac{1}{2} \\ 0 & \text{for} \quad |z| > \frac{1}{2} \end{cases} \qquad \text{and} \qquad \tilde{H}(r) = \begin{cases} 1 & \text{for} \quad r \leq 0 \\ 0 & \text{for} \quad r > 0 \end{cases} \tag{2.53}$$

The final expression of the effective volume is therefore :

$$\begin{aligned} V_{\text{eff}}^{m,p} = & \frac{1}{M} \int_{-\infty}^{+\infty} dz |E_x(z)|^2 \int_0^{2\pi} \int_0^{+\infty} r dr d\theta \varepsilon_0 \left[E_+ E_+^*(r,\theta) + E_- E_-^*(r,\theta) \right] \\ & + \frac{1}{M} \int_{-h/2}^{+h/2} dz |E_x(z)|^2 \int_0^{2\pi} \int_0^{R} r dr d\theta \varepsilon_0 (\varepsilon_r - 1) \left[E_+ E_+^*(r,\theta) + E_- E_-^*(r,\theta) \right] \end{aligned} \tag{2.54}$$

This expression differs from that one would obtain by simply multiplying the prior effective length (eq. (2.31)) and effective area (eq. (2.48)). For a TE mode with $m = 41$ and $p = 1$, represented in figure 2.5, the effective volume is equal to 0.181 $\mu m^3 \simeq 7.5(\lambda/n)^3$ (i.e. $\simeq 7.2\%$ of the microdisk volume) consistent with values reported in [117, 118] for different wavelength range/material. FEM simulations predict a similar value $\simeq 0.179$ μm^3.

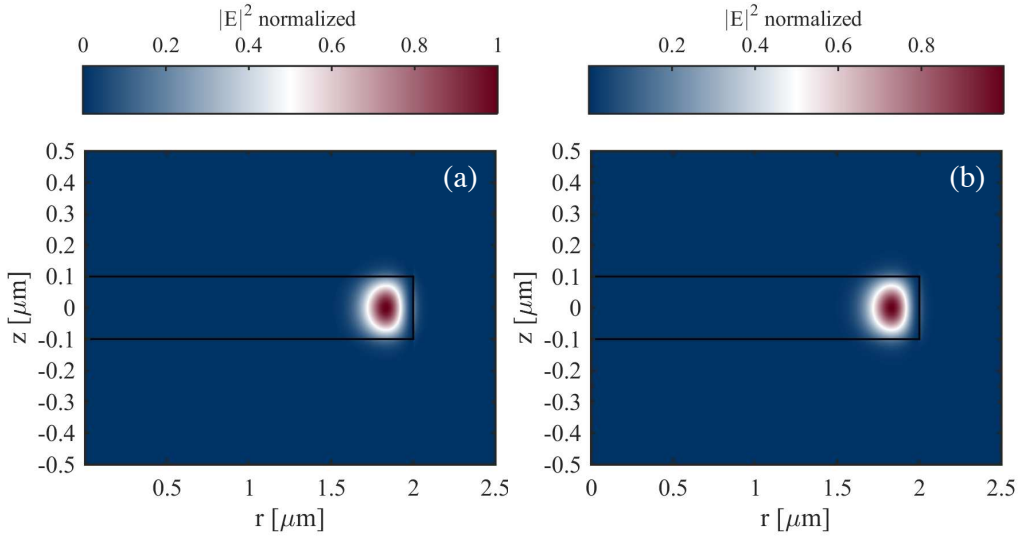

Figure 2.5 – Norm of the electric field for a TE WGM ($m = 41$ and $p = 1$), obtained with our 2D+1 model (a) λ_c= 860.35 nm, and with FEM simulation (b) λ_c= 859.58 nm. Disk radius $R = 2$ μm; thickness $h = 200$nm

2.1.4 Quantization of the electromagnetic field and vector potential

This section aims to express the field operators in terms of the normal modes found above. The expression will serve then to treat the interaction between light and matter.

Without following the strict procedure of quantization of the electromagnetic field, using a Lagrangian approach, we highlight here the similarities between the Hamiltonian of the electromagnetic field and that from a harmonic oscillator, identify the corresponding momentum and position operators, before writing these in terms of annihilation and creation operators. For more details on the procedure, see [119].

We start back with Helmholtz equation (2.5), which we rewrite for convenience :

$$\begin{cases} \nabla^2 \boldsymbol{E} + \frac{n^2}{c^2} \frac{\partial^2 \boldsymbol{E}}{\partial t^2} = 0 \\ \nabla^2 \boldsymbol{H} + \frac{n^2}{c^2} \frac{\partial^2 \boldsymbol{H}}{\partial t^2} = 0 \end{cases} \tag{2.55}$$

A solution can be written as an expansion in normal modes, where the time dependence and the spatial variations are separated:

$$\boldsymbol{E}(\boldsymbol{r}, t) = \sum_n A_n(t) \boldsymbol{u_n}(\boldsymbol{r}) \tag{2.56}$$

The normal modes $\{\boldsymbol{u_n}\}$ form a basis and obey the bulk and boundary conditions of Maxwell's equations:

$$\nabla^2 u_n = -k_n^2 u_n \qquad \nabla \cdot \boldsymbol{u_n} = 0 \qquad \boldsymbol{n}_\perp \times \boldsymbol{u_n} = \boldsymbol{0} \tag{2.57}$$

where $\boldsymbol{n}_\perp$ is a unit vector normal to the boundary surface [6]. The modes also satisfy the orthonormality condition :

$$\int \boldsymbol{u_n}(\boldsymbol{r}) \boldsymbol{u}^*_{\boldsymbol{n'}}(\boldsymbol{r}) d^3\boldsymbol{r} = \delta_{n,n'} \tag{2.58}$$

Substituting the expression (2.57) in the wave equation leads to an equation for $A_n(t)$:

$$\sum_n \frac{d^2 A_n(t)}{dt^2} + \frac{c^2}{n^2} k_n^2 A_n(t) = 0 \tag{2.59}$$

Since the modes are independent :

$$\frac{d^2 A_n(t)}{dt^2} + \frac{c^2}{n^2} k_n^2 A_n(t) = 0 \tag{2.60}$$

This equation is that of an harmonic oscillator with frequency $\omega_n = ck_n/n$, hence $A_n(t) \propto e^{\pm j\omega_n t}$. In a similar fashion we can express the magnetic field with a separation of variables, $\boldsymbol{H}(\boldsymbol{r}, t) = \sum_n B_n(t) \nabla \times \boldsymbol{u_n}(\boldsymbol{r})$, where the coefficient B_n must satisfy Maxwell's equations:

$$\begin{aligned} \nabla \times \boldsymbol{E} = -\mu_0 \frac{\partial \boldsymbol{H}}{\partial t} \;\Rightarrow\; \sum_n A_n(t) \nabla \times \boldsymbol{u_n} &= -\mu_0 \sum_n \partial_t B_n(t) \nabla \times \boldsymbol{u_n} \\ \Rightarrow \frac{dB_n(t)}{dt} &= -\frac{1}{\mu_0} A_n(t) \end{aligned} \tag{2.61}$$

6. This third condition is imposed because the mode are considered transverse toward infinity

Using Maxwell Ampere equation, we see that B_n obeys an harmonic oscillator equation as well:

$$\frac{d^2 B_n(t)}{dt^2} + \frac{c^2}{n^2} k_n^2 B_n(t) = 0 \tag{2.62}$$

For the sake of clarity, we write the energy as function of the real fields $\boldsymbol{E}_0$ and $\boldsymbol{H}_0$:

$$\hat{H} = \frac{1}{2} \int d^3\boldsymbol{r} \left(\varepsilon \boldsymbol{E}_0^2 + \mu_0 \boldsymbol{H}_0^2 \right) \tag{2.63}$$

and substituting the expression of the electric and magnetic field we obtain:

$$\begin{aligned} \hat{H} = \frac{1}{2} \sum_{n',n} \Bigg(& \varepsilon A_n(t) A_{n'}(t) \int \boldsymbol{u_n}(\boldsymbol{r}) \boldsymbol{u_{n'}}(\boldsymbol{r}) d^3\boldsymbol{r} + \\ & \mu_0 B_n(t) B_{n'}(t) \int (\nabla \times \boldsymbol{u_n}(\boldsymbol{r})) \cdot (\nabla \times \boldsymbol{u_{n'}}(\boldsymbol{r})) d^3\boldsymbol{r} \Bigg) \\ = \sum_n \frac{1}{2} & \left(\varepsilon A_n^2(t) + \mu_0 k_n^2 B_n^2(t) \right) \end{aligned} \tag{2.64}$$

where we have used $\int (\nabla \times \boldsymbol{u_n}(\boldsymbol{r})) \cdot (\nabla \times \boldsymbol{u_{n'}}(\boldsymbol{r})) d^3\boldsymbol{r} = k_n^2 \delta_{n,n'}$. The electromagnetic Hamiltonian is hence similar to the Hamiltonian of a set of harmonic oscillators:

$$\hat{H}_{h.o.} = \sum_n \frac{1}{2} \left(\frac{P_n^2(t)}{2m} + m\omega_n^2 Q_n^2(t) \right) \tag{2.65}$$

with Q_n and $P_n = \frac{dQ_n}{dt}$ the position and momentum. We can hence identify A_n and B_n to an equivalent position and momentum:

$$Q_n(t) \quad \Longleftrightarrow \quad A_n(t) = \sqrt{\frac{m\omega_n^2}{\varepsilon}} Q_n(t) \tag{2.66}$$

$$P_n(t) \quad \Longleftrightarrow \quad B_n(t) = \sqrt{\frac{1}{\mu_0 k_n^2 m}} P_n(t) \tag{2.67}$$

The position and momentum are themselves quantized and associated to an operator:

$$\hat{Q}_n(t) = \sqrt{\frac{\hbar}{2m\omega_n}} \left(\hat{a}_n^\dagger(t) + \hat{a}_n(t) \right) \tag{2.68}$$

$$\hat{P}_n(t) = j\sqrt{\frac{\hbar m\omega_n}{2}} \left(\hat{a}_n^\dagger(t) - \hat{a}_n(t) \right) \tag{2.69}$$

with $\hat{a}_n$ and $\hat{a}_n^\dagger$ the annihilation and creation operator of the quantum harmonic oscillator (bosonic ladder operators). By analogy an operator is associated to the normal mode coefficients A_n and B_n :

$$\hat{A}_n(t) = \sqrt{\frac{\hbar\omega_n}{2\varepsilon}}\left(\hat{a}_n^\dagger(t) + \hat{a}_n(t)\right) \tag{2.70}$$

$$\hat{B}_n(t) = j\frac{c}{n}\sqrt{\frac{\hbar}{2\mu_0\omega_n}}\left(\hat{a}_n^\dagger(t) - \hat{a}_n(t)\right) \tag{2.71}$$

The electric and magnetic fields are defined as the sum over these normal modes. We can hence write the field operators at any position and time as [7]:

$$\hat{E}(\boldsymbol{r},t) = \sum_n \sqrt{\frac{\hbar\omega_n}{2\varepsilon}}\left(\hat{a}_n \boldsymbol{u}_n(\boldsymbol{r})e^{-j\omega_n t} + h.c\right) \tag{2.72}$$

$$\hat{H}(\boldsymbol{r},t) = -\sum_n j\frac{c}{n}\sqrt{\frac{\hbar}{2\mu_0\omega_n}}\left(\hat{a}_n \nabla\times\boldsymbol{u}_n(\boldsymbol{r})e^{-j\omega_n t} - h.c\right) \tag{2.73}$$

Given these expressions, the Hamiltonian of the system now reads:

$$\hat{H} = \sum_n \frac{\hbar\omega_n}{2}\left(\hat{a}_n^\dagger\hat{a}_n + \hat{a}_n\hat{a}_n^\dagger\right) = \sum_n \hbar\omega_n\left(\hat{a}_n^\dagger\hat{a}_n + \frac{1}{2}\right) \tag{2.74}$$

This derivation is general and valid for an electromagnetic system governed by equations (2.55) and (2.57). Going back to the WGMs of a dielectric resonator, we select a set of normal modes satisfying the conditions of orthonormality and the conditions (2.57):

$$\boldsymbol{u}_{m,p}(\boldsymbol{r}) = \frac{\boldsymbol{E}^\sigma_{m,p}(\boldsymbol{r})\sqrt{\varepsilon(\boldsymbol{r})}}{\sqrt{V_{\text{eff}}^{m,p}}\sqrt{\max\left(\varepsilon(\boldsymbol{r})\left|\boldsymbol{E}^\sigma_{m,p}(\boldsymbol{r})\right|^2\right)}} = \frac{\tilde{E}_{m,p}(\boldsymbol{r})\boldsymbol{e}_\sigma}{\sqrt{V_{\text{eff}}^{m,p}}} = \frac{\tilde{E}_x(z)\tilde{E}_{m,p}(r,\theta)(\boldsymbol{r})\boldsymbol{e}_\sigma}{\sqrt{V_{\text{eff}}^{m,p}}} \tag{2.75}$$

with $\boldsymbol{e}_\sigma$ the polarization vector of the mode. In the case of WGMs, the set of harmonic oscillators is no longer characterized by a unique quantum number n but by a couple of azimuthal and radial numbers m and p [8]. We can hence express the electric field operator for a disk resonator as:

$$\hat{\boldsymbol{E}}(\boldsymbol{r},t) = \sum_{m=-\infty}^{+\infty}\sum_{p=1}^{+\infty}\sqrt{\frac{\hbar\omega_{m,p}}{2\varepsilon V_{\text{eff}}^{m,p}}}\left(\hat{a}_{m,p}\tilde{E}_{m,p}(\boldsymbol{r})e^{-j\omega_{m,p}t}\boldsymbol{e}_\sigma + h.c.\right) \tag{2.76}$$

To obtain an expression of the vector potential operator, we need to choose a gauge. We choose the Coulomb gauge, where the vector potential is transverse ($\nabla\cdot\boldsymbol{A} = 0$) and in the absence of free charges, the scalar potential is null ($\Phi = 0$). In that case, the relation between the electric field and the vector potential is:

7. The evolution of the operator $\hat{a}_n(t)$ and $\hat{a}_n^\dagger(t)$ derives from the Heisenberg equation of motion $\frac{d\hat{a}_n}{dt} = -\frac{j}{\hbar}[\hat{H},\hat{a}_n(t)] = -j\omega_n\hat{a}_n$, hence $\hat{a}_n(t) = \hat{a}_n(0)e^{-j\omega_n t}$. For convenience we wrote $\hat{a}_n(0)$ as $\hat{a}_n$.

8. We consider in this thesis disks that are thin enough to only support the fundamental slab mode, hence we will not explicitly involve a third quantization number to parametrize the vertical confinement

$$\boldsymbol{E} = -\frac{\partial \boldsymbol{A}}{\partial t} \tag{2.77}$$

Implying that the electric field is also a transverse vector [9]. The vector potential operator expressed in the WGMs basis is:

$$\hat{\boldsymbol{A}}(\boldsymbol{r},t) = j \sum_{m=-\infty}^{+\infty} \sum_{p=1}^{+\infty} \sqrt{\frac{\hbar}{2\varepsilon\omega_{m,p} V_{\text{eff}}^{m,p}}} \left(\hat{a}_{m,p} \tilde{E}_{m,p}(\boldsymbol{r}) e^{-j\omega_{m,p}t} \boldsymbol{e}_\sigma - h.c. \right) \tag{2.78}$$

One can freely change the origin of the time in (2.78) and obtain the following equivalent expression for the vector potential:

$$\hat{\boldsymbol{A}}(\boldsymbol{r},t) = \sum_{m=-\infty}^{+\infty} \sum_{p=1}^{+\infty} \sqrt{\frac{\hbar}{2\varepsilon\omega_{m,p} V_{\text{eff}}^{m,p}}} \left(\hat{a}_{m,p} \tilde{E}_{m,p}(\boldsymbol{r}) e^{-j\omega_{m,p}t'} \boldsymbol{e}_\sigma + h.c. \right) \tag{2.79}$$

2.2 Mechanical modes of an elastic disk : Radial Breathing Modes

The vibrational modes of an elastic object can be determined by solving the linear equations of elasticity. The linear approximation is only valid for small strains (typically under 10^{-3}). The fundamental dynamics relation writes:

$$\rho \frac{\partial^2 u_i}{\partial t^2} = \partial_j \sigma_{ji} + F_i \tag{2.80}$$

where u_i is the i-component of the displacement, ρ the density of the material, σ_{ji} the ji-element of the stress-tensor, and F the external forces acting on the object. A linear relation between the stress and the strain is added to obtain the elastic equation. The mechanical eigenmodes have eigenfrequencies ω_m and a spatial pattern $\boldsymbol{u}(\boldsymbol{r})$.

$$\boldsymbol{u}(\boldsymbol{r},t) = \boldsymbol{u}(\boldsymbol{r}) \cos(\omega_m t) \tag{2.81}$$

The collection of mechanical modes of a disk embeds two categories of interest: "in-plane" modes and "out of plane" modes ("flexural modes"). If one assumes the elastic material to be isotropic, the elastic disk problem acquires a rotation-invariance along the disk vertical axis z [10]. In such case, once can write the displacement field spatial pattern as $u(r,\theta,z) = u(r,z)\cos(M\theta + \Phi)$, where $M \in \mathbb{Z}$ is called the mechanical azimuthal number. For $M = 0$, the mode presents an azimuthal invariant profile. Furthermore, as for the optical

9. In the 2D+1 approximate description, the divergence of a TM mode is actually not strictly null, as a consequence of the approximation.

10. Note that GaAs is not isotropic elastically, hence this assumption will serve only for first-order description

WGMs, there is a mechanical radial number P as well which indicates the number of radial oscillations [120]. Different approaches can be employed to solve for $u(r, z)$.

2.2.1 Analytical model

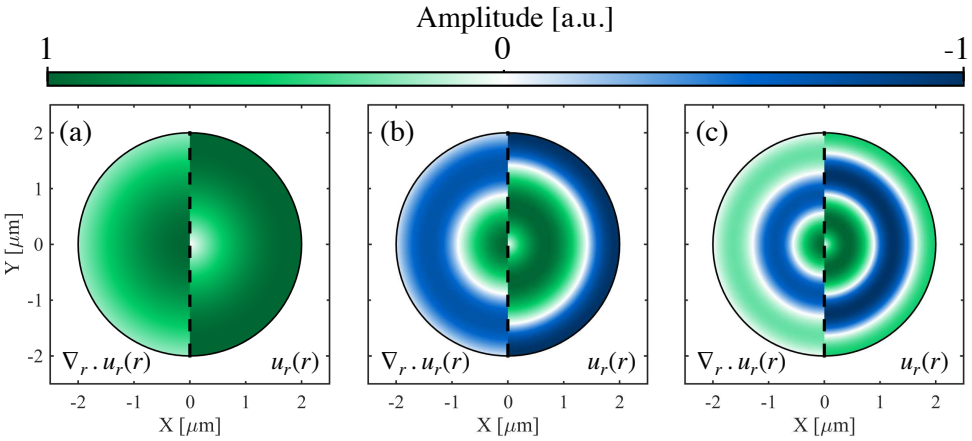

Figure 2.6 – Radial displacement $u_r(r)$ and strain $\nabla_r \cdot u_n(r)$ for the three first RBMs computed with the analytical model (a) RBM1 - (b) RBM2 - (c) RBM3

In this thesis, we are in particular interested in the "in-plane" modes, since they lead to a better optomechanical coupling with the WGMs. Three types of "in-plane" modes are generally discussed: Radial Breathing Modes (RBMs), tangential modes, and wineglass modes [121, 122]. From the optomechanical point of view, RBMs are the best candidates to obtain large coupling. At first order of description, and for a thin disk, one can approximate the deformation profile of a RBM, $\boldsymbol{u}(r, z) = u_r(r)\boldsymbol{r}$, hence neglecting at that stage the out-of-plane component u_z as well as the variation of u_r along z. Under these assumptions, and assuming plane-stress-conditions, there exists an analytic solution to this RBM problem [11] [113, 123, 124]:

$$\begin{aligned} u_n(r) &= A_n J_1(\alpha_n r) \\ \nabla_r \cdot u_n(r) = \frac{1}{r}\frac{\partial}{\partial r}\left[r u_n(r)\right] &= A_n \alpha_n J_0(\alpha_n R) \\ A_n^{-1} &= \sqrt{J_1^2(\alpha_n R) - J_0(\alpha_n R) J_0(\alpha_n R)} \end{aligned} \tag{2.82}$$

with A_n a normalization factor insuring that $\int_V d\boldsymbol{r} u_n(r) u_m(r) = V\delta_{n,m}$, R the radius of the disk, and α_n a constant depending on the properties of the material and the frequency of the mode:

$$\alpha_n = \omega_n \sqrt{\frac{\rho}{\left(\frac{E}{1+\sigma}\right) + \left(\frac{E\sigma}{1-\sigma^2}\right)}} \tag{2.83}$$

11. In this section the quantities u are dimensionless.

with ρ, E, and σ the density, Young modulus, and Poisson ratio of the material, reported in appendix C.1. RBMs of subsequent order are labeled with the number n. The eigenfrequency ω_n of the RBM of order n is found by solving the implicit equation:

$$\frac{\lambda_n J_0(\lambda_n)}{J_1(\lambda_n)} = 1 - \sigma \qquad \text{with} \qquad \lambda_n = \omega_m(n) R \sqrt{\frac{\rho(1-\sigma^2)}{E}} \tag{2.84}$$

λ_n has no dimension and only depends on the properties of the material. For a given λ_n, smaller disks have higher mechanical frequency (the frequency scales as $1/R$). The radial displacement and strain profile associated with the first three RBMs are represented in figure 2.6.

2.2.2 Numerical simulation

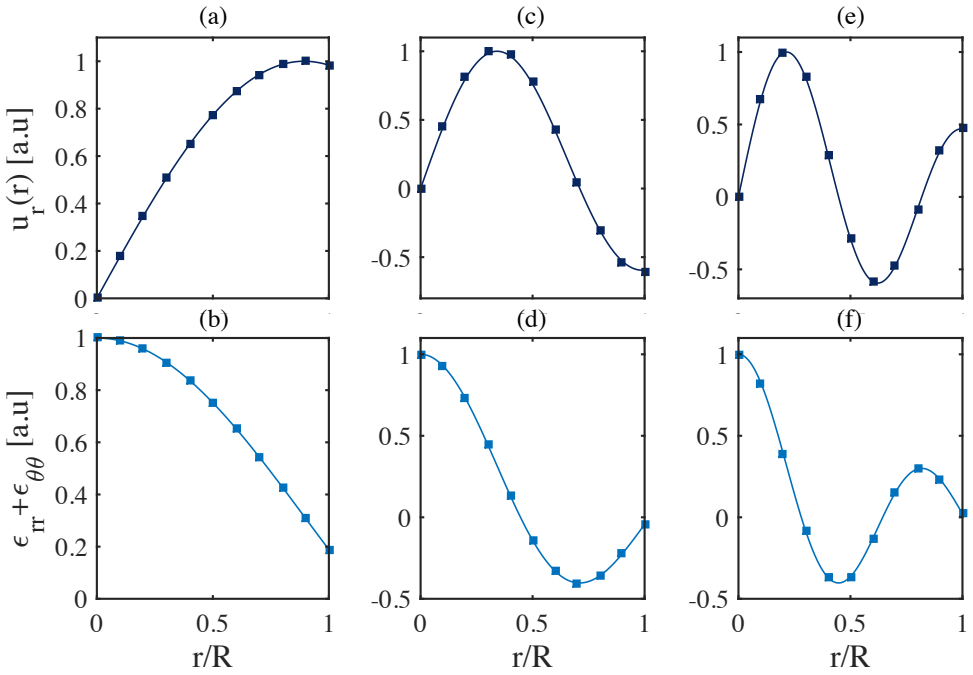

Figure 2.7 – Radial displacement $u_r(r)$ (dark blue) and strain $\nabla_r \cdot u_n(r)$ (light blue) profile for the three first RBMs obtain with 2D axis symmetric FEM simulations (continuous lines) and via the plane stress analytical model (square symbols). (a)-(b) RBM1 - (c)-(d) RBM2 - (e)(f) RBM3

We compare the results obtained via the above analytic approach with FEM simulations. As can be seen in figure 2.7, the results are almost identical, confirming the validity of the model. Table 2.1 lists the mechanical frequencies for the three first RBMs of our disk, calculated with the two approaches. The results are close (gap below 1%) for 2D axisymmetric and 3D simulations, especially for the RBM1. More pronounced differences among the different approaches appear for higher-order RBMs. One limitation of the analytical model is that u_r does not depend on z, which is only valid for the RBM1.

$\omega_m/2\pi$ [MHz]	Material	RBM1	RBM2	RBM3
Plane-stress analytical	Isotropic	695.9	1820.8	2894.7
2D axisymmetric FEM simulation	Isotropic	695.5	1815.2	2871.7
3D FEM simulation	Isotropic	695.5	1815.6	2873.6
3D FEM simulation	Anisotropic	708.6	1964.8	3145.5
3D FEM simulation (AlGaAs pedestal included)	Anisotropic	703.5	1849.6	2893.6

Table 2.1 – RBMs frequencies computed via different approaches

An important interest of FEM simulations is the possibility to include the effect of the pedestal supporting the disk and/or the anisotropy of the GaAs crystal. For the face-centered cubic lattice of GaAs, the thirty-six components of the elastic tensor C are reduced to three : C_{11}, C_{12}, C_{44}. Using such an anisotropic elastic tensor in the simulations leads to the profiles represented in figure 2.8. With pedestal and anisotropy, the values for the mechanical frequencies start deviating from the isotropic plane-stress model (Table 2.1).

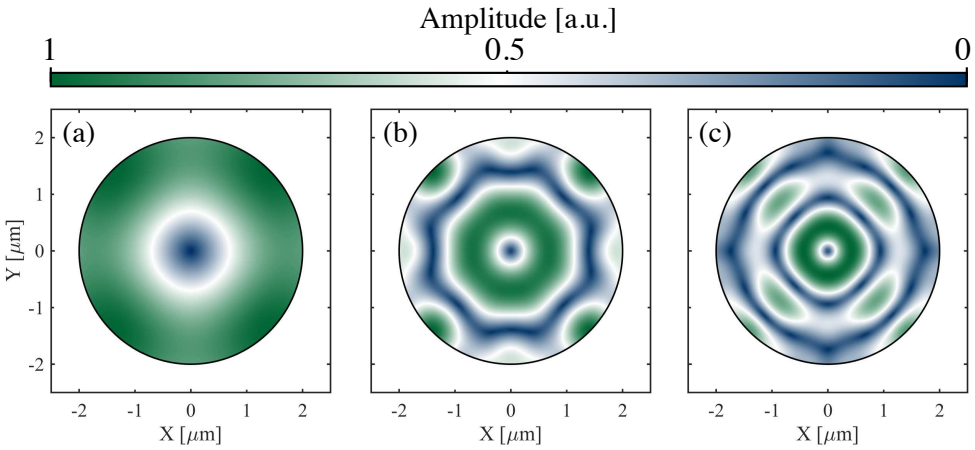

Figure 2.8 – Total displacement for the three first RBMs obtain via 3D FEM simulations including the anisotropy of the GaAs crystal. (a) RBM1 - (b) RBM2 - (c) RBM3

So far we considered our disk as constituted of a homogeneous GaAs whereas, in reality, different materials compose the disk layer, given the presence of the hetero-structure. Simulating the impact of the other materials by FEM simulations will be computationally costly since the involved material layers are extremely thin (typically a few nanometers). Besides, the mechanical properties of these alloys layers are close to those of plain GaAs (see appendix C.2). We hence assume that these few layers do not impact the values of mechanical frequency.

2.2.3 Effective mass and choice of the reduction point r_0

Our mechanical disk is a 3D vibrating object, which we would like to describe with an effective 1D mass on a spring picture. To do so, the displacement at a specific *reduction point*

r_0 will be taken as reference, which will in consequence determine an effective mass and an effective spring for each mechanical mode [125]. For a RBM in the plane-stress description, and a reduction point located at r_0 from the origin, the ratio of effective mass to the true mass of the disk is:

$$\frac{m_{\text{eff}}}{m} = \left(1 - \frac{J_0(\alpha_n r_0) J_2(\alpha_n r_0)}{J_1^2(\alpha_n r_0)}\right) \tag{2.85}$$

The notion of reduction point will be very useful to define optomechanical parameters such as the frequency-pull $g_{om} = -\partial\omega_c/\partial x$, which depends on the chosen reference displacement x. To circumvent the dependence of g_{om} on the chosen reduction point, we will instead use the vacuum coupling $g_0 = x_{\text{ZPF}} g_{om}$, with $x_{\text{ZPF}} = \sqrt{\hbar/(2m_{\text{eff}}\omega_m)}$.

Practically speaking, the reduction point is often chosen to sit on the disk periphery ($r_0 = R$): in that case for the three first RBMs we obtain a ratio m_{eff}/m of 0.789, 0.969, 0.988. The value of the effective mass can also be computed by FEM simulations: in this case, we generally chose the reduction point where the displacement is maximal.

2.3 Quantum-well excitons in a disk

2.3.1 Crystalline and electronic properties of GaAs

This section introduces some basic properties of GaAs that can be extended to other members of the III-V semiconductors group, like InAs or AlAs for instance. Most of the III-V compounds semiconductors grow in the zinc-blende structure, a structure formed by two intersecting face-centered cubic (FCC) lattices, which are shifted by one-quarter of the cubic space diagonal against each other. The reciprocal lattice of such structure is a body-centered cubic (BCC) lattice, whose first Brillouin zone (FBZ) is the Wigner-Seitz shown in figure 2.9 (a). It exhibits high symmetry points, like Γ, L, or X.

Eight electrons per unit cell contribute to the chemical bonds in the III-V group: three for Ga ($4s^2 4p^1$) and five for As ($4s^2 4p^3$). The s and p orbitals of neighboring atoms overlap and hybridize, forming bonding and antibonding orbitals. Since the crystal consists of a very large number of unit cells, these bonding, and antibonding orbitals form bands. The conduction band of the material is formed by the antibonding orbitals of the lowest energy: at the Γ point, the atomic part of the wavefunction in this band has a s orbital symmetry. The valence bands are formed by the highest energy bonding orbitals: in these bands, the wavefunction has a p symmetry for their atomic part. The band structure of GaAs is shown in figure 2.9 (b).

In absence of spin-orbit coupling, the three p bands are degenerated at the Γ point; the inclusion of the spin-orbit coupling lifts the degeneracy. p orbitals have an angular momentum $L = 1$, that sums with the spin, $J = L + S$, to get two possible values $J = 1/2$ or $J = 3/2$. This leads to two multiplets: a quadruplet with Γ_8 symmetry ($J = 3/2$) and a doublet with Γ_7 symmetry ($J = 1/2$). This last doublet has lower energy and gives rise to

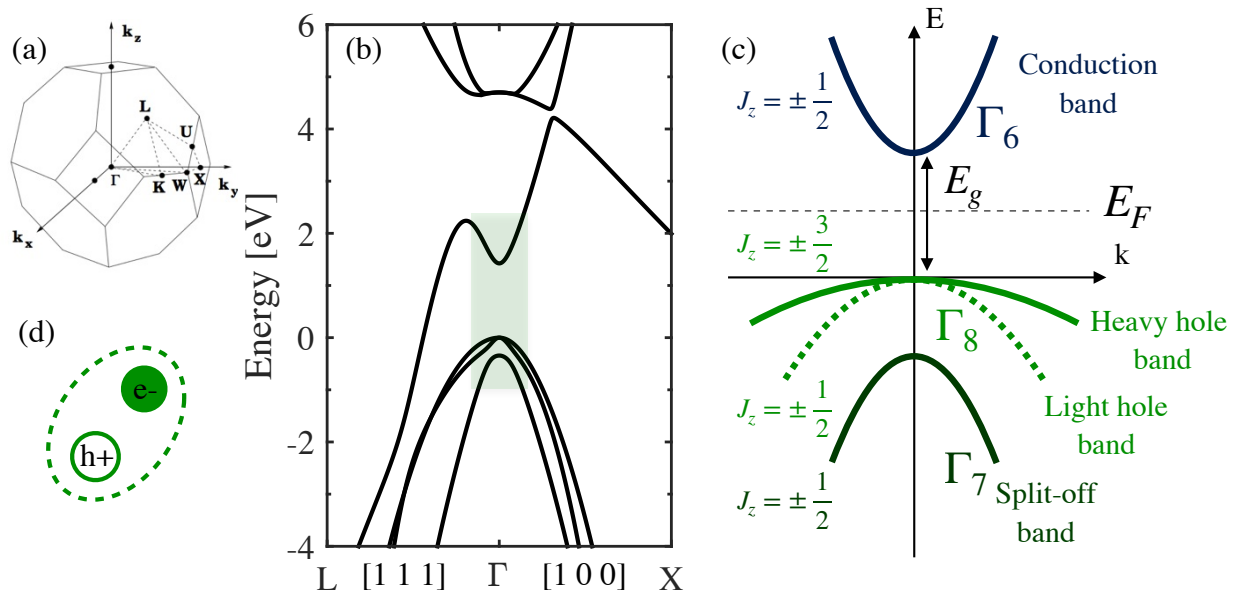

Figure 2.9 – (a) First Brillouin zone of a zinc-blende lattice (b) Electronic bandstructure of bulk GaAs computed with a 14-band $\boldsymbol{k} \cdot \boldsymbol{p}$ method [126, 127]. The green shaded area is schematized in (c), with four different bands around the Γ point, and a position of the Fermi level E_F between the conduction and valence band. (d) Schematic representation of a bound electron hole pair.

the so-called *split-off bands*. The Γ_8 quadruplet is subdivided into two doublets, according to the value of the angular momentum along z J_z. These two sub-bands have the same energy at $k = 0$ but their dispersion, hence effective mass is different. The band associated to $J_z = \pm 3/2$ is called *heavy hole band*, while that associated to $J_z = \pm 1/2$ is called *light hole band*. This four-band model is illustrated in figure 2.9 (c).

2.3.2 Exciton in bulk semiconductor

Exciton is the name given to the bound state of an electron-hole pair [12] (see scheme in figure 2.9 (d)). An exciton is hence a collective excitation of the many-body electrons system in the crystal, including the interaction between electrons. In a minimal $\boldsymbol{k} \cdot \boldsymbol{p}$ approach, semiconductor electrons are described by a model with two bands (valence and conduction), quadratic dispersion, and direct bandgap E_g [128]. The energy dispersion of the electron inside each band is given by:

12. Two types of excitons can be distinguished, mostly by the size and the binding energy: Frenkel and Wannier-Mott excitons, the latter having a Bohr radius much larger than the interatomic spacing of the crystal ($a_B \simeq 10$ nm) and weak binding energy ($E_b \simeq 1 - 10$ meV). The physical properties and therefore the type of excitons is determined by the value of the dielectric constant inside the material. A rather high value for the dielectric constant, like in semiconductors, leads to a screening of the effective electron-hole interaction, and thus to weaker binding energy, and large Bohr radius, i.e. Wannier-Mott excitons.

$$E_v(\boldsymbol{k}) = -\frac{\hbar^2 k^2}{2m_v^*}, \qquad E_c(\boldsymbol{k}) = E_g + \frac{\hbar^2 k^2}{2m_c^*}, \tag{2.86}$$

where m_c^* and m_v^* represents respectively the effective mass of conduction and valence electrons (the convention $m_c^*, m_v^* > 0$ has been used). In second quantization, the Hamiltonian without interaction, $\hat{H}_0$, takes the form:

$$\hat{H}_0 = \sum_k \left(E_v(\boldsymbol{k}) \hat{c}_{v\boldsymbol{k}}^\dagger \hat{c}_{v\boldsymbol{k}} + E_c(\boldsymbol{k}) \hat{c}_{c\boldsymbol{k}}^\dagger \hat{c}_{c\boldsymbol{k}} \right) \tag{2.87}$$

Here $\hat{c}_{v/c\boldsymbol{k}}$ and $\hat{c}_{v/c\boldsymbol{k}}^\dagger$ are the annihilation and creation operators for Bloch electrons in the valence and conduction band respectively. In the $\boldsymbol{r}$-representation, the wavefunction for the electron is:

$$\langle \boldsymbol{r} | \hat{c}_{\alpha\boldsymbol{k}}^\dagger | 0 \rangle = \langle \boldsymbol{r} | \alpha \boldsymbol{k} \rangle = \frac{1}{\sqrt{V}} e^{-j\boldsymbol{k}\boldsymbol{r}} u_{\alpha\boldsymbol{k}}(\boldsymbol{r}), \quad \alpha \equiv c/v \tag{2.88}$$

with V the quantization volume and $u_{\alpha\boldsymbol{k}}(\boldsymbol{r})$ the periodic Bloch function.

The Hamiltonian for the interband interaction between the valence and conduction electrons is given by [129, 130] (jellium model) :

$$\begin{aligned} \hat{H}_I &= \frac{1}{2} \sum_{\boldsymbol{k}_1\boldsymbol{k}_2\boldsymbol{k}_3\boldsymbol{k}_4}^{\boldsymbol{k}_1 \neq \boldsymbol{k}_4} f_{\boldsymbol{k}_1\boldsymbol{k}_2\boldsymbol{k}_3\boldsymbol{k}_4} \hat{c}_{v\boldsymbol{k}_1}^\dagger \hat{c}_{c\boldsymbol{k}_2}^\dagger \hat{c}_{c\boldsymbol{k}_3} \hat{c}_{v\boldsymbol{k}_4} \\ f_{\boldsymbol{k}_1\boldsymbol{k}_2\boldsymbol{k}_3\boldsymbol{k}_4} &= \langle \boldsymbol{k}_1 v, \boldsymbol{k}_2 c | \hat{V} | \boldsymbol{k}_3 c, \boldsymbol{k}_4 v \rangle = \frac{e^2}{\varepsilon_0 \varepsilon_r V} \frac{1}{|\boldsymbol{k}_1 - \boldsymbol{k}_4|^2} \delta_{\boldsymbol{k}_1 - \boldsymbol{k}_4, \boldsymbol{k}_3 - \boldsymbol{k}_2} \end{aligned} \tag{2.89}$$

Therefore the total exciton Hamiltonian reads :

$$\begin{aligned} \hat{H}_{ex} &= \hat{H}_0 + \hat{H}_I \\ &= \sum_{\boldsymbol{k}} \left(E_g + \frac{\hbar^2 \boldsymbol{k}^2}{2m_c^*} \right) \hat{c}_{c\boldsymbol{k}}^\dagger \hat{c}_{c\boldsymbol{k}} + \sum_{\boldsymbol{k}} \left(-\frac{\hbar^2 \boldsymbol{k}^2}{2m_v^*} \right) \hat{c}_{v\boldsymbol{k}}^\dagger \hat{c}_{v\boldsymbol{k}} \\ &+ \sum_{\boldsymbol{k}_1\boldsymbol{k}_2\boldsymbol{k}_3\boldsymbol{k}_4}^{\boldsymbol{k}_1 \neq \boldsymbol{k}_4} \frac{e^2}{4\pi\varepsilon_0 \varepsilon_r V} \frac{1}{|\boldsymbol{k}_1 - \boldsymbol{k}_4|^2} \hat{c}_{v\boldsymbol{k}_1}^\dagger \hat{c}_{c\boldsymbol{k}_2}^\dagger \hat{c}_{c\boldsymbol{k}_3} \hat{c}_{v\boldsymbol{k}_4} \delta_{\boldsymbol{k}_1 - \boldsymbol{k}_4, \boldsymbol{k}_3 - \boldsymbol{k}_2} \end{aligned} \tag{2.90}$$

The ground state of the system is found by occupying all electron states of the valence band: it is described by a Slater determinant [131]:

$$\Psi_0 = \mathbb{A}\{\psi_{v\boldsymbol{k_1}}(\boldsymbol{r_1}), \psi_{v\boldsymbol{k_2}}(\boldsymbol{r_2}), ..., \psi_{v\boldsymbol{k_N}}(\boldsymbol{r_N})\} \tag{2.91}$$

where the symbol $\mathbb{A}$ indicates the anti-symmetric state, and N is the total number of electrons in the crystal, or equivalently in second quantization :

$$|\Psi_0\rangle = \prod_{\boldsymbol{k}} \hat{c}_{v\boldsymbol{k}}^\dagger |\boldsymbol{0}\rangle \tag{2.92}$$

where $|\mathbf{0}\rangle = |0,0,...,0\rangle = |0\rangle \otimes |0\rangle \otimes ... \otimes |0\rangle$ is the many body vacuum state. $|\Psi_0\rangle$ is an eigenstate of the total Hamiltonian (2.90), with the following eigenvalue:

$$E_0 = \sum_{\boldsymbol{k}} E_v(\boldsymbol{k}) \tag{2.93}$$

The excited states correspond to superpositions of possibilities to promote one electron from the valence to the conduction band:

$$|\Psi\rangle = \sum_{\boldsymbol{k},\boldsymbol{k'}} O(\boldsymbol{k},\boldsymbol{k'}) \, |\boldsymbol{k},\boldsymbol{k'}\rangle = \sum_{\boldsymbol{k},\boldsymbol{k'}} O(\boldsymbol{k},\boldsymbol{k'}) \hat{c}^{\dagger}_{c\boldsymbol{k}} \hat{c}_{v\boldsymbol{k'}} \, |\Psi_0\rangle \tag{2.94}$$

The amplitude $O(\boldsymbol{k},\boldsymbol{k'})$ is an *envelope function* in the reciprocal space [128]. It is convenient to define new variables namely:

$$\boldsymbol{K} = \frac{m_c^* \boldsymbol{k'} + m_v^* \boldsymbol{k}}{M} \tag{2.95}$$

$$\boldsymbol{q} = \boldsymbol{k} - \boldsymbol{k'} \tag{2.96}$$

With the previous definitions, relation (2.94) becomes:

$$|\Psi\rangle = \sum_{\boldsymbol{q},\boldsymbol{K}} O_{\boldsymbol{q}}(\boldsymbol{K}) \hat{c}^{\dagger}_{c,\boldsymbol{K}+(m_c^*/M)\boldsymbol{q}} \hat{c}_{v,\boldsymbol{K}-(m_v^*/M)\boldsymbol{q}} \, |\Psi_0\rangle \tag{2.97}$$

where the summation index has been changed and where $O_{\boldsymbol{q}}(\boldsymbol{K}) = O(\boldsymbol{K}+(m_c^*/M)\boldsymbol{q}, \boldsymbol{K}-(m_v^*/M)\boldsymbol{q})$. This choice corresponds to the electron-hole system in the center of mass frame. (2.97) is an eigenstate of the Hamiltonian (2.90) if the coefficients $O_{\boldsymbol{q}}(\boldsymbol{K})$ obey the *effective-mass equation* (see appendix B.1 for the derivation) that takes the following form for a given couple $(\boldsymbol{K},\boldsymbol{q})$:

$$\left[-\bar{E} + \frac{\hbar^2 \boldsymbol{K}^2}{2\mu} + \frac{\hbar^2 \boldsymbol{q}^2}{2M}\right] O_{\boldsymbol{q}}(\boldsymbol{K}) + \sum_{\boldsymbol{K'}} \frac{e^2}{\varepsilon_0 \varepsilon_r V} \frac{1}{|\boldsymbol{K}-\boldsymbol{K'}|^2} O_{\boldsymbol{q}}(\boldsymbol{K'}) = 0 \tag{2.98}$$

with $M = m_c^* + m_v^*$ the total effective mass of the two-particle system, $\mu = \frac{m_c^* m_v^*}{m_v^* + m_v^*}$ the reduced effective mass, and $\bar{E} = E - E_0 - E_g$. Taking the Fourier transform of the coefficients $O_{\boldsymbol{q}}(\boldsymbol{K})$ we introduce an *envelope function* in real space:

$$\Psi_{env}(\boldsymbol{r},\boldsymbol{R}) = \frac{1}{V} \sum_{\boldsymbol{q},\boldsymbol{K}} O_{\boldsymbol{q}}(\boldsymbol{K}) e^{-j(\boldsymbol{qR}+\boldsymbol{Kr})} \tag{2.99}$$

The Fourier transform of eq. (2.98) leads to the Schrodinger equation of two particles in an attractive Coulomb potential in the center of mass frame:

$$\left(-\frac{\hbar^2}{2M}\nabla^2_{\boldsymbol{R}} - \frac{\hbar^2}{2\mu}\nabla^2_{\boldsymbol{r}} - \frac{e^2}{4\pi\varepsilon_0\varepsilon_r \boldsymbol{r}}\right) \Psi_{env} = \bar{E}\Psi_{env} \tag{2.100}$$

This result is remarkable: starting from a many-body problem (repulsive Coulomb interaction between an electron of the conduction band and many other electrons in the valence

band) we finally obtain an Hamiltonian of two particles in an attractive Coulomb potential, equivalent to a hydrogenic problem. Separating the variations in $\boldsymbol{r}$ and $\boldsymbol{R}$, eq. (2.100) admits the following solutions [132]:

$$\Psi_{env}^{\boldsymbol{q},n}(\boldsymbol{r},\boldsymbol{R}) = e^{j\boldsymbol{q}\boldsymbol{R}}\Phi_n(\boldsymbol{r}), \quad E_n(\boldsymbol{q}) = E_g - E_{b,n}^{3D} + \frac{\hbar^2|\boldsymbol{q}|^2}{2M} = E_g - \frac{Ry^*}{n^2} + \frac{\hbar^2|\boldsymbol{q}|^2}{2M} \quad n \in \mathbb{N}^* \tag{2.101}$$

where Φ_n represents the atomic orbital state of the hydrogen problem and the choice $E_0 = 0$ has been made. The effective Rydberg energy Ry^* is given by $Ry^* = \hbar^2/(2\mu a_{B,3D}^2)$, with the exciton Bohr radius in 3D $a_{B,3D} = 4\pi\hbar^2\varepsilon/(\mu e^2)$,which is about two orders of magnitude larger than the atomic Bohr radius, owing to the large dielectric constant and small effective mass. The exciton energy levels lie below the bandgap of the semiconductor, and the spectrum becomes increasingly dense at higher energy.

The eigenstates and eigenvalues of the exciton Hamiltonian are now defined, and we introduce the exciton creation operator [13]:

$$\hat{d}_{\boldsymbol{q},n}^\dagger = \sum_{\boldsymbol{K}} O_{\boldsymbol{q}}^n(\boldsymbol{K})\hat{c}_{c,\boldsymbol{K}+(m_c^*/M)\boldsymbol{q}}^\dagger \hat{c}_{v,\boldsymbol{K}-(m_v^*/M)\boldsymbol{q}} \tag{2.102}$$

Calculating the following commutator for excitons of zero momentum [133]

$$\left[\hat{d}_{0,n}, \hat{d}_{0,n}^\dagger\right] = \sum_{\boldsymbol{K}} |O_0^n(\boldsymbol{K})|^2 \left[1 - \hat{c}_{c,\boldsymbol{K}}^\dagger \hat{c}_{c,\boldsymbol{K}} - \hat{c}_{v,\boldsymbol{K}}\hat{c}_{v,\boldsymbol{K}}^\dagger\right] \tag{2.103}$$

,we show that excitons behave approximately as bosons, and that the deviation is proportional to the density of electrons in the conduction band and holes in the valence band. The expectation value of the commutator for arbitrary momentum is [134]:

$$\left\langle \left[\hat{d}_{\boldsymbol{q},n}, \hat{d}_{\boldsymbol{q},n}^\dagger\right] \right\rangle = 1 - O(da_B^3) \tag{2.104}$$

where d is the density of excitons in the system. Excitons behave as bosons as long as the distance between them is larger than their spatial extent, parametrized by the Bohr radius. In the following, we focus on the lowest internal state (i.e. $\Phi_n = \Phi_1$) and thus drop the index n. The wavefunction for this state is given by :

$$\Phi_1^{3D}(\boldsymbol{r}) = \frac{1}{\sqrt{\pi a_{B,3D}^3}} e^{-\boldsymbol{r}/a_{B,3D}} \qquad \Phi_1^{3D}(\boldsymbol{K}) = \frac{\sqrt{8\pi} a_{B,3D}^{3/2}}{(1 + a_{B,3D}^2\boldsymbol{K}^2)^2} \tag{2.105}$$

2.3.3 Exciton in a Quantum well

Up to now, we considered excitons in the bulk material. In this thesis we are interested in excitons of a quantum well (QW), more precisely a type-I QW, where electrons and holes are confined in the same layer. We have to introduce a QW 1D potential for carriers, which

13. $\boldsymbol{q}$ represents the total momentum of the electron-hole system conserved in the model, it is a good quantum number to label the exciton wavefunctions and creation operators

will reduce the dimensionality from 3D to 2D.

In this configuration the effective mass equation (2.100) is transformed into [128, 135]:

$$\left(-\frac{\hbar^2}{2m_c^*}\nabla^2_{\boldsymbol{r}_c} - \frac{\hbar^2}{2m_v^*}\nabla^2_{\boldsymbol{r}_v} - \frac{e^2}{\varepsilon\,|\boldsymbol{r}_c - \boldsymbol{r}_v|} + V_c(\boldsymbol{r}_c) + V_v(\boldsymbol{r}_v) - \bar{E}\right)\Psi_{env}(\boldsymbol{r}_c, \boldsymbol{r}_v) = 0 \tag{2.106}$$

where $V_{c/v}(\boldsymbol{r}_{c/v})$ represents the QW confinement potential energy for the electron in the conduction and valence band respectively. We assume these z-direction confinement potentials to be strong enough, and the well layer to be sufficiently thin, to confine the exciton in the $x-y$ plane (narrow well hypothesis). Therefore the Coulomb potential only depends on the in-plane separation $\boldsymbol{\rho} = \boldsymbol{\rho}_c - \boldsymbol{\rho}_v$. For such strong confinement, we can separate the z and in-plane variations of the potential :

$$V_c(\boldsymbol{r_c}) = V_{c,\parallel}(\boldsymbol{\rho}_c) + V_{c,\perp}(z_c) \qquad V_v(\boldsymbol{r_v}) = V_{v,\parallel}(\boldsymbol{\rho}_v) + V_{v,\perp}(z_v) \tag{2.107}$$

This couple of equation implies that the Hamiltonian (2.106) is separable in z and $\boldsymbol{\rho}$, and the exciton wave function can be written as:

$$\Psi_{env}(\boldsymbol{r}_c, \boldsymbol{r}_v) = \Phi(\boldsymbol{\rho}_c, \boldsymbol{\rho}_v)\chi_c(z_c)\chi_v(z_v) \tag{2.108}$$

$\chi_c(z_c)$ and $\chi_v(z_v)$ are the eigenfunctions for a particle in a 1D box with rectangular potential. We restrict the discussion to the lowest order wavefunction χ associated to the fundamental state of this 1D potential in z-direction. The remaining problem is to solve the in-plane Hamitonian:

$$\left(-\frac{\hbar^2}{2m_c^*}\nabla^2_{\boldsymbol{\rho}_c} - \frac{\hbar^2}{2m_v^*}\nabla^2_{\boldsymbol{\rho}_v} - \frac{e^2}{\varepsilon\,|\boldsymbol{\rho}|} + V_{c,\parallel}(\boldsymbol{\rho}_c) + V_{v,\parallel}(\boldsymbol{\rho}_v) - \bar{E} + E_{c,\perp} + E_{v,\perp}\right)\Phi(\boldsymbol{\rho}_c, \boldsymbol{\rho}_v) = 0 \tag{2.109}$$

where $E_{c/v,\perp}$ are the energies of the conduction/valence band electron in the 1D potential along z. By introducing the center of mass coordinates, we can expand the confinement potential in power of $\boldsymbol{\rho}$:

$$\boldsymbol{\rho} = \boldsymbol{\rho}_c - \boldsymbol{\rho}_v \tag{2.110}$$

$$\boldsymbol{R}_\parallel = \frac{(m_c^*\boldsymbol{\rho}_c + m_v^*\boldsymbol{\rho}_v)}{M} \tag{2.111}$$

$$\begin{aligned} V_{c/v,\parallel}(\boldsymbol{\rho}_{c/v}) &= V_{c/v,\parallel}(\boldsymbol{R}_\parallel \pm \frac{m^*_{v/c}}{M}\boldsymbol{\rho}) = V_{c/v,\parallel}(\boldsymbol{R}_\parallel) + \nabla V_{c/v,\parallel}(\boldsymbol{R}_\parallel)\frac{m^*_{c/v}}{M}\boldsymbol{\rho} + O(\boldsymbol{\rho}^2) \\ &\simeq V_{c/v,\parallel}(\boldsymbol{R}_\parallel) \end{aligned} \tag{2.112}$$

The last approximation is justified by the fact that the spatial scale of the 2D confinement is much larger than the Bohr Radius of the exciton. The Hamiltonian (2.109) can then be separated in the relative and center-of-mass in-plane coordinates. The exciton envelope function takes the following form :

$$\Psi_{env}(\boldsymbol{r}_c, \boldsymbol{r}_v) = \Phi(\boldsymbol{\rho}) F(\boldsymbol{R}_\parallel) \chi_c(z_c) \chi_v(z_v) \tag{2.113}$$

• $\Phi(\boldsymbol{\rho})$ is the solution of the 2D-hydrogen-like problem:

$$\left(-\frac{\hbar^2}{2\mu} \nabla^2_{\boldsymbol{\rho}} - \frac{e^2}{\varepsilon \left| \boldsymbol{\rho} \right|} \right) \Phi(\boldsymbol{\rho}) = E^{2D}_{b,n} \Phi(\boldsymbol{\rho}) \tag{2.114}$$

where $E^{2D}_{b,n}$ is the 2D binding energy, which relates to 3D through [136]:

$$E^{2D}_{b,n} = 4E^{3D}_{b,n} \quad a_{B,2D} = a_{B,3D}/2 \tag{2.115}$$

However, in real QW structures the exciton is not exactly two dimensional, and its biding energy lies between $E^{3D}_{b,n}$ and $4E^{3D}_{b,n}$. Here as well we will restrict our discussion to the lowest order orbital $n = 1$, with the associated wavefunction:

$$\Phi^{2D}_1(\boldsymbol{r}) = \sqrt{\frac{2}{\pi}} \frac{2}{a_{B,2D}} e^{-2\boldsymbol{r}/a_{B,2D}} \qquad \Phi^{2D}_1(\boldsymbol{K}) = \frac{\sqrt{2\pi} a_{B,2D}}{(1 + a^2_{B,2D} \boldsymbol{K}^2/4)^{3/2}} \tag{2.116}$$

• $F(\boldsymbol{R}_\parallel)$ is the solution of the problem:

$$\left[-\frac{\hbar^2}{2M} \nabla^2_{\boldsymbol{R}_\parallel} + V_{c,\parallel}(\boldsymbol{R}_\parallel) + V_{v,\parallel}(\boldsymbol{R}_\parallel) \right] F(\boldsymbol{R}_\parallel) = E_\parallel F(\boldsymbol{R}_\parallel) \tag{2.117}$$

In the simple case of a free exciton in a infinite 2D plane $V_{c/v,\parallel}(\boldsymbol{R}_\parallel) = 0$.

The eigenenergies of a bound 2D exciton state are consequently:

$$E = E_g + E_{c,\perp} + E_{v,\perp} + E^{2D}_{b,n} + E_\parallel \tag{2.118}$$

Like in the case of the bulk exciton we define the creation operator:

$$\hat{d}^\dagger_\alpha = \sum_{\boldsymbol{k},\boldsymbol{k'}} O_\alpha(\boldsymbol{k}, \boldsymbol{k'}) \hat{c}^\dagger_{c,\boldsymbol{k}} \hat{c}_{v,\boldsymbol{k'}} \tag{2.119}$$

$O_\alpha(\boldsymbol{k}, \boldsymbol{k'})$ is a Fourier transform of the exciton wave function (2.113). The wave vector will be later-on split in its in-plane and out of plane components $\boldsymbol{k} = (\boldsymbol{k}_\perp, \boldsymbol{k}_\parallel)$. α is a set of numbers that label and characterize the state of relative and center of mass motion in the plane. Calculating the commutator of these new bosonic operators leads to :

$$
\begin{aligned}
\left[\hat{d}_{\alpha}, \hat{d}^{\dagger}_{\alpha'}\right] &= \sum_{\boldsymbol{k_1},\boldsymbol{k_2},\boldsymbol{k_3},\boldsymbol{k_4}} O_{\alpha}(\boldsymbol{k_1},\boldsymbol{k_2}) O^{*}_{\alpha'}(\boldsymbol{k_3},\boldsymbol{k_4}) \left[\hat{c}^{\dagger}_{v,\boldsymbol{k_2}} \hat{c}_{c,\boldsymbol{k_1}}, \hat{c}^{\dagger}_{c,\boldsymbol{k_3}} \hat{c}_{v,\boldsymbol{k_4}}\right] \\
&= \sum_{\boldsymbol{k_1},\boldsymbol{k_2}} O_{\alpha}(\boldsymbol{k_1},\boldsymbol{k_2}) O^{*}_{\alpha'}(\boldsymbol{k_1},\boldsymbol{k_2}) - \sum_{\boldsymbol{k_1},\boldsymbol{k_2},\boldsymbol{k_4}} O_{\alpha}(\boldsymbol{k_1},\boldsymbol{k_2}) O^{*}_{\alpha'}(\boldsymbol{k_1},\boldsymbol{k_4}) \hat{c}_{v,\boldsymbol{k_4}} \hat{c}^{\dagger}_{v,\boldsymbol{k_2}} \\
&- \sum_{\boldsymbol{k_1},\boldsymbol{k_2},\boldsymbol{k_3}} O_{\alpha}(\boldsymbol{k_1},\boldsymbol{k_2}) O^{*}_{\alpha'}(\boldsymbol{k_3},\boldsymbol{k_4}) \hat{c}^{\dagger}_{c,\boldsymbol{k_3}} \hat{c}_{c,\boldsymbol{k_1}} \\
&= \delta_{\alpha,\alpha'} - \sum_{\boldsymbol{k_1},\boldsymbol{k_2},\boldsymbol{k_4}} O_{\alpha}(\boldsymbol{k_1},\boldsymbol{k_2}) O^{*}_{\alpha'}(\boldsymbol{k_1},\boldsymbol{k_4}) \hat{c}_{v,\boldsymbol{k_4}} \hat{c}^{\dagger}_{v,\boldsymbol{k_2}} \\
&- \sum_{\boldsymbol{k_1},\boldsymbol{k_2},\boldsymbol{k_3}} O_{\alpha}(\boldsymbol{k_1},\boldsymbol{k_2}) O^{*}_{\alpha'}(\boldsymbol{k_3},\boldsymbol{k_4}) \hat{c}^{\dagger}_{c,\boldsymbol{k_3}} \hat{c}_{c,\boldsymbol{k_1}}
\end{aligned}
\tag{2.120}
$$

A result similar to the bulk case, i.e. excitons obey a bosonic behaviour if the exciton density is smaller than a saturation density $n_{sat} \simeq 1/(2\pi a^2_{B,2D})$ [137].

2.3.4 Exciton in a circularly patterned quantum well

So far we considered free excitons in a 2D-plane (therefore the $F(\boldsymbol{R}_{\parallel}) = e^{j\boldsymbol{k}_{\parallel}\cdot\boldsymbol{R}_{\parallel}}$). In this thesis, we are here interested in QW-exciton inside a disk, meaning that the QW layer is now patterned with a circular symmetry. The wave function obeys then the Schrödinger equation:

$$
\left[-\frac{\hbar^2}{2M}\nabla^2_{\boldsymbol{R}_{\parallel}} + V(\boldsymbol{R}_{\parallel})\right] F(\boldsymbol{R}_{\parallel}) = E_{\parallel} F(\boldsymbol{R}_{\parallel}) \tag{2.121}
$$

with $V(\boldsymbol{R}_{\parallel})$ a potential defined by :

$$
V(\boldsymbol{R}_{\parallel}) = \begin{cases} 0 & \text{for } \boldsymbol{R}_{\parallel} < R \\ \infty & \text{for } \boldsymbol{R}_{\parallel} > R \end{cases} \tag{2.122}
$$

where R is the radius of the disk. The polar-coordinates system (r, θ) is again natural to treat the problem. The equation (2.121) becomes:

$$
-\frac{\hbar^2}{2M}\left[\frac{\partial^2}{\partial r^2} + \frac{1}{r}\frac{\partial}{\partial r} + \frac{1}{r^2}\frac{\partial^2}{\partial \theta^2}\right] F(r,\theta) + V(r,\theta) F(r,\theta) = E_{\parallel} F(r,\theta) \tag{2.123}
$$

Substituting $F(r,\theta) = L(r)N(\theta)$ in (2.123) yields the following angular equation:

$$
\frac{d^2 N(\theta)}{d\theta^2} = -m'^2 N(\theta) \tag{2.124}
$$

and to the following radial equation inside the circular potential well:

$$
-\frac{\hbar^2}{2M}\left[\frac{\partial^2}{\partial r^2} + \frac{1}{r}\frac{\partial}{\partial r} - \frac{m'^2}{r^2}\right] L(r) = E_{\parallel} L(r) \tag{2.125}
$$

The normalized solutions of (2.124) are given by:

$$N(\theta) = \frac{1}{\sqrt{2\pi}} e^{-jm'\theta} \quad m' \in \mathbb{Z} \tag{2.126}$$

Taking $k = \sqrt{2ME_{\parallel}}/\hbar$, equation (2.125) is transformed into:

$$\left[\frac{\partial^2}{\partial r^2} + \frac{1}{r}\frac{\partial}{\partial r} + \left(k^2 - \frac{m'^2}{r^2}\right)\right] L(r) = 0 \tag{2.127}$$

The solutions of a such equation are given by the Bessel functions of first kind $J_{m'}(kr)$. For an infinite potential barrier we adopt the boundary condition $L(R) = 0$ and the allowed values of k are those satisfying the equation $J_{m'}(kR) = 0$. If we call $x_{m',p'}$ the p'-th root of the Bessel function of order m', the allowed values of k are $k_{m',p'} = x_{m',p'}/R$, and the eigenenergies are given by $E_{\parallel,m',p'} = \hbar^2 x^2_{m',p'}/2MR^2$.

For $m' \neq 0$, there are two eigenstates, corresponding each to the eigenenergy $E_{m',p'}$:

$$F_{m',p'}(r,\theta) = K_{m',p'} J_{m'}\left(\frac{x_{m',p'}r}{R}\right) e^{-jm'\theta} = L(r)N(\theta) \tag{2.128}$$

where $K_{m',p'}$ is a normalization constant. For $m' = 0$ there is only one eigenstate. All eigenstates are normalized:

$$\iint r dr d\theta \left|F(r,\theta)\right|^2 = \int_0^R r dr \left|L(r)\right|^2 \int_0^{2\pi} d\theta \left|N(\theta)\right|^2 = 1 \tag{2.129}$$

The function $N(\theta)$ requires a factor $\frac{1}{\sqrt{2\pi}}$ to be normalized, the normalization constant $K_{m',p'}$ thus obeys:

$$\int_0^R r dr \left|K_{m',p'} J_{m'}\left(\frac{x_{m',p'}r}{R}\right)\right|^2 = \frac{1}{2\pi} \tag{2.130}$$

Since we have the relation [138]:

$$\int_0^R r J^2_{m'}(kr) dr = \frac{R^2}{2}\left(J^2_{m'}(kR) - J_{m'-1}(kR)J_{m'+1}(kR)\right) \tag{2.131}$$

Using $J_{m'-1}(k_{m',p'}R) = -J_{m'+1}(k_{m',p'}R)$ the normalization constant $K_{m',p'}$ is given by :

$$K_{m',p'} = \frac{\sqrt{2}}{R}\frac{1}{\sqrt{2\pi}}\frac{1}{\sqrt{J_{m'-1}(x_{m',p'})J_{m'+1}(x_{m',p'})}} = \frac{1}{R\sqrt{\pi}}\frac{1}{|J_{m'-1}(x_{m',p'})|} \tag{2.132}$$

The in-plane profile of the final envelope function is illustrated in figure 2.10.

Similarly to the WGMs, the exciton wavefunction is characterized by a pair of quantum numbers: the azimuthal number m' and the radial number p'. Consequently, we can introduce the following 2D exciton creation operator :

$$\hat{d}^{\dagger}_{m',p'} = \sum_{\boldsymbol{k},\boldsymbol{k'}} O_{m',p'}(\boldsymbol{k},\boldsymbol{k'}) \hat{c}^{\dagger}_{c,\boldsymbol{k}} \hat{c}_{v,\boldsymbol{k'}} \tag{2.133}$$

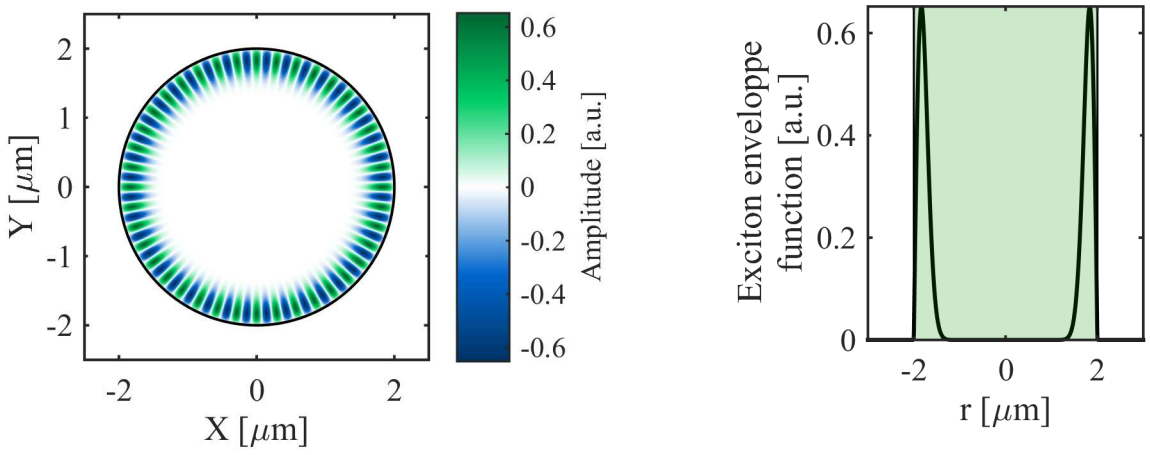

Figure 2.10 – Exciton enveloppe function in a circularly patterned quantum well (m'=40, p'=1) - Left : 2D-view - Right : radial distribution.

2.4 Optomechanical (photon-phonon) coupling

We now have described separately the optical, mechanical, and excitonic modes of our resonators. The purpose of this section is to detail their coupling and provide tools to compute the coupling parameter g_0.

2.4.1 Optically induced forces

After having introduced the optomechanical formalism in section 1.2, we discuss here the microscopic interactions at the origin of the coupling between light and mechanical motion. When photons are confined inside a semiconductor disk resonator, they exert different types of stress on the device. We express here all forces at play with a stress tensor formalism, which relates to volume forces via:

$$F_i = -\partial_j \sigma_{ij} \tag{2.134}$$

2.4.1.1 Radiation pressure

In the case of a circular resonator, like our GaAs disk, a simple analysis through energy and momentum conservation shows that the radial momentum transfer is equal to $2\pi\hbar k$ per round trip of a photon, where k represents the wave-vector in the dielectric material [122]. A more exact way to estimate radiation pressure in an arbitrary geometry is to compute the Maxwell Stress Tensor (MST) $\overline{\overline{T}} = -\overline{\overline{\sigma}}^{(RP)}$, which directly connects the electromagnetic fields and the volume radiation pressure force [139]:

$$F_i^{(RP)} = -\partial_j \sigma_{ji}^{(RP)} = \partial_j T_{ji} = \partial_j \left[\varepsilon_0 \varepsilon_r (E_i E_j - \frac{1}{2}\delta_{ij}|E|^2) + \mu_0 \mu_r (H_i H_j - \frac{1}{2}\delta_{ij}|H|^2) \right] \quad (2.135)$$

with $\varepsilon_r \equiv \varepsilon_r(x,y,z)$ and $\mu_r \equiv \mu_r(x,y,z)$ the relative permittivity and permeability of the dielectric material. This formalism can be used to calculate both normal and shear ($i \neq j$) stresses. Usually, since mechanical devices cannot respond instantaneously to the fast varying optical fields, the average value of the optical stress is computed.

2.4.1.2 Electrostriction

The above calculation of the MST assumed a perfectly rigid dielectric material which is an approximation. To represent a deformable dielectric one can imagine a collection of different dielectric domains: under an external electric field, every small domain polarizes and gets attracted to the high-field regions. This provokes a contraction (expansion) in the direction of the field and an expansion (contraction) in the perpendicular direction, as a consequence of the Poisson effect. The generated displacement is thus proportional to E^2, in contrast to the piezoelectric effect where the displacement is proportional to E. In order to compute the electrostrictive stress, we use the photoelastic tensor $\overline{\overline{p}}$, which links a change in the material's dielectric tensor $\overline{\overline{\varepsilon}}$ to the strain field S_{ij} [122, 140, 141]:

$$\varepsilon_{i,j}^{-1}(S_{k,l}) = \varepsilon_{i,j}^{-1}(0) + \Delta(\varepsilon_{i,j}^{-1}) = \varepsilon_{i,j}^{-1}(0) + p_{i,j,k,l} S_{k,l} \quad (2.136)$$

where $\Delta(\varepsilon_{i,j}^{-1})$ represents the change in the inverse dielectric tensor due to the strain. The electrostrictive stress and volume force are given by [125]:

$$\left\langle \sigma_{i,j}^{(ES)} \right\rangle = -\frac{1}{2}\varepsilon_0 (\varepsilon_{k,m} p_{m,n,i,j} \varepsilon_{n,l}) E_k E_l \quad (2.137)$$

$$F_i^{(ES)} = -\partial_i \left\langle \sigma_{i,j}^{(ES)} \right\rangle \quad (2.138)$$

In the case of a cubic semiconductor like GaAs or silicon, the electrostrictive stress components can be expressed as [122, 142]:

$$\begin{pmatrix} \sigma_{x,x}^{(ES)} \\ \sigma_{y,y}^{(ES)} \\ \sigma_{z,z}^{(ES)} \\ \sigma_{z,y}^{(ES)} = \sigma_{y,z}^{(ES)} \\ \sigma_{x,z}^{(ES)} = \sigma_{z,x}^{(ES)} \\ \sigma_{x,y}^{(ES)} = \sigma_{y,x}^{(ES)} \end{pmatrix} = -\frac{1}{2}\varepsilon_0 n^4 \begin{pmatrix} p_{11} & p_{12} & p_{12} & 0 & 0 & 0 \\ p_{12} & p_{11} & p_{12} & 0 & 0 & 0 \\ p_{12} & p_{12} & p_{11} & 0 & 0 & 0 \\ 0 & 0 & 0 & p_{44} & 0 & 0 \\ 0 & 0 & 0 & 0 & p_{44} & 0 \\ 0 & 0 & 0 & 0 & 0 & p_{44} \end{pmatrix} \begin{pmatrix} E_x^2 \\ E_y^2 \\ E_z^2 \\ E_y \quad E_z \\ E_x \quad E_z \\ E_x \quad E_y \end{pmatrix} \quad (2.139)$$

where the dielectric tensor has been reduced to $\varepsilon_{i,j} = \varepsilon \delta_{i,j} = n^2 \delta_{i,j}$, with n the refractive index of the material. At high refractive index, electrostrictive contributions usually have an important role. This is indeed the case in our GaAs resonators. It is also important to note that the photoelastic coefficients strongly increase near the GaAs band gap [143–148].

2.4.1.3 Photothermal force

Light is absorbed, producing heat in the device, which strains under the effect of thermal expansion: this is the photothermal stress effect. When a material is submitted to a local temperature change ΔT, a local strain is generated:

$$\Delta S_{i,j}^{(TH)} = \beta_{i,j} \Delta T \tag{2.140}$$

where $\beta_{i,j}$ is the thermal expansion tensor. The thermal induced stress is thus given by [125, 149]:

$$\sigma_{i,j}^{(TH)} = C_{i,j,k,l} \beta_{k,l} \Delta T \tag{2.141}$$

where $C_{i,j,k,l}$ is the stiffness tensor.

This photothermal force has usually a large magnitude [97, 150–152], that can overcome the radiation pressure/electrostriction force. However, the thermal expansion coefficient of GaAs is vanishing at cryogenic temperature [153], reducing the contribution of the photothermal force. Nevertheless, it can positively contribute to optomechanical operations like self-oscillation [154] or cooling [155], especially at room temperature but not only (see chapter 5).

2.4.2 Numerical simulations of optomechanical coupling

In a photoelastic material, we have seen that a strain changes the refractive index, and hence the optical eigenfrequency of the resonator. The optomechanical frequency-pull g_{om} can therefore be split into two different contributions:

$$g_{om} = -\frac{d\omega_c}{dx} = \underbrace{-\frac{\partial \omega_c}{\partial R}\frac{\partial R}{\partial x}}_{g_{om}^{geo}} \underbrace{-\frac{d\omega_c}{d\varepsilon}\frac{d\varepsilon}{dx}}_{g_{om}^{pe}} \tag{2.142}$$

The g_{om}^{geo} contribution corresponds to the modification of the geometry of the resonator (here its radius R), while g_{om}^{pe} translates the change in the electric permittivity ε of the resonator (hence refractive index).

2.4.2.1 Geometric contribution g_{om}^{geo}

In the 2D+1 approach for a WGM $g_{om}^{geo} \simeq \omega_c / R$ [10, 37]. This approximation works well for the RBM1. To determine g_{om}^{geo} for an arbitrary deformation profile, we use a perturbation theory of Maxwell equations in the case of moving material boundaries [156, 157]:

$$g_{om}^{geo} = -\frac{\omega_C}{2} \frac{\iint_S \boldsymbol{q}.\boldsymbol{n} \left[\Delta(\varepsilon_{12}) |\boldsymbol{E}_{\parallel}|^2 - \Delta(\varepsilon_{12}^{-1}) |\boldsymbol{D}_{\perp}|^2\right] dA}{\iiint_V \varepsilon(r) |\ \boldsymbol{E}\ |^2 d^3\boldsymbol{r}} \tag{2.143}$$

where the integral is performed over the disk surface S, $\boldsymbol{q}$ is the normalized displacement vector, $\boldsymbol{n}$ is the normal vector orthogonal to the disk surface, $\boldsymbol{E}_{\parallel}$ and $\boldsymbol{D}_{\perp}$ the tangential

electric field and orthogonal electric displacement field, and $\Delta(\varepsilon_{12}) = \varepsilon_1 - \varepsilon_2$ the dielectric constant contrast between the disk ($\varepsilon_1 = n^2$) and the surrounding medium (vacuum $\varepsilon_2 = 1$).

2.4.2.2 Photoelastic contribution g_{om}^{pe}

The photoelastic contribution is computed using to the following formula [149, 158, 159]:

$$g_{om}^{pe} = -\frac{\omega_c}{2} \frac{\iiint_V \boldsymbol{e} \cdot \overline{\overline{\varepsilon}} \cdot \boldsymbol{e} dA}{\mathrm{Max}(u(\boldsymbol{r})) \iiint_V \varepsilon(r) |\ \boldsymbol{E}\ |^2 d^3\boldsymbol{r}} = \frac{1}{2} \frac{\iiint_V \sigma_{ij}^{(ES),1} S_{i,j}}{\hbar u(r_0)} \tag{2.144}$$

where $\sigma_{ij}^{(ES),1}$ is the electrostriction tensor exerted by a single photon and $\boldsymbol{e}$ the direction of the electric field.

2.4.2.3 Results

Numerical simulation results are summarized in table 2.2 and illustrated in figure 2.11, (the mechanical anisotropy of the GaAs is included in these simulations). Two different WGMs are used: one that sits in the telecom band and a second in the exciton band [14]. Optomechanical coupling values g_0 in our system evolve in the $2\pi \times 100$ kHz range. Higher values are obtained for modes in the exciton wavelength range, as expected from the greater photoelastic coefficients close to the bandgap.

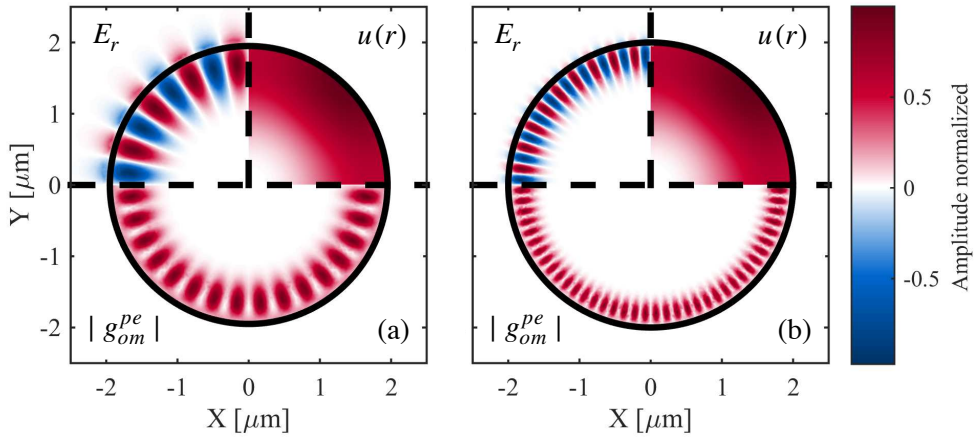

Figure 2.11 – 2D X-Y cut plane of 3D-FEM simulations exhibiting the radial component of the electric field E_r, the total mechanical displacement $u(r)$ and the absolute value of the local photoelastic contribution of the optomechanical coupling g_{om}^{pe} for 2 different WGMs (a) TE $m = 16$, $p = 1$ - $\lambda_c = 1566,9$ nm (b) TE $m = 38$, $p = 1$ - $\lambda_c = 855,9$ nm

14. We are interested to study our disk in these two different wavelength ranges

WGM	TE $m = 16$, $p = 1$ - $\lambda_c = 1566,9$ nm	TE $m = 38$, $p = 1$ - $\lambda_c = 855,9$ nm
f_m [MHz]	708.6	
m_{eff}/m (RBM1	0.629	
x_{ZPF} [m]	$1.18 \cdot 10^{-15}$	
g_{om}^{geo} [THz/nm]	0.463	1.05
g_0^{geo} [rad/s]	$5.49 \cdot 10^5$	$1.24 \cdot 10^6$
g_{om}^{pe} [THz/nm]	0.343	1.284
g_0^{pe} [rad/s]	$4.07 \cdot 10^5$	$1.52 \cdot 10^6$
g_{om} [THz/nm]	0.81	2.33
$g_0/2\pi$ [MHz]	0.152	0.433

Table 2.2 – Comparaison between geometric (g^{geo}) and photoelastic (g^{pe}) contributions to the optomechanical coupling for the first RBM of a 2 μm radius, 200 nm thick, GaAs disk at room temperature, obtained through 3D FEM simulations with anisotropy. The results are computed for two different WGMs in two different wavelength regions.

2.5 Optoelectronical (photon-exciton) coupling

Dipolar interaction:

We present here an original derivation to calculate the Rabi-splitting for a quantum-well exciton embedded in a disk WGM resonator. This rigorous derivation is one of the theoretical outcomes of this thesis. The Hamiltonian of the system we consider is :

$$\hat{H} = \hat{H}_{ex} + \hat{H}_{EM} + \hat{H}_I \tag{2.145}$$

with $\hat{H}_{ex}/\hat{H}_{EM}$ the excitonic (electromagnetic) Hamiltonian, and where we introduce the following interaction Hamiltonian (minimal coupling Hamiltonian [86, 160–162]):

$$\hat{H}_I = -\frac{e}{2m}\sum_n \hat{\boldsymbol{A}}(\hat{\boldsymbol{r}}_n)\cdot\hat{\boldsymbol{p}}_n + \hat{\boldsymbol{p}}_n\cdot\hat{\boldsymbol{A}}(\hat{\boldsymbol{r}}_n) + \frac{e^2}{2m}\sum_n \left|\hat{\boldsymbol{A}}(\hat{\boldsymbol{r}}_n)\right|^2 \tag{2.146}$$

where m is the electron mass, $\hat{\boldsymbol{r}}_n$ ($\hat{\boldsymbol{p}}_n$) are the position (momentum) operator of the n-th QW electron, and the sum runs over all the electrons in the system [15]. We leave aside the self interaction term in $\left|\hat{\boldsymbol{A}}(\hat{\boldsymbol{r}}_n)\right|^2$ for a moment and focus on the exciton-photon interaction. In the Coulomb gauge the vector potential commutes with the electron momentum $\left[\hat{\boldsymbol{A}}(\hat{\boldsymbol{r}}_n), \hat{\boldsymbol{p}}_n\right] = 0$, since $\nabla\hat{\boldsymbol{A}} = 0$. The interaction term can be rewritten as:

$$\hat{H}_I = \frac{je}{\hbar}\sum_n \hat{\boldsymbol{A}}(\hat{\boldsymbol{r}}_n)\cdot\left[\hat{\boldsymbol{r}}_n, \hat{H}_{ex}\right] \tag{2.147}$$

15. Note that in this section we place ourselves in the Schrödinger (S) picture, where operators do not have an explicit time dependence. The expression of the vector potential $\hat{\boldsymbol{A}}$ differs from the one introduced in the Heisenberg picture (H) in equation (2.78). The relation between the two expressions is given by:$\hat{\boldsymbol{A}}^H = \hat{U}^\dagger\hat{\boldsymbol{A}}^S\hat{U}$ with $\hat{U} = e^{-j\hat{H}_{EM}t/\hbar}$ the evolution operator

since $\hat{\boldsymbol{p}}_n = j\frac{m}{\hbar}\left[\hat{H}_{ex}, \hat{\boldsymbol{r}}_n\right]$ [16]. The states $|\Psi_\alpha\rangle = \hat{d}^\dagger_\alpha |\Psi_0\rangle$ form a complete basis to describe the single exciton formed in the many body system. We express the interaction Hamiltonian in terms of exciton wave-functions by inserting the unity operator twice and using the completeness relation:

$$\sum_\alpha |\Psi_\alpha\rangle \langle\Psi_\alpha| = \mathbb{I} \tag{2.148}$$

$$\hat{H}_I = \frac{je}{\hbar} \sum_{\alpha,\beta} |\Psi_\alpha\rangle \langle\Psi_\alpha| \sum_n \hat{\boldsymbol{A}}(\hat{\boldsymbol{r}}_n) \cdot \left[\hat{\boldsymbol{r}}_n, \hat{H}_{ex}\right] |\Psi_\beta\rangle \langle\Psi_\beta| \tag{2.149}$$

Using $\hat{H}_{ex} |\Psi_\alpha\rangle = E_\alpha |\Psi_\alpha\rangle$, and the fact that $\hat{\boldsymbol{A}}(\hat{\boldsymbol{r}})$ commute with $\hat{H}_{ex}$ in the Coulomb gauge, the equation can be rewritten as [17]:

$$\hat{H}_I = \frac{je}{\hbar} \sum_{\alpha,\beta} (E_\beta - E_\alpha) \langle\Psi_\alpha| \sum_n \hat{\boldsymbol{A}}(\hat{\boldsymbol{r}}_n) \cdot \hat{\boldsymbol{r}}_n |\Psi_\beta\rangle |\Psi_\alpha\rangle \langle\Psi_\beta| \tag{2.150}$$

Circular disk case:

We limit the exciton basis to the two lowest states, i.e. the ground state $|\Psi_0\rangle$ and the first excited state $|\Psi_{m',p'}\rangle$. We drop the index α/β and use the azimuthal/radial number m'/p' instead, since our exciton state is fully characterized by those two quantum numbers. With those notations the interaction Hamiltonian (2.150) becomes:

$$\begin{aligned}
\hat{H}_I = je \sum_{m'=-\infty}^{+\infty} \sum_{p'=1}^{+\infty} \omega_{m',p'} & \left[- \langle\Psi_{m',p'}| \sum_n \hat{\boldsymbol{A}}(\hat{\boldsymbol{r}}_n) \cdot \hat{\boldsymbol{r}}_n |\Psi_0\rangle |\Psi_{m',p'}\rangle \langle\Psi_0| \right] \\
& + \left[\langle\Psi_0| \sum_n \hat{\boldsymbol{A}}(\hat{\boldsymbol{r}}_n) \cdot \hat{\boldsymbol{r}}_n |\Psi_{m',p'}\rangle |\Psi_0\rangle \langle\Psi_{m',p'}| \right] \\
\hat{H}_I = je \sum_{m'=-\infty}^{+\infty} \sum_{p'=1}^{+\infty} \omega_{m',p'} & \left[- \langle\Psi_{m',p'}| \sum_n \hat{\boldsymbol{A}}(\hat{\boldsymbol{r}}_n) \cdot \hat{\boldsymbol{r}}_n |\Psi_0\rangle \hat{d}^\dagger_{m',p'} \right] \\
& + \left[\langle\Psi_0| \sum_n \hat{\boldsymbol{A}}(\hat{\boldsymbol{r}}_n) \cdot \hat{\boldsymbol{r}}_n |\Psi_{m',p'}\rangle \hat{d}_{m',p'} \right] \\
\hat{H}_I = e \sum_{m'=-\infty}^{+\infty} \sum_{p'=1}^{+\infty} \omega_{m',p'} & \left[j \langle\Psi_0| \sum_n \hat{\boldsymbol{A}}(\hat{\boldsymbol{r}}_n) \cdot \hat{\boldsymbol{r}}_n |\Psi_{m',p'}\rangle \hat{d}_{m',p'} + h.c. \right]
\end{aligned} \tag{2.151}$$

Where we identified $|\Psi_{m',p'}\rangle \langle\Psi_0|$ as the creation operator $\hat{d}^\dagger_{m',p'}$ and $|\Psi_0\rangle \langle\Psi_{m',p'}|$ as the annihilation operator $\hat{d}_{m',p'}$. We evaluate the expression $\hat{X}_{m',p'} = \langle\Psi_0| \sum_n \hat{\boldsymbol{A}}(\hat{\boldsymbol{r}}_n) \cdot \hat{\boldsymbol{r}}_n |\Psi_{m',p'}\rangle$

16. This relation formulated for single-particle operators, remains valid with Coulomb interactions as considered here, this is because $\hat{V}_{\text{Coulomb}}(r)$ commutes with $\hat{r}$ for the single considered particle

17. $\langle\Psi_\alpha| \sum_n \hat{\boldsymbol{A}}(\boldsymbol{r}_n) \cdot \boldsymbol{r}_n |\Psi_\beta\rangle$ is an operator that only acts on the photon Hilbert space

by expressing the action of $\sum_n \hat{\boldsymbol{A}}(\hat{\boldsymbol{r}}_n)\cdot\hat{\boldsymbol{r}}_n$ on the many-electron states in the Bloch function basis.

According to the second quantization formalism [89], the expansion is given by:

$$\sum_n \hat{\boldsymbol{A}}(\hat{\boldsymbol{r}}_n)\cdot\hat{\boldsymbol{r}}_n = \sum_{\boldsymbol{k},\boldsymbol{k}',\alpha,\alpha'} f_{\boldsymbol{k},\boldsymbol{k}',\alpha,\alpha'}\hat{c}^\dagger_{\alpha,\boldsymbol{k}}\hat{c}_{\alpha',\boldsymbol{k}'} \tag{2.152}$$

where $\hat{c}^\dagger_{\alpha,\boldsymbol{k}}$,$\hat{c}_{\alpha',\boldsymbol{k}'}$ are the creation and annihilation operators introduced in eq. (2.88) and $f_{\boldsymbol{k},\boldsymbol{k}',\alpha,\alpha'}$ represents the matrix element:

$$f_{\boldsymbol{k},\boldsymbol{k}',\alpha,\alpha'} = \langle\alpha\boldsymbol{k}|\hat{\boldsymbol{A}}(\hat{\boldsymbol{r}})\cdot\hat{\boldsymbol{r}}|\alpha'\boldsymbol{k}'\rangle \tag{2.153}$$

Using the orthogonality of the state $\hat{c}^\dagger_{\alpha,\boldsymbol{k}}\hat{c}_{\alpha',\boldsymbol{k}'}\,|\Psi_0\rangle$ in association with the relation (2.133) we obtain a new expression for the factor $X_{m',p'}$:

$$\hat{X}_{m',p'} = \sum_{\boldsymbol{k},\boldsymbol{k}'} f_{\boldsymbol{k},\boldsymbol{k}',v,c}O_{m',p'}(\boldsymbol{k}',\boldsymbol{k}) \tag{2.154}$$

We will compute $\hat{X}_{m',p'}$, knowing that its conjugate can be obtained through [18]

$$\sum_{\boldsymbol{k},\boldsymbol{k}'} f_{\boldsymbol{k},\boldsymbol{k}',v,c}O_{m',p'}(\boldsymbol{k}',\boldsymbol{k}) = \left(\sum_{\boldsymbol{k},\boldsymbol{k}'} f_{\boldsymbol{k}',\boldsymbol{k},c,v}O^*_{m',p'}(\boldsymbol{k}',\boldsymbol{k})\right)^\dagger$$

.

We employ an explicit expression for the matrix element f for a TE optical mode [19]:

$$\begin{aligned} f_{\boldsymbol{k},\boldsymbol{k}',v,c} &= \langle v\boldsymbol{k}|\hat{\boldsymbol{A}}(\hat{\boldsymbol{r}})\cdot\hat{\boldsymbol{r}}|c\boldsymbol{k}'\rangle \\ &= \sum_{m=-\infty}^{+\infty}\sum_{p=1}^{\infty}\frac{1}{V}\int d\boldsymbol{r}e^{-j(\boldsymbol{k}'-\boldsymbol{k})\boldsymbol{r}}C_{m,p}\left[\hat{a}_{m,p}\tilde{E}_{m,p}(\boldsymbol{r})\boldsymbol{e}+\hat{a}^\dagger_{m,p}\tilde{E}^*_{m,p}(\boldsymbol{r})\boldsymbol{e}^*\right] \\ &\qquad\qquad\cdot u^*_{\boldsymbol{k}v}(\boldsymbol{r})\boldsymbol{r}u_{\boldsymbol{k}'c}(\boldsymbol{r}) \end{aligned} \tag{2.155}$$

where $C_{m,p} = \sqrt{\frac{\hbar}{2\varepsilon_0 n_r^2\omega_{m,p}V_{\text{eff}}^{m,p}}}$ and where V is the quantization volume for the Bloch functions.

The first term of equation (2.155) will give in the final Hamiltonian a term proportional to $\hat{d}_{m',p'}\hat{a}_{m,p}$, which we will be eliminated due to its non resonant nature. We therefore neglect this term, and reintroduce the matrix element f into $\hat{X}_{m',p'}$ to obtain:

$$\begin{aligned} \hat{X}_{m',p'} = \sum_{m=-\infty}^{+\infty}\sum_{p=1}^{+\infty}C_{m,p}\hat{a}^\dagger_{m,p}\int d\boldsymbol{r}\left\{\frac{1}{V}\sum_{\boldsymbol{k},\boldsymbol{k}'}O_{m',p'}(\boldsymbol{k}',\boldsymbol{k})e^{-j(\boldsymbol{k}'-\boldsymbol{k})\boldsymbol{r}}\right\}\tilde{E}^*_{m,p}(\boldsymbol{r})\boldsymbol{e}^* \\ \cdot u^*_{\boldsymbol{k}v}(\boldsymbol{r})\boldsymbol{r}u_{\boldsymbol{k}'c}(\boldsymbol{r}) \end{aligned} \tag{2.156}$$

18. $f^*_{\boldsymbol{k},\boldsymbol{k}',v,c} = f_{\boldsymbol{k}',\boldsymbol{k},c,v}$ since $\hat{\boldsymbol{A}}$ commutes with $\hat{\boldsymbol{r}}$ in the Coulomb gauge and both operators are hermitian.

19. Here $\tilde{E}^{\text{TE}}_{m,p}(\boldsymbol{r})\boldsymbol{e}_{TE} = \tilde{E}_{m,p}(\boldsymbol{r})\boldsymbol{e}(r,\theta)$, in the following the later vector is noted $\boldsymbol{e}$ for compactness

We place ourselves at the band edge, i.e. $\boldsymbol{k}, \boldsymbol{k'} \simeq 0$, thus $u_{\boldsymbol{k}c/v} \simeq u_{0c/v} \equiv u_{c/v}$ and the only k-dependence is inside the curly braces [20]. With this approximation, we identify the expression between curly braces as the Fourier transform of the exciton envelope function (eq. (2.99)), taken with the electron and the hole at the same position $\boldsymbol{r}$:

$$\frac{1}{V}\sum_{\boldsymbol{k},\boldsymbol{k'}} O_{m',p'}(\boldsymbol{k'},\boldsymbol{k}) e^{-j(\boldsymbol{k'}-\boldsymbol{k})\boldsymbol{r}} = \Phi(0) F_{m',p'}(\boldsymbol{R}_{\parallel}) \chi_c(z_c)\chi_v(z_v) \tag{2.157}$$

To evaluate the remaining integral [21],

$$I = \int d\boldsymbol{r} \Phi(0) F_{m',p'}(\boldsymbol{R}_{\parallel}) \chi_c(z)\chi_v(z) \tilde{E}^*_{m,p}(\boldsymbol{r}) \boldsymbol{e}^* \cdot u_v^*(\boldsymbol{r}) \boldsymbol{r} u_c(\boldsymbol{r}) \tag{2.158}$$

we decompose the space into a sum of atomic unit cells:

$$\int d\boldsymbol{r} \Longrightarrow \sum_i \int_{cell} d\boldsymbol{r}_i \tag{2.159}$$

where $\boldsymbol{r}_i = \boldsymbol{r} - \boldsymbol{r}_i^0$ and $\boldsymbol{r}_i^0$ denotes the position of the i-th atom in the crystal. At the scale of a unit cell ($\simeq 0.1$ nm), the functions appearing in the integral of eq.(2.158) do not change noticeably, except for the atomic Bloch parts u_c and u_v^*.

$$\begin{aligned} I = &\sum_i \int_{cell} d\boldsymbol{r}_i \Phi(0) F_{m',p'}(\boldsymbol{R}^0_{\parallel,i} + \boldsymbol{R}_{\parallel,i}) \chi_c(z_i^0 + z_i)\chi_v(z_i^0 + z_i) \tilde{E}^*_{m,p}(\boldsymbol{r}_i + \boldsymbol{r}_i^0)\boldsymbol{e}^* \\ &\cdot u_v^*(\boldsymbol{r}_i + \boldsymbol{r}_i^0)(\boldsymbol{r}_i + \boldsymbol{r}_i^0) u_c(\boldsymbol{r}_i + \boldsymbol{r}_i^0) \\ &\simeq \sum_i \Phi(0) F_{m',p'}(\boldsymbol{R}^0_{\parallel,i}) \chi_c(z_i^0)\chi_v(z_i^0) \tilde{E}^*_{m,p}(\boldsymbol{r}_i^0)\boldsymbol{e}^* \cdot \int_{cell} d\boldsymbol{r}_i u_v^*(\boldsymbol{r}_i)\boldsymbol{r}_i u_c(\boldsymbol{r}_i) \end{aligned} \tag{2.160}$$

The remaining integral is independent of i, and is precisely (up to the charge) the usual dipole matrix element between the valence and conduction-band atomic Bloch functions:

$$\boldsymbol{r}_{vc} = \frac{1}{V_{cell}} \int_{cell} d\boldsymbol{r} u_v^*(\boldsymbol{r}) \boldsymbol{r} u_c(\boldsymbol{r}) = \langle u_v | \boldsymbol{r} | u_c \rangle \tag{2.161}$$

By re-transforming the sum into an integral $\sum_i \Longrightarrow \frac{1}{V_{cell}} \int$ we obtain:

$$I = \boldsymbol{r}_{vc} \cdot \int d\boldsymbol{r} \Phi(0) F_{m',p'}(\boldsymbol{R}_{\parallel}) \chi_c(z)\chi_v(z) \tilde{E}^*_{m,p}(\boldsymbol{r}) \boldsymbol{e}^* \tag{2.162}$$

and $\hat{X}_{m',p'}$ take the following form:

$$\hat{X}_{m',p'} = \sum_{m=-\infty}^{+\infty} \sum_{p=1}^{+\infty} C_{m,p} \hat{a}^\dagger_{m,p} \boldsymbol{r}_{vc} \cdot \int d\boldsymbol{r} \Phi(0) F_{m',p'}(\boldsymbol{R}_{\parallel}) \chi_c(z)\chi_v(z) \tilde{E}^*_{m,p}(\boldsymbol{r}) \boldsymbol{e}^* \tag{2.163}$$

20. This approximation is justified since the $\boldsymbol{k} \cdot \boldsymbol{p}$ method that we will use later to determine momentum matrix element works for low value of $\boldsymbol{k}$.

21. With electron and hole occupying the same position we have $z_c = z_v$ hence $\boldsymbol{r} = \boldsymbol{R}_{\parallel} + \boldsymbol{z}$

Using again the commutator between the Hamiltonian and position operator, we derive the following relation between matrix elements [163, 164]:

$$\boldsymbol{r}_{vc} = \boldsymbol{p}_{vc} \cdot \frac{-j\hbar}{m_0(E_v - E_c)} \simeq \boldsymbol{p}_{vc} \cdot \frac{j}{m_0 \omega_{m',p'}} \tag{2.164}$$

with m_0 the free electron mass. $\hat{X}_{m',p'}$ becomes:

$$\hat{X}_{m',p'} = \sum_{m=-\infty}^{+\infty} \sum_{p=1}^{\infty} \frac{1}{\omega_{m',p'} m_0} C_{m,p} \Phi(0) I(z) I(r,\theta) \hat{a}^{\dagger}_{m,p} \tag{2.165}$$

with

$$I(z) = \int dz \chi_c(z) \chi_v(z) \tilde{E}^*_x(z) \simeq \tilde{E}^*_x(z_{QW}) \int dz \chi_c(z) \chi_v(z) \tag{2.166}$$

$$I(r,\theta) = \int r dr d\theta F_{m',p'}(r,\theta) \tilde{E}^*_{m,p}(r,\theta) \left[\boldsymbol{p}_{vc} \cdot \boldsymbol{e}^*(r,\theta)\right] \tag{2.167}$$

$I(z)$ is practically identical to the overlap integral of the electron and hole wave function along the z axis. This integral also involves the z distribution of the electromagnetic mode: this implies that the exciton can only couple to a cavity mode sharing the same parity in z. In our case, these z-dependent functions are symmetric: cosine function inside the disk, with exponentially decreasing tails outside. At the scale of the quantum well, one can neglect the z-variations of the electric field, thus $\tilde{E}^*_x(z) \simeq \tilde{E}^*_x(z_{QW})$. Here the QW sits in the middle of disk, as represented in figure 2.2 (b), hence $\tilde{E}^*_x(z_{QW}) = 1$

After injecting the expressions in equation (2.151), the interaction Hamiltonian takes the form:

$$H_I = \sum_{m,m'=-\infty}^{+\infty} \sum_{p',p=1}^{+\infty} \hbar g_{cx}^{m,m',p,p'} (\hat{a}_{m,p} \hat{d}^{\dagger}_{m',p'} + \hat{a}^{\dagger}_{m,p} \hat{d}_{m',p'}) \tag{2.168}$$

with

$$\hbar g_{cx}^{m,m',p,p'} = \frac{e}{m_0} C_{m,p} \Phi(0) I(z) I(r,\theta) \tag{2.169}$$

The scalar product $\left[\boldsymbol{p}_{vc} \cdot \boldsymbol{e}^*(r,\theta)\right]$ is evaluated using standard momentum matrix elements, we present the calculation in appendix B.4. The coupling parameter g_{cx} can now be expressed for the disk WGM and excitonic wavefunction:

$$\begin{aligned}\hbar g_{cx}^{m,m',p,p'} &= \frac{e}{\sqrt{2}m_0} C_{m,p}\Phi(0)I(z)P_x \int r dr d\theta F_{m',p'}(r,\theta)[\tilde{E}^*_{m,p,+}e^{j\theta} + \tilde{E}^*_{m,p,-}e^{-j\theta}](r,\theta) \\ &= \frac{e}{m_0}\frac{C_{m,p}\Phi(0)I(z)P_x\sqrt{2}}{\sqrt{\max\left(\varepsilon(\boldsymbol{r})|\boldsymbol{E}_{m,p}(\boldsymbol{r})|^2\right)}} \quad \int_0^R dr \frac{\sqrt{\varepsilon(r)}}{\beta_{m,p}} E_{0-m,p} K_{m',p'} m J_{m'}(\frac{x_{m',p'}r}{R}) J_m(\beta_{m,p}r) \\ &\qquad \times \int_0^{2\pi} e^{j(m-m')\theta} d\theta \end{aligned} \tag{2.170}$$

where $P_x = |\boldsymbol{p}_{cv}| = \sqrt{\frac{E_P m_0}{2}}$ is a parameter linked to the tabulated Kane energy E_P. Transition to the second line is done using the equations (2.49) and (2.128). The second integral imposes $m = m'$ to obtain non-zero coupling: as required by symmetry, the azimuthal number m is conserved in the coupling. Using the definition of the oscillator strength per unit of area:

$$\frac{f}{S} = \frac{2}{m_0 \hbar \omega_{m',p'}} |\boldsymbol{p}_{cv}|^2 |\Phi(0)|^2 \left| \int dz \chi_c(z)\chi_v(z) \right|^2 \tag{2.171}$$

and assuming that $\omega_{m',p'} \simeq \omega_{m,p}$ the final expression for the coupling constant is:

$$\hbar g_{cx}^{m,p,p'} = \frac{2\pi P_0}{\sqrt{\max\left(\varepsilon(\boldsymbol{r})\left|\boldsymbol{E}^{\sigma}_{m,p}(\boldsymbol{r})\right|^2\right)}} \int_0^R dr \frac{\sqrt{\varepsilon(r)}}{\beta_{m,p}} E_{0-m,p} K_{m',p'} m J_m(\frac{x_{m,p'}r}{R}) J_m(\beta_{m,p}r) \tag{2.172}$$

where

$$P_0 = \hbar \sqrt{\frac{e^2}{2\varepsilon_0 \varepsilon_r m_0 V_{\text{eff}}^{m,p}} \frac{f}{S}}$$

is a parameter taking into account the properties of the quantum well (oscillator strength) and the WGM (mode volume). The final result takes the form of an exciton-photon overlap integral, which has the dimension of a length, multiplied by the parameter P_0 which has the dimension of an energy divided by a length. Interestingly, there is no strict selection rule on the radial quantum number p'/p: the overlap can be non-zero even if $p \neq p'$. This said, for $m = m'$ and $p = p'$ the exciton wavefunction and the electromagnetic mode distribution have similar geometry, governed by the Bessel function, and the overlap integral is maximized.

Figure 2.12 shows the results obtained for the computation of $\hbar g_{cx}^{m,p,p'}$ for different couples (m,p): all these modes lie in the spectral vicinity of the exciton energy at cryogenic temperature for our experimental device. The coupling is very sensitive to the radial number p and seems to be less impacted by a change of the azimuthal number m. Despite the absence of a strict selection rule for the radial number, the coupling is still greatly reduced when $p' \neq p$, as expected from the shape of the overlap integral. However, for increasing p, this behavior becomes less pronounced, and non-negligible coupling can exist between a

photonic and excitonic mode of distinct radial number ($p' = p \pm 1$). For low p values, the two Bessel functions are almost in perfect accordance ($\beta_{m,p} \simeq x_{m,p}/R$), and the overlap integral behave almost as a Dirac function.

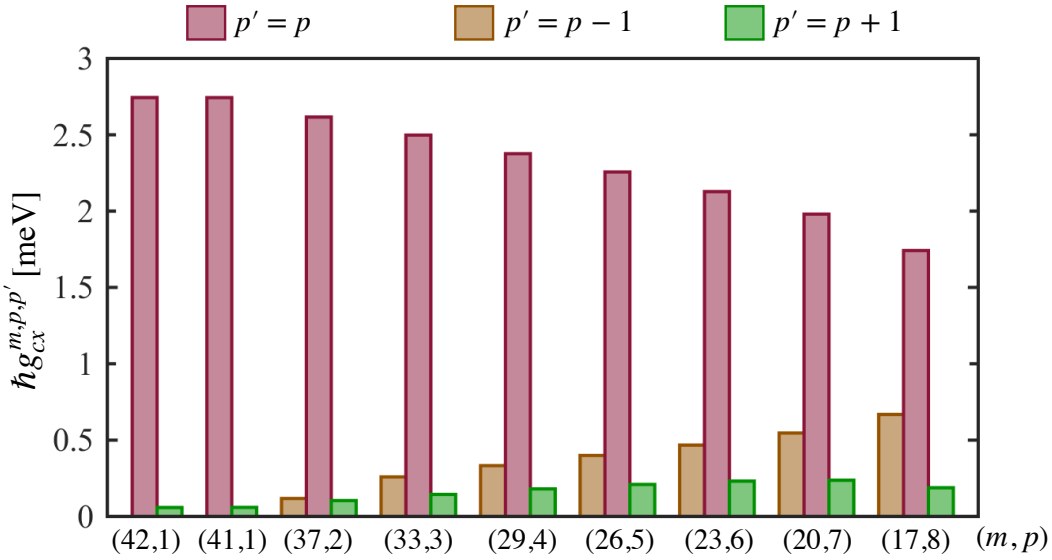

Figure 2.12 – Calculation of the coupling energy $\hbar g_{cx}^{m,p,p'}$ for a single QW located in the middle of the disk considered in our experiments, for different couples of azimuthal and radial numbers (m,p). Three situations are considered: $p' = p$ (red), $p' = p-1$ (brown) and $p' = p+1$ (green).

The formula (2.172) derived in the case of the a single QW generalizes to the MQW case [22] :

$$\hbar g_{cx}^{m,p,p'}(N_{QW}) = \sqrt{\sum_{i=1}^{N_{QW}} \frac{\eta_i^2}{N_{QW}}} \cdot \sqrt{N_{QW}} \hbar g_{cx}^{m,p,p'} = \sqrt{\sum_{i=1}^{N_{QW}} \frac{1}{N_{QW}} \frac{E_x^2(z_{QW,i})}{E_x^2(0)}} \cdot \sqrt{N_{QW}} \hbar g_{cx}^{m,p,p'} \tag{2.173}$$

with N_{QW} the number of QW in the structure. The coupling of the QW to the electromagnetic field depends on its position along the z-axis: its contribution is weighted by the quantity η. For five QWs, a structure that we use in our sample (structure 2 in figure 3.22), the enhanced coupling is equal to $1.89 \times g_{cx}^{m,p',p}$, instead of the idealized factor $\sqrt{5} \simeq 2.23$ that one may have in mind.

2.6 Electromechanical (exciton-phonon) coupling

Up to now, we have successfully described the optical, mechanical, and excitonic modes of our hybrid disk, as well as their optomechanical and optoelectronic coupling. The last

22. See appendix B.5 for derivation.

piece of the tripartite puzzle is to describe the coupling between excitons and phonons, i.e. the electro-mechanical coupling.

2.6.1 Deformation potential

It is a well-known fact that mechanical strain has an effect on the electronic properties of a semiconductor [79, 80, 165–168]. When a piece of semiconductor material undergoes vibrations, the local distribution of atoms in the crystal lattice is modified, ergo its electronic properties change. The electron energy shift caused by this mechanism is grasped by the deformation potential [169, 170]:

$$\hat{E}(\boldsymbol{r_c}, \boldsymbol{r_v}) = a_c \boldsymbol{\nabla} \cdot \boldsymbol{U}(\boldsymbol{r_c}) - a_v \boldsymbol{\nabla} \cdot \boldsymbol{U}(\boldsymbol{r_v}) \tag{2.174}$$

where $\boldsymbol{r_c}/\boldsymbol{r_v}$ are the positions of the carriers in the conduction/valence band, $\boldsymbol{\nabla} \cdot \boldsymbol{U}(\boldsymbol{r})$ the strain at $\boldsymbol{r}$, and a_c/a_v the volume deformation potential for electrons and holes [23] (listed in the tables C.1 and C.2 of appendix C.3). Here the mechanical displacement is defined as $\boldsymbol{U} = x_{\mathrm{ZPF}} \cdot \boldsymbol{u}(\boldsymbol{r})$, with x_{ZPF} the amplitude of the zero-point fluctuations and $\boldsymbol{u}(r)$ the normalized adimensional mechanical wavefunctions introduced in (2.82). The exciton-phonon Hamiltonian corresponding to the deformation potential interaction in second quantization is given by [169, 171, 172]:

$$H_{xm} = -\hbar g_{xm} \hat{d}^\dagger \hat{d} \hat{b} + h.c. \tag{2.175}$$

2.6.2 The disk case

In the case of the disk resonator, the excitonic operators $\hat{d}$ and $\hat{d}^\dagger$ are characterized by a set of quantum numbers $\alpha = (m', p')$, corresponding to the wavefunction considered. The phononic operator is labeled by a single number n, if we restrict the discussion to the coupling with RBMs of order n:

$$H_{xm} = -\hbar g_{xm}^{\alpha,n} \hat{d}_\alpha^\dagger \hat{d}_\alpha \hat{b}_n + h.c. \tag{2.176}$$

In the course of this Ph.D. work carried in tight link with the work of Zakari Denis [173], an expression was derived for the exciton-phonon coupling in the disk [113]:

$$\begin{aligned} -\hbar g_{xm}^{\alpha,n} &= \langle 0, \Psi_{env}^\alpha | \hat{E} | u_n, \Psi_{env}^\alpha \rangle = \int_V d\boldsymbol{r_c} d\boldsymbol{r_v} \Psi_{env}^{\alpha *}(\boldsymbol{r_c}, \boldsymbol{r_v}) E(\boldsymbol{r_c}, \boldsymbol{r_v}) \Psi_{env}^\alpha(\boldsymbol{r_c}, \boldsymbol{r_v}) \\ &= \int_V d\boldsymbol{R}_\parallel d\boldsymbol{\rho} dz_c dz_v |F_\alpha(\boldsymbol{R}_\parallel)|^2 |\Phi(\boldsymbol{\rho})|^2 \\ &\qquad \times \left[a_c \boldsymbol{\nabla} \cdot \boldsymbol{U}(\frac{m_c^*}{M} \boldsymbol{\rho} + \boldsymbol{R}_\parallel) |\chi(z_c)|^2 - a_v \boldsymbol{\nabla} \cdot \boldsymbol{U}(-\frac{m_v^*}{M} \boldsymbol{\rho} + \boldsymbol{R}_\parallel) |\chi(z_v)|^2 \right] \end{aligned} \tag{2.177}$$

23. The effect of the shear in the deformation potential is here neglected, since it involves contribution of $\varepsilon_{r,\theta}$ and $\varepsilon_{r,\theta}$ which are precisely null in the case of RBMs, moreover under the plane stress condition the contribution of the b terms vanish as well, see appendix C.3

This expression can be simplified by assuming two things: the Bohr radius is small compared to the mechanical in-plane wavelength, and the thickness of the quantum well is small compared to the out-of-plane variation scale of the strain, ideally infinite for a RBM. The calculation of the exciton-phonon coupling is this way reduced to a simple 2D overlap integral in the disk plane between the exciton envelope and the strain distribution for a single phonon :

$$-\hbar g_{xm}^{\alpha,n} = (a_c - a_v) \int_S d\boldsymbol{R}_\parallel |F_\alpha(\boldsymbol{R}_\parallel)|^2 \boldsymbol{\nabla} \cdot \boldsymbol{U}(\boldsymbol{R}_\parallel, \boldsymbol{z_{QW}}) \tag{2.178}$$

The single-phonon mechanical strain is obtain with the analytic formula (2.82):

$$\begin{aligned} \boldsymbol{\nabla} \cdot \boldsymbol{U}(\boldsymbol{R}_\parallel) = \varepsilon_{rr} + \varepsilon_{\theta\theta} + \varepsilon_{zz} &= \left(1 - \frac{\sigma}{1-\sigma}\right)(\varepsilon_{rr} + \varepsilon_{\theta\theta}) \\ &= \left(1 - \frac{\sigma}{1-\sigma}\right) A_n x_{\mathrm{ZPF}}^n J_0(\alpha_n \boldsymbol{R}_\parallel) \end{aligned} \tag{2.179}$$

where the plain-stress condition has been used again. All in all, we obtain in the disk case:

$$-\hbar g_{xm}^{m',p',n} = (a_c - a_v)\left(1 - \frac{\sigma}{1-\sigma}\right) \frac{2 x_{\mathrm{ZPF}}^{(n)} A_n \alpha_n}{|J_{m'-1}(x_{m',p'})|^2} \int_0^1 \zeta d\zeta J_{m'}^2(x_{m',p'}\zeta) J_0(\alpha_n \zeta R) \tag{2.180}$$

As α_n is inversely proportional to the radius of the disk R, so is the ratio $g_{xm}^{m',p',n}/x_{\mathrm{ZPF}}^{(n)}$, a relation that reminds that of the geometric contribution to the optomechanical frequency-pull $g_{om}^{geo} \simeq \omega_c/R$.

The results computed for the electromechanical coupling are reported in figure 2.13 for the first three RBMs of the type of disk investigated in this thesis. As we can see the value of the electromechanical coupling can be several times larger than the optomechanical coupling at the exciton wavelength, which was computed in section 2.4. It is yet about a decade larger than the optomechanical coupling at telecom wavelength.

In the case of the disk resonator, the strain is maximal towards the center of the disk ($r \simeq 0$), regardless of the order of the RBM. This is an area where the amplitude of the exciton wavefunction is expected to be null (see figure 2.10). In consequence, the absolute value of g_{xm} decreases when the exciton azimuthal number increases (see figure 2.13-(d)), which pushes the exciton wavefunction towards the disk periphery. For higher-order RBMs, g_{xm} is likely to change sign as a function of m' and p', and even to frankly decrease when the radial variation of the exciton wavefunction will be on a scale small with respect to the mechanical wavelength.

As for the absolute value one can expect from g_{xm}: it also depends on this mechanical wavelength. If the mechanical wavelength becomes small enough to approach the quantum-well thickness, routes are open for an increased strain at the quantum-well position z_{QW}. In

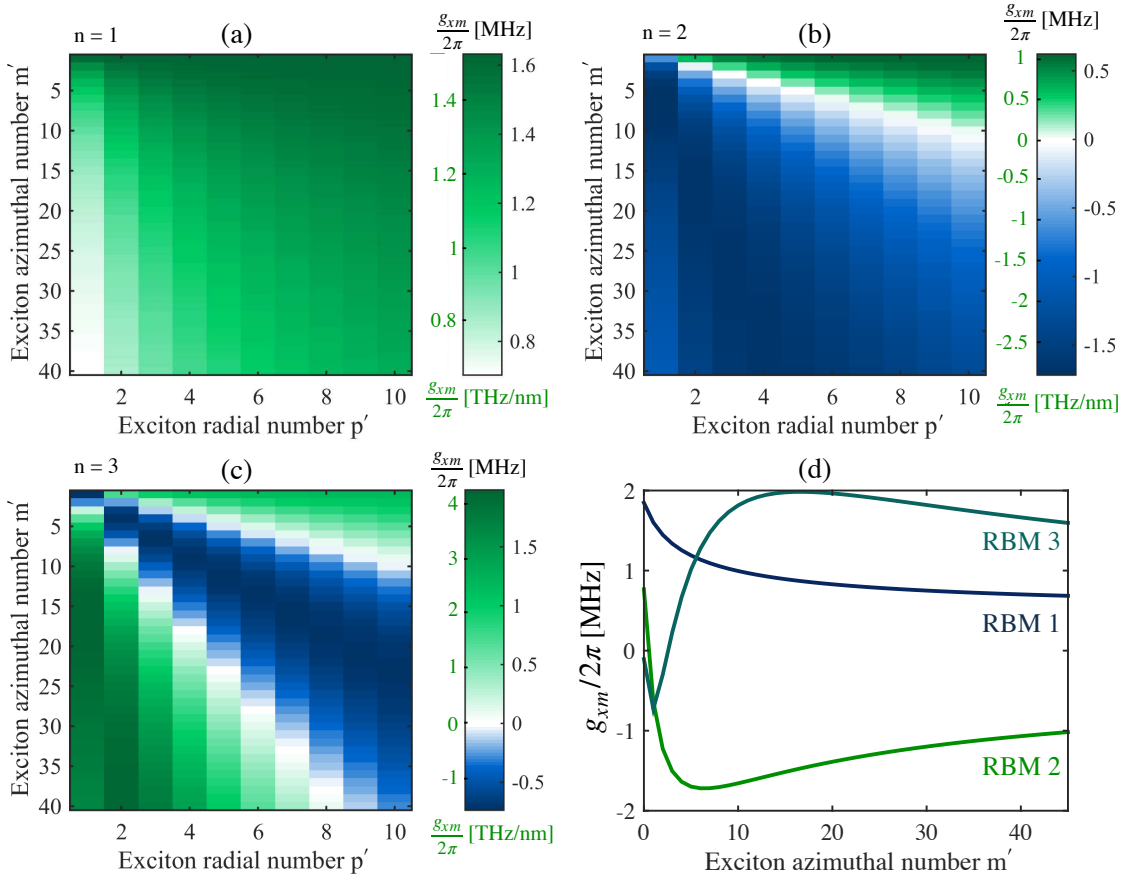

Figure 2.13 – Electromechanical coupling constants as a function of the exction azimuthal m' and radial number p'. Disk radius R=2 μm, thickness h=200 nm (a) RBM 1 (b) RBM 2 (c) RBM3 (d) Cuts taken for p'=1 for the first three RBMs.

this regard, higher-order mechanical modes of a disk, or Bragg modes of a micropillar, offer the prospect of getting increased g_{xm}.

Chapter 3

Experimental set-up, device design and clean-room fabrication

Summary : This chapter yields an overview of all the experimental techniques involved in this thesis. We provide first (section 3.1) a detailed description of the employed cryogenic optical set-up. In section 3.2 we review the tools involved in the conception of our disk resonator. Section 3.3 illustrates the clean-room techniques used to fabricate our resonator samples.

3.1 Experimental set-up

In this section, we describe the setup employed to carry out optomechanical experiments, photo-luminescence (PL), as well as our spectroscopy measurements. A general description is issued first, followed by a more precise discussion of the different apparatus.

3.1.1 General description

A schematic representation of the set-up is given in figure 3.1. A continuous tunable laser source is used to generate a monochromatic light either in the telecom band ($\lambda \in [1.5, 1.63]$ μm) or in the exciton band ($\lambda \in [800, 900]$ nm). This light is injected into a single-mode fiber and sent into a variable optical attenuator (VOA), and then goes through a Fiber Polarization Controller (FPC) which allows us to select the polarization for TE or TM WGMs. The light path continues to a cold environment (~ 3.4 K), where the sample sits on a cold sample holder. At this stage, light is injected into the sample's waveguides (input port) thanks to a first microlensed fiber (μ-lensed fiber) (figure 3.3 (c)) and then collected through the other opposite (output) port of the waveguide with a second μ-lensed fiber. The optical output is then analyzed by using a quasi-DC photo-diode (PD_{DC}, ThorLabs PDA 10CS-EC, range 900-1700 nm - ThorLabs PDA 36A2, range 350-1100 nm) for WGMs laser spectroscopy or with an Optical Spectrum Analyzer (OSA HP 70951A, range 600-1700 nm) for PL experiments. For mechanical mode measurements, we switch to a fast (AC) photo-diode (PD_{AC}, ThorLabs DET08CFC/M, range 800-1700 nm, 5 GHz - NewPort 818-45-BB, range 500-900 nm, 12.5 GHz) and analyze the photo-diode output signal with an Electrical Spectrum Analyzer (ESA Rhode & Swartz ZVL, 3GHz). When moving our experiments from the telecom band to the exciton band, we replace the whole single-mode fiber path from SMF28 to 780HP, including the μ-lensed fibers, which are fabricated for a specific target wavelength.

On top of such optical experiments through the waveguide, our setup opens the dual possibility of using a confocal microscope on top, in a direction perpendicular to the sample plane (Optical Head in figure 3.1). This confocal microscope allows to visualize the sample in the cryostat with a camera and perform confocal spectroscopy and excitation/collection experiments.

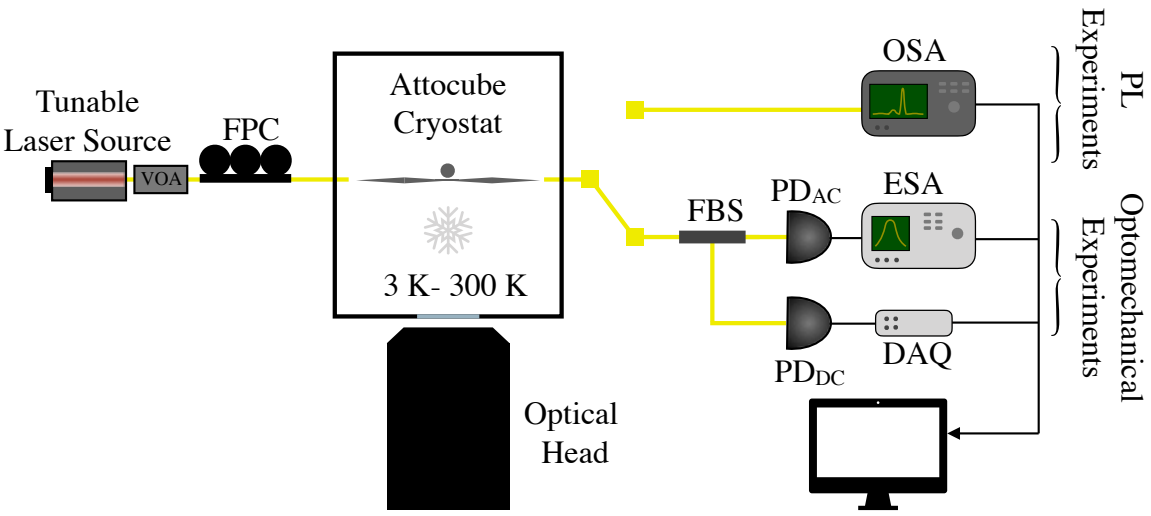

Figure 3.1 – Global setup. The yellow lines represent optical single mode fibers, the black lines electric cables. FBS : Fiber Beam Splitter - DAQ : Electronic Data Acquisition card.

3.1.2 Cryostat

It is pivotal (not essential, but most natural) to work at cryogenic temperature to perform quantum optomechanical experiments. Furthermore, we work here with quantum well excitons and seek to get the best excitonic signal. PL signals at room temperature are usually broader and weaker due to enhanced non-radiative channels, and excitons are destroyed by the thermal motion ($k_B T \gg E_b$). Another benefit of working at cryogenic temperatures is the improvement of Q_m, in our case by a factor of 10 to 50. For all these reasons, we need to cool down our device: all our experiments at cryogenic temperature were carried out with the *Attocube Photonic Probe Station cryostat* [174]. This apparatus combines a dry cryocooler (*Cryomech Cryogenic Refrigerator PT407*), a piezo-controlled movable station where the μ-lensed fibers and the sample sits, and an optical head that allows us to observe the sample "from the top" (it is actually from below since the sample is mounted upside-down) and perform confocal PL experiments. A picture and a scheme of the apparatus are provided in figure 3.2.

The cooling power of the cryostat comes from a pulsed-tube refrigerator. This type of cryocooler offers several advantages: first no need to fill the cryostat with liquid helium since the operation principle is based on a gaseous helium closed-loop circuit, second the temperature reached is often below the 4 K, 3.4 K during our experiments and 2.6 K in the best case, third the maintenance is relatively easy. In our cryostat set-up, a coaxial configuration is adopted: the pulsed tube is placed on top of the cryostat chamber where two stages can be distinguished. During a cycle of compression/decompression of the gaseous helium, heat is extracted from the first stage, which typically reaches a temperature close to 56 K, this stage, in turn, extracts heat from the second stage where the probe station itself lies, with the sample and the lensed fibers. This last stage reaches a temperature of about 3 K. The chamber of the cryostat is pumped to $\sim 10^{-6} - 10^{-7}$ mbar to avoid heat transfer through the wall of the cryostat. A cooling cycle takes approximately 12 hours. Further

details on the working principle of pulse tube refrigerators can be found in [175].

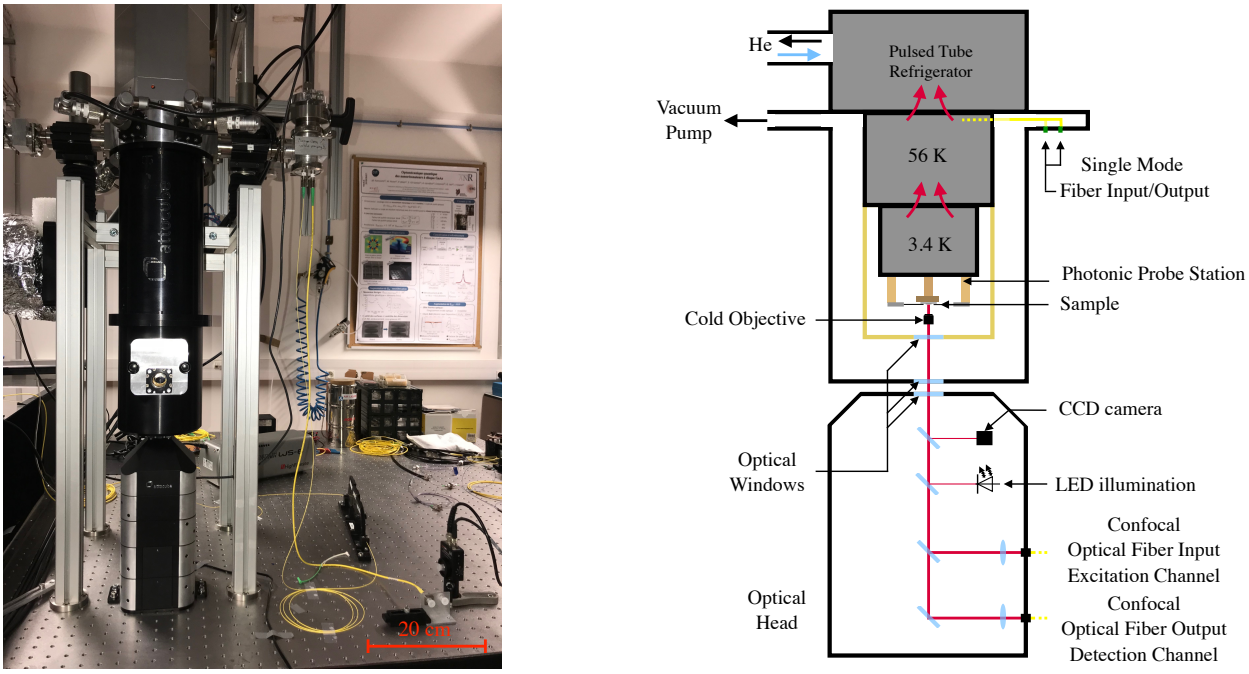

(a) (b)

Figure 3.2 – (a) Picture and (b) Scheme of the Attocube cryostat dubbed with the Photonic Probe Station (first generation). The red arrows in (b) represent the heat transfer between the different stages of the chamber

Photonic probe station and optical head :

At the 3 K stage, we find the probe station itself (see figure 3.3 (a)), this station includes a piezo stage with two degrees of freedom X and Y, on which sit the sample holder and two XYZ piezo stepper-positioners working on the "slip-stick" principle [176]. These positioners combine a large traveling range (∼6 mm) and a nanometer position resolution, and support the μ-lensed fibers holders. By using the three degrees of freedom (XYZ), we can achieve a good coupling between the μ-lensed fibers and the waveguide of the sample (see figure 3.3 (b)). The piezo-positioners are controlled with the attocube ANC300 and ANC350 controllers. Note that the sample is rigidly stuck with vacuum grease on the sample holder. Moving the first XY piezo stage in one direction moves the whole structure consisting of μ-lensed fibers+sample. Under the sample holder, a microscope objective (magnification $\times$ 100) mounted on a Z-piezo is placed. The optical axis of this objective is fixed and coincides with the optical axis of the cryostat, while the sample is moved in the XY plane perpendicular to this axis. The output optical signal of the objective is partially collected by a CCD camera placed in an "optical head" unit located just outside and under the cryostat chamber (figure 3.3 (b)). This camera enables imaging the sample and aligning the μ-lensed fibers to the waveguides. The optical head contains as well other channels that can be configured for confocal laser excitation or detection. Each channel has a fiber port, a collimator, and θ/ϕ

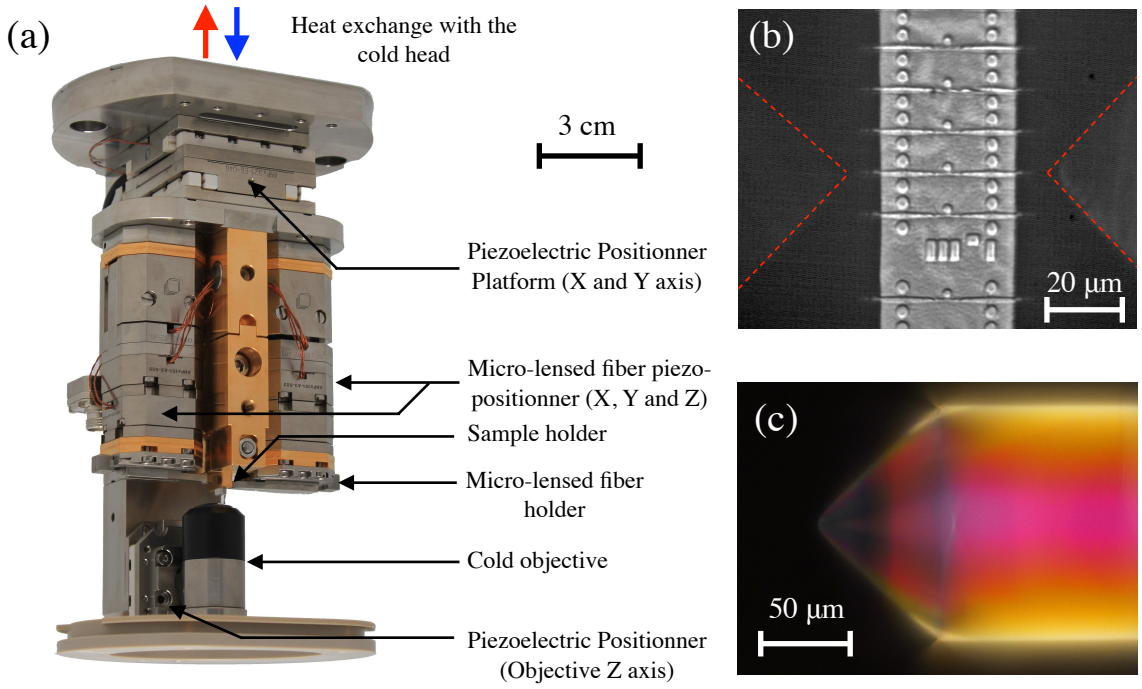

Figure 3.3 – (a) Attocube photonic probe station. (b) View of the sample obtained with the CCD camera inside the cryostat, μ-lensed fiber are in the vicinity of the sample highlighted by red dashed lines (c) Microscope picture of the μ-lensed fiber, Magnification = 500

tilt mirrors that guide the optical beams in free space within the unit before entering or leaving the cryostat through an optical window located next to the microscope insert. Thanks to this, we can carry out PL/optical spectroscopy experiments in three different configurations:

- First configuration: traditional confocal micro-photoluminescence scheme (C-μPL): a tunable laser source is sent onto the top of the disk via the microscope objective and the scattered and emitted signal is collected confocally. (Figure 3.4 (a))
- Second configuration: Confocal excitation/ collection through waveguides. In this configuration, the laser excitation is performed confocally but we employ suspended waveguides integrated into the vicinity of the disk-like antennas, collecting the emitted light from the disk. μ-lensed fibers are then located at the tips of the waveguides to extract the light out of the cryostat chamber. (Figure 3.4 (b))
- Third configuration: traditional in-plane laser spectroscopy configuration. Tunable laser light is injected at one port of the waveguide, collected at the other port. (Figure 3.4 (c))

The probe station also includes two resistive heaters (one at each stage 3 K and 56 K), that allow us to vary the temperature inside the cryostat. The temperature is monitored with a temperature controller (LakeShore 335) with configurable PID control loops.

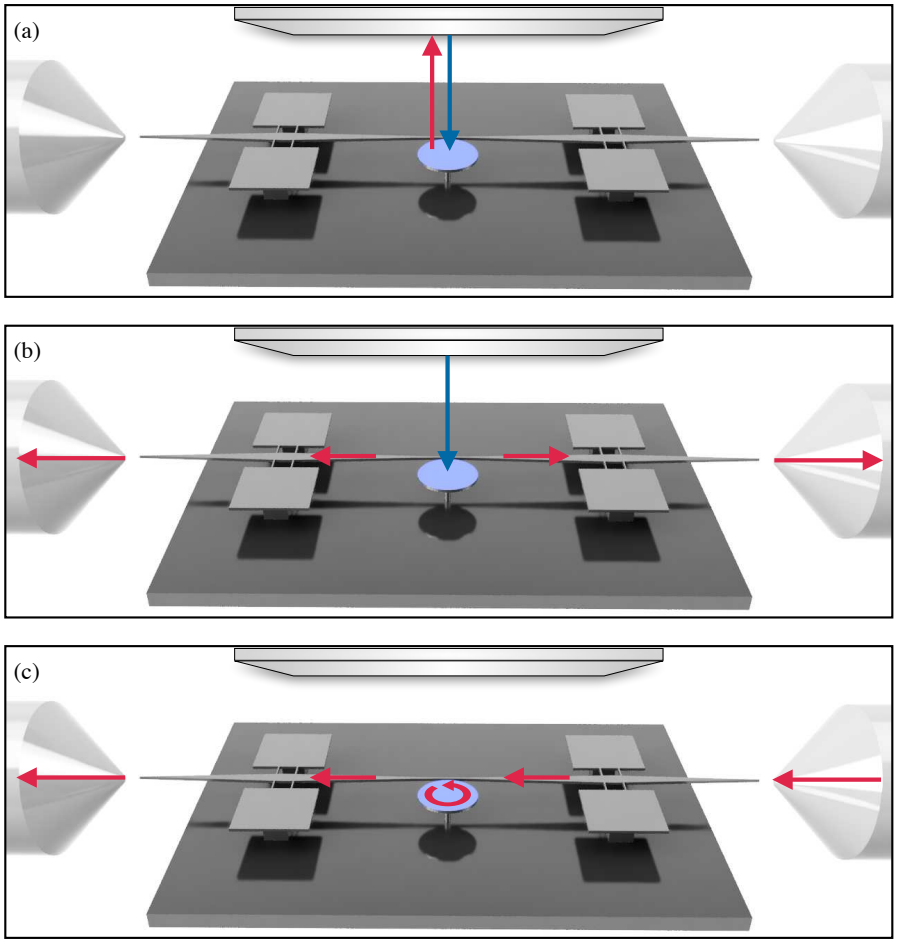

Figure 3.4 – (a) C-μPL configuration (b) Confocal excitation and collection through waveguides. Blue arrows indicate excitation light beams with an energy higher than the exciton. Red arrows in (a), (b) correspond to light close to the exciton energy. (c) In-plane laser spectroscopy configuration. The red arrows in (c) represent tunable laser light either in the telecom band or in the exciton band.

3.1.3 Laser sources

For optomechanical experiments, we need a stable monochromatic source of light with low noise. Two different wavelength ranges are used that correspond to two different laser sources:

- 800-900 nm : Exciton band with a M-squared SolsTiS laser
- 1500-1630 nm : Telecom band with a Yenista Tunics T100S-HP

Both options have strengths and drawbacks. In the exciton band, WGMs are usually more confined within the disk, but the vicinity in energy to the GaAs gap can lead to extra linear absorption. However, since photoelastic constants rise sharply near the gap we can expect a higher optomechanical coupling. Working in the telecom band for small disks

($R \leq 2\mu m$, $h = 200$ nm) increases bending losses and lowers Q_{opt}. However, an erbium-doped optical fiber amplifier (EDFA) of very low noise can be used in this range, which eases the mechanical motion readout.

3.1.3.1 Titanium sapphire : M-squared SolsTiS laser

Principles of operation : Ti:S laser sources typically operate in a 700-1000 nm range thanks to the broad optical gain of the Ti:S (Ti-Al_2O_3) crystal. The picture and architecture of the laser are represented in figure 3.5. The gain medium is pumped by a very stable green ($\lambda = 532$ nm) solid-state laser (Lighthouse Sprout-G laser; absorption of Ti:S typically occurs between 400 to 600 nm). The cavity geometry is the "bow-tie" ring cavity geometry, which forces the light to travel uni-directionally, and results in the absence of standing waves depleting the gain medium and producing spatial-hole burning. To select the output wavelength of the cavity several components are used. First of all, a birefringent filter (BRF) is placed in the optical path: by rotating the BRF a wavelength-dependent loss in the cavity is introduced and a selection of the lasing modes is achieved. Nevertheless, this selection is relatively coarse compared to the free spectral range (FSR) of the bow-tie cavity (mode spacing ~ 416 MHz or ~ 1 pm for a center wavelength at 850 nm [177]), thus to increase the selectivity, an etalon Fabry-Pérot resonator is introduced. This Fabry-Pérot has a relatively short cavity length ($\sim$ 1mm), resulting in a small FSR (~ 0.4 nm for a center wavelength of 850nm). By changing its length (thanks to a piezoelectric translator PZT), fine-tuning can be achieved (the cavity has a high finesse resulting in the selection of a unique longitudinal mode). At this point, single-mode lasing is achieved but depending on external fluctuations (mechanical vibrations, change in temperature/pressure, pump power fluctuations...) the laser can oscillate between two or several frequencies. To address this undesirable effect an electronic locking of the etalon is added.

Always seeking for the narrowest possible linewidth, several improvements are made to the architecture of the laser. One of the mirrors of the bow-tie cavity is mounted on a slow and long-range PZT: tuning the cavity length allows perfectly matching the single oscillating longitudinal cavity mode frequency of the etalon. Another improvement is the addition of one highly stable reference cavity (Fabry-Pérot) with high finesse. This cavity is used as a reference for feedback in a Pound-Drever-Hall stabilization scheme [178]. Indeed, a small fraction of the output light of the laser is directed to the reference cavity and the main laser cavity becomes slaved to this reference. The error signal is then sent to the PZT-mounted mirror of the main cavity, which also possesses a fast and short-range PZT for rapid stabilization. All these improvements enable reaching a linewidth inferior to 50kHz.

Scanning modes : In order to perform laser spectroscopy experiments, we need to carry out scans of the laser wavelength. We need to reach a resolution close to 50 GHz since the typical spectral linewidth of the WGMs lies in this range and above, between 1 to 200 pm. When a rotation of the BRF is operated, the laser frequency is tuned in steps following the FSR of the etalon, close to 0.4 nm, which is not fine enough for our purpose. To overcome this limitation, a *stiching* scheme is implemented into the system to effectively enable a *con-*

(a)

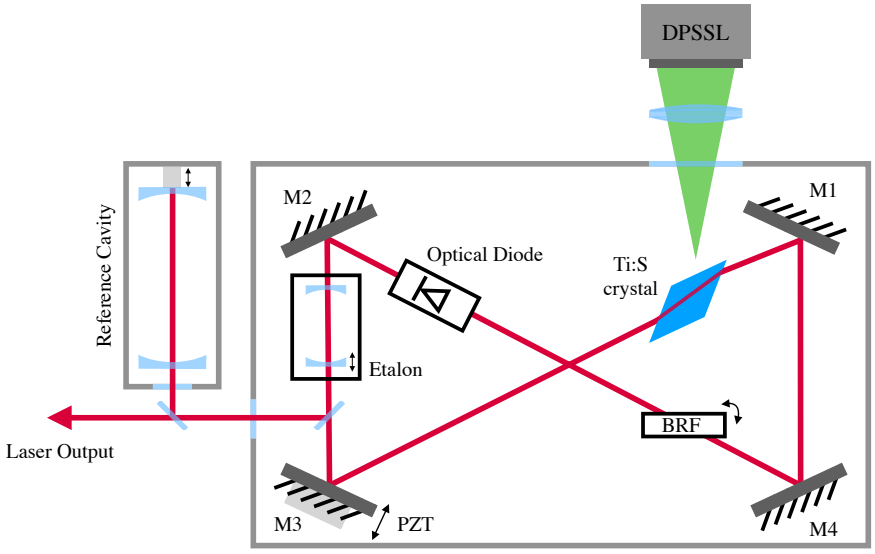

(b)

Figure 3.5 – (a) Picture and (b) Scheme of the bow-tie cavity of the M-Squared SolsTiS laser. DPSSL : Diode Pumped Solid State Laser.

tinuous scan. The principle is as follows: the wavelength is continuously scanned by varying the dimension of the etalon or by modifying the cavity length with the piezo-mounted mirror: at a certain point the lasing mode hops, the etalon is sent back to its original position and the BRF is rotated to retrieve the last wavelength obtained before hopping. The scan is then taken over, repeating these steps until the final wavelength of the scan is reached. This allows us to carry out long-range scans ($\sim$ 100 nm). This comes however with some limitations: firstly it is not a true continuous scan if we monitor the evolution of the wavelength along time the curve looks like a linear curve superposed with a sawtooth pattern. Secondly, this mode of scan is long: the stitching takes $\sim$ 10 seconds, which results in a total scan time of 40-60 minutes for a 100 nm scan range.

3.1.3.2 Telecom Tunics laser

The Tunics laser is an External Cavity Diode Laser (ECDL): its operation principle is rather simple. A laser diode chip is integrated into a frequency selective element like a diffraction grating, completed with a collimating lens. The chip typically possesses an anti-reflection coated facet and a high-reflectivity coated facet. In the case of the Tunics laser, the Littrow architecture is adopted. The 1^{st}-order diffracted beam provides optical feedback to the laser diode chip, whereas the 0^{th}-order is the laser output. By rotating the diffraction grating, the wavelength at the output is tuned. One of the main advantages of this kind of laser is that the whole wavelength range can be scanned in just a few seconds, which is extremely convenient for spectroscopy experiments. There are no mode hops in the Tunics laser, at variance with the SolsTiS.

3.1.4 Optical and mechanical readout

Optical mode characterization : Optical modes are generally measured by laser spectroscopy (third configuration figure 3.4). We vary the laser wavelength and measure the voltage at the output. The electrical signal is directly proportional to the optical transmission of the waveguide-disk structure. By calibrating the different stages of the set-up we directly access the circulating power inside the disk. A typical optical spectrum is presented in figure 3.6 (a), it can be modeled as a Lorentzian and the full width at half maximum (FWHM) $\Delta\lambda$, is linked to the optical quality factor $Q_{\text{opt}} = \lambda_c/\Delta\lambda$.

Mechanical mode characterization : Mechanical modes are measured thanks to the AC photodetector since the optical signal is modulated at the mechanical frequency. We set the laser on the blue-flank of the resonance ($\Delta > 0$) and detect the fluctuations of output optical power caused by the mechanical motion. For low optical power, the optomechanical dissipation rate Γ_{om} is negligible compared to the intrinsic mechanical dissipation rate Γ_m. The optical-spring frequency shift $\delta\omega_m$ is also small compared to the mechanical frequency ω_m. The mechanical spectrum can be also fitted to a Lorentzian (see figure 3.6 (b)), where the FWHM Γ_m, is associated to the mechanical quality factor $Q_{\text{m}} = \omega_m/\Gamma_m$.

The value of Γ_m is set by multiple sources of mechanical dissipation:

- Viscous/fluidic damping: mechanical dissipation due to the surrounding fluid. When the disk boundaries move the mechanical energy is dissipated through viscosity and emission of acoustic waves in the fluid.

- Clamping losses: the disk's mechanical dissipation can take place through the pedestal of the disk. Work has been made in the group on the design of the disk and its pedestal, by adding a shield. Reduction of the mechanical dissipation through the anchoring point was this way observed [179].

- Thermo-elastic losses: the deformation profile of the mechanical modes is note uniform, regions of the material under compressive strain heat up, while regions under

tensile strain cool down. As a result, a heat flow is generated between the "hot" and "cold" areas, leading to the creation of entropy and dissipation. This is one example of losses induced by phonon-phonon interactions resulting from the non-harmonicity of the lattice. These losses are greatly diminished working at cryogenic temperature [122].

- Material Induced losses: material losses are caused by the relaxation of defects (two-level systems) mainly localized at the surface of the resonator, but also present within the bulk. These losses tend to diminish at lower temperatures, at least in most crystalline materials [180].

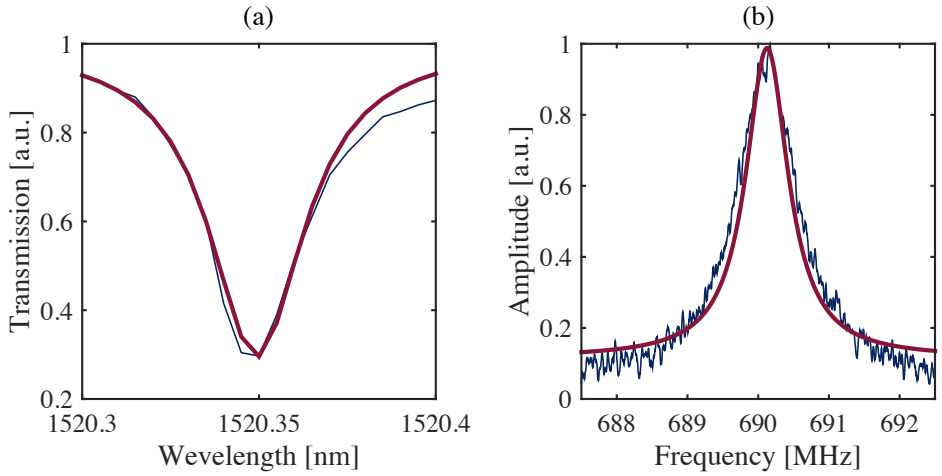

Figure 3.6 – (a) Optical transmission spectrum for a TE mode in the telecom band, $Q_{\text{opt}} \simeq 10^5$ (b) Mechanical spectrum for the RBM1 at room temperature in vacuum $Q_m \simeq 10^3$

3.2 Sample design

We provide a short overview of the key features of the sample design. First how we couple light inside disk resonators using "fully-suspended" waveguides, and second how these waveguides are designed. We also review the mechanisms responsible for optical losses in the resonators.

A crucial point in the design of the sample is also the choice of the quantum-well heterostructure, which will directly tailor the properties of the exciton. Including such a heterostructure inside the disk comes at a price: optical properties of the disk/waveguide are impacted, equivalently some properties of the bare hetero-structure are impacted by the disk geometry and fabrication process.

3.2.1 Disk resonator-waveguide coupling

Our GaAs disks are WGMs resonators with an intrinsically good quality factor, now the key point for applications is to efficiently couple light to them. Correct excitation of the modes can be reached by spatial and temporal matching. Experimentally speaking, this can be achieved by using a tapered waveguide, where the evanescent field of the guide overlaps with that of the resonator modes.

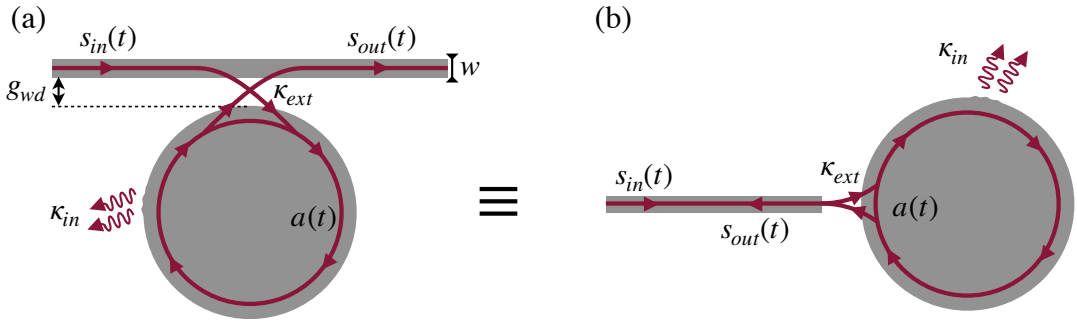

Figure 3.7 – Waveguide/disk coupling described by the CMT. (a) Waveguide coupled optical cavity (b) Single sided coupled optical cavity. The two schemes are equivalent. g_{wd} represents the gap distance between the disk and the waveguide, w represent the width of the waveguide.

3.2.1.1 Coupled Mode theory

A good way to describe the resonator-waveguide coupling is to use the Coupled Mode Theory (CMT) under a slowly varying envelope assumption. In this perturbative theory, the presence of the waveguide in the vicinity of the resonator does not modify the WGMs of the disk resonator, reciprocally the presence of the disk does not impact the modes of the waveguide. A full presentation of this theory is found in [121, 122, 181, 182], we will just review here the main useful relations and apply the formalism from [183].

The resonator-waveguide coupling is described with three parameters: ω_c the cavity resonance frequency, κ_{in} the intrinsic cavity loss rate, and κ_{ex} the cavity coupling to the waveguide, with the relation $\kappa_c = \kappa_{\text{in}} + \kappa_{ex}$, for κ_c the total loss rate of the cavity mode (see figure 3.7). The time evolution of the fields inside the cavity and the waveguide are given by :

$$\frac{da(t)}{dt} = -(j\omega_c + \frac{\kappa_{\text{in}}}{2} + \frac{\kappa_{\text{ext}}}{2})a(t) + \sqrt{\kappa_{\text{ext}}}s_{\text{in}}(t) \tag{3.1}$$

$$s_{\text{out}}(t) = +s_{\text{in}}(t) - \sqrt{\kappa_{\text{ext}}}a(t) \tag{3.2}$$

where $s_{\text{in}}(t)$ and $s_{\text{out}}(t)$ represent respectively the incident and output field onto/from the cavity. Note that we retrieve here precisely eq. (1.15) of chapter 1, obtained with the input-output formalism (apart from the optomechanical term and the vacuum input noise

$\hat{a}_{\text{in}}$ that is absent in classical CMT). $a(t)$ and $s_{\text{in}}(t)$ have different dimensions, since $|a|^2$ corresponds to the normalized resonator electromagnetic energy and $|s_{\text{in}}|^2$ the normalized incoming power. In absence of input field and intrinsic losses, the energy of the resonator evolves as :

$$\frac{d|a(t)|^2}{dt} = -\kappa_{\text{ext}}|a(t)|^2 \tag{3.3}$$

i.e. all the energy stocked in the disk leaks to the waveguide output.

We usually use the ansatz $s_{\text{in}} \propto e^{-j\omega_l t}$ to describe the incoming port, and assume that the system responds linearly, which means that the cavity field evolves at the same frequency ($a \propto e^{-j\omega_l t}$). In this case eq. (3.1) leads to the following expression :

$$a = \frac{\sqrt{\kappa_{\text{ext}}}s_{\text{in}}}{+j\Delta - (\frac{\kappa_{\text{in}}}{2} + \frac{\kappa_{\text{ext}}}{2})} \tag{3.4}$$

with $\Delta = \omega_l - \omega_c$ the laser-cavity detuning. The number of photons in the WGM is given by :

$$N_{\text{cav}} = \frac{|a|^2}{\hbar\omega_l} = \frac{\frac{\kappa_{\text{ext}}}{\hbar\omega_l}}{\Delta^2 + (\frac{\kappa_{\text{in}}}{2} + \frac{\kappa_{\text{ext}}}{2})^2}|s_{\text{in}}|^2 \tag{3.5}$$

Using (3.2) we obtain the outgoing field s_{out}, finally leading to the optical transmission T [1] through the waveguide :

$$T = \frac{|s_{\text{out}}|^2}{|s_{\text{in}}|^2} = \frac{\Delta^2 + (\frac{\kappa_{\text{in}}}{2} - \frac{\kappa_{\text{ext}}}{2})^2}{\Delta^2 + (\frac{\kappa_{\text{in}}}{2} + \frac{\kappa_{\text{ext}}}{2})^2} \tag{3.6}$$

The transmission contrast C is then given by :

$$C = 1 - T(\Delta = 0) = \frac{\kappa_{\text{in}}\kappa_{\text{ext}}}{(\frac{\kappa_{\text{in}}}{2} + \frac{\kappa_{\text{ext}}}{2})^2} \tag{3.7}$$

Figure 3.8 represents the normalized transmission and the number N_{cav} of photons in the cavity in function of the wavelength, for different values of the ratio $r = \kappa_{\text{ext}}/\kappa_{\text{in}}$. The linewidth that appears in the transmission resonance reflects the total loss and the loaded quality factor (Q_{opt}) is given by :

$$\frac{1}{Q_{\text{opt}}} = \frac{1}{Q_{\text{ext}}} + \frac{1}{Q_{\text{in}}} = \frac{\kappa_{\text{ext}}}{\omega_c} + \frac{\kappa_{\text{in}}}{\omega_c} = \frac{\kappa_c}{\omega_c} \tag{3.8}$$

Different regimes can be identified as a function of the ratio r. When $\kappa_{\text{ext}} = \kappa_{\text{in}}$ ($r = 1$), the so-called *critical coupling regime*, the contrast in transmission is 100% and the number of photons in the cavity is maximal. When $\kappa_{\text{ext}} < \kappa_{\text{in}}$ ($r < 1$), in the *under-coupled regime,* the contrast is below 100%, the linewidth of the resonance is narrower but photons tend to

1. Since we collect the light that is passing through the waveguide we refer to a transmission measurement. However, as illustrated in figure 3.7, s_{out} can actually rather be seen as the field "reflected" by the cavity, in a single-port vision.

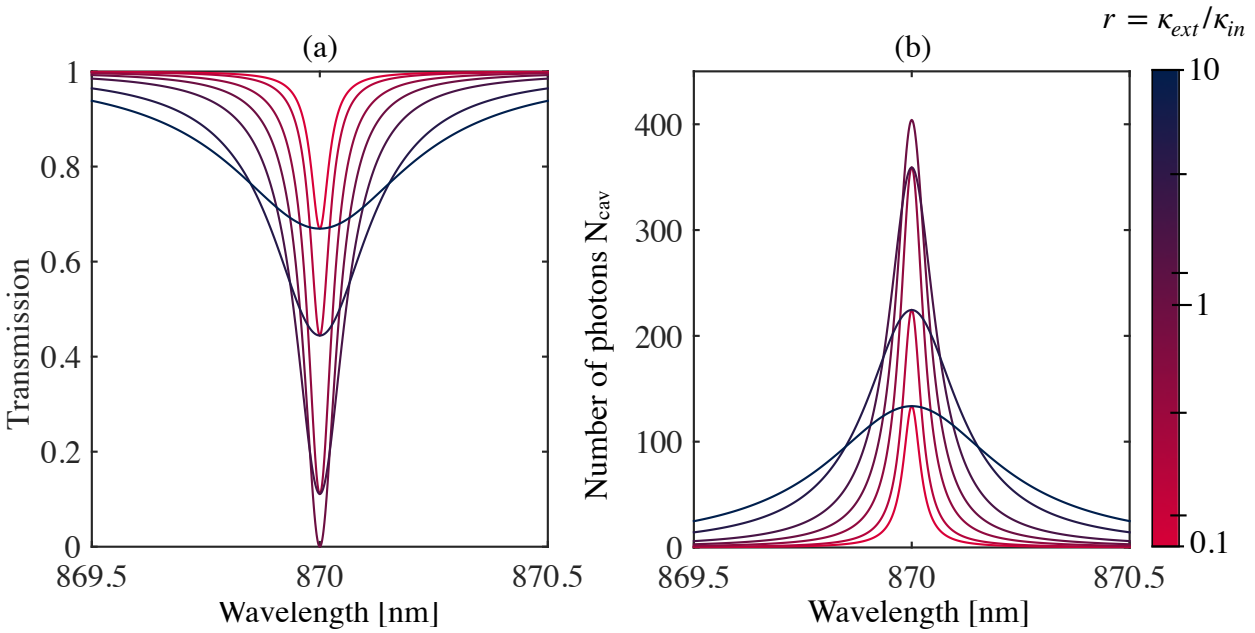

Figure 3.8 – (a) Waveguide transmission and (b) Number of photons N_{cav} in the cavity in function of the laser wavelength for different value of the ratio $r = \kappa_{\text{ext}}/\kappa_{\text{in}}$. Parameters of the mode (in the exciton band) : $Q_{\text{in}} = \frac{\omega_c}{\kappa_{\text{in}}} = 2 \cdot 10^4$, $\lambda_c = \frac{2\pi c}{\omega_c} = 870$ nm, $|s_{\text{in}}|^2$=10μW.

be intrinsically lost by the disk, which means a loss of information. When $\kappa_{\text{ext}} > \kappa_{\text{in}}$ ($r > 1$), in the *over-coupled regime*, the contrast is still below 100%, the linewidth of the resonance is broader but photons tend to preferentially escape from the disk through the waveguide, i.e. can be collected on the photodetector.

In a perfect circular disk, two WGMs coexist at the same energy: the clockwise (CW) and the counterclockwise (CCW). Surface roughness or departure from the circular symmetry is responsible for lifting this degeneracy and creating two standing wave modes. This CW-CCW coupling is characterized by a coefficient β [184]. In that case, the number of photons in the cavity and the transmission of the waveguide are given by [121] :

$$N_{\text{cav}} = \left(\frac{1}{(\Delta-\beta)^2 + \left(\frac{\kappa_{\text{in}}}{2} + \frac{\kappa_{\text{ext}}}{2}\right)^2} + \frac{1}{(\Delta+\beta)^2 + \left(\frac{\kappa_{\text{in}}}{2} + \frac{\kappa_{\text{ext}}}{2}\right)^2}\right) \frac{\kappa_{\text{ext}} |s_{\text{in}}|^2}{2\hbar\omega_l} \tag{3.9}$$

$$T = \frac{|s_{\text{out}}|^2}{|s_{\text{in}}|^2} = \left| \frac{-\Delta^2 + j\kappa_{\text{in}}\Delta + \beta^2 + \left(\frac{\kappa_{\text{in}}}{4} - \frac{\kappa_{\text{ext}}}{4}\right)^2}{-\Delta^2 + \left(\frac{\kappa_{\text{in}}}{2} + \frac{\kappa_{\text{ext}}}{2}\right)^2 + \beta^2 + 2j\Delta\left(\frac{\kappa_{\text{in}}}{2} + \frac{\kappa_{\text{ext}}}{2}\right)} \right|^2 \tag{3.10}$$

As seen in the figure 3.9, in the case of CW-CCW coupling the shape of the singlet resonance is transformed into a doublet. N_{cav} is still maximal at the critical regime ($r = 1$) but the transmission contrast is not anymore. For our small disk, this CW-CCW phenomenon is more pronounced for WGMs in the telecom band, whose electromagnetic fields are closer to the edges of the disk.

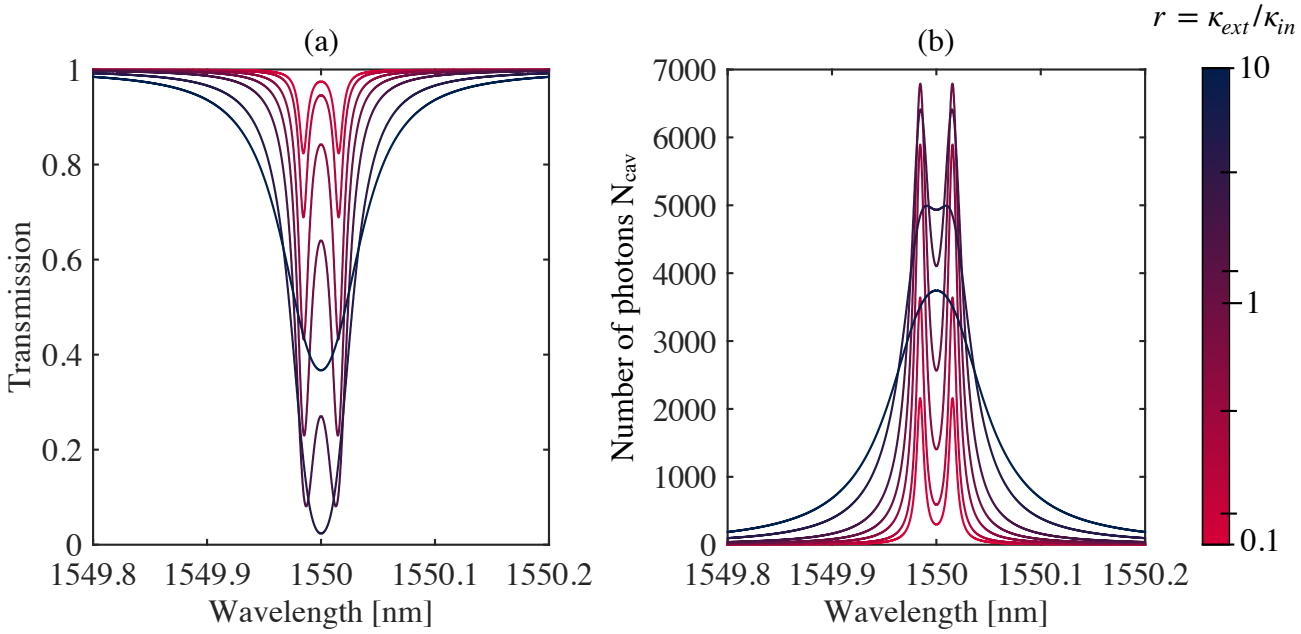

Figure 3.9 – (a) Waveguide transmission and (b) Number of photons N_{cav} in the cavity in function of the laser wavelength for different value of the ratio $r = \kappa_{\text{ext}}/\kappa_{\text{in}}$. Parameters of the mode (in the telecom band) : $Q_{\text{in}} = \frac{\omega_c}{\kappa in} = 2 \cdot 10^5$, $\lambda_c = \frac{2\pi c}{\omega_c} = 1550$ nm, $|s_{\text{in}}|^2$=10μW, $\beta = 2\kappa_{\text{in}}$.

Achieving the critical coupling regime is often useful in our experiments : it maximizes N_{cav} while maintaining a good Q_{opt}. We have distinguished extrinsic losses ($Q_{\text{ext}} = {}^{\omega_c}/_{\kappa_{\text{ext}}}$) from intrinsic losses ($Q_{\text{in}} = {}^{\omega_c}/_{\kappa_{\text{in}}}$). To obtain $r = 1$ we should ideally understand and control both terms.

3.2.1.2 Origin of optical losses - κ_{in}

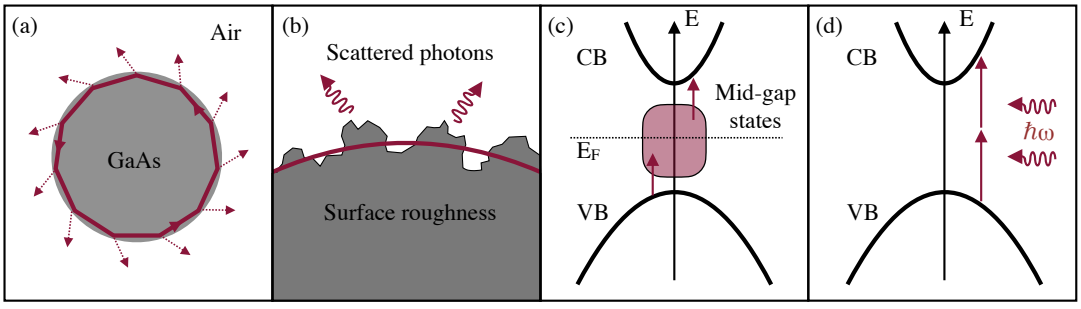

Figure 3.10 – Mechanisms responsible for intrinsic optical losses in the disk (a) Bending losses (b) Surface scattering due to disk roughness (c) Linear absorption, an arbitrary Fermi level E_F is represented (d) Two-photon absorption TPA

Sources of intrinsic loss are multiple : bending losses Q_{bend}^{-1}, scattering losses Q_{scat}^{-1}, linear absorption losses Q_{abs}^{-1} and the non-linear two-photon absorption losses (TPA) Q_{TPA}^{-1} (see

figure 3.10). We treat these channels of dissipation as independant. The intrinsic quality factor of the WGM resonator can be therefore written as [121, 182] :

$$Q_{\text{in}}^{-1} = Q_{bend}^{-1} + Q_{scat}^{-1} + Q_{\text{abs}}^{-1} + Q_{\text{TPA}}^{-1} \tag{3.11}$$

Q_{bend} : Bending losses of a WGM (see figure 3.10 (a)) depend on the curvature of the disk resonator. They increase when the radius of the disk decreases, and can in general not be neglected even for an ideal material and perfect fabrication. These losses can be computed by FEM simulations (see figure 3.11): a Perfectly Matched Layer (PML) is placed around the simulation domain, mimicking absorption of the radiated field at infinity. The losses are manifested by the appearance of an imaginary part in the eigenfrequency ω_c :

$$Q_{bend} = \frac{\text{Re}(\omega_c)}{2\text{Im}(\omega_c)} \tag{3.12}$$

Numerically the limitations of our FEM calculations places an upper bound of $Q_{bend} \simeq 10^{9-10}$. For a given disk, the bending losses tend to increase at a larger optical wavelength.

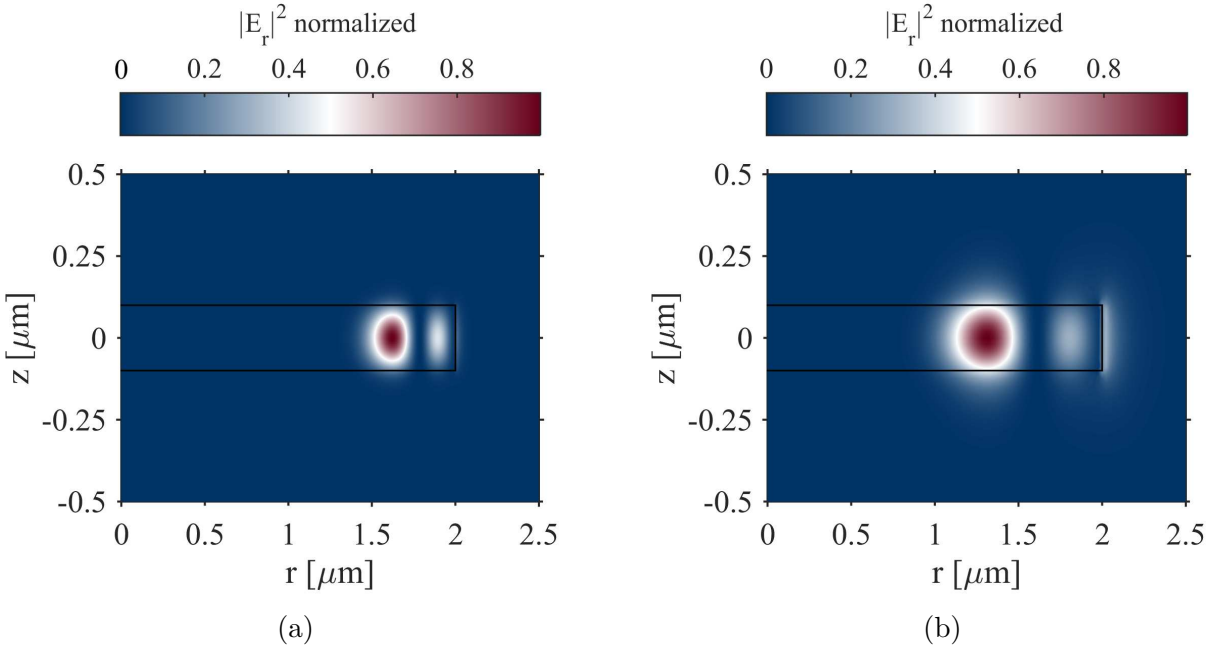

Figure 3.11 – FEM 2D axi-symmetric simulations of WGM optical modes (a) Exciton-band TE mode : $m = 37$, $p = 2$, $\lambda_c = 843{,}28$ nm (b) Telecom-band TE mode : $m = 12$, $p = 2$, $\lambda_c = 1563{,}72$ nm

Q_{scat} : Scattering losses take their origins in imperfections of the circular geometry of the disk. Indeed despite the excellent nanofabrication protocol a residual roughness, as well as a GaAs reconstruction layer are present at the disk surfaces (see figure 3.10 (b)). These imperfections have been previously analyzed by TEM observations [121, 185] and possess a spatial correlation length from 20 to 70 nm. Scattering can be important especially for low

radial p number WGMs, i.e. modes localized close to the disk borders. Another way to understand this effect is to consider the refractive index perturbation that causes polarization currents disrupting the cavity modes [121, 184, 185]. The scattering also affects tiny disks, where imperfections represent a larger fraction of the disk volume.

$Q_{\mathbf{abs}}$ and $Q_{\mathbf{TPA}}$: The absorption of photons stored in WGMs is another source of optical losses. Linear absorption occurs naturally when the energy of photons exceeds the GaAs bandgap. At room temperature the bandgap is at 1.42 eV ($\sim$ 873 nm), and at cryogenic temperature (T $\sim$ 3K) at 1.52 eV ($\sim$ 816 nm). For these two temperatures, working with telecom wavelength (between 0.76 and 0.82 eV) should not lead to absorption. However linear absorption of telecom photons still occurs in our disk, evidenced by the thermo-optic distortion of WGMs resonances (see section 3.2.1.2). Experiments indicate that most of this linear absorption happens at the surface of the disk [185]. The GaAs surface reconstruction layer ($\simeq$ 2 nm thick) is again accountable for this effect: it can host new electronic states that reside within the GaAs bandgap. These "mid-gap states" can assist linear absorption (see figure 3.10 (c)), hence the importance of reducing their influence by using an ALD process after the device fabrication (see section 3.3.6). ALD treatment can improve by a factor 10 the Q_{opt} showing the preponderant role played by surface states [105].

If we now consider photons in the exciton band (energy between 1.38 and 1.55 eV), we can expect an increase in the linear absorption. Even with exciton-band photons with an energy slightly below the GaAs bandgap, the presence of the QW hetero-structure inside the disk is believed to provoke the apparition of bulk defects increasing linear absorption. The typical energy of the QW fundamental transition lies between 1.3 and 1.4 eV depending on the temperature (see section 3.2.2.1). This situation is all the more problematic as the waveguide, just like the disk, also contains the hetero-structure. Its transmission will be greatly impacted by these absorptive transitions. Only photons with smaller energy will have the chance to pass through the waveguide with small attenuation.

On top of these linear phenomena comes nonlinear two-photon absorption (TPA). If one photon of the telecom band is not energetic enough (E=0.8 eV at λ=1550 nm) to promote an electron from the valence band to the conduction band, two photons have sufficient energy to do so, even at cryogenic temperature (2$\times$0.8 eV $>$ 1.52 eV). This non-linear effect becomes clearly visible in our experiments when high optical powers are involved [185]. It scales with the square of optical intensity inside the disk :

$$\frac{dI(z)}{dz} = -\alpha I(z) - \beta I(z)^2 \tag{3.13}$$

where $I(z)$ represents the light intensity along an optical path z, α the linear absorption coefficient and β the TPA coefficient (between 5 and 10 cm/GW for λ=1550 nm at room temperature), which should decrease when decreasing the temperature [186]. For photons in the exciton band, a model [187] predicts that when the energy of photons becomes comparable with the energy band gap, the coefficient β vanishes. We can expect a lower impact

of TPA in the exciton band.

All these sources of intrinsic losses are limiting Q_{opt}. Typically we expect the best values of Q_{in} in the range of $10^4 - 10^5$ for modes in the exciton band and $10^5 - 10^6$ in the telecom band.

Signature of absoprtion : Thermo-optic distortion

The thermo-optic distortion is a phenomenon directly linked to the absorption processes mentioned above. We will provide a phenomenological description and refer the reader to [121, 185] for a more complete one.

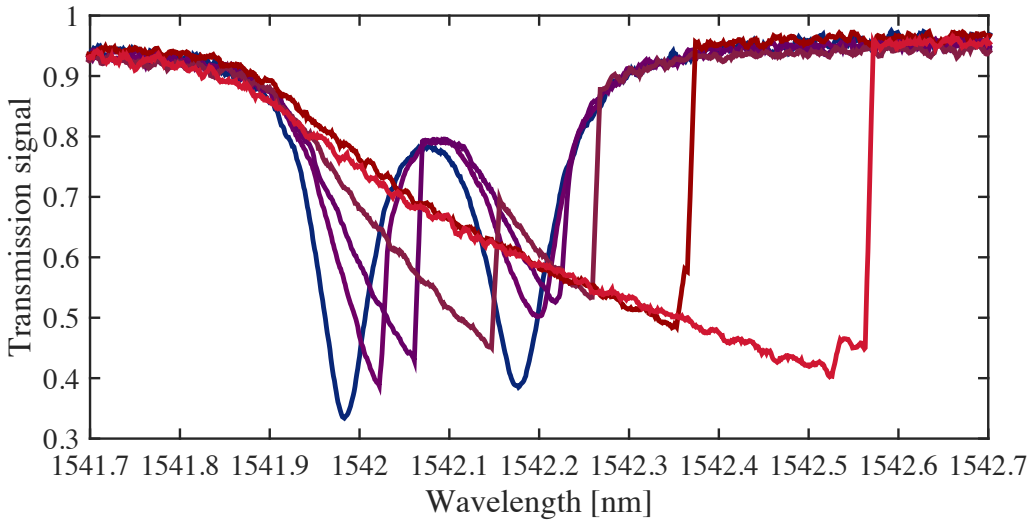

Figure 3.12 – Thermo-optic distortion of a telecom-band WGM resonance, measured in the waveguide optical transmission spectrum. The optical power is increased from blue to red (7 μW, 40 μW, 59 μW, 88 μW, 128 μW and 186 μW respectively of input power), progressively revealing the thermo-optic triangular shape of the resonance. Here the resonance has a doublet structure due to the CW-CCW coupling. Disk radius is 2 μm.

The thermo-optic distortion of optical resonances is a consequence of temperature elevation in the resonator, induced by absorption of light. When the laser sits on the blue flank of a WGM resonance, photons are injected into the disk, and the optical power increases. A fraction of this power is absorbed, which increases the temperature. The refractive index increases due to the positive thermo-optic coefficient of GaAs and the WGM resonance is red-shifted. As the laser wavelength is further swept towards resonance this thermo-optic redshift increases all the more, effectively pushing the resonance to the red. When the laser wavelength finally reaches the resonance condition, this effect ceases and the optical transmission suddenly recovers its out-of resonance value, resulting in a response that adopts a triangular shape as observed in figure 3.12. For a higher laser power, the heating is more pronounced and the shift extends to larger wavelengths.

3.2.1.3 Efficient waveguide to disk coupling - κ_{ext}

We shall now assess the value of the extrinsic losses κ_{ext} and try to match it with κ_{in} in order to reach the critical regime. This can be done by waveguide design: varying the distance between the disk and the tapered part of the waveguide (g_{dw}), as well as modifying the width of this taper w_t (see figure 3.13). It is more comfortable to work with a large waveguide, since it leads to a more confined guided mode and with a "large" gap distance between the disk and waveguide, to minimize proximity effects during the fabrication process (see section 3.3.2.3).

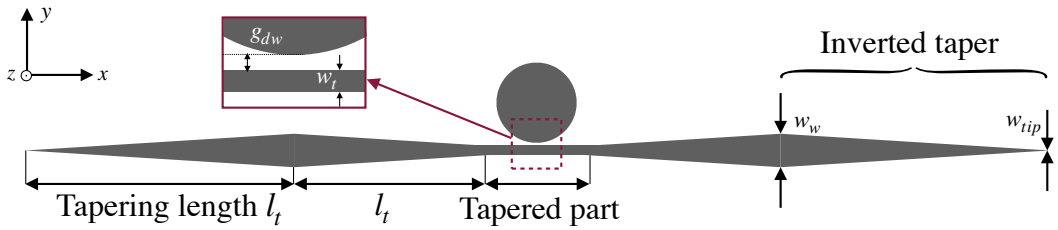

Figure 3.13 – Sketch representing the design of the inverted taper waveguide. The central taper is crucial for the coupling to the disk whereas the inverted tapers at the guide endings tip are designed to optimize the coupling to the μ-lensed fibers

The value of κ_{ext} will greatly depend on the range of wavelengths: exciton band or the telecom band. These two ranges differ in the value of the GaAs refractive index n. As seen in figure 3.14, n is larger in the exciton band, the variation with wavelength is more pronounced. A direct consequence will be on the evanescent part of the fields. The higher n, the higher the effective refractive index n_{eff} in the GaAs slab from which we start. As seen in section 2.1 for an infinite dielectric slab, the exponential decay rate is given by $\gamma = k_0\sqrt{n_{eff}^2 - 1}$. For a similar slab, the decay rate of the fundamental TE mode is 2.3 times faster at 900 nm than at 1550 nm. The same arguments hold for WGMs, we can locally assimilate the edge of the disk to a straight waveguide [188] and approximate the Hankel function with a decaying exponential : $H_m^{(2)}(kr) \sim J_m(kn_{eff}R)e^{-\gamma(r-R)}$. WGMs in the telecom range have hence longer evanescent tails (as already visible in figure 3.11), which means that a good overlap between the waveguide mode and the WGM can be achieved even with a large gap distance.

If the dielectric slab effective index model is relatively valid in the case of the disk (since its aspect ratio is relatively high: $R/h = 10$) it is not the case for the tapered part of the waveguide where the dimensions have been reduced in two directions z and y (figure 3.13). To compute the field in this narrow dielectric rod of rectangular cross-section we use Marcatili's approach [191, 192]. In this method, the cross-section of the waveguide is divided into nine regions of different refractive indexes. The fields in the four corner regions are not considered since these regions are less essential for the waveguiding properties (see inset in figure 3.15). For the other regions, the fields are assumed to be (co)sinusoidally distributed inside the waveguide and decaying exponentially outside. In the case of a highly symmetric waveguide, where the refractive index of all the surrounding regions is the same (in our case vacuum n=1), the problem consists in solving the case of two intersected dielectric slabs:

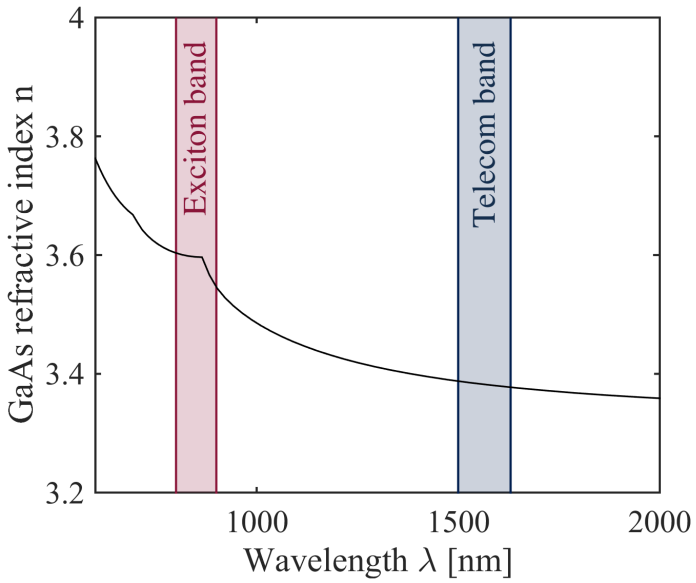

Figure 3.14 – GaAs refractive index in function of the wavelength at room temperature - Theoretical model adapted from [189], the values are extremely close to the the ones recently measured by ellipsometry in [190]

one vertical and one horizontal. In the original paper of Marcatili, the refractive index of the dielectrics was slightly larger than that of the surroundings, but since then some works extended the method to a high index contrast [192], where Marcatilis's method works only in the well-guided case, at high enough frequencies. The effective refractive index of Marcatili's method agrees well with the values obtained by FEM simulations, as illustrated in figure 3.15.

Marcatili's method is also interesting to compute the number of modes supported by the waveguide. We have assumed in the framework of the coupled-mode theory that the disk was coupled to a single-mode waveguide, but in practice, it could sometimes be different. For instance in figure 3.15 (c) if we work with w_t=400 nm, two TE and two TM modes are supported. If the disk couples to these modes it can induce changes in the transmission expression, depending on employed experimental conditions [193]. In this context, Marcatili's method allows calculating the cut-off frequency of the tapered waveguide. As seen in the figure 3.16, TE and TM modes only appear when the taper has a sufficient width. For wavelengths in the exciton band (curves 1 and 2 in figure 3.16), they appear for relatively narrow taper (∼150 nm for TE, less than 100 nm for TM). As the wavelength increases (and refractive index of GaAs decreases), the cut-off frequency is reduced and modes in the telecom range only appear for wider taper waveguide. This effect is particularly pronounced for the case of TM modes (curves 8 and 9 figure 3.16 (b)).

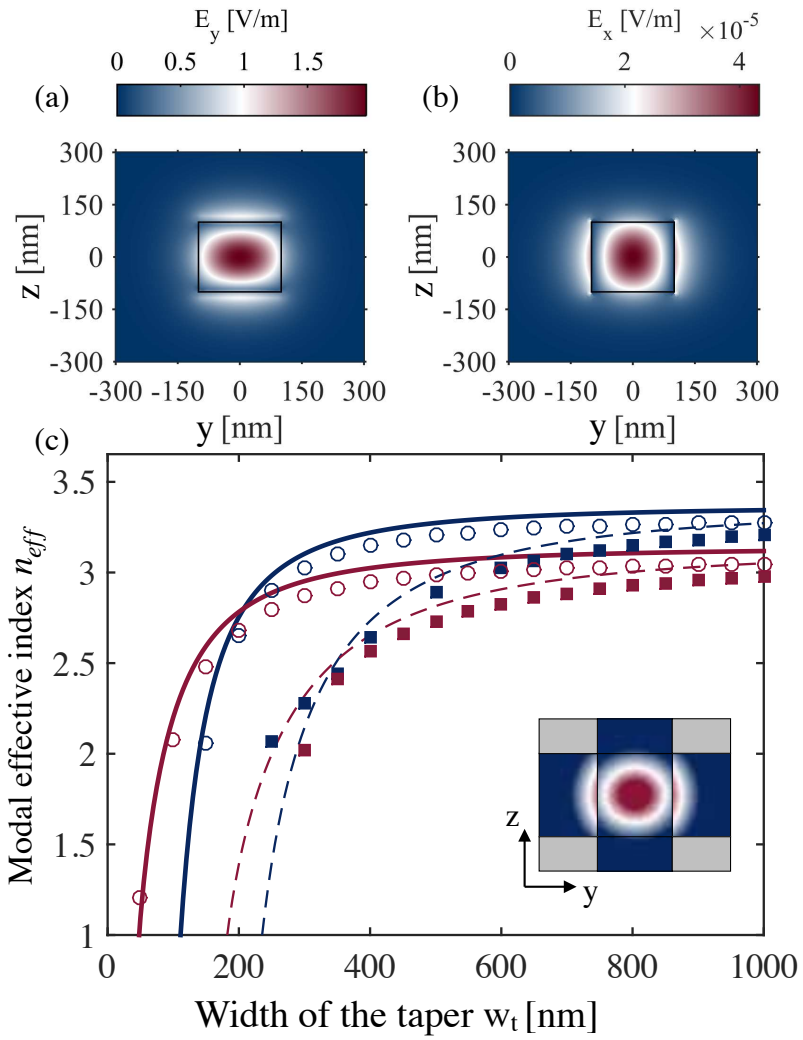

Figure 3.15 – (a)/(b) Cross section of TM/TE-like guided mode for a symmetric 200 nm square waveguide surrounded by vacuum obtain by FEM simulations, $\lambda = 800$nm (c) Variation of the effective refractive index of different modes in function of the width of the waveguide (waveguide height h=200 nm) - Marcatili's method at $\lambda = 800$nm ; Blue continuous line : TE00 mode - Blue dashed line TE10 mode ; Dark red continuous line : TM00 mode - Dark red dashed line TM10 mode. The markers are the values of effective index obtained by FEM simulations : Blue open circles : TE00 mode - Blue squares TE10 mode - Dark red open circles : TM00 mode - Dark red squares TM10 mode. The inset is representing a cross section of the waveguide and the different regions considered in Marcatili's approach

Within the Coupled Mode Theory, the coupling rate κ_{ext} between the disk and the waveguide is calculated by a three-dimensional overlap of the resonator field E_r with the waveguide field E_w. This overlap integral in the case of the disk resonator is [194]:

$$\sqrt{\kappa_{\text{ext}}} = j\frac{\varepsilon_0\omega}{4}\int_{-y_t/2}^{y_t/2} dy \iint_{x,z} dxdz(n^2-1)E_r^* E_w e^{-j\beta y} \tag{3.14}$$

where the coordinates x, y and z match those of figure 3.13, y_t is the interaction length, taken here as the length of the tapered central part, and β is the modal waveguide propagation constant. This equation underlines the importance of phase matching to obtain proper coupling. The WGM field possesses an azimuthal phase dependence ($e^{\pm jm\theta}$) that should match that of the waveguide: this condition will determine the optimal width of the taper w_t and gap distance g_{dw}. This obviously depends on the selected WGM, different WGMs will couple to the waveguide with different κ_{ext}.

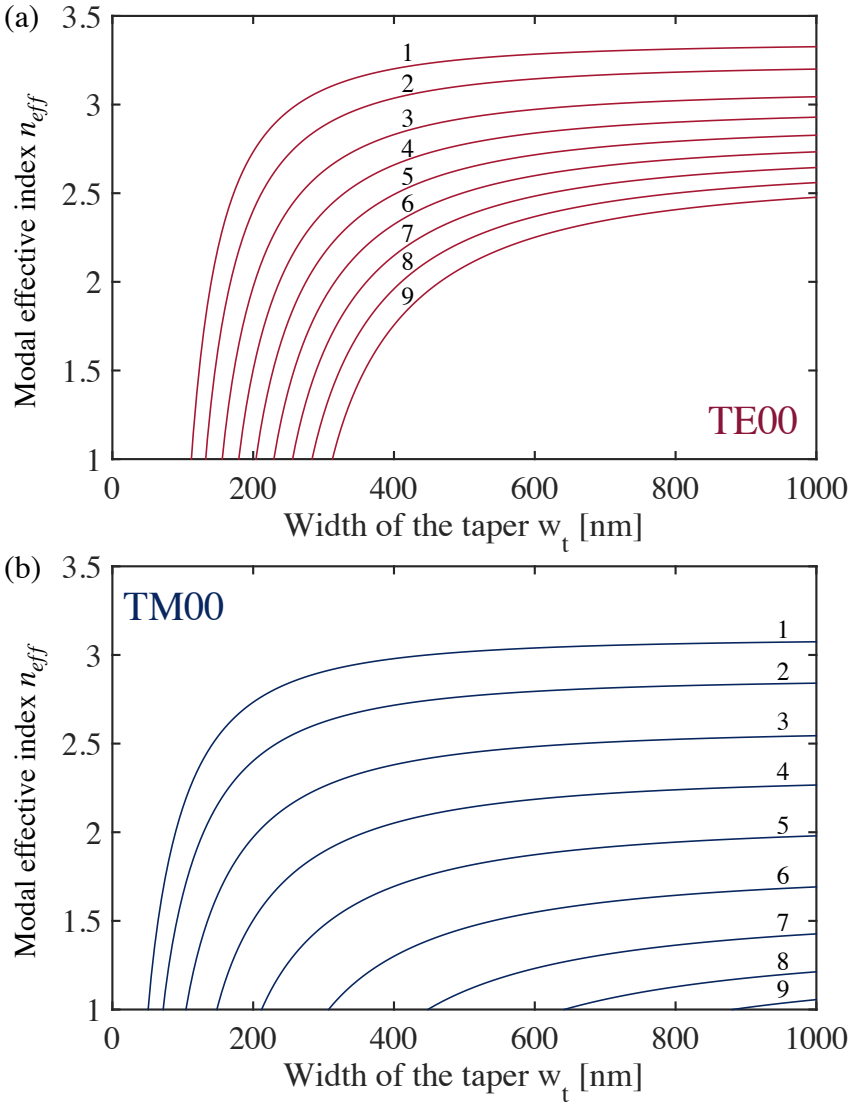

Figure 3.16 – (a)/(b) Variation of the effective refractive index of mode TE/TM00 mode in function of the width of the waveguide, for different wavelengths - Marcatili's method. λ = 800,900,1000,1100,1200,1300,1400,1500 and 1600 nm labelled with number from 1 to 9. Waveguide height h=200 nm

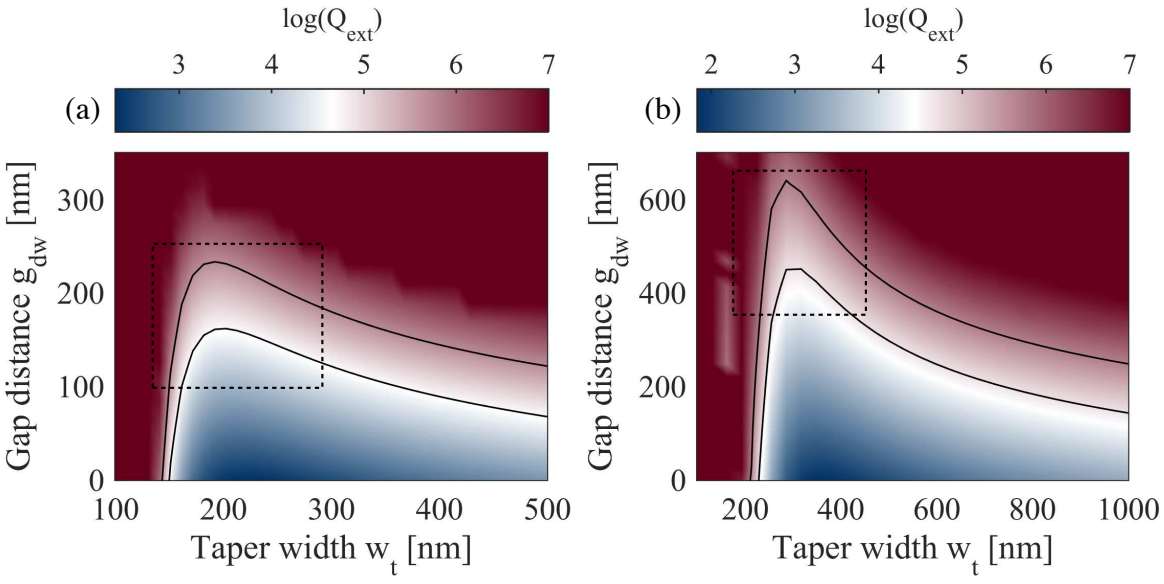

Figure 3.17 – Maps showing the coupling quality factor $Q_{\text{ext}} = {}^{\omega_c}/_{\kappa_{\text{ext}}}$ as function of the taper width w_t and gap distance g_{dw}. (a) Exciton-band mode : TE ; m=40 ; p=1 (b) Telecom-band mode : TE ; m=19 ; p=1. The solid black lines mark a region where Q_{ext} is between $5 \cdot 10^4$ and $5 \cdot 10^5$. Our targeted technological compromise is highlighted by a dashed square

Equation (3.14) enables computing maps of Q_{ext} in function of the taper width and gap distance (see figure 3.17). These maps confirm our intuition: working in the exciton band requires a narrower taper and smaller gap distance with respect to the telecom band usually employed in our group. This represents a technical challenge we had to face in this thesis. A too wide waveguide would turn multimode and reconfine the mode, which should be compensated by a smaller gap distance, incompatible with fabrication. The compromised target region is shown in figure 3.17. These results are only valid for a specific WGM, for different radial/azimuthal numbers p/m the phase-matching condition is not the same [2].

Global waveguide/disk coupling simulations with FEM

To complement Couple Mode Theory, simulations that can assess the evanescent coupling efficiency and calculate the waveguide transmission spectrum are provided by FEM. In such a simulation, we excite one port of the waveguide with a fundamental mode and collect the signal at the other port. An example of such simulation is shown in figure 3.18, where a TE WGM is efficiently excited. Simulations like that are extremely demanding in 3D, but they can be run of a standard computer in 2D if the slab-effective index method is employed.

2. A more flexible solution would be to use a "pulley scheme" [179, 180, 195], where the coupling taper wraps around the disk resonator (see figure 3.38 (b)). In that configuration, the interaction length is increased and can counteract the impact of poor phase matching.

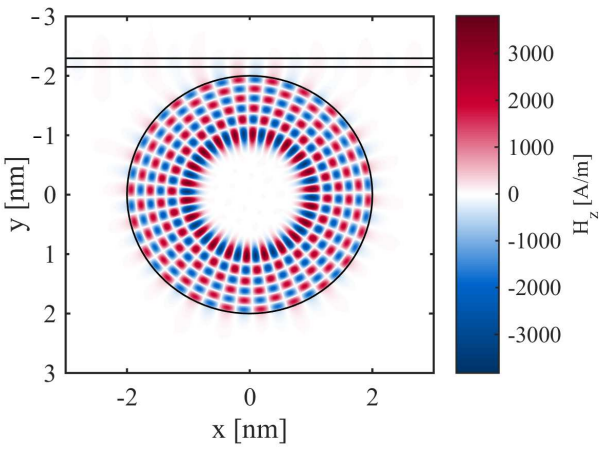

Figure 3.18 – FEM eigenmode analysis simulations. A fundamental TE mode is injected on the left side of the waveguide, the fraction of power that passes through the structure is collected on the right side. The waveguide is 140 nm wide. TE mode m=44 p=6, is excited at $\lambda \simeq 863.7$ nm.

3.2.1.4 Efficient waveguide

Light injection in the waveguide

We should now take care of the coupling between the μ-lensed fibers and the waveguide. Our μ-lensed fibers typically deliver a 2 μm waist diameter Gaussian beam [3]. In order to couple efficiently our guide to this mode, we should design a proper "mode matcher" that allows for low loss and displacement tolerant coupling. The chosen design consists of an inverted taper [196], which relies on an adiabatic expansion of the waveguide mode, while simultaneously reducing the mode effective index to match that of the μ-lensed fiber. This allows converting the confined mode of the guide into the deconfined mode at the tip of the guide's ending. The key parameters for the design are the width of the tip w_{tip}, the width of the waveguide w_w at its largest part and the tapering length l_t (see figure 3.13). Our inverted tapers are fully-suspended, which provides a large index contrast.

This inverted taper is optimized by Finite Difference Time Domain (FDTD) simulations. The end of the inverted taper is excited by a pulsed source with 2 μm waist diameter Gaussian beam, with 100 nm spectral width and a central wavelength of 850 nm for the exciton band and of 1550 nm for the telecom band. The propagation is simulated and we collect at the other end of the inverted taper the power flowing in the waveguide cross-section. We compute this way the transmission, varying the geometric parameters and obtaining the correct set of parameters for optimal transmission. We obtain a good transmission ($T \sim 70 - 80\%$) in both wavelength ranges. Inverted tapers optimized for the exciton band are typically thinner ($w_{tip} \sim 50$ nm, $w_w \sim 400$ nm for the TE case) than their telecom counterparts ($w_{tip} \sim 75$ nm, $w_w \sim 1000 - 1500$ nm for the TE case). The tapering length also has great importance in terms of transmission but its value is rather set by the adiabatic

3. For both exciton and telecom-band optimized μ-lensed fibers

criterion discussed now.

Love adiabatic criterion

In our waveguide design (see figure 3.13) we find two types of tapers : the first is used to evolve from w_{tip} to w_w and the second from w_w to the central taper width w_t. We would like the taper length to be as short as possible to make the fully-suspended structure robust. However, if the tapering is too abrupt, energy is coupled from the fundamental guided mode into higher-order modes along with the propagation. Modes that may be not supported by the taper part, resulting in a power loss. According to Love, [197] this power transfer is minimized if the tapering length l_t is larger than the beat length l_b, i.e. the coupling length between the fundamental and high-order modes :

$$l_b = \frac{2\pi}{\beta_1 - \beta_2} \tag{3.15}$$

where β_1 and β_2 are the propagation constants of the fundamental and high order mode (second here). For linear tapering, this sets a minimum tapering length. As demonstrated in figure 3.19 this minimal length is longer for waveguides in the exciton band, where the difference between indices of the fundamental and second-order modes is smaller. In the telecom case, we only obtain a criterion for TE modes since no higher-order TM mode is supported in the range of width considered here.

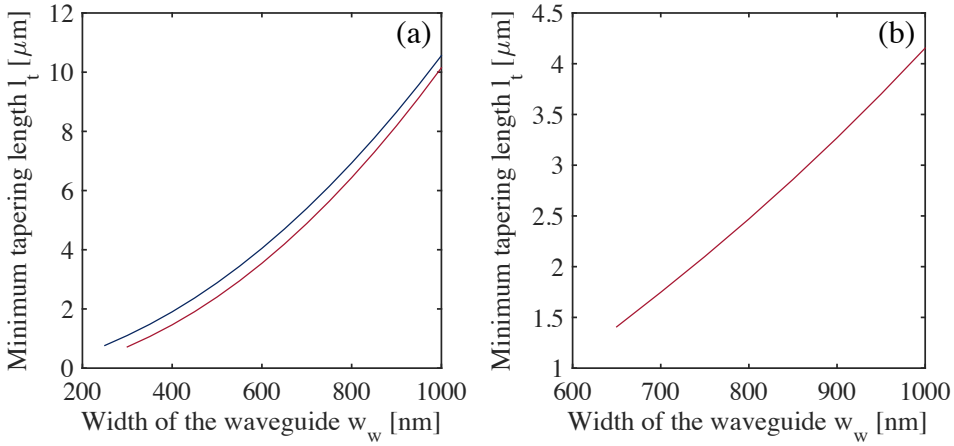

Figure 3.19 – Love adiabatic criterion for a waveguide optimized in the (a) exciton band (λ = 850 nm) (b) telecom band (λ = 1550 nm). Waveguide thickness = 200 nm. Red curves : TE modes - Blue curve : TM modes

Total waveguide simulation

With all geometric parameters of the final design of our waveguide, we can simulate the whole structure with FDTD simulations, as illustrated in figure 3.20. The global transmission (injection μ-lensed fiber to collection μ-lensed fiber) according to FDTD is between

50 and 60%, which corresponds to about the square of the transmission of one inverted taper structure, which means that we can safely neglect all losses along the path of the whole waveguide structure. Of course, the simulations do not take into account all the other possible sources of losses such as the residual roughness or the absorption. Typically for a waveguide in the telecom range the global transmission, we obtain in our experiments is around 25%, corresponding μ-lensed fiber to inverted taper transmission of around 50%.

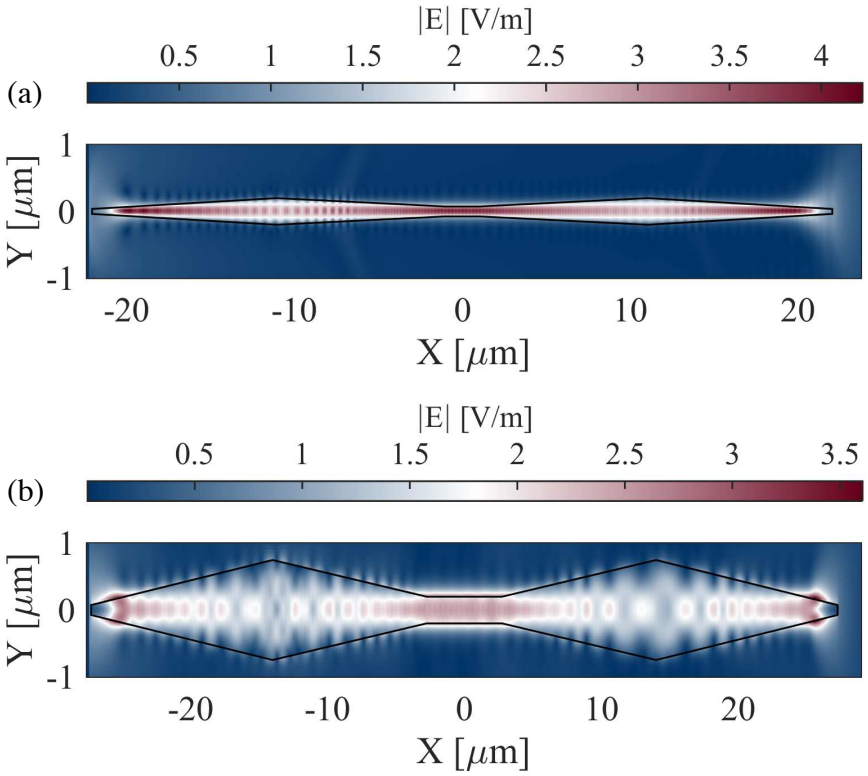

Figure 3.20 – FDTD TE simulation results for the whole waveguide structure (a) Exciton band : central wavelength 850 nm - Transmission $\sim$ 60% (b) Telecom band : central wavelength 1550 nm - Transmission $\sim$ 55%

One source of losses that we can simulate as well is the impact of the anchoring points that hold the waveguide suspended. Those anchorings should be thin enough to minimize scattering. We routinely used 100 nm wide anchors to hold the guide, for such a geometry FDTD simulations (see figure 3.21) show a minor impact on the total transmission, inducing a drop of only 2-3%.

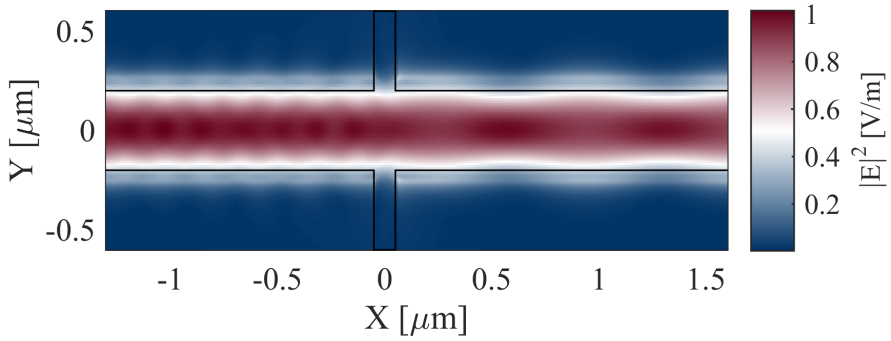

Figure 3.21 – FDTD simulations of anchoring point losses. The waveguide is 400 nm wide and the anchoring point 100 nm. A fundamental TE mode is injected on the left side of the waveguide, and collected on the right side. In this configuration the transmission only drops by 2-3% when the anchoring point are present. λ= 900 nm.

3.2.2 Quantum well hetero-structure

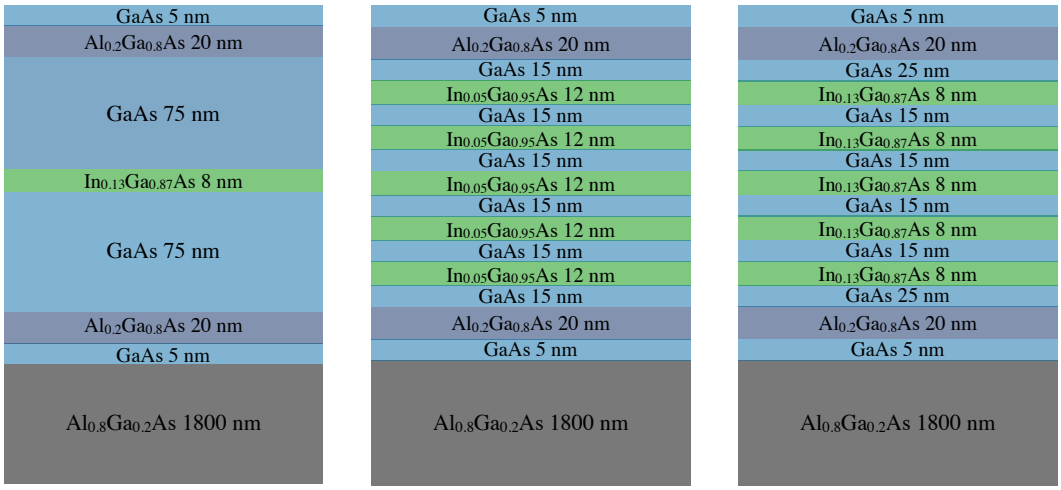

Figure 3.22 – Different hetero-structures employed during this thesis. Structure 1 : Single InGaAs QW with 13% of Indium - Structure 2 : MQW with 5% of Indium - Structure 3 : MQW with 13% of Indium. h represents the total thickness of the disk embedding the "active" layer

We review in this section the different characteristics of the hetero-structure present in core of the "active" disk. During the course of this thesis we try several structures represented in figure 3.22. **Structure 1** corresponds to a single InGaAs QW inside GaAs with a fraction of indium equal to 13%. **Structure 2** and **3** are InGaAs Multiple Quantum Wells (MQW) inside GaAs with 5 QWs and a fraction of indium of 5% and 13% respectively.

The two 20 nm $Al_{0.2}Ga_{0.8}As$ layers visible in figure 3.22, do not belong to the QW

structure : they were added to improve the confinement of carriers in the GaAs barriers and consequently in the well. To avoid oxidation of these extra layers, which would obviously lead to degradation of the resonator, two cap layers of 5 nm of GaAs were placed at the bottom and top of the disk layer.

3.2.2.1 Energy of the transitions

The energy diagram of the well in 1D can be calculated using a finite one-dimensional potential well for a particle with a mass equal to the effective mass of the considered band. This implies to solving a transcendental equation similar to the infinite dielectric slab case :

$$\begin{aligned} k\frac{m_b^*}{m_w^*}\tan\left(kL/2\right) &= \alpha \quad \text{for even cases} \\ k\frac{m_b^*}{m_w^*}\cot\left(kL/2\right) &= -\alpha \quad \text{for odd cases} \end{aligned} \tag{3.16}$$

with $k = \sqrt{\frac{2m_b^*}{\hbar^2}(E+V_0)}$ the 1D wavevector, $\alpha = \sqrt{-\frac{2m_b^*}{\hbar^2}E}$, E the energy of the wave parametrized by k, m_b^* the effective mass in the barrier, m_w^* the effective mass in the well, L the length of the well and V_0 the well depth.

The method described above is not perfectly adequate for the valence bands, as states are derived from more than one bulk band (valence band mixing). A more sophisticated method is to compute a discrete version of the 1D Schrödinger equation for a Zinc-Blende semiconductor such as GaAs and its alloys. The non parabolicity can be implemented thanks to $\boldsymbol{k}\cdot\boldsymbol{p}$ theory and the 2-band Kane model [126, 198] for the conduction band and with a $\boldsymbol{k}\cdot\boldsymbol{p}$ theory and 6-band Luttinger-Kohn model [199] for the valence band. With this $\boldsymbol{k}\cdot\boldsymbol{p}$ approach, the effect of the strain, which we will detail later, can be included via the Bir-Pikus Hamiltonian [79]. The results of such computations are shown in figure 3.23. For the sake of clarity, we have represented the fundamental transition (C-HH) only, but other transitions involving notably light holes and heavy holes exist in both structures, they are poorly interesting in the context of this thesis. The evolution of the energies with temperature is computed using Varshni's model [200].

Regarding the design of the MQW (**Structure 2** and **3**), particular attention was paid to having wide enough barriers to avoid wavefunctions of adjacent wells to overlap. In other words, the tunneling probability from well to well was essentially set to zero. Within the previous computation of the electronic states, we calculate this tunneling probability T via :

$$T = \frac{4E(V_0-E)}{4E(V_0-E)+V_0^2\sin^2\left(\sqrt{\frac{2m(V_0-E)}{\hbar}}L\right)} \tag{3.17}$$

In our designed MQW structures, the tunneling probability was always below 0.01 % both at room and cryogenic temperatures.

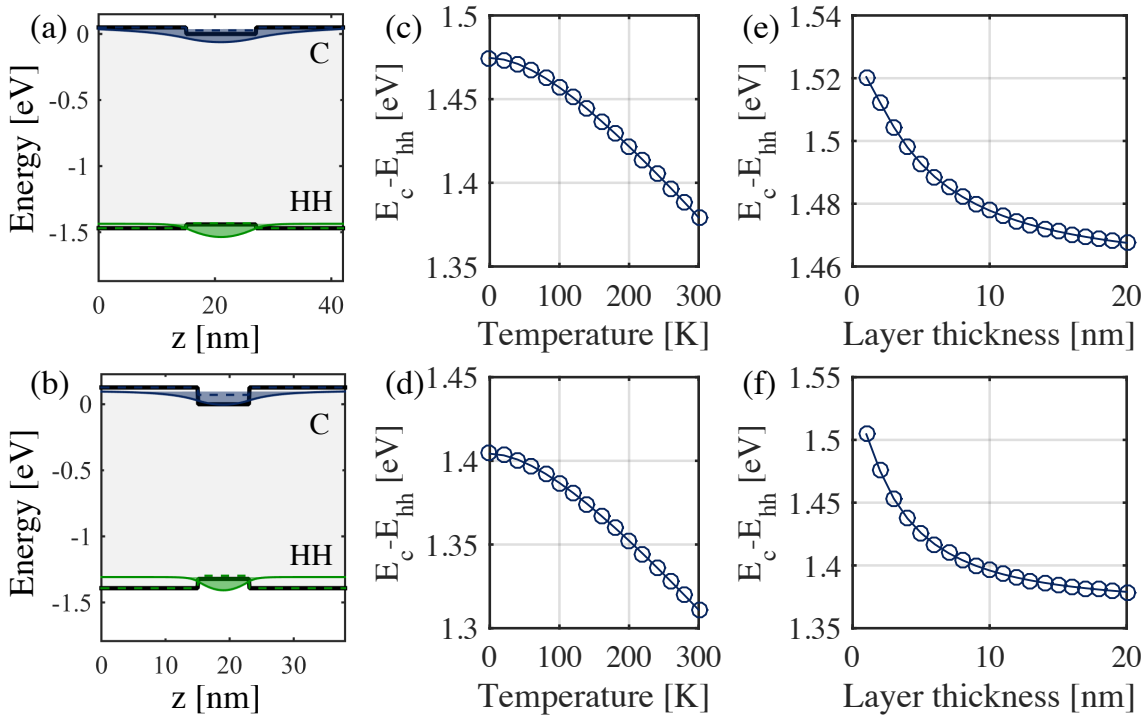

Figure 3.23 – QW energy band calculations as function of the temperature and the well layer thickness for a fraction of indium equal to 5% ((a)-(c)-(e)) and 13% ((b)-(d)-(f)). Figure (a) and (b) are representing the energy diagram calculated at cryogenic temperature (T = 3 K). The black lines trace the conduction and valence band profile. The calculated energies (dashed lines) and envelope functions $\chi_{c/v}$ (solid lines) for the electrons and heavy-holes along the growth axis z are respectively represented in blue and green. (c) and (d) are for a well thickness of 12 and 8 nm. The temperature in (e) and (f) is 3 K.

3.2.2.2 Effect of the residual strain on the exciton energy

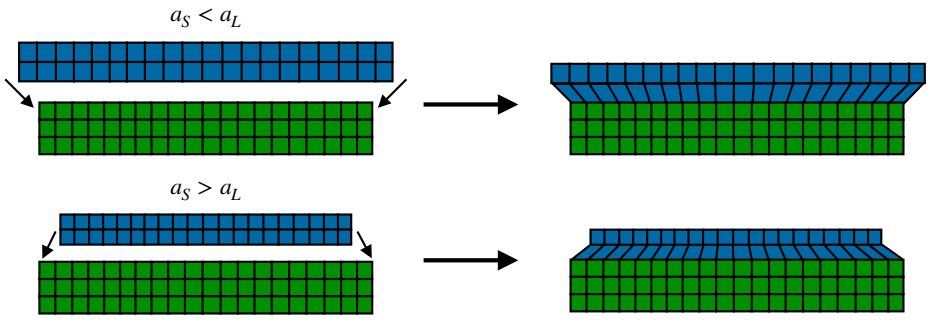

Figure 3.24 – Sketch representing the built-in strain generated when an over-layer is grown on top of a substrate with a different lattice parameter.

As we have already mentioned earlier, the strain affects the energy band of semiconductor material: this phenomenon is particularly of interest for epitaxially grown hetero-structure.

When an over-layer with lattice constant a_L is grown on a substrate with lattice constant a_S and adapts to it, the strain in the deposited over-layer can be approximated to :

$$\varepsilon_{\parallel} = \frac{a_S - a_L}{a_L} \qquad \varepsilon_{\perp} = -\frac{\varepsilon_{\parallel}}{\sigma} \tag{3.18}$$

with σ the Poisson ratio. For a small lattice mismatch, the over-layer initially grows in perfect match with the substrate. However, the strain energy grows as the over-layer thickness increases. At some point, it becomes more favorable for the over-layer to accommodate dislocations. In simple theories, this occurs for a critical thickness given by [201] :

$$d_c \simeq \frac{a_S}{2\left|\varepsilon_{\parallel}\right|} \tag{3.19}$$

In table 3.1 we list the built-in strains and critical thicknesses for all interfaces encountered in this thesis: we can see that our grown layers are always below the critical thickness. We can hence safely assume that a limited amount of dislocations is generated in our wafer and that a non-negligible amount of built-in strain exists. Note that more advanced models are available to compute this effect [187, 202–204].

Substrate	Over-layer	$\varepsilon_{\parallel}$ (%)	d_c (nm)	ΔE_{C-HH} (meV)
$Al_{0.8}Ga_{0.2}As$	GaAs	0.11	257	−13.9
GaAs	$Al_{0.2}Ga_{0.8}As$	−0.0027	1030	−0.35
GaAs	$In_{0.05}Ga_{0.95}As$	−0.36	75	45.9
GaAs	$In_{0.13}Ga_{0.87}As$	−0.81	35	100.2

Table 3.1 – Built-in strain, critical thickness, and ΔE_{C-HH} energy shift computed for all the interfaces encountered in this thesis. The parameters required to compute these results are discussed in section C.2

To compute the effect of strain on the energy bands, we use the Bir-Pikus Hamiltonian, an extension of the Luttinger-Kohn Hamiltonian, detailed in appendix C.3. For a strained layer on a (001) substrate the strain components are given by [205, 206]:

$$\varepsilon_{xx} = \varepsilon_{yy} = \varepsilon_{\parallel} \quad \varepsilon_{zz} = \varepsilon_{\perp} = -\frac{\varepsilon_{xx}}{\sigma} \quad \sigma = \frac{C_{11}}{2C_{12}} \tag{3.20}$$

where C_{11} and C_{12} are components of the material stiffness tensor. The evolution of the fundamental transition (C-HH) is thus given by (see appendix C.3) :

$$E_{C-HH}(k=0) = E_{C-HH}(\varepsilon=0) + 2a\varepsilon_{\parallel}(\frac{C_{11}-C_{12}}{C_{11}}) + b\varepsilon_{\parallel}(\frac{C_{11}+2C_{12}}{C_{11}}) \tag{3.21}$$

The values of these energy shifts for different over-layers are reported in table 3.1.

A feature of particular interest in the case of our suspended disk resonators is the state of this built-in strain once the disk is under-etched and sitting on its pedestal. Indeed, at the end of the fabrication process, the periphery of the disk is completely under-etched

with no underneath AlGaAs layer anymore. In this released state, strain relaxation occurs: the strain distribution in the suspended disk is not uniform anymore (see figure 3.25 (a)). The strain tends to zero at the periphery of the disk while it is still pronounced close to the pedestal. The pedestal is of paramount importance for this strain distribution. In figure 3.25 (b), we plot the calculated energy shift of the conduction band of GaAs, grown on $Al_{0.8}Ga_{0.2}As$ layer and then under-etched into a disk, for different pedestal size and as a function of the position along the radius of the disk. For small pedestals (blue curve, $R_{ped} = 0.1 \cdot R$) we have a large homogeneous portion of the disk where the energy of the conduction band is constant, equal to that of free GaAs. When the size of the pedestal increases (green curves), the energy is not uniform and can locally be higher or lower than the free crystal case. A similar yet more complex reasoning can be carried out for the valence band, indicating that energy of the HH should slightly decrease towards the center of the disk. In consequence of these effects, we should expect varying energy for the C-HH exciton depending on its position in the under-etched structure. This was indeed experimentally measured in this thesis, illustrated in figure 3.25 (c). By reducing the size of the pedestal we minimize these under-etch effects and obtain one signal for the exciton in the disk at fixed energy.

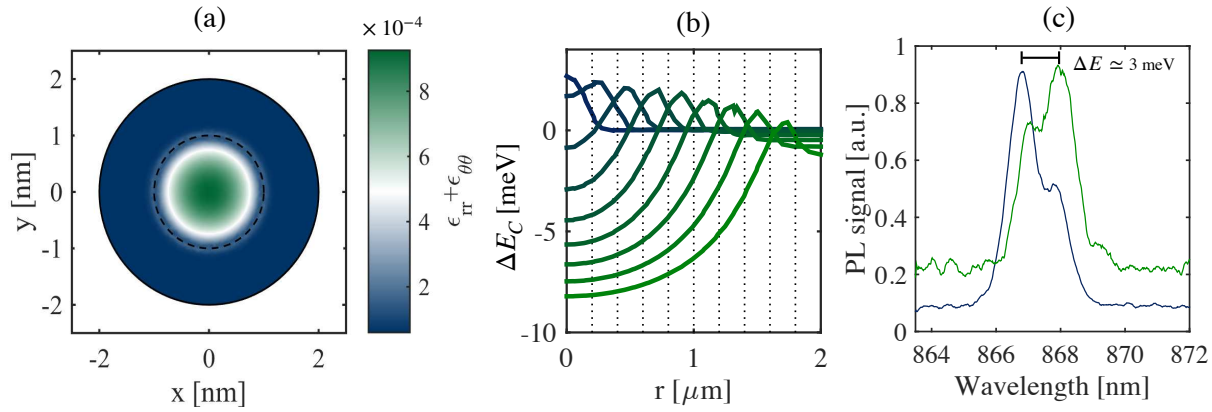

Figure 3.25 – (a) Strain in an under-etched disk : color map of the strain component $\varepsilon_{rr}+\varepsilon_{\theta\theta}$ across the plane of the disk (diameter R=2 μm, $R_{ped} = 0.5 \cdot R$ the position of the pedestal is represented by a dark dashed line). (b) Evolution of the energy of the (1D) conduction band of GaAs as a function of the radial position in the suspended disk. The pedestal radius is taken to vary $R_{ped} = 0.1 - 0.9 \cdot R$ from dark blue to green curves, Radius R=2μm (c) C-μPL spectra measured at the periphery (blue curve) and at the center (green curve) of a suspended disk at low temperature (diameter R=2 μm, $R_{ped} = 0.5 \cdot R$).

Similar effects were observed in a different platform involving a bulk active material [207]: our argumentation developed here works well and fits experimental observations. In the case of a heterostructure, the phenomenon was also observed [208], but the interpretation is more complex there since different materials are present. In every interface of our hetero-structures in this thesis, the critical thickness was sufficiently large to consider that grown layers would adopt the lattice constant of the underlying part. This is the assumption we took to compute strain relaxation by FEM in figure 3.25 (a). However this intuition should be confirmed, an analysis of the strain in the structure with X-ray diffraction spectroscopy would be very

enlightening.

3.2.2.3 Impact of the Indium fraction

We review here the influence of the indium fraction on the properties of our InGaAs QW hetero-structures. A relatively high fraction of indium (>10%) presents both benefits and challenges. On one hand, the carriers are better confined due to the lower gap of InAs compare to GaAs: this means thinner layers, both for wells and barriers and an overall more compact structure, especially useful in the case of a MQW. On the other hand, one might face issues during the epitaxial growth, mostly due to a higher lattice mismatch (dislocations, residual strain), triggering large inhomogeneous broadening of the exciton and possible alloys fluctuations. Concerning the energy of the transitions, the lower the indium fraction the higher the energy of the fundamental $C-HH$ transition, as expected from the electronic band parameters listed in appendix C.1.

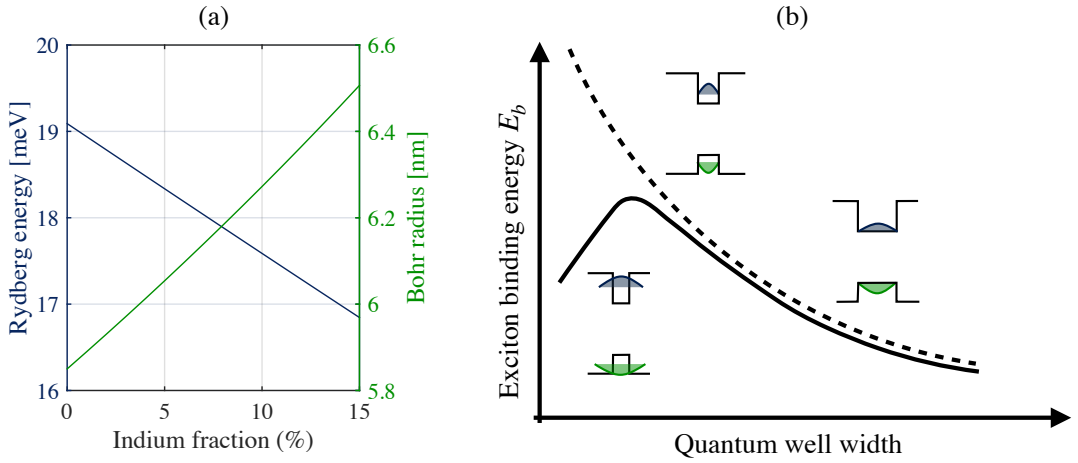

Figure 3.26 – (a) Rydberg energy and Bohr radius as a function of the Indium fraction - 2D ideal case (b) Exciton binding energy as a function of the QW width, the different insets show the QW potential and wave functions of electrons for different QW widths. The dashed line represents the infinite well case. Adapted from [209, 210]

Regarding exciton properties, increasing the indium fraction reduces the binding energy and increases the Bohr radius as illustrated in figure 3.26 (a) in the ideal case of a 2D QW. We see that for the fraction we employ (between 5% and 13%) the thickness of the QW is larger than the Bohr radius: in that case, the hypothesis of the narrow (thin) QW is no longer true. The bounded exciton itself is confined by the well and keeps the internal structure of a 3D hydrogen atom. In such case, the separation of variables in z (perpendicular to the QW plane) and ρ (parallel to the QW plane) is not valid. One alternative to face this difficulty is the definition of an effective pseudo-potential for the relative in-plane motion of electrons and holes [209]:

$$\left[\frac{-\hbar^2}{2\mu}\nabla_\rho^2 - \frac{e^2}{\varepsilon}\iint dz_c dz_v \frac{|\chi(z_c)|^2|\chi(z_v)|^2}{\sqrt{\rho^2-(z_e-z_h)^2}}\right]\Phi(\rho) = E_{b,n}^{2D}\Phi(\rho) \tag{3.22}$$

In the limit of the ideal 2D case where the separation of variables holds, $\chi(z_{c/v}) = \delta(z_{c/v})$ and the previous equation is transformed into (2.114).

For realistic QW structures the exciton binding energy ranges from $E_{b,n}^{3D}$ to $4E_{b,n}^{3D}$ and depends on the QW width and barrier heights for electrons and holes. The binding energy increases if the exciton confinement strengthens: following that argument one can guess why the dependence of the binding energy on the QW becomes non-monotonous as depicted in figure 3.26 (b). For relatively thick wells the confinement increases when the thickness decreases, while for narrow wells the trend is inverted due to the tunneling effect of wave functions into the barriers. In the case of an infinite-barrier well, the confinement simply increases when the well thickness decreases. Consequently, by playing with the indium fraction, one can tune to the optimum in terms of well thickness and binding energy.

3.2.2.4 The polariton linewidth and spectral broadening

The homogeneous radiative exciton linewidth of a quantum well can be expressed by [160, 211]:

$$\hbar\kappa_x = \frac{e^2}{4\varepsilon_r^2\varepsilon_0 m_0 c}\frac{f}{S} \tag{3.23}$$

where f/S is the oscillator strength of the exciton per unit area, a quantity directly linked to the strength of the exciton interaction with the electromagnetic field and that amounts to [128, 212, 213]:

$$\frac{f}{S} = \frac{2}{m\hbar\omega_x}|\langle u_v \mid \boldsymbol{e}\cdot\boldsymbol{p} \mid u_c\rangle|^2|\phi(0)|^2\left|\int dz\chi_c(z)\chi_v(z)\right|^2 \tag{3.24}$$

where $u_{c,v}$ are the conduction and valence band atomic Bloch function, $\boldsymbol{e}$ the polarization vector associated to the vector potential $\boldsymbol{A}$ representing the electromagnetic field, $\boldsymbol{p}$ the momentum, ϕ is in-plane relative motion of the electron and hole, $\chi_{c,v}$ the envelope wavefunctions for the electron and hole along the z axis, and $|\langle u_v \mid \boldsymbol{e}\cdot\boldsymbol{p} \mid u_c\rangle|$ the Kane optical matrix element. Given the structure of the QW we use in our experiments ($In_{0.05}Ga_{0.95}As/GaAs$) we found $\hbar\kappa_x \simeq 0.06$ meV which is an order of magnitude lower than κ_c.

However this picture is only partially true: excitons greatly suffer from inhomogeneous broadening, a mechanism that takes its origin in different sort of microscopic phenomena such as disorder [68,214–216], coloumbian interactions between excitons [217–219] or exciton-phonon interactions [169]. At very low exciton density the collisional Coulomb interaction between excitons can be neglected, and we assume that all the relaxation phenomena can be treated independently. Variations in the QW-thickness over the sample, fluctuations in the alloys composition, residual rugosity, built-in strain, and interactions with acoustic phonons are all factors that contribute to inhomogeneous broadening. As a result of this inhomogeneous broadening, the expected individual peak in the photo-luminescence/absorption spectrum can turn into several narrow peaks as depicted in figure 3.27-(a). This situation corresponds to an ensemble of spectrally separated emitters, that can be used to simulate the spectral broadening of quantum-well exciton-polaritons [160, 220–222]. In this model the

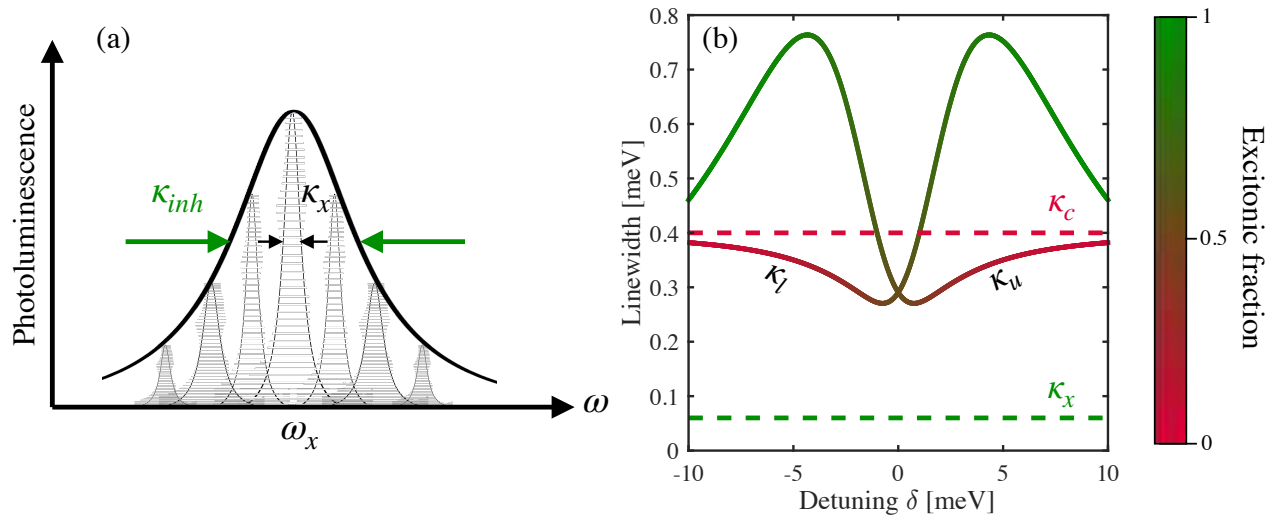

Figure 3.27 – (a) Inhomogeneous distribution of the exciton, modeled as an ensemble of emitters following a Gaussian distribution. κ_x represents the homogeneous linewidth of one emitter and κ_{inh} the FWHM of the distribution (b) UP and LP linewidth ($\hbar\kappa_{u/l}$) as a function of the cavity-exciton detuning δ, taking into account the inhomogenenous broadening of the exciton. The color map corresponds to the excitonic fraction (X). Ω_R=5 meV, κ_c=0.4 meV, κ_x=0.06 meV, κ_{inh}=2 meV

polariton linewidth dependence on the inhomogeneous broadening ρ of the exciton transition is given by [223–225]:

$$\begin{aligned}\kappa_l &= X^2\tilde{\kappa}_x + C^2\kappa_c = X^2[\kappa_x + \pi\delta_{xl}^2\rho(\delta_{xl})] + C^2\kappa_c \\ \kappa_u &= C^2\tilde{\kappa}_x + X^2\kappa_c = C^2[\kappa_x + \pi\delta_{xu}^2\rho(\delta_{xu})] + X^2\kappa_c\end{aligned} \tag{3.25}$$

with $\delta_{xu/l}$ the exciton to upper/lower polariton detuning $\hbar\delta_{xu/l} = E_x - E_{u/l} = -\hbar\delta/2 \mp \hbar\sqrt{\delta^2 + \Omega_R^2}$ and ρ the spectral density function describing the inhomogeneous broadening of the exciton taken here as a Gaussian distribution :

$$\rho(\omega) = \frac{1}{\kappa_{\text{inh}}}\sqrt{\frac{4\ln(2)}{\pi}}e^{\left(-4\ln(2)\frac{(\omega-\omega_x)^2}{\kappa_{\text{inh}}^2}\right)} \tag{3.26}$$

where κ_{inh} is the FWHM of the distribution. Those definitions yield an expression for the polariton linewidth that depends on the cavity-exciton detuning δ. Those variations are plotted in figure 3.27-(b). They drastically differ from the ones plotted in figure 1.5-(c). In the case of the LP, for an increasing excitonic fraction X we observe an increase in the polariton linewidth that overcomes at some point κ_c. For large detuning this increase stops and the LP linewidth slowly gets back to the exciton homogenous linewidth κ_x [226, 227], since $\delta_{xl}\rho(\delta_{xl})$ tends to zero. A similar discussion can be made for the UP analyzing the cavity fraction C.

A direct consequence of this effect is the modification of the optomechanical cooperativity enhancement :

$$\frac{C_0^{lm}}{C_0} = \frac{\left(X^2 \frac{g_{xm}}{g_{cm}} + C^2\right)^2}{X^2 \frac{\tilde{\kappa}_x}{\kappa_c} + C^2}, \qquad \frac{C_0^{um}}{C_0} = \frac{\left(C^2 \frac{g_{xm}}{g_{cm}} + X^2\right)^2}{C^2 \frac{\tilde{\kappa}_x}{\kappa_c} + X^2} \tag{3.27}$$

As illustrated in figure 3.28 the enhancement of the cooperativity greatly depends on the value of the exciton inhomogeneous broadening and the boost is diminished with respect to the ideal situation plotted in figure 1.7. However, for a reasonable value of the broadening ($\kappa_{\text{inh}} \simeq 1$ meV), we see that this enhancement can still be of a least two orders of magnitude for a certain range of cavity-exciton detuning δ.

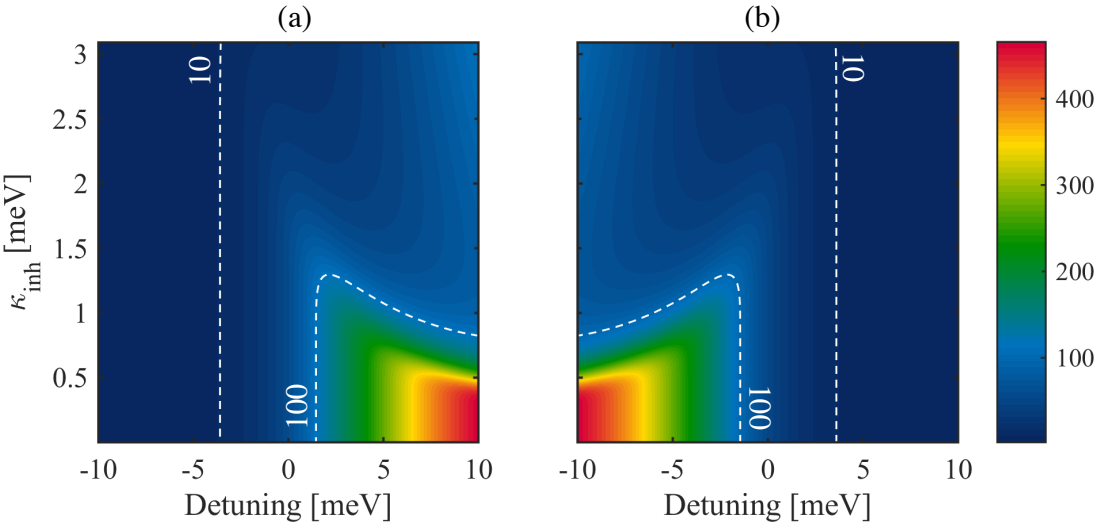

Figure 3.28 – Cooperativity enhancement as a function of the cavity-exciton detuning δ and the exciton inhomogeneous broadening κ_{inh} (a) LP - C_0^{lm}/C_0. (b) UP - C_0^{lm}/C_0. $\Omega_R = 5$ meV, κ_c =0.4 meV, $\kappa_x = 0.06$ meV, $g_{xm}/g_{cm} = 10$

In summary, the inhomogeneous broadening of the exciton κ_{inh} is responsible for increasing the polariton linewidth. This broadening is usually one or two orders of magnitude larger than the exciton radiative decay rate κ_x, impacting the cooperativity of the tripartite system. It is therefore of crucial importance to reduce it, notably by improving the fabrication of the hetero-structure.

3.3 Sample fabrication

We present the different tools and methods involved in the fabrication of our hybrid optomechanical systems. All fabrication steps, except the growth of the epitaxial structure, are carried in the *Matériaux et Phénomènes Quantiques* clean room at the Université de Paris.

Several wafers were used in this thesis: some were grown at the *Centre de Nanosciences et de Nanotechnologies* in Palaiseau, in collaboration with the team of Aristide Lemaitre,

and some others were grown in the *III-V lab* of Thales/Nokia/CEA-LETI, also located in Palaiseau. The hetero-structures are grown on top of a commercial GaAs buffer layer and then consist of : a 500 nm thick layer of epitaxial GaAs, a sacrificial 1.8 μm layer of $Al_{0.8}Ga_{0.2}As$, and a 200 nm active layer of GaAs with an embedded InGaAs quantum well (QW) or multiple InGaAs quantum wells (MQW). Further details on the quantum well structures are provided in the prior section 3.2.2.

Even though the protocol presented in this section is the evolution of developments, improvements, and hard work of several Ph.D. students in past years, the fabrication remains extremely delicate and tricky. The slightest mistake in one of the protocol steps can yield to a failure of the global fabrication process. In this Ph.D. thesis, the main originality in terms of fabrication is: (1) the presence of a hetero-structure in the active layer, which provokes larger built-in strains distorting suspended structures (see section 3.2.2.2); (2) working in the exciton-band ($\simeq$ 900 nm), which implies smaller dimensions of the suspended waveguides, evanescent couplers, and inverted tapers. These have generated specific fabrication challenges in this thesis.

3.3.1 Protocol steps

The protocol steps of the fabrication are as follows:

- A piece of wafer is first cleaved
- The chip obtained is cleaned and prepared for the first resist deposition (Fig 3.29 (a))
- The resist is spin-coated on the surface of the chip, then baked and exposed with an Electron Beam Lithography (EBL) system (Fig 3.29 (b))
- After exposition the resist is developed, only the exposed parts remain on the chip (Fig 3.29 (c))
- A first non-selective Inductively Coupled Plasma (ICP) Reactive Ion Etching (RIE) is carried on the sample (Fig 3.29 (d)), followed by a second selective chemical hydrofluoric acid (HF) under-etching (Fig 3.29 (e)) : this defines the resonators and waveguides and let them suspended.
- A second resist is spin-coated on the surface of the chip to prepare an optical lithography and define the so-called *mesa* structure (Fig 3.29 (f))
- A second non-selective chemical etching (H_3PO_4/H_2O_2 or BCK solution) is then carried out (Fig 3.29 (g)) to etch the mesa laterally.
- The resist is then washed in hot acetone and the sample is flash-dried and ready to be used (Fig 3.29 (h))

All these steps are detailed in the following sections.

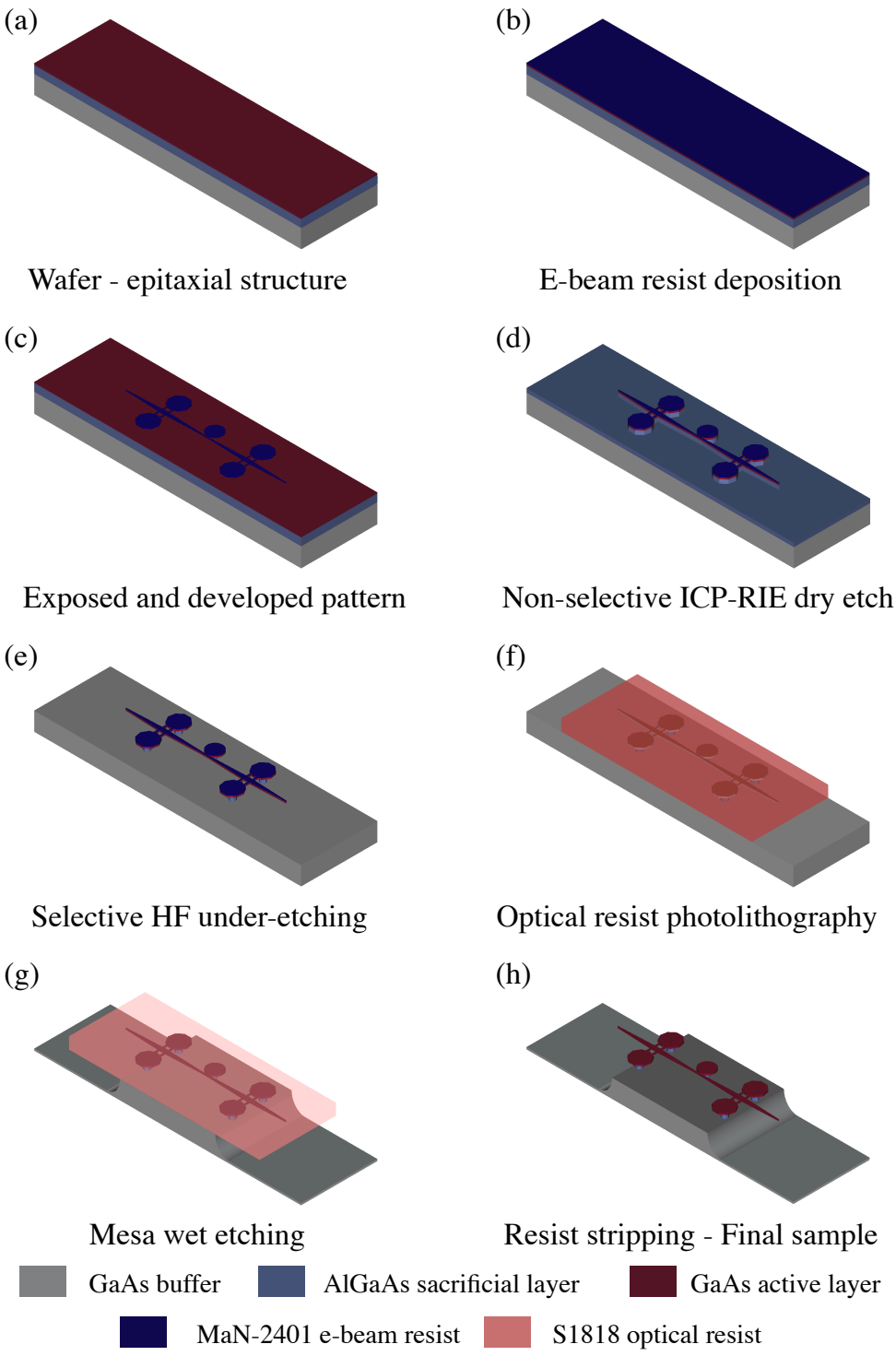

Figure 3.29 – Protocol steps of the fabrication. The different sketches are zoomed in one structure waveguide-microdisk, the anchoring point of the waveguide and its support pillars are represented as well

3.3.2 E-beam lithography

3.3.2.1 Preparation of the chip

The first important thing is to prepare the chip by cleaning and avoiding the presence of dust and residuals which can impact the precision of EBL. We start by cleaving a small chip (usually 1cm × 1cm) from the wafer. We dip it in acetone (good polar solvent used mostly to remove the organic contaminant from the wafer) and sonicate it for 10 minutes. Without drying the sample, we place it in isopropanol, (IPA, secondary solvent suited to remove the contaminant related to acetone and the nonpolar contaminant left on the wafer) and again sonicate it for 5 minutes. The sample is then dried with dinitrogen (N_2) and dehydrated on a 220°C hot plate for 10 minutes. The sampled is now ready for the resist deposition (Fig 3.29 (a)).

3.3.2.2 E-beam resist deposition

	Speed	**Ramp**	**Time**
Ti-Prime	6000 rpm	3	30 s
MaN-2401	3000 rpm	5	30 s

Table 3.2 – Parameters used for the spin coating

For the EBL we use a negative tone e-beam resist, the MaN-2401 [4] (i.e. exposed patterns will stay on the surface of the sample after the development). To obtain good adhesion of the resist, we deposit first a thin layer of adhesion promoter called Ti-prime. This primer is directly spin-coated on the surface of the sample after the dehydration procedure: it makes the surface hydrophobic since water can damage the resist adhesion. The sample is then baked at 120°C for 2 minutes. The MaN-resist is then spin-coated on top of this primer and baked at 95°C for 65 seconds. This second baking eliminates the solvent that is contained in the resist film. The parameters used during the spin-coating like the rotation speed and the acceleration (ramp) are very important: they define the resist layer thickness and its homogeneity. We seek to obtain a 100 nm thick resist layer with the parameters listed in 3.2.

As the resist is very viscous, surface tension will provoke accumulation in the edges of the chip: therefore the chip surface must be sufficiently large to obtain a homogeneous working area in the middle (Fig 3.29 (b)). The thickness is also a function of the age of the resist: an "old" resist prepared several months ago contains less solvent [5] and leads to thicker layer. Thickness is a key parameter since it impacts the resolution of the written patterns and the dose required for exposure in the EBL.

We must also be careful with the baking time and temperature of the resist since it can lead to thermally induced cross-linking and increase the development time after exposure.

4. Mix of a phenolic resist and a photocrosslinker, bisazide
5. Batch of resist are fabricated from a stock solution with a solvent that can evaporate in time

For all these reasons it is judicious to perform a "dose test" before executing the lithography of the whole sample. All these steps are carried out in a UV-free environment since this resist is also UV-sensitive.

3.3.2.3 E-beam exposure and lithography

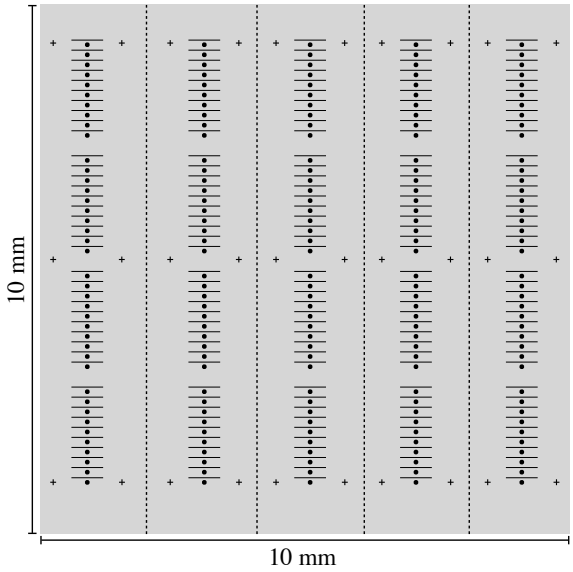

Figure 3.30 – Schematic of the chip and e-beam waveguide/disk patterns (scale is not respected). The little crosses located on both sides of patterns are markers used for the photolithography alignment. The dashed lines are cutting lines meant to separate the different samples

The design of the mask is implemented with the E-line software and then adapted to the Raith EBL system of our cleanroom. There are several distinct sample designs per chip (usually 5 designs) : the chip will be cleaved in several samples after the ICP process (Fig 3.30). We review here several parameters used for the EBL :

- An acceleration voltage of 20 kV is used: this value is a compromise between the resolution of the lithography and the settings of the beam parameters. It determines also the writing time of the lithography: higher voltage leads to faster lithography.
- The typical dose used for exposure is 100 μC/cm^2, insuring a good pattern quality. The dose is not uniform on the mask. A crucial point is to avoid proximity effects, when a pattern is exposed with a high dose, electrons scattered away from the beam spot expose nearby parts involuntarily. Small gaps between two patterns, like the waveguide and the disk, can be closed by this effect, making the sample useless. The dose is generally higher for the narrow patterns of the mask, such as the waveguide anchoring points, or the tip of the waveguide.
- The aperture is 10 μm (current around 26 pA)
- Step size is 10 nm

- Write-field is 100 μm: during the lithography, the electron beam is deflected to expose patterns contained in a 100 μm × 100 μm square centered on the central (un-deflected) beam position. Then the platform moves to the next write-field and repeats the procedure, until the end of the mask. Aligning those write fields is another paramount point.

3.3.2.4 Development of the e-beam resist

A chemical solution of tetramethylammonium hydroxide ($[(CH3)_4N^+, OH^-]$, very strong base), AZ-276-MIF, is used to develop the resist after exposure. The cross-linked part of the resist, i.e. the part exposed during the EBL, is the only one to remain on the surface after development. The procedure of development consists of a repetition of several dippings: AZ-276-MIF for 8 seconds, distilled water (DI-H_2O) for 10 seconds, and in another beaker, DI-H_2O for 30 seconds. We repeat this procedure at least 2 or 3 times and check between each cycle, with an optical microscope (magnification 50 or 150), the state of the sample, and if another cycle is necessary or not. The sample at this stage of the process is represented in the figure (Fig 3.29 (c)).

To improve the roughness of the sidewalls and lateral patterns, a resit reflow can be carried out. This technique consists of heating briefly (∼ 30 seconds) the sample, up to the resist softening temperature. Due to surface tension, the resist forms back smooth interfaces, hence reducing roughness. Two pictures of the resist mask after the reflow are represented in figure 3.31. Improving the roughness of sidewalls enhances the optical quality factor of the disk [121]. To improve the quality of the waveguide/ disk edges, and remove properly resist residuals stuck in the gap, an extra oxygen O_2-plasma step (18 seconds) or an O_2-RIE (10 seconds) can be added to the protocol. Nevertheless, this process provokes a reduction of the resist layer thickness, which can lead to a weaker mask for the next step.

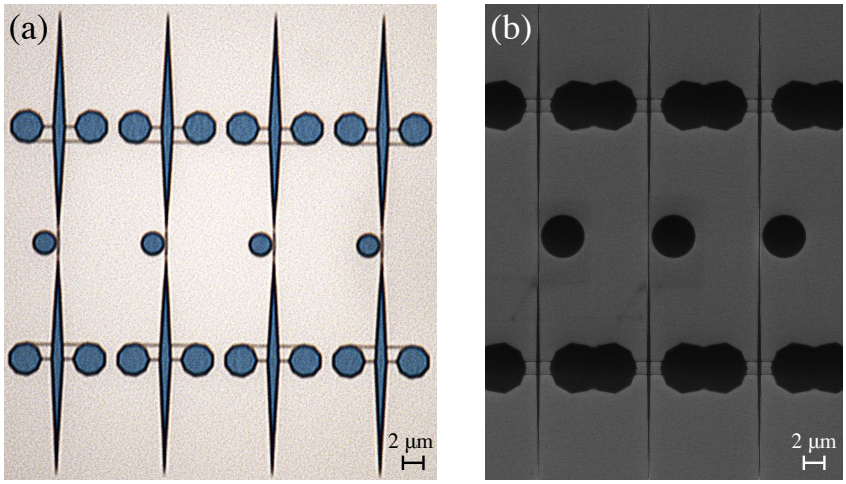

Figure 3.31 – (a)Optical microscope picture of the resist mask after reflow, disk radius 1 μm - Magnification = 1.5K (b) SEM micrograph of the resist mask after reflow , disk radius 2 μm - Magnification ∼ 2.3K

3.3.3 Inductively Coupled Plasma Reactive Ion Etching

The ICP-RIE is a conventional etching technique used to manufacture semiconductor devices : based on an inductively coupled plasma (ICP) source and illustrated in figure 3.32. Inside the ICP chamber, we place the sample as well as a gaseous mix of different species. Thanks to the action of a magnetic field generated by a first RF antenna (coil), we obtain a high-density plasma. A second RF antenna induces a bias that displaces first the electrons (self-bias), and then attracts the ions to the sample surface. Ions having a larger mass than electrons, their impact on the sample surface induces a physical sputtering and starts the etching process. This simple picture is incomplete, as the etching mechanism does also rely on the chemical reaction of free radicals, generated in the chamber, with GaAs/AlGaAs. This etching is often referred as *dry* since it does not involve solution, and *anisotropic*, as ICP-etching can be almost vertical when the ions are accelerated vertically. The gas mix employed in our ICP chamber is composed of argon (Ar) and silicon tetrachloride ($SiCl_4$), the temperature is around 10°C, and the pressure is low, around 0.1 Pa, in order to limit collision between ions and improve the anisotropy. Species like $SiCl_4$ in the plasma are *active* and chemically react with the sample, others serve to locally increase the temperature and generate radicals.

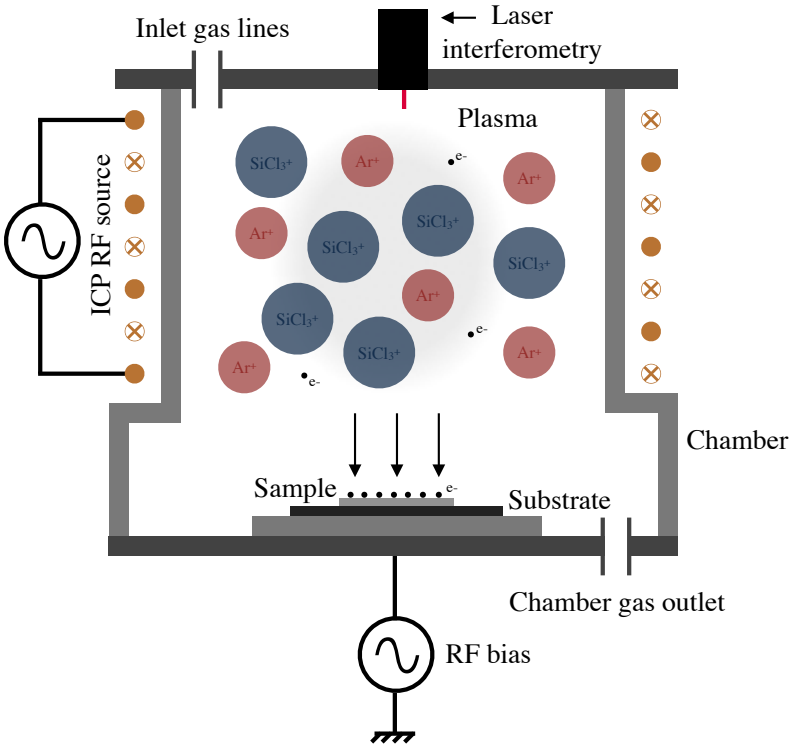

Figure 3.32 – ICP-RIE etching. see text for principles of operation. The first RF antenna (ICP RF) creates the plasma. The second RF antenna (RF bias), creates the final attraction of ions onto the surface. The laser interferometer serves to track the etching depth.

The duration of the ICP process depends on the depth of etching: usually, we seek to etch the whole GaAs disk layer and approximately the same depth in the AlGaAs sacrificial

layer. The progress in etching is monitored by laser interferometry. During this Ph.D. thesis, the etching process never exceeded 45 minutes. For longer etching, it is essential to carefully choose resist parameters since the resist mask gets damaged during etching. Thicker resist layer leads to deeper anisotropic etch. For very deep etching the MaN should be replaced by a more resistant resist mask such as obtained with HSQ.

The nature of the gaseous mix, the temperature, the pressure in the chamber, the plasma density, the bias as well as the hardness of the resist are numerous parameters to be mastered in order to obtained state-of-the-art etching and performances. For further details on the ICP etching method, see [121, 179, 180, 228–230]. A SEM micrograph of a test sample after ICP etching is presented in figure 3.33.

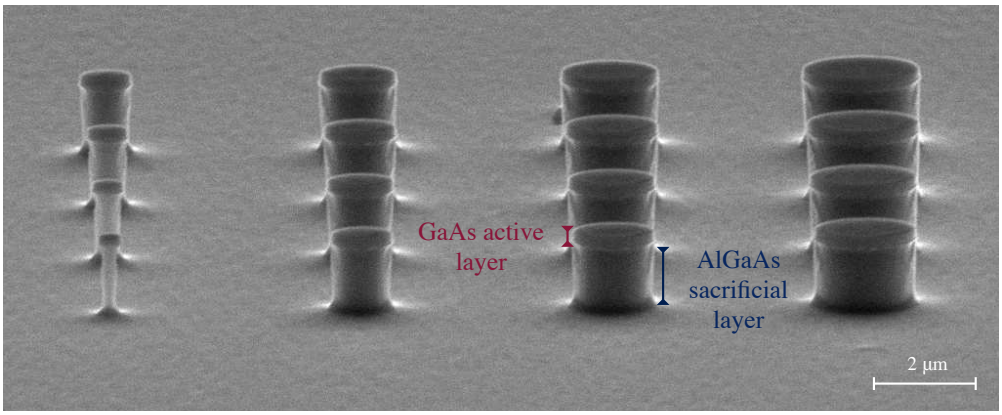

Figure 3.33 – SEM micrograph after the ICP-etching. Test sample containing disk of different size. The duration of etching has been increased to completely etch the AlGaAs layer and check the smoothness of the sidewalls

E-beam resist removal

After the ICP etching is completed, samples are immediately split, dipped, and kept in IPA in order to avoid the creation of a thin oxide layer that can damage the following fabrication steps. The size of the chips at this stage is $\sim$ 2 mm $\times$ 10 mm.

The next step consists in removing the e-beam resist, the reason for that is twofold: on one hand, remaining resist on top of the disk can affect both its optical and mechanical properties (refractive index contrast altered and mechanical friction in the resist long polymer chains). On the other hand parasite chemical reactions can happen between the resist and the HF solution: disturbing the under-etching, or making the resist mask more resistant and harder to remove. It is therefore essential to strip the e-beam resist mask on top of the sample surface. Both resist reflow and ICP process have already heated the resit mask, while a simple acetone solution is usually sufficient to remove unbaked MaN resist, it is not working here. We use a specific resist stripper called SVC-14, heated in a *bain-marie* at 80°C, and let the samples inside for 1 to 2 hours. SVC-14 can be used at higher temperatures compared

to acetone and is non-corrosive for GaAs and AlGaAs. In practice, this removal procedure is not 100% efficient, some residuals might remain, another possible solution is to perform an O_2-plasma cleaning for several minutes.

3.3.4 Selective wet under-etching

In order to create the fully suspended waveguide structure as well as the pedestal under the disk, we need to get rid of the sacrificial AlGaAs layer selectively. For a content of aluminum superior to 50% in an $Al_xGa_{1-x}As$ alloy, using concentrated HF solutions (40 to 50%) leads to an extremely selective etching [231, 232]. HF etches $Al_xGa_{1-x}As$ a million times faster than GaAs. However, since this reaction is extremely violent and releases a large quantity of dihydrogen (H_2) at room temperature, we need to reduce the concentration of HF and cool down the etchant solution to slow down. We typically use a solution of 1.25% HF at 4°C and achieve an average etching speed around 10-20 nm/sec. Moreover cooling down the solution helps to obtain smoother, more regular pedestals.

When the ICP etch does not remove the entire AlGaAs layer, a great amount of reaction products of AlGaAs with HF are generated (aluminum hydroxides), which are poorly soluble in HF and water and can re-deposit on the surface. To remove these by-products we use a strong base potassium hydroxide (KOH) solution that favors their solubility [233]. Before moving the sample from the HF solution to the KOH solution, we perform a quick dip in water to drastically increase the sample pH and avoid exothermic reactions. The following procedure is employed:

- HF 1.25% at 4°C typically for 2 to 3 minutes.
- DI-H_2O (first beaker) for 3 seconds.
- KOH solution, (10 g/100 mL) for 2 minutes.
- DI-H_2O (second beaker) for 10 seconds
- DI-H_2O (third beaker) for 3 minutes
- IPA (first beaker) for 20 seconds
- IPA (final beaker) for 30 seconds

These steps can be repeated until the desired amount of etching is obtained. Taking into account the hazardous nature of these chemical products, all steps are carried out under a dedicated chemical hood and extra protections (extra pair of gloves, mask, disposable apron) are required. The HF under-etching of $Al_xGa_{1-x}As$, at least in our conditions, favors some crystallographic axes. Manually steering the sample in the HF solution is important to mitigate this anisotropy. Without proper steering (steering the sample with a moderate speed in all possible directions) "square" pedestal is obtained, which impacts the mechanical performances of the resonator. The disks fabricated for this thesis are rather small (1 or 2 μm radius), and these anisotropy effects were only observed for larger disks with an under-etching performed at room temperature. The structures, once released, become very brittle (fully suspended waveguides): the sample should be manipulated with extra care. SEM micrographs of a sample at this stage of the fabrication are presented in figure 3.34.

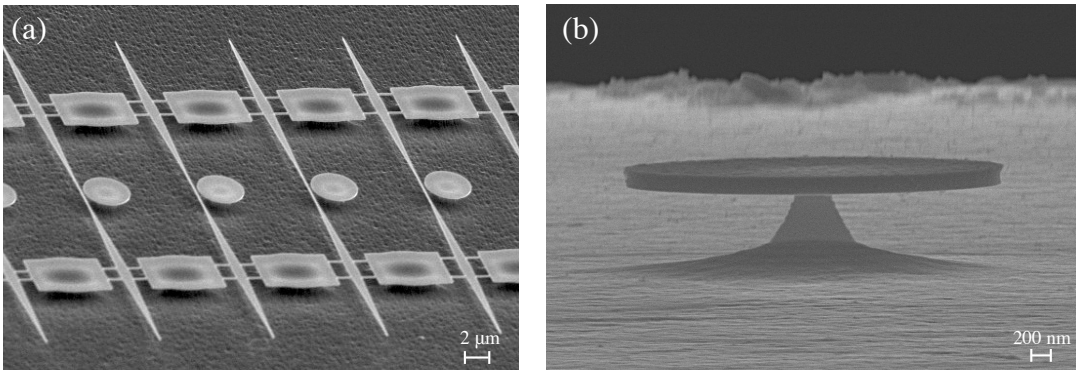

Figure 3.34 – SEM micrographs after the HF under-etching, disk radius 2 μm. (a) 5 disk with their waveguides, Magnification $\sim$ 1.4K (b) Isolated disk, Magnification $\sim$ 20.7K

Flash-dry

Once the selective HF under-etching is finished, we do not dry the samples or remove them from the liquid, as the suspended waveguides might collapse under the action of surface tension of the liquid and capillary forces. The procedure we have retained to avoid this issue is to place the sample in IPA, whose surface tension is lower than that of water, and then put it on a very hot plate (270°C) and perform a *flash-dry* for less than 5 seconds. This high temperature (but perfectly fine for GaAs) decreases the surface tension and locally provokes the evaporation of IPA. This process turns out to be efficient in our case and prevents the suspended structures to collapse on the substrate. An alternative method could be using a critical point drying machine.

3.3.5 Mesa Fabrication

The last part of the fabrication procedure and the most delicate is the creation of a mesa, elevating the fully suspended waveguide structure above the substrate and freeing the tips of the waveguide. This mesa aims at giving room to place the μ-lensed fibers in the vicinity of the fully suspended waveguide, (see figure 3.35 and figure 3.37 (b), (c)): we need the depth of the mesa to be close to the μ-lensed fibers diameter, i.e. around 100 μm. To achieve that we use this time optical lithography coupled to a wet chemical etching. For such deep etching, using a physical method like ICP is less appropriate since the time of etching would be extremely long.

3.3.5.1 Photosensitive mask for the mesa

We first deposit an optical resist on the sample. For this photosensitive mask, we use a positive (non-exposed parts remain after the development) UV-photoresist, the S-1818. This resist has the advantage to be transparent for the visible spectrum, which turns out to be crucial to control the advancement of the mesa etch. We apply a spin coating procedure close to the prior one (Ramp 5, Speed 5000 rpm, Time 30s) but we double the resist layer, i.e. we repeat twice the operation. The resist is baked at 110°C for 1 minute after each spin-coating process. In the end, the thickness of the resist layer is around 3.6 μm, a thick-

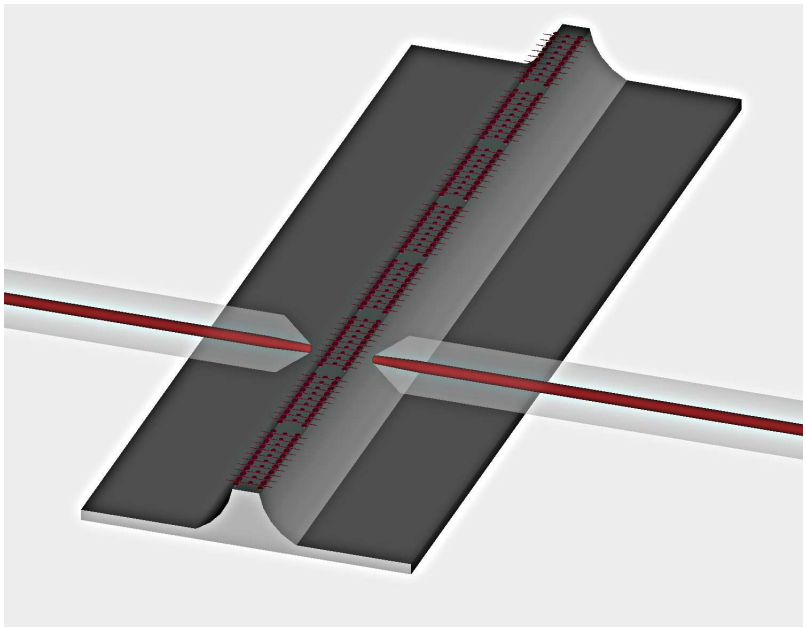

Figure 3.35 – Sketch of the sample with mesa, with the μ-lensed fibers positioned it the vicinity of the structures. The scale is not respected

ness that is large enough to protect the structures. Again surface tension of S-1818 provokes accumulation of the resist on the chip edges, however, the width of the chip is now divided by five, which makes the problem more severe. To prevent it, we place dummy pieces of wafer around the chip to virtually increase its surface and reduce resist accumulation at the edges.

We then expose the resist with UV ($\lambda = 350 - 450$ nm, the resist is optimized for the UV-G line, $\lambda = 436$ nm). The employed mask is a glass plate with a thin metal layer (the metal absorbs the UV). The mask design is a 2 mm wide rectangle. We align this rectangle with the marker structures (Figure 3.30) of the sample thanks to a *MJB4* aligner. The markers are located at 80 μm distance from the waveguide tips on both sides: the etching process being more or less isotropic, with this distance it will reach the required depth. We expose the resist for 40 seconds and repeat the operation on the other side of the sample: we obtain a resist strip with a width around 200 μm. After the exposure, we develop the resist in an alkaline solution (MF319) and rinse the sample in distilled water. Generally, another cycle of exposure and development is required to get proper results. The choice of the resist strip width is important: a too-large strip might collapse during the etching process.

Despite its lower resolution, photo-lithography is convenient for the mesa since the time of exposure is short and a very large zone can be exposed at the same time. For such a deep etching process (~ 100 μm) the thickness of the sample is greatly reduced, resulting in an overall fragility that makes the sample difficult to handle. We protect the back surface of the sample with some resist to help. It is impossible to use standard spin-coating techniques for this task since it would damage the structures: with the help of a cotton q-tip, we gently

deposit a thin layer of resist on the back of the sample.

3.3.5.2 Mesa wet etching

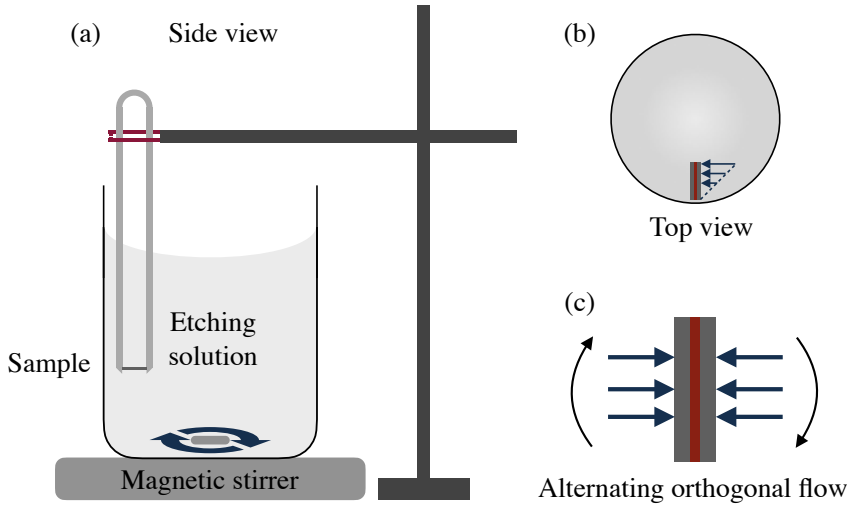

Figure 3.36 – Schematic of the sample steering during the mesa etching. (a) Side view (b) Top view (c) Flow around the sample

For the mesa we would prefer vertical walls (as represented in Figure 3.35): we need the lateral etch speed to be slightly lower than the vertical one. GaAs wet etching consists in the formation of an oxide at the surface, followed by the dissolution of these oxidized products by a base or an acid [234]. Hence the key ingredients to any wet etchant are an oxidizer (**Ox**), a strong acid (for example) (**Ac**) and a diluent (**D**), to help the transport of the reactants and control the different etch rates [235]. We have at our disposal two etching solutions that have proved to efficiently generate nice mesa structures:

- BCK: solution made with an isovolumic mixing of hydrobromic acid (HBr, **Ac**), acetic acid (CH_3COOH, **D**) and potassium dichromate ($K_2Cr_2O_7$, **Ox**) aqueous solutions [236].
- H_3PO_4/H_2O_2 : solution made with an isovolumic mixing of phosporic acid (H_3PO_4, **Ac**), hydrogen peroxide (H_2O_2, **Ox**) and water (H_2O, **D**) [237, 238]

Each option has strengths and drawbacks. BCK possesses a vertical speed that is higher than the lateral: it produces smooth walls and is not dependent on the crystallographic orientation. However, the solution is highly toxic (it requires extra equipment to handle it) and it is turbid with a dark brown/black color that forbids seeing the sample through. On the other hand, H_3PO_4/H_2O_2 is colorless and transparent, also less toxic, but the choice of the mask orientation with respect to the crystal is paramount: one of the orientations leads to a lateral speed higher than the vertical, which is a no-go for our purpose. In short, if we know the orientation of the mask with respect to the crystal we can choose H_3PO_4/H_2O_2, otherwise, we should use BCK. Other compositions are possible for the two solutions, and

different etch speeds and mesa shapes can be expected.

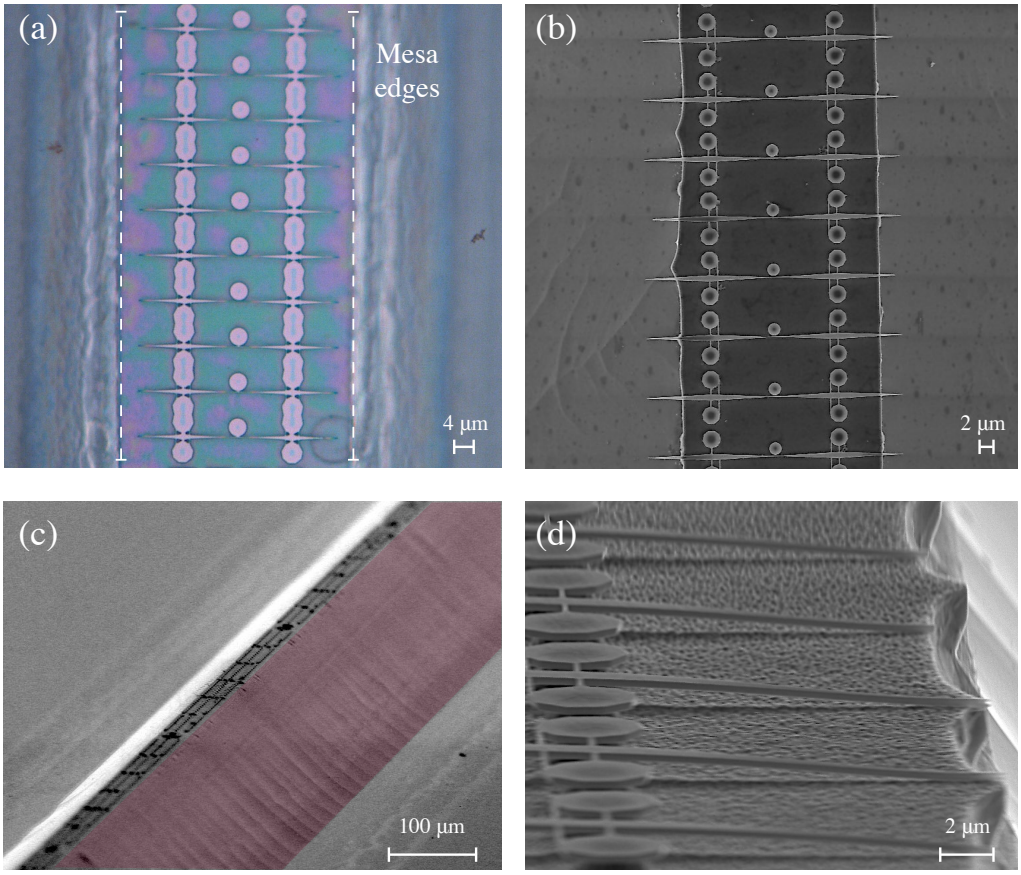

Figure 3.37 – (a) Optical microscope image of a sample after 18 minutes of etching in H_3PO_4/H_2O_2 : the mesa edges can be seen through the resist mask and the etching is symmetric and regular ; disk radius 2 μm, Magnification = 500. (b) SEM micrograph after the mesa process and removing the resist : the tips of the waveguides are free and the mesa walls are symmetric (left/right), disk radius : 1 μm, Magnification $\sim$ 1K. (c) SEM micrograph after the mesa process, exhibiting mesa walls (colored in light-red) that are not very steep but do not hinder the fibers approach, Magnification $\sim$ 130 (d) SEM micrograph, the mesa was asymmetric here resulting in waveguide tips stuck on the substrate Magnification $\sim$ 5K

After having chosen the right option, we place the sample at room temperature in a beaker containing the etching solution (see figure 3.36 (a)). The sample is held by acid proof Teflon tweezer, itself firmly hold by a mount. As for HF etching, the steering conditions are very important: we use here a magnetic stirrer in the etching solution to control the flow of etchant impinging the sample. The most efficient way to etch for us is to use an orthogonal flow [179] (see figure 3.36 (c)): we place the sample close and perpendicular to the beaker's edge. To have a symmetric mesa etching we need to alternate in time the rotation of the magnetic rod (clockwise and counter-clockwise). The tangential speed profile is not uniform (see figure 3.36 (b)): this will impact the etch speed and result in a symmetric

but not equally advanced mesa. To prevent that we rotate the sample at half the etching duration: this is why it is also very important that the design was centered on the sample. Images of symmetric (left-right) mesa with disks and suspended waveguides at different stages of fabrication are shown in figures 3.37 (a), (b), and (c). An asymmetric mesa can lead to waveguide tips stuck to the substrate, which obviously make the optical coupling to the disk impossible (see Figure 3.37 (d)). Despite these precautions, the mesa etching is not highly reproducible: the slightest perturbation in the steering or defects in the S-1818 resist strip, can have severe consequences on the final mesa and its operation for experiments.

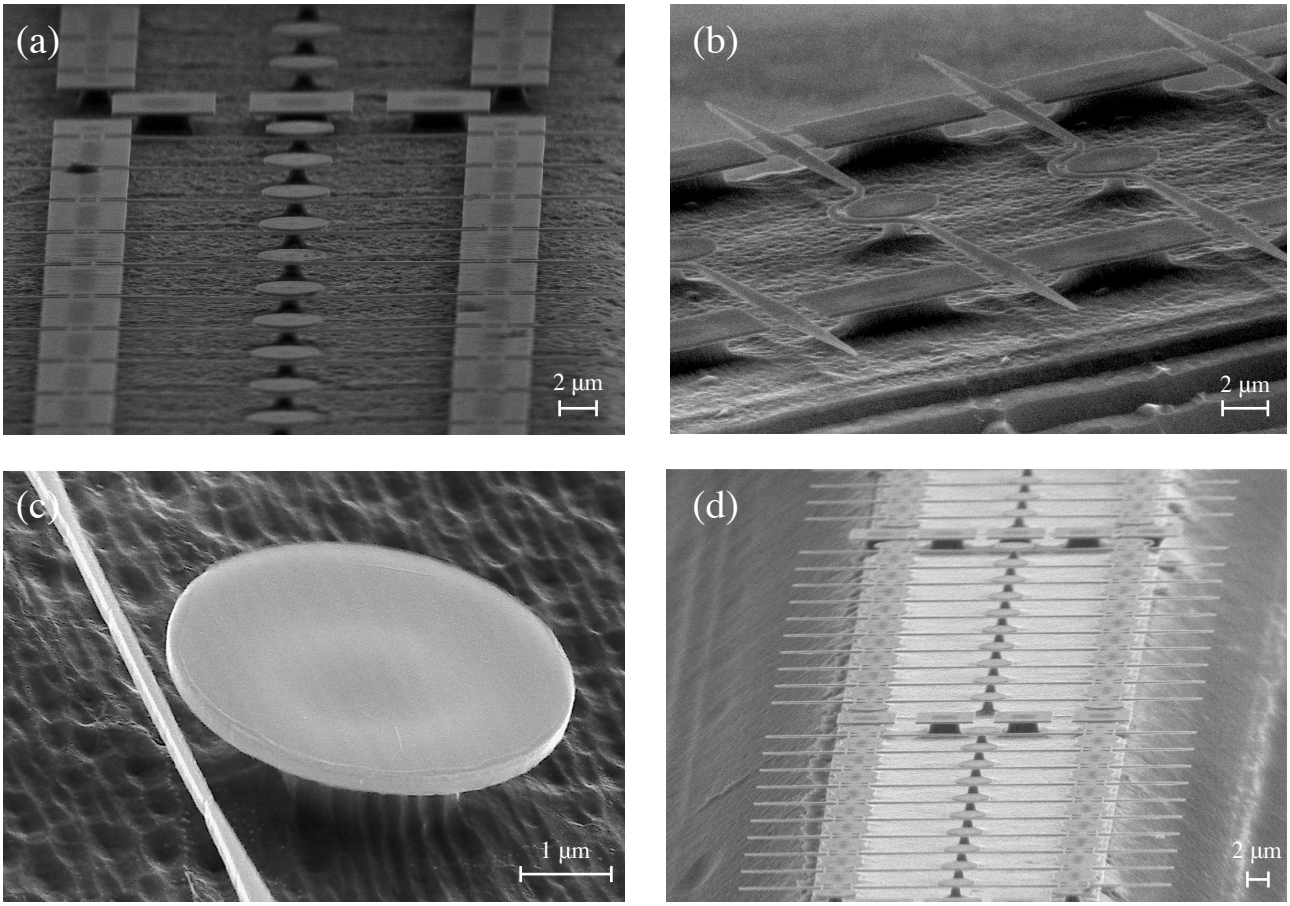

Figure 3.38 – SEM micrographs compilation of different fabricated sample (a) Magnification $\sim$ 2.4K. (b) Magnification $\sim$ 4.4K (c) Magnification $\sim$ 14.8K (d) Magnification $\sim$ 1.8K

The average lateral etching speed for the mesa is in the range 4-8 μm/min: etching speed is always higher for freshly-prepared solutions and decreases in time. The total etching time is around 20-30 minutes. To reach the desired mesa, we check on several occasions the amount of etching under an optical microscope (see figure 3.37 (a)): for this, we rinse the sample in a first beaker of distilled water for 30 seconds and repeat the operation in a second beaker. When the target dimension is obtained, we remove the resist in an SVC-14 beaker, place the sample in a water bath (80°C) for 1-2 hours (can be even longer), and proceed to a flash dry. The sample is now ready to be measured, we keep it in a vacuum box to avoid

oxidation and contamination. The final state of the sample is presented in SEM pictures (figure 3.38).

3.3.6 Atomic Layer Deposition and surface passivation

Recently an effort was made in our group regarding the passivation of surface states of the microresonator [105]. Mid-gapes states at the surface of resonators can absorb photons of energy below the bandgap and generate optical losses [239]. Atomic Layer Deposition (ALD) of alumina (Al_2O_3) increases the performances of GaAs based nano-electronic structures [240]. The addition of an ALD nanolayer improves the surface quality and the quality factor of the disk. A quality factor of several million could be fabricated thanks to this technique [105]. Different ALD oxide materials, both amorphous or poly-crystalline have been also tested to understand and control surface mechanical dissipation in our resonators [101].

ALD post-treatment also has positive effects on the exciton, since improving the surface state also has a positive influence on the multiple dissipation mechanisms of the exciton. We have observed that for an ALD treated sample, the required power of excitation to obtain the same level of PL-signal than for a bare sample is divided by a factor 6. We also observed a lowering of the lasing threshold. Regarding the exciton linewidth, we have mixed conclusions: we have not observed an improvement of exciton linewidth with ALD.

Chapter 4

Observation of quantum-well exciton polaritons in whispering gallery resonators

Summary: This chapter reports the observation of exciton-polariton in our hybrid quantum-well whispering gallery mode resonators. We start by presenting the polaritonic expectations in terms of spectra and signal behavior. We then show the different techniques used to observe polaritons and the models used to fit the associated data. A discussion of the phenomenon of polariton lasing at high excitation power ends the chapter.

4.1 Conditions for exciton-photon strong coupling

We review the conditions required to observe strong coupling regime, more precisely in the case of the WGM-resonators and quantum-wells.

4.1.1 Experimental signature of strong coupling

The most famous signature of strong coupling is the observation of an anti-crossing between the upper and lower polariton branches. Several experiments of optical reflection, transmission, or PL can be imagined to witness this phenomenon. Observing two peaks in an optical spectrum near the resonance, instead of one, is insufficient to claim strong coupling, since such doublet can have different physical origins. For instance, one could observe two excitonic modes with slightly different energy because of a different nature (HH and LH). In the course of this thesis, we observed a doublet in the PL spectra of disks (see figure 3.25-(c)), which was due to strain relaxation and was disappearing for sufficient under etching. A solid proof of strong coupling regime relies at best on the anti-crossing behavior (illustrated in figure 1.4), observed as a function of the cavity-exciton detuning. This detuning δ can be changed in different manners:

- **Cavity mode tuning**: A suitable design fabrication of the sample can be carried out where a linear variation of the energy of the cavity mode is implemented. One can imagine a linear variation of the thickness of the cavity for instance, like in the pioneering work of Weisbuch [241] or in [76]. One can tune the cavity modes directly inside the set-up using condensation of gas [242–244]. In our system of WGMs supported by disks, it is natural to tune the cavity through the disk radius.

- **Exciton mode tuning**: One can tune the exciton energy with a gradient in the thickness of the QW epitaxial structure, or by wisely playing with the device strain [245, 246]. A coarse way of doing this is also at the epitaxial level, by playing with the QW alloy composition.

- **Cavity and exciton mode tuning**: It is possible to tune at the same time both energies by changing the temperature of the device [247–250]. Of course, this makes sense if the two energies do not evolve identically with temperature. This can be done over a limited temperature range, since the exciton tends to disappear above a certain threshold.

Note that other methods are available to identify the strong coupling regime, such as time-resolved experiments [251] (direct observation of the Rabi oscillations) or angle-resolved photo-luminescence experiments [252]. In this work we will focus on the anti-crossing behavior: thanks to our original set-up with three configurations (see figure 3.4), we will be able to perform non-resonant PL studies as well as resonant spectroscopy. And this despite the highly confined nature of WGMs, which we investigate both through out-of-plane and in-plane experiments. Before going further we should determine the aspect of the two kinds of spectrum.

4.1.2 Spectrum calculation

4.1.2.1 Without exciton inhomogeneous broadening

Let us take back the quantum linear model from eq. (1.27).

$$\hat{H}_{cx} = \hbar\omega_c \hat{a}^\dagger \hat{a} + \hbar\omega_x \hat{d}^\dagger \hat{d} + \frac{\hbar\Omega_R}{2}\left(\hat{a}^\dagger \hat{d} + \hat{a}\hat{d}^\dagger\right) \tag{4.1}$$

Using again the input-output approach (see appendix A.2), we derive the quantum Langevin equations for the operators $\hat{a}$ and $\hat{d}$:

$$\begin{aligned} \dot{\hat{a}} &= (j\Delta - \frac{\kappa_c}{2})\hat{a} - j\frac{\Omega_R}{2}\hat{d} + \sqrt{\kappa_{\text{ext}}}\alpha_{\text{ext}} + \sqrt{\kappa}\hat{a}_{\text{in}} \\ \dot{\hat{d}} &= (j\Delta' - \frac{\kappa_x}{2})\hat{d} - j\frac{\Omega_R}{2}\hat{a} + \sqrt{\kappa_x}\hat{d}_{\text{in}} \end{aligned} \tag{4.2}$$

where we used the rotating wave approximation $\left(\hat{U} = \exp\left(-j\omega_l(\hat{a}^\dagger\hat{a} + \hat{d}^\dagger\hat{d})t\right)\right)$to recenter the dynamics of both degrees of freedom around the laser frequency, hence $\Delta' = \omega_l - \omega_x$.

We now rewrite equations (4.2) for the mean value of the fields ($\bar{a}$,$\bar{d}$) and look for their solutions in the steady-state :

$$\begin{aligned} 0 &= (j\Delta - \frac{\kappa_c}{2})\bar{a} - j\frac{\Omega_R}{2}\bar{d} + \sqrt{\kappa_{\text{ext}}}\alpha_{\text{ext}} \\ 0 &= (j\Delta' - \frac{\kappa_x}{2})\bar{d} - j\frac{\Omega_R}{2}\bar{a} \end{aligned} \tag{4.3}$$

which leads us to

$$\bar{a} = \frac{\sqrt{\kappa_{\text{ext}}}\alpha_{\text{ext}}}{(\frac{\kappa_c}{2} - j\Delta) + \frac{\Omega_R^2}{4(\frac{\kappa_x}{2} - j\Delta')}} \qquad \bar{d} = \frac{-j\frac{\Omega_R}{2}}{(\frac{\kappa_x}{2} - j\Delta')}\bar{a} \tag{4.4}$$

Using now the input-output relations (eq. 3.2) conditions we obtain the following expression for the waveguide transmission:

$$T = \left| 1 + \frac{-\frac{\kappa_c}{2}(\frac{\kappa_x}{2} - j\Delta')}{(\frac{\kappa_c}{2} - j\Delta)(\frac{\kappa_x}{2} - j\Delta') + \frac{\Omega_R^2}{4}} \right|^2 \tag{4.5}$$

where the critical coupling regime for photons ($\kappa_{\text{ext}} = \kappa_c/2$) is assumed. For $\Omega_R = 0$ we recover the expression of the transmission (eq. (3.6)) at the critical coupling regime. Transmission spectra are plotted in figure 4.1 for different values of the cavity-exciton detuning δ. We recognize two lorentzian dips with resonances located at $\tilde{E}_{u/l}$ [253, 254] and linewidth equal to $\kappa_{u/l}$.

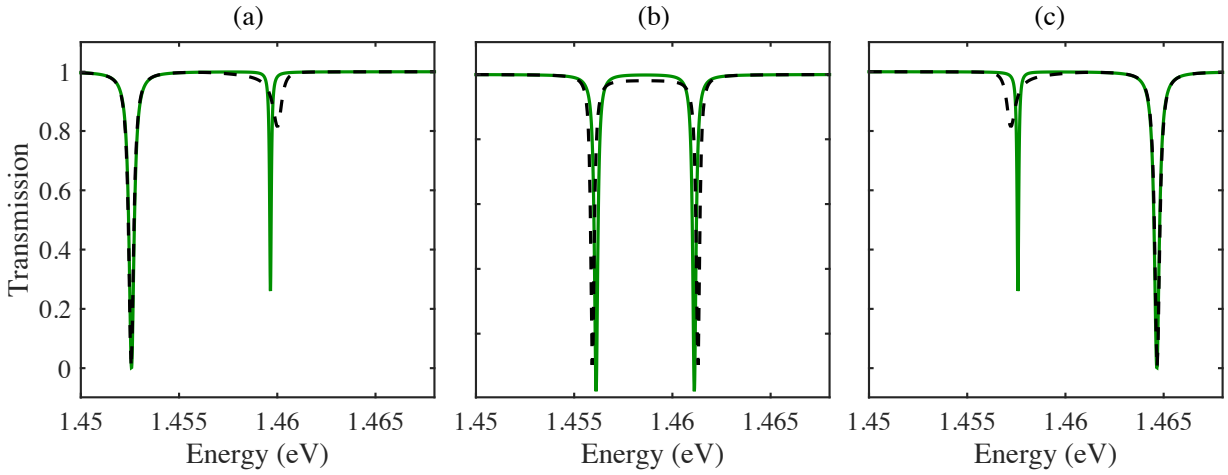

Figure 4.1 – Waveguide optical transmission spectrum for different cavity-exciton detuning (a) $\delta = -\Omega_R$ - (b) $\delta = 0$ - (c) $\delta = \Omega_R$. Green (black dashed) curves corresponds to $\kappa_{\text{inh}} = 0$ (2) meV

4.1.2.2 With exciton inhomogeneous broadening

If we now account for the effect of the exciton inhomogeneous broadening (introduced in the previous chapter, section 3.2.2.4), we replace the operator $\hat{d}$ by a collection of excitonic operators $\hat{d}_\omega$ of frequency ω distributed around the central exciton frequency ω_x, all having the same linewidth κ_x. Accordingly, the Hamiltonian of the system is transformed into [255]:

$$\hat{H}_{cx} = \hbar\omega_c \hat{a}^\dagger \hat{a} + \int d\omega \hbar\omega \hat{d}_\omega^\dagger \hat{d}_\omega + \frac{\hbar\Omega_R}{2} \int d\omega \alpha(\omega) \left(\hat{a}^\dagger \hat{d}_\omega + \hat{a} \hat{d}_\omega^\dagger \right) \tag{4.6}$$

where we have ignored interactions between excitons. The coefficient $\alpha(\omega)$ is proportional to the contribution of each excitonic mode to the coupling with photon (each exciton is coupled with a strength $\Omega_R \alpha(\omega)/2$). We assume a Gaussian distribution with κ_{inh} as FWHM like in section 3.2.2.4:

$$\alpha(\omega) = \left[\frac{1}{\kappa_{\text{inh}}} \sqrt{\frac{4\ln(2)}{\pi}} e^{\left(-4\ln(2) \frac{(\omega-\omega_x)^2}{\kappa_{\text{inh}}^2} \right)} \right]^{1/2} \tag{4.7}$$

The total oscillator strength of the exciton should remain unchanged therefore we have $\int d\omega \alpha^2(\omega) = 1$. By following the same approach as above, we derive the quantum Langevin equations for $\hat{a}$ and $\hat{d}_\omega$:

$$\begin{aligned} \dot{\hat{a}} &= (j\Delta - \frac{\kappa_c}{2})\hat{a} - j\frac{\Omega_R}{2} \int d\omega \alpha(\omega) \hat{d}_\omega + \sqrt{\kappa_{\text{ext}}}\alpha_{\text{ext}} + \sqrt{\kappa}\hat{a}_{\text{in}} \\ \dot{\hat{d}}_\omega &= (j\Delta' - \frac{\kappa_x}{2})\hat{d}_\omega - j\frac{\Omega_R}{2}\hat{a} + \sqrt{\kappa_x}\hat{d}_{\text{in}} \end{aligned} \tag{4.8}$$

and rewrite them in the steady-state regime:

$$
\begin{aligned}
0 &= (j\Delta - \frac{\kappa_c}{2})\bar{a} - j\frac{\Omega_R}{2}\int d\omega\alpha(\omega)\bar{d}_\omega + \sqrt{\kappa_{\text{ext}}}\alpha_{\text{ext}} \\
0 &= (j\Delta' - \frac{\kappa_x}{2})\bar{d}_\omega - j\frac{\Omega_R}{2}\bar{a}
\end{aligned}
\tag{4.9}
$$

By introducing a linear combination of all the excitonic operator $\hat{d}_\omega$:

$$
\hat{d} = \int d\omega\alpha(\omega)\hat{d}_\omega \tag{4.10}
$$

we find a set of equations that is close to the homogeneous case (4.4):

$$
\begin{aligned}
0 &= (j\Delta - \frac{\kappa_c}{2})\bar{a} - j\frac{\Omega_R}{2}\bar{d} + \sqrt{\kappa_{\text{ext}}}\alpha_{\text{ext}} \\
0 &= (j\overline{\Delta'} - \frac{\overline{\kappa_x}}{2})\bar{d} - j\frac{\Omega_R}{2}\bar{a}
\end{aligned}
\tag{4.11}
$$

with Δ' and κ_x replaced by $\overline{\Delta'}$ and $\overline{\kappa_x}$ defined by:

$$
\overline{\Delta'} = \frac{-\operatorname{Im}\{\sigma(\omega_l)\}}{\mid \sigma(\omega_l) \mid^2}, \quad \overline{\kappa_x} = \frac{\operatorname{Re}\{\sigma(\omega_l)\}}{\mid \sigma(\omega_l) \mid^2} \quad \text{with} \quad \sigma(\omega') = \int d\omega \frac{\alpha^2(\omega)}{\frac{\kappa_x}{2} - j(\omega - \omega')} \tag{4.12}
$$

Figure 4.1 compares optical spectra obtained with and without exciton inhomogeneous broadening. For $\kappa_{\text{inh}} = 0$ the splitting between the peaks and their linewidth are fully determined by the homogeneous linewidth of the exciton and the photon. When $\kappa_{\text{inh}} > 0$ at zero-detuning, the splitting, as well as the linewidth, remain almost unchanged. Far from zero-detuning, the inhomogeneous broadening has a relatively important impact on the spectrum: the excitonic resonance is noticeably displaced and broader, while the photonic peak seems little affected.

The optical absorption A of the system can also be derived using the simple relation $A = 1 - T$. It is represented as a map in figure 4.2. It exhibits as well the characteristic anti-crossing behavior, and the higher the excitonic fraction in the polariton, the larger the absorption signal. Since absorption is intrinsically linked to the PL, in our experiments we will often use the PL spectrum to visualize the anti-crossing. Our polaritons share the properties of WGMs and excitons: their PL will adopt a radiation pattern similar to that of the WGMs. Extracting the PL signal with such radiation pattern is not an easy task: understanding this pattern is required to establish the best strategy to collect the PL signal.

4.1.3 WGMs radiation pattern

We study here the radiation pattern (far-field emission) of our disk optical resonator. For WGMs, it is quite natural to think that this emission is mostly contained in the equatorial plane of the disk. It is also natural to think that geometric irregularities may scatter

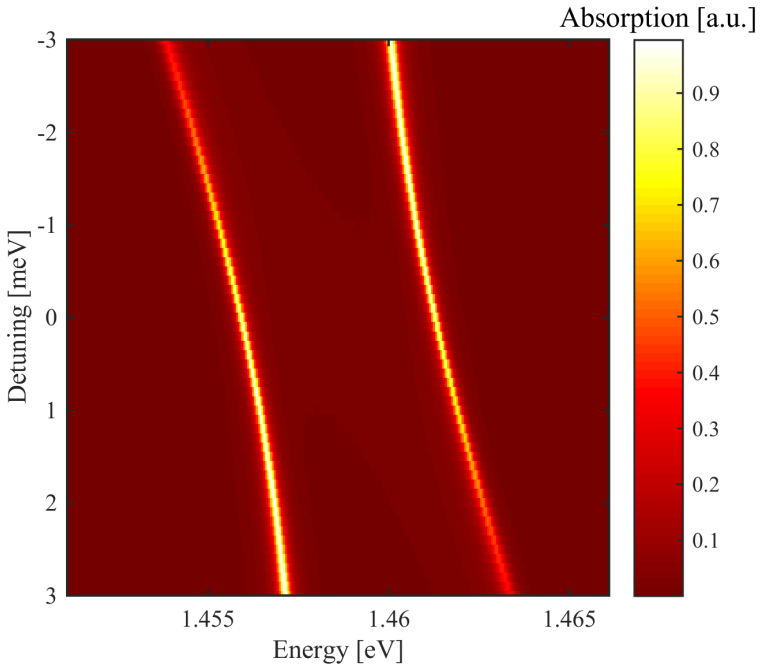

Figure 4.2 – Absorption spectrum as a function of cavity-exciton detuning. $\Omega_R = 5$ meV, $\kappa_{\text{inh}} = 2$ meV.

light and provoke partial re-direction of the emission in the vertical direction of the disk. Nevertheless, for a good sample with a high quality of fabrication (no mask residues on the top of the disk, smooth vertical ICP-etching...) the number of geometric defects is small and the emission in the normal direction should be negligible.

To better understand this radiation pattern we follow the approach introduced in [256], where the authors develop a diffraction scalar theory in cylindrical coordinates that yields a formula for the far-field intensity distribution:

$$I(\theta) \propto \frac{1}{\rho}\left|\frac{F(k\sin\theta)}{H_m^{(2)}(kR\cos\theta)}\right|^2 \tag{4.13}$$

with $\rho = \sqrt{r^2+z^2}$,$k = 2\pi/\lambda$, $\cos\theta = r/\rho$, $\sin\theta = z/\rho$ and $F(k\sin\theta)$ the Fourier transform of the near field distribution (see figure 4.3 (a)). The width of the Hankel function term $1/\left|H_m^{(2)}(kR\cos\theta)\right|^2$ being narrower that the width of $\left|F(k\sin\theta)\right|^2$, it dominates the angular distribution of the far field:

$$I(\theta) \propto \left|\frac{1}{H_m^{(2)}(kR\cos\theta)}\right|^2 \tag{4.14}$$

The angular distribution is represented in figure 4.3 (b): the maxima are located around 0 and 180°, and their angular width is around 22°. However, in contrast to [256], our disk

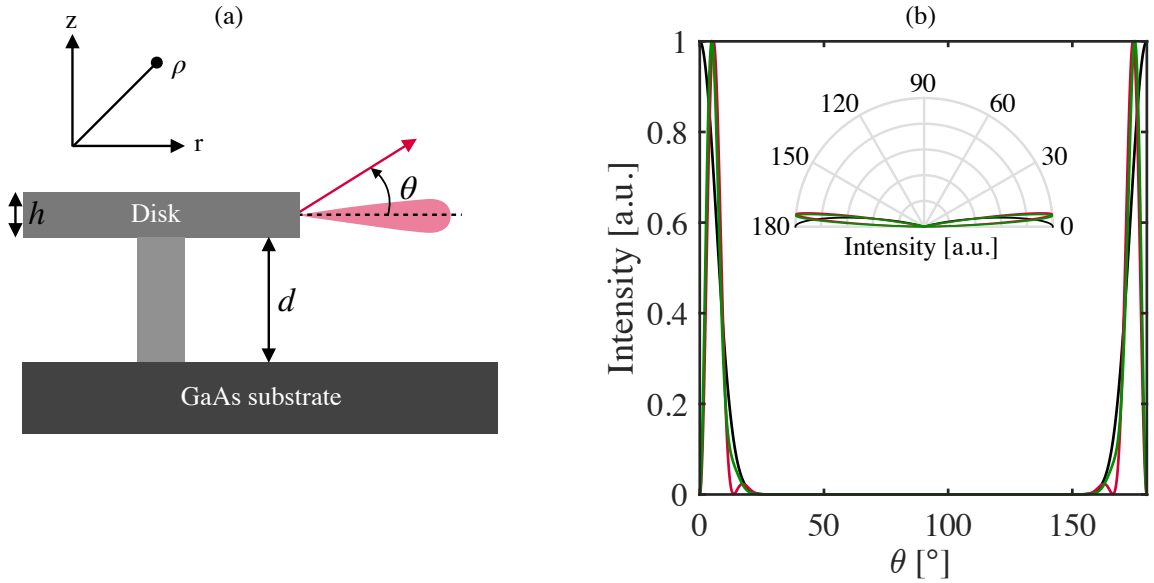

Figure 4.3 – (a) Sketch of the disk resonator and representation of the radiation pattern for θ between 0 and 180°. (b) Intensity angular distribution of the far-field emission for a WGM with $m = 40$, $R = 2\mu$m, $\lambda = 850$nm, $d = 1.8\mu$m. Black curve : no reflection on the GaAs substrate - Red curve : s-polarization - Green curve p-polarization. The inset shows the same results represented in polar coordinates

resonators are not located at the edge of the chip and we should take into account the underlying GaAs substrate. The radiation pattern transforms to:

$$I(\theta) \propto \left| \frac{1}{H_m^{(2)}(kR\cos\theta)} \right|^2 \left| 1 + r(\theta) e^{jk2d\sin\theta} \right|^2 \tag{4.15}$$

where d is the distance between the disk and the GaAs substrate (we neglect the thickness of the disk) and $r(\theta)$ is the reflection coefficient of the substrate given by the Fresnel laws :

$$r_s = \frac{\sin\theta - n\sqrt{1 - \left(\frac{\cos\theta}{n}\right)^2}}{\sin\theta + n\sqrt{1 - \left(\frac{\cos\theta}{n}\right)^2}}, \qquad r_p = \frac{n\sin\theta - \sqrt{1 - \left(\frac{\cos\theta}{n}\right)^2}}{n\sin\theta + \sqrt{1 - \left(\frac{\cos\theta}{n}\right)^2}} \tag{4.16}$$

for the s and p polarization (electric field perpendicular/parallel to the incident plane). The radiation pattern in these two cases is added in figure 4.3 (b): notice that the maxima are no longer centered around 0 and 180° but rather at 5°, while their angular distribution is thinner, around 10°. Reflection on the substrate also creates a secondary maximum located at 17° for the s-polarization and 14.5° for the p-polarization.

In practise, TE and TM WGMs are a combination of s and p polarizations. Still, we expect a radiation pattern with narrow angular distribution close to the equatorial plane of the disk, and with an azimuthal symmetry around the disk axis. The extraction of light in this configuration is quite complex. In order to collect efficiently the PL signal coming from

WGMs we understand that a standard (vertical) confocal configuration (figure 3.4 (a)) is inadequate. In this thesis, we will instead often rely on a near-field approach, employing our suspended waveguides, which have been engineered and optimized to couple with WGMs. They will act as dielectric antennae collecting the signal of PL and guiding it to our fibers. Because the coupling is selective, this collection approach will naturally filter out spurious light blurring our signals (stray light). At the same time, this will enable us to perform direct selective resonant laser spectroscopy of the WGM resonators.

4.1.4 Nuances and intricacies

In this section we highlight two features making our observation of polaritons more complex: first, we have several cavity/exciton modes in our system; second, it is impossible in practice to observe the upper-polaritons (UPs).

4.1.4.1 Multimode polaritons

So far we only considered the strong coupling between a single exciton and a single photon. The system can be generalized to more than one exciton or photon mode. This will generate multimode polaritons [257, 258], whose Hamiltonian $\hat{H}_{cx}^{m}$ is derived from the single-mode one $\hat{H}_{cx}$(eq.(1.27)), by summation over the exciton and photon modes :

$$\hat{H}_{cx}^{m} = \sum_{i}^{N_c} \hbar\omega_{ci}\hat{a}_i^\dagger\hat{a}_i + \sum_{j}^{N_x} \hbar\omega_{xj}\hat{d}_j^\dagger\hat{d}_j + \sum_{i,j}^{N_c,N_x} \hbar\frac{\Omega_R^{ij}}{2}(\hat{a}_i^\dagger\hat{d}_j + \hat{a}_i\hat{d}_j^\dagger) \tag{4.17}$$

where N_c and N_x represent respectively the number of cavity and exciton modes. In most cases, the photon and exciton modes are not all coupled to one another, i.e. Ω_R^{ij} can be null and is certainly likely to vary as a function of i and j.

In our case we have a priori an infinity of cavity and excitonic modes, characterized by the azimuthal and radial numbers m, m', p, p', as introduced in chapter 2:

$$\begin{aligned}\hat{H}_{cx}^{m} = &\sum_{m=-\infty}^{+\infty}\sum_{p=1}^{+\infty} \hbar\omega_{m,p}\hat{a}_{m,p}^\dagger\hat{a}_{m,p} + \sum_{m'=-\infty}^{+\infty}\sum_{p'=1}^{+\infty} \hbar\omega_{m',p'}\hat{d}_{m',p'}^\dagger\hat{d}_{m',p'} \\ &+ \sum_{m,m'=-\infty}^{+\infty}\sum_{p,p'=1}^{+\infty} \hbar\frac{\Omega_R^{m,m',p,p'}}{2}(\hat{a}_{m,p}^\dagger\hat{d}_{m',p'} + \hat{a}_{m,p}\hat{d}_{m',p'}^\dagger)\end{aligned} \tag{4.18}$$

Obviously only a finite number of WGMs, N_{WGM}, are close enough to the energy of the exciton to give rise to appreciable hybridization. What about the number of excitonic modes ? The energy of the different excitonic modes is given by relation (2.118), notably indicating that they are extremely close to one another. Two different exciton modess $(m_1', p_1'$ and $m_2', p_2')$ only differ by the in-plane envelope function shape of their center of mass. This means that their energies differ by an amount $(x_{m_1',p_1'} - x_{m_2',p_2'})\hbar^2/2MR^2$. For two adjacent excitonic modes with $(m_1', p_1') = (40, 1)$ and $(m_2', p_2') = (39, 1)$ this energy difference is about

1.7 μeV, well below our OSA resolution, and well below the binding energy E_b. Hence, in practice, in experiments we will only deal with one excitonic mode $\omega_{m',p'} \simeq \omega_x$. Moreover each WGM will couples preferably to the exciton mode giving the best overlap and largest value for $\Omega_R^{m,m',p,p'}$, hence respecting the selection rule $m' = m$. In the end, the Hamiltonian will take the following structure [1]:

$$\hat{H}_{cx}^{m} = \bigoplus_{i=1}^{N_{\mathrm{WGM}}} \begin{pmatrix} E_x & \frac{\hbar\Omega_R^i}{2} \\ \frac{\hbar\Omega_R^i}{2} & E_c^i \end{pmatrix} = \begin{pmatrix} E_x & \frac{\hbar\Omega_R^1}{2} & 0 & 0 & \dots & 0 & 0 \\ \frac{\hbar\Omega_R^1}{2} & E_c^1 & 0 & 0 & \dots & 0 & 0 \\ 0 & 0 & E_x & \frac{\hbar\Omega_R^2}{2} & & \vdots & \vdots \\ 0 & 0 & \frac{\hbar\Omega_R^2}{2} & E_c^2 & & & \\ \vdots & & & & \ddots & & \\ 0 & 0 & \dots & & & E_x & \frac{\hbar\Omega_R^{N_{\mathrm{WGM}}}}{2} \\ 0 & 0 & \dots & & & \frac{\hbar\Omega_R^{N_{\mathrm{WGM}}}}{2} & E_c^{N_{\mathrm{WGM}}} \end{pmatrix} \tag{4.19}$$

This matrix is block diagonal: we can diagonalize each block via the Hopfield method, in the end, we obtain $2 \times N_{\mathrm{WGM}}$ eigenenergies with corresponding set of Hopfield coefficients. The energy spectrum of a four-WGMs cavity is depicted in figure 4.4 (a).

Note that the dimension of the polariton Hilbert space (number of polariton branches) is open to discussion [258]. Two formalisms are encountered in the literature: one single Hamiltonian with a dimension equals to the sum of photonic modes and excitonic resonances $(N_x + N_c) \times (N_x + N_c)$, involving the appearance of mid-polaritons branches [259–261], or a set of independent Hamiltonians (one for each photon mode) with a dimension equal to $(N_c N_x + N_c) \times (N_c N_x + N_c)$ [262, 263]. Transitions between these two situations can appear for different experimental realizations [257]. Here, we clearly have chosen the second option to describe our system, a Hilbert space consisting in N_{WGM} independent sub-spaces.

4.1.4.2 Anticrossing with the exciton line

The anticrossing between the UPs and LPs for a multimode polariton and single polariton case is illustrated in figure 4.4 (a) and (b), forming the hallmark of strong coupling. In deeply etched structures, the UP branch is not visible in experiments [73, 76, 264, 265]; and our work in this thesis indicates that the same is true in our disk. This is in contrast to historical 2D planar cavities. As a consequence, we had in this thesis to rather analyze the anti-crossing between the LP and the exciton line, the latter turning out by chance to in contrast visible. The reason for UPs to be hardly visible on the PL spectra, and difficult to access by other emission means is until today not perfectly understood. Our interpretation

1. The cavity modes are orthogonal, hence each cavity mode will couple finally to a single excitonic mode; giving birth to orthogonal polariton sub-spaces. In practice, because we took $\omega_{m',p'} \simeq \omega_x$, we will no further differentiate the excitonic modes and consider that we have a single excitonic mode coupled independently to a set of WGMs

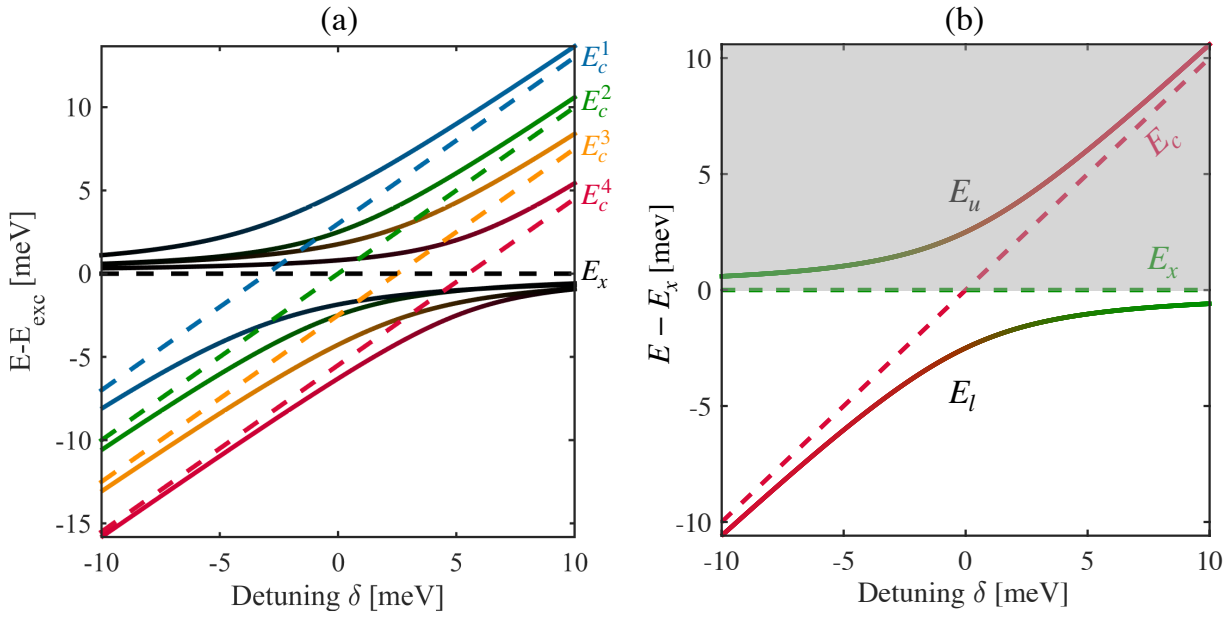

Figure 4.4 – (a) Polaritons branches produced by the coupling of four cavity modes with one exciton. The black dashed curve is representing the energy of the exciton, considered fixed, and the colored dashed curves the energy of the cavity modes, as a function of the cavity-exciton detuning. The plain lines are the UP/LP branches, the color code indicates the excitonic fraction of each of the four polaritons from black ($X^2 = 1$) to blue, green, orange or red ($X^2 = 0$). The cavity modes are not degenerated and their Rabi coupling to the exciton are different. $[E_c^1 - E_x, E_c^2 - E_x, E_c^3 - E_x, E_c^4 - E_x] = [\delta + 3, \delta, \delta - 2.5, \delta - 5.5]$ meV - $[\Omega_R^1, \Omega_R^2, \Omega_R^3, \Omega_R^4] = [1.2 \cdot \Omega_R, \Omega_R, 1.1 \cdot \Omega_R, 0.9 \cdot \Omega_R]$ with $\Omega_R = 5$ meV. (b) Illustration of the anticrossing with the exciton line

builds on different remarks:

- The bare exciton line remains observable in PL, even in the polariton regime for WGMs. Some exciton emission does not pass through WGMs and couples to other electromagnetic modes, enabling collection, (inefficient) in confocal configuration for example.

- At such small disk diameters, confined electromagnetic modes, like WGMs, are probably coupled to the free 3D electromagnetic continuum through geometric irregularities of the disk.

- Polaritons tend to relax towards the lowest energy states available: UPs should in any case have a weaker PL signal compared to LPs [225, 266].

- In order to observe polaritons, we collected signals using the suspended waveguide located close to the disk. Those waveguides, by construction, also contain the MQW structure: they can hence absorb photons at high energy and emit photons at the

energy of the exciton.

These remarks call for further investigations, but they show that we had direct experimental access to the exciton line even in the polariton regime. The anticrossing of LPs with the exciton line (as represented in figure 4.4 (b)) served us as a mean to investigate the strong exciton-photon coupling regime.

4.2 Observation of the strong coupling

We start this section by focusing on PL measurements: those are performed at cryogenic temperatures (3 to 4K) using our pulsed-tube cryostat. The excitation beam is provided by our continuous-wave Ti:Sapphire laser (energy 1.530 eV), focused with a cryogenic microscope objective onto a $\sim 2\mu$m radius spot (see chapter 3). The beam waist was measured using knife-edge techniques in reflection [267]. To increase the collection of polaritons emission, and prevent the inadequate spatial filtering caused by the radiation pattern of WGMs, we use the suspended waveguides integrated on-chip in the vicinity of the disk. In this configuration (see figure 3.4 (b)) the waveguides act like antennae, collecting the emitted light of the hybrid exciton-photon system. μ-lensed fibers are then located at the tips of the waveguides to extract the light from the cryostat up to photodetectors.

In order to experimentally prove the polaritonic nature of the different signals observed in the PL or resonant waveguide transmission signal, the latters need to present the characteristic anti-crossing with the exciton line. To vary the exciton detuning $\delta = E_c - E_x$ we chose two strategies: use the temperature to tune simultaneously the cavity and exciton modes, and tune the cavity energy by slightly varying the radius of the disk.

4.2.1 Exciton and Cavity energy variation in function of temperature

By increasing the temperature at the sample holder inside the cryostat chamber, we observe a redshift in energy of both the exciton and the WGMs, as shown in 4.5-(a). The variation of the MQW excitonic energy with temperature is in agreement with theoretical prediction based on three different models: Varshni (eq. 4.20), Viña (eq. 4.21) and Passler (eq. 4.22) [200, 268, 269]:

$$E_x(T) = E_x(0) - \alpha \frac{T^2}{\beta + T} \tag{4.20}$$

$$E_x(T) = E_B - a_B \left[1 + \frac{2}{\exp(\Theta_b/T) - 1} \right] \tag{4.21}$$

$$E_x(T) = E_x(0) - \frac{\alpha\Theta}{2} \left[\sqrt[p]{1 + \left(\frac{2T}{\Theta} \right)^p} - 1 \right] \tag{4.22}$$

Those models were originally proposed to compute the energy of the bandgap in semiconductor materials, but they also operate for the energy of QW excitons [270]. The model of Varshni, the oldest one, is purely empirical: $E_x(0)$ is the energy of the exciton at 0 K, and α and β are fitting parameters to be determined. Viña's model is a semi-empirical model based on the Bose-Einstein distribution: $E_B - a_B$ is the energy at 0 K and $\Theta_b \equiv \hbar\omega/k_B$ is an effective phonon energy, expressed on the temperature scale. The last model, Passler's, is also a semi-empirical theory: it takes into account the effect of lattice expansion and electron-phonon interactions on the gap energy. $E_x(0)$ represents the exciton energy at 0 K, α is the high-temperature limit of the forbidden entropy, Θ the effective average phonon temperature, and p a parameter related to the electron-phonon spectral function. The fitting results for these three models are grouped in Table 4.1. They all lead to a good agreement with experimental data, notably Vina's and Passler's models. For the rest of the thesis, we choose to fit the exciton energy variations with the model of Viña, as shown in figure 4.5 (a), since it uses only three fitting parameters instead of four for Passler's.

Model	Parameters				
Varshni	$E_x(0)$ [eV]	α [$\times 10^{-4}$ eV/K]	β[K]	...	r^2
	$1.4732 \pm 4.41 \times 10^{-6}$	11.999 ± 2.2	998.9 ± 195.5	...	0.981
Viña	E_B [eV]	a_B [eV]	Θ_b [K]	...	r^2
	$1.4832 \pm 3.51 \times 10^{-5}$	$0.01033 \pm 3.57 \times 10^{-5}$	109.29 ± 0.165	...	0.998
Passler	$E_x(0)$ [eV]	α [$\times 10^{-4}$ eV/K]	Θ [K]	p	r^2
	$1.4729 \pm 1.13 \times 10^{-6}$	1.8354 ± 0.012	85.58 ± 0.54	3.442 ± 0.15	0.999

Table 4.1 – Fitting parameters for the Varshni, Viña and Passler models, r^2 represents the correlation coefficient, the values are indicated with 95% confidence intervals

The redshift of the optical WGMs when temperature increases is mostly due to the refractive index variation (thermal expansion of the disk is negligible in comparison). Modeling these thermo-optic variations at cryogenic temperature is a tricky task: the effect of temperature on the semiconductors refractive index and in particular of GaAs was the subject of many publications [271–275]. In these works, the refractive index is given in form of a Sellmeier equation with a varying number of poles. The parameters involved in such an equation are usually measured far from our cryogenic temperatures (T$\simeq 3-4$ K). To our knowledge, no model is available to describe the variation of GaAs refractive index in our range of temperatures. Additionally, since we study WGMs that are quite close in energy we decided to disregard the impact of wavelength and simply model the evolution of the refractive index as a Taylor expansion function of the temperature:

$$n = n_0 + A_1 T + A_2 T^2 + A_3 T^3 + ... \tag{4.23}$$

where n_0 represents the value of the refractive index at 0 K and A_1,A_2,A_3 are fitting parameters to determine. We then choose an approximate relation for the WGMs resonant wavelength of the disk cavity :

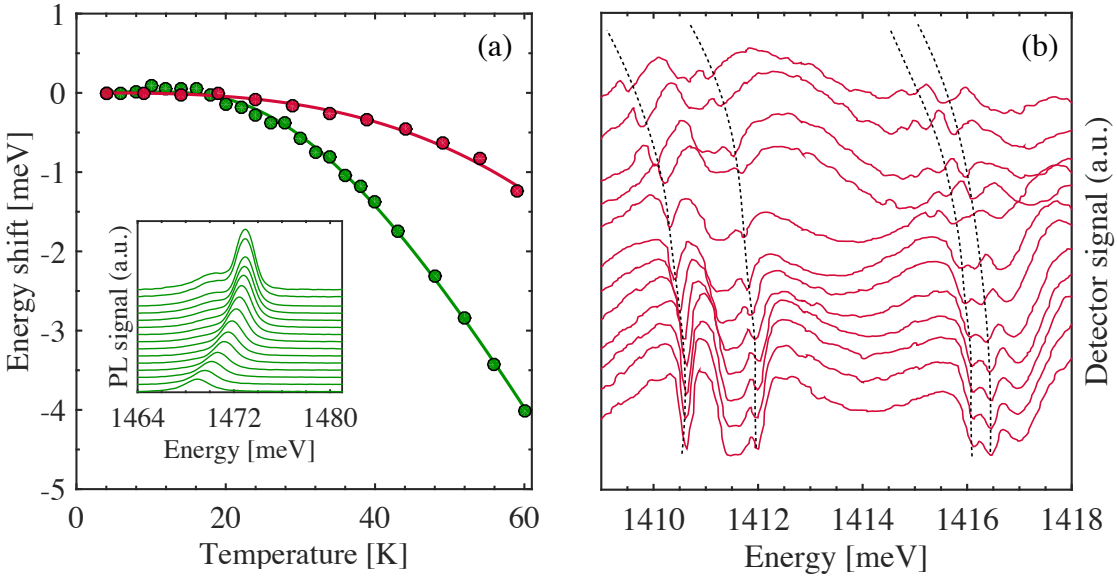

Figure 4.5 – (a) Fitting models for the energy shift of the exciton (E_x - green) and the WGMs (E_c - red) energies according to the temperature. Dots: Experimental data - Green Solid line: Viña's Model ($r^2 \simeq 0.999$) - Red Solid line: custom model ($r^2 \simeq 0.992$). Inset: Confocal μPL spectra taken at different temperature inside the cryostat, spectra shifted for clarity. (b) WGMs transmission spectra taken by varying the temperature in cryostat, the spectra had been shifted for clarity, the black dotted lines are guides to the eye.

$$2\pi R n_{\text{eff}} \simeq m\lambda \tag{4.24}$$

where m is the azimuthal number of the considered WGM, R is an effective radius of the disk, and n_{eff} the effective index of the disk slab layer. Expressing this last condition in terms of energy leads to a custom expression for the temperature variation of a WGM energy :

$$E_c^{\text{WGM}} = \frac{mhc}{2\pi R} \frac{1}{n_{\text{eff}}^0 + A_1 T + A_2 T^2 + A_3 T^3 + ...} \tag{4.25}$$

Stopping the development at the cubic power leads to a good agreement with our experimental data as shown in figure 4.5 (a). We used this model to fit the variations of more than 20 distinct WGMs, and the values extracted for fitting parameters A_1,A_2, and A_3 were always agreeing with relative variations under 5 %. The WGMs used to test this model had to be quite far from any excitonic resonance in our experiments in order to avoid the influence of the MQW on the energy variations. In figure 4.5 (b) we present the waveguide transmission spectra showing resonances of different WGMs, as function of temperature. The modes are spectrally separated by 20 to 30 meV from the MQW exciton, and therefore behave as pure cavity modes (polaritonic effects can be neglected).

4.2.2 Cavity energy variation as a function of the disk radius

The second tuning parameter employed is the dimension of the disk, upon which WGMs are extremely sensitive. Increasing the radius R of the cavity provokes a decrease in WGMs eigenenergy. To quantify this variation we use two methods. The first one is to model the evolution of eigenenergies directly by FEM, as presented in figure 4.6(a). With the COMSOL software, we predict an almost perfect linear variation of the energy with the radius with the same slope for three investigated WGMs, equal to -0.62 meV per nm. Similar results are obtained using the effective index method presented in section 2.1.3. The second method is based on PL measurements using a pump laser diode ($\lambda = 810$ nm) at high power to reach the lasing threshold. Using a high excitation power and a sample that only contained one QW, guarantees that we are in the exciton-photon weak coupling regime. By precisely measuring the wavelength of the lasing signal, we deduce the spectral position of the cavity mode, as shown in figure 4.6(b) and (c). Competition is present between several WGMs: by tracking the lasing spectrum as a function of each disk radius, we can plot the evolution of the energy for each WGM. From these results, we also infer a linear variation of the WGMs eigenenergies with the radius. The slope, however, varies from mode to mode and is smaller between -0.2 and -0.4 meV per nm.

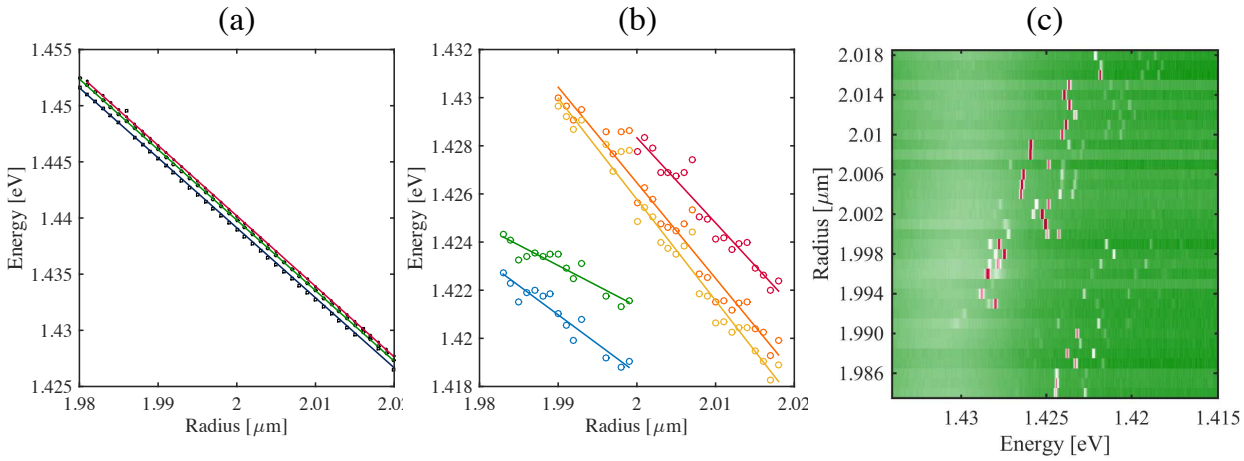

Figure 4.6 – (a) Variation of different WGMs energies as a function of the disk radius calculated with COMSOL, for a disk thickness of 200 nm. Solid lines are linear fits : Green TE, $m = 41$, $p = 1$, $r^2 = 1$ - Red TE, $m = 32$, $p = 3$, $r^2 = 1$ - Blue TE, $m = 36$, $p = 2$, $r^2 = 0.997$. Black markers are FEM computed. (b) Cavity modes energies deduced from (c) as a function of the disk radius. The colored solid lines are linear fits ($r^2 \simeq 0.9$) and the colored open symbols the experimental values. (c) PL lasing map as a function of microdisk radius. Laser excitation power > 2 mW

From a practical point of view, it is hard to control the size of the disk at the nm scale, which is below e-beam lithography and nano-fabrication resolution (which explains the fluctuations observed in figure 4.6 (b)). The sample contains a distribution of different disks designed to have a radius varying by step of 1 nm: in this way even if the radius variation between two neighboring disks is not perfectly respected, the evolution of WGMs eigenener-

gies, at the scale of the whole sample, will still follow in average the expected evolution. This systematic radius variation on the sample, allows us to work with the same set of WGMs, but with slightly varying initial detuning $\delta_0 = \delta(T = 4K)$.

These imperfections in the fabrication process might mitigate the 1 nm variation per disk. This can explain the different values obtained for the slope in figure 4.6. The fact that the WGMs observed in the PL spectra are probably different from the one simulated explain also this discrepancy.

4.2.3 Lower Polaritons PL spectrum variations and Hopfield model fit

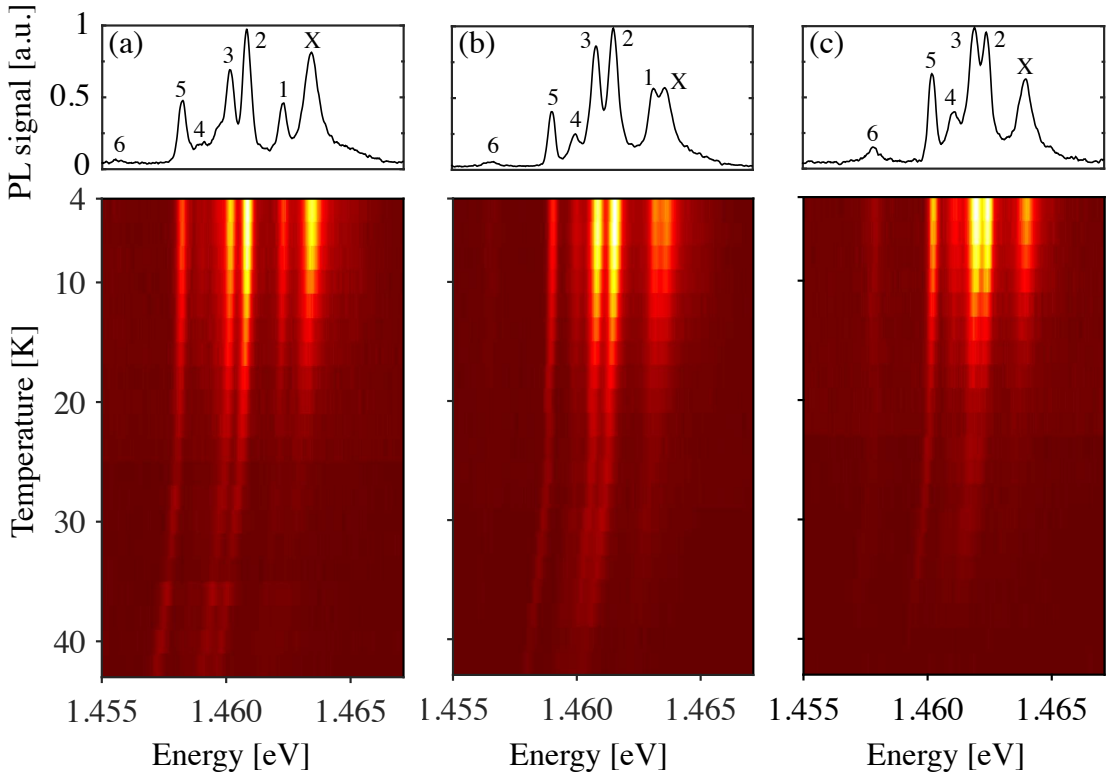

Figure 4.7 – PL signal as a function of temperature for 3 different disks of slightly decreasing radius ((a) $R = 1.992\ \mu m$ (b) $R = 1.989\ \mu m$, (c) $R = 1.984\ \mu m$). The top panels represent the spectrum of each disk at 4 K, exhibiting the exciton signal (labeled as X), as well as several lower-polariton lines (labeled with numbers). In the 2D maps the temperature starts at 4K (top), and is then incremented in steps of 2K.

Figure 4.7 presents PL maps measured for three disks of different diameters, acquired by varying the temperature inside the cryostat [276]. The PL is excited confocally by a non-resonant laser at $\lambda = 810$ nm, and the emission signal is collected through the suspended waveguides in the near-field of the disk. The spectrum located at the top of each

map is the initial spectrum taken at 4 K. The maps exhibit several peak features: the exciton line (labeled as X), and the emission lines of six different LP branches labeled in order of increasing detuning to the exciton (decreasing excitonic fraction X^2). Each LP branch corresponds to a different WGM. When the radius of the disk decreases, the energy of the WGMs increases and the detuning δ_0 between WGMs and exciton increases. Consequently, a gradual blueshift of the different LPs lines is observed. On the last map, the LP1 branch seems to vanish: in fact for increasing detuning, LPs are adopting a more pronounced exciton character, hence their PL signal will merge with the signal of the exciton.

To ensure that the different signals we observe are polaritons, we used the Hopfield model to reproduce our observations on the different LP branches, as a function of disk radius and function of temperature. We model the evolution of the eigenenergies of UPs and LPs with temperatures according to:

$$E_{u/l}(T,m,p) = \frac{1}{2}\left(E_x(T) + E_c(T,m,p) \pm \hbar\sqrt{\delta^2(T,m,p) + \Omega_R^2(m,p)}\right) \tag{4.26}$$

where the $\pm$ sign stands respectively for UPs/LPs, and Ω_R^2 represents the Rabi splitting between the exciton and WGM (m,p). The energy variation of the cavity (E_c) and the exciton (E_x) with temperature are given by the above mentioned models (figure 4.5 (a)). In eq. (4.26), we efficiently neglect the effect of the radial number p in the temperature variation. Without assuming a precise model for Ω_R at first level (it can actually be calculated as we show in section 2.5), we are at first sight let with a fitting model only containing two independent fitting parameters, the Rabi splitting Ω_R and the azimuthal number m, for each polariton branch. By slightly varying the radius of the disk, we vary the initial detuning $\delta_0 = \delta(4K)$. Since the value of the Rabi splitting is almost identical for disks of similar radii, like the three disks considered here, we can fit simultaneously the data coming from the three disks, and taking $\Omega_R^2(m)$ as a common parameter, letting the azimuthal number m as a free parameter for each individual LP branch.

Radius R	δ_0 of LP2 [meV]	δ_0 of LP3 [meV]	δ_0 of LP5 [meV]
1.992 μm	1.6897	- 0.9435	- 1.2041
1.989 μm	3.3248	0.2741	0.0390
1.984 μm	5.3273	2.0049	1.7335

Table 4.2 – Evolution of the exciton-cavity initial detuning as function of radius, for different LP modes 2,3 and 5.

Figure 4.8 presents the evolution of the LPs energy with temperature for the three different disks of different radius, for three different modes (LP2, LP3 and LP5) [276]. The data are fitted by the Hopfield model taking into account five different disks (only three are represented here for convenience). We see the influence of cavity radius on the detuning: decreasing the radius increases the initial detuning δ_0 at 4 K (see Table 4.2). According to

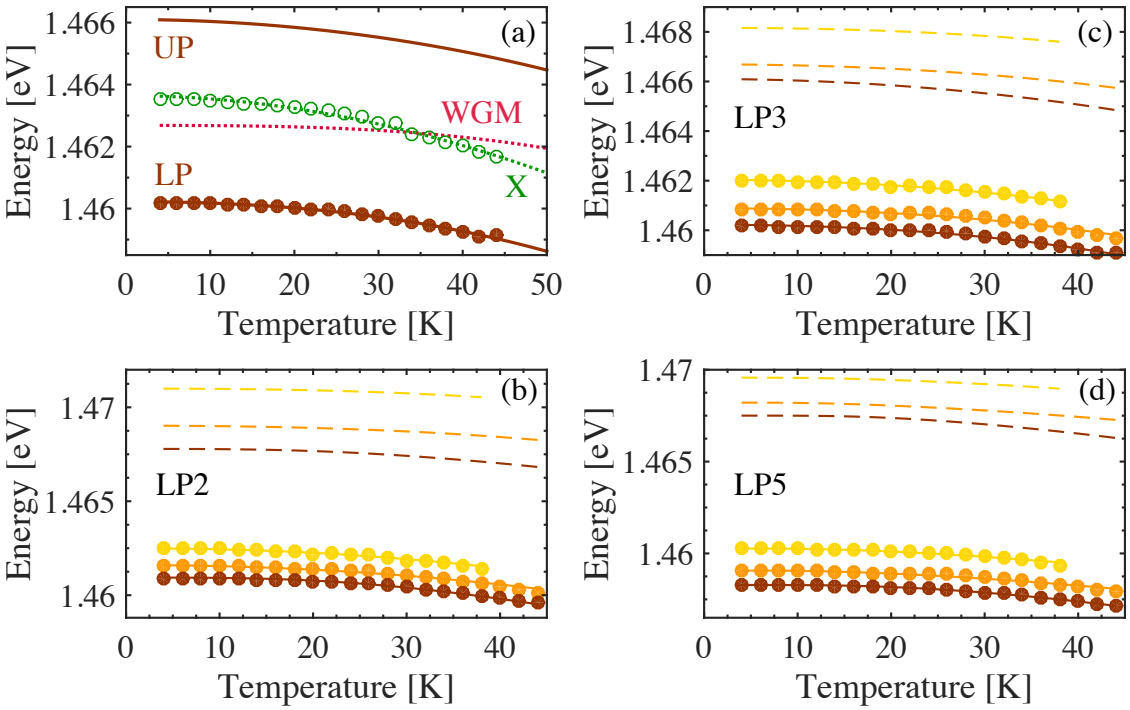

Figure 4.8 – (a) Exciton/LP3 PL peak energy as function of temperature. Brown circles: Measured LP2 emission energy; Solid brown line: LP fit derived from the Hopfield model; Dashed brown lines: UP line derived from the Hopfield model; Open green circles: Measured exciton emission energy; Dotted green line: Exciton fit model; Dotted red line: WGM fit model - $R = 1.992\ \mu m$. (b)-(c)-(d) LP2, 3 and 5 PL peak position as function of temperature for 3 disks of decreasing radius (Brown $R = 1.992\ \mu m$ - Orange $R = 1.989\ \mu m$ - Yellow $R = 1.984\ \mu m$). Solid Lines: LP; Dashed Lines: UP branches predicted by Hopfield model; Plain circles: Experimental data

the sign of δ_0, an anticrossing may, or may not, be observed as illustrated in 4.9.

Potential improvement of the employed Hopfield fitting model is possible by taking into account the dissipation of the system to write the complex eigenenergies (eq. (1.35)):

$$\begin{aligned}\tilde{E}_{u/l}(T,m,p) =& \frac{1}{2}\left[(E_x(T)+E_c(T,m,p)) - j\hbar\left(\kappa_c(T,m,p)+\kappa_x(T)\right)\right] \\ & \pm \frac{\hbar}{2}\left[\sqrt{\left[\delta(T,m,p) - j(\kappa_c(T,m,p)-\kappa_x(T)\right]^2 + \Omega_R^2(m,p)}\right]\end{aligned} \tag{4.27}$$

Such a dissipative model requires the knowledge of both the exciton and cavity linewidth, their variations with temperature. If the information on the linewidth of the exciton is easily accessible, it is far more complicated for the cavity modes. In our experimental configuration, the linewidth we measure on the WGM signals certainly include information about the intrinsic losses of the WGM κ_c but, also information on the extrinsic losses i.e. the coupling of the WGM to the waveguide. κ_c is different for each WGM, a rough estimation being here

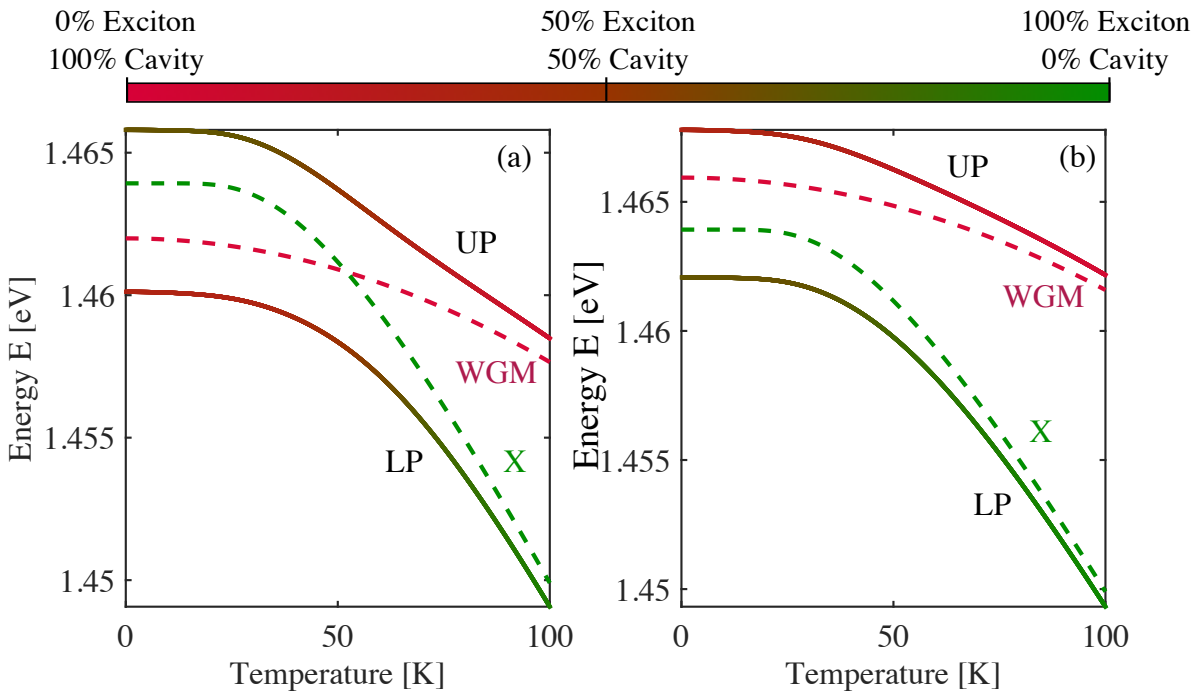

Figure 4.9 – Energy dispersion of the exciton (X) in our system, of a WGM of our disk, and of UP/LP branches according to the Hopfield model (a) Negative initial detuning ($\delta_0 \simeq -2$ meV) (b) Positive initial detuning ($\delta_0 \simeq 2$ meV). UP and LP lines are color-coded according to the excitonic Hopfield coefficient. Green : exciton (X) - Red : WGM. Ω_R =5 meV

comprised between 0.2 and 0.3 meV. Taking this into account leads to an underestimation of the Rabi splitting by 6% for κ_c =0.3 meV, $\tilde{\kappa}_x$ =2 meV and $\Omega_R = 5$ meV.

LP mode	n°2	n°3	n°5
Ω_R [meV]	6.64	5.79	9.14

Table 4.3 – Rabi Splitting energy extracted from the fitting of the PL signal

Comparison of inferred Rabi-splitting with theoretical expectation The Rabi splitting values extracted from the Hopfield model of our data are listed in table 4.3. These values can be compared to those obtained by the theoretical model introduced in section 2.5. For the 5-QW structure and for the WGMs employed here, this model leads to values of $\hbar\Omega_R = 2 \cdot \hbar g_{cx}$ between 6.4 meV and 10.2 meV. The value found experimentally are lower than expected (typically 10-20%). Several explanations are possible to account for this difference. Imperfections in the fabrication/design of the wafer, ultimately responsible for a decrease of the QWs oscillator strength, reduce the Rabi-splitting energy. The material parameters (effective masses, Kane energy...) used in the calculation of Rabi energy depends on the epitaxial growth, different estimations are found in the literature leading to relatively large value interval for the Rabi energy. Also, as mentioned above disregarding

the dissipation lead to an underestimation of Ω_R from our experimental data.

We present in figure 4.10 complementary PL maps measured for seven disks of different diameters, acquired by varying the temperature inside the cryostat. These measurements can be split into two sets: first set (figure 4.10 (a) to (e)) is acquired with the same experimental conditions as the ones used to obtain figure 4.7, the radii of the disks are different; for the second set (figure 4.10 (f) to (i)), a higher excitation is used (7 times more powerful with respect the power used before), allowing to keep track of the PL signal at a higher temperature. Nevertheless, using a power this high brings us close to lasing-related phenomena, a regime where exciton-exciton or polariton-polariton interactions can occur, and the energy dispersion of the polariton branches is likely to change (see section 4.3).

4.2.4 Waveguide transmission spectrum for direct resonant spectroscopy of polaritons

Figure 4.11 (a) shows the LPs energy measured on a disk using two different configurations: Non-resonant confocal excitation PL and collection via the waveguides, and resonant spectroscopy through the waveguide (illustrated respectively in figure 3.4 (b) and (c)). One waveguide optical transmission spectrum for T=4 K, obtained using resonant spectroscopy is illustrated in figure 4.11 (b). Small differences appear between the two sets of results, explained by the fact that the energies are not measured by the same apparatus (not calibrated identically). Apart from this effect, the temperature variations seem to be consistent in both configurations, as well as the energy separation between the LP branches. Both configurations have benefits and drawbacks. In the resonant laser spectroscopy configuration, one advantage is to collect a larger number of LPs signals: indeed LPs that are strongly negatively detuned behave almost as pure photonic cavity modes and are consequently hardly visible in PL spectrum. In resonant laser spectroscopy through the waveguide we resolve them, explaining why in figure 4.11 some signals are only present using this configuration. However, the MQW is also present in the plane of the waveguide, resulting in an absorption of the light of the tunable laser, and mitigating the resolution of the exciton signal. Moreover, because of this absorption, a non-negligible quantity of the injected light is lost, and it is hard to estimate the fraction of the power that makes its way to the disk WGMs. Finally, we choose the second experimental configuration (figure 3.4) most of the time since it leads to a cleaner signal.

Let us summarize: in figure 4.8 (a) we did observe the LP-exciton anti-crossing for LP3, and fitted it with Hopfield model. We tested this behavior as function of detuning in figure 4.8 (b). We extended this observation to several other LP branches and showed two of them in figure 4.8 (c) and (d). The measured Rabi energy was consistent with our independent theoretical model of section 2.5. Similar observations were made in PL and resonant spectroscopy. This all forms a solid level of proof that strong coupling polariton particles are indeed present in our WGM resonators.

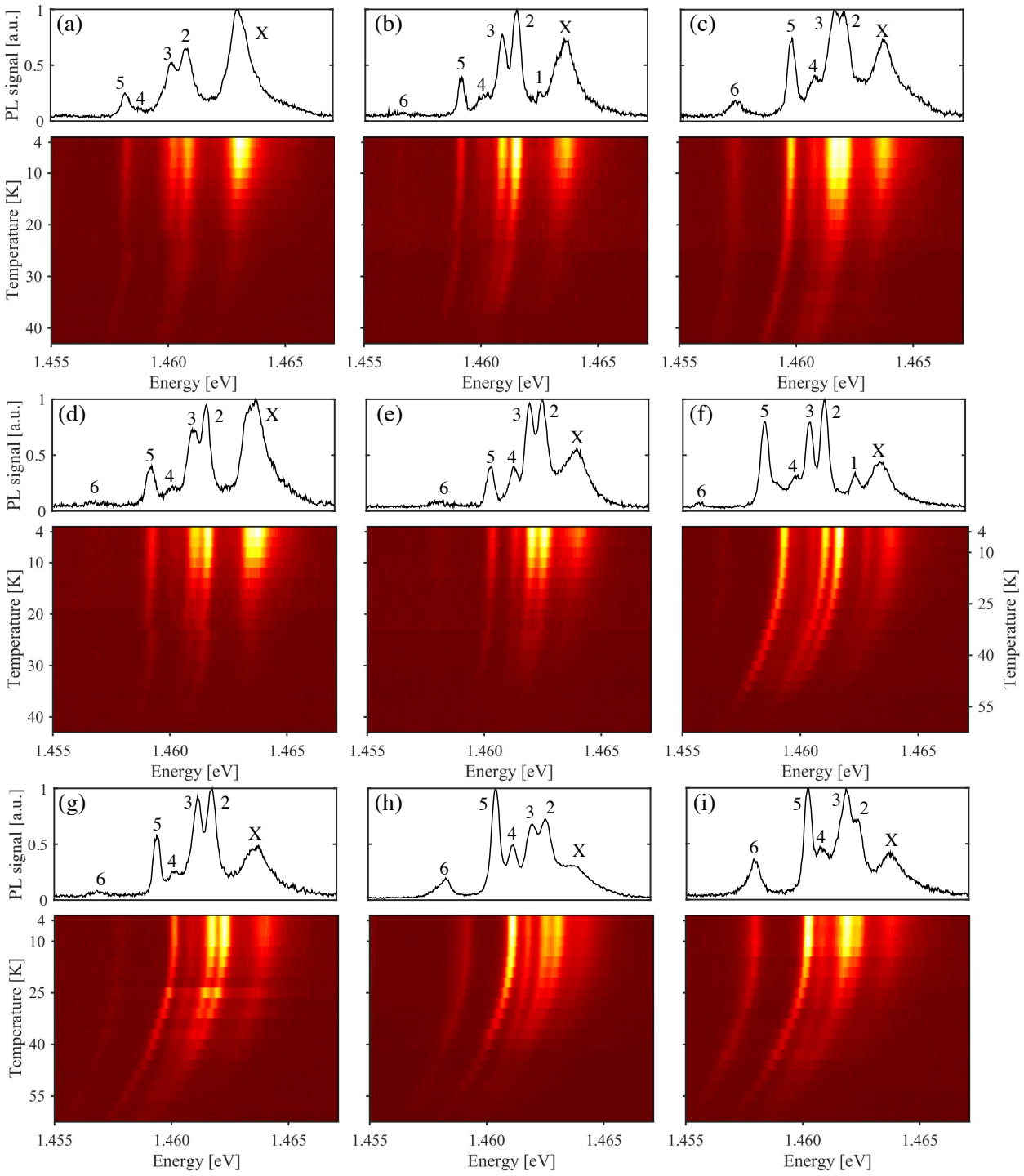

Figure 4.10 – PL signal as a function of temperature for 7 different disks of varying radius ((a)/(g) $R = 1.991\ \mu m$, (b) $R = 1.990\ \mu m$, (c) $R = 1.988\ \mu m$, (d) $R = 1.986\ \mu m$, (e)/(h) $R = 1.985\ \mu m$, (f) $R = 1.992\ \mu m$, (i) $R = 1.984\ \mu m$. The top panels represent the spectrum of each disk at 4 K, exhibiting the exciton signal (labeled as X), as well as several lower-polariton lines (labeled with numbers). In the 2D maps (a) to (e) the temperature starts at 4K, and is then incremented in steps of 2K. For the maps (f) to (i) the temperature starts at 4K, and is then incremented in steps of 3K.

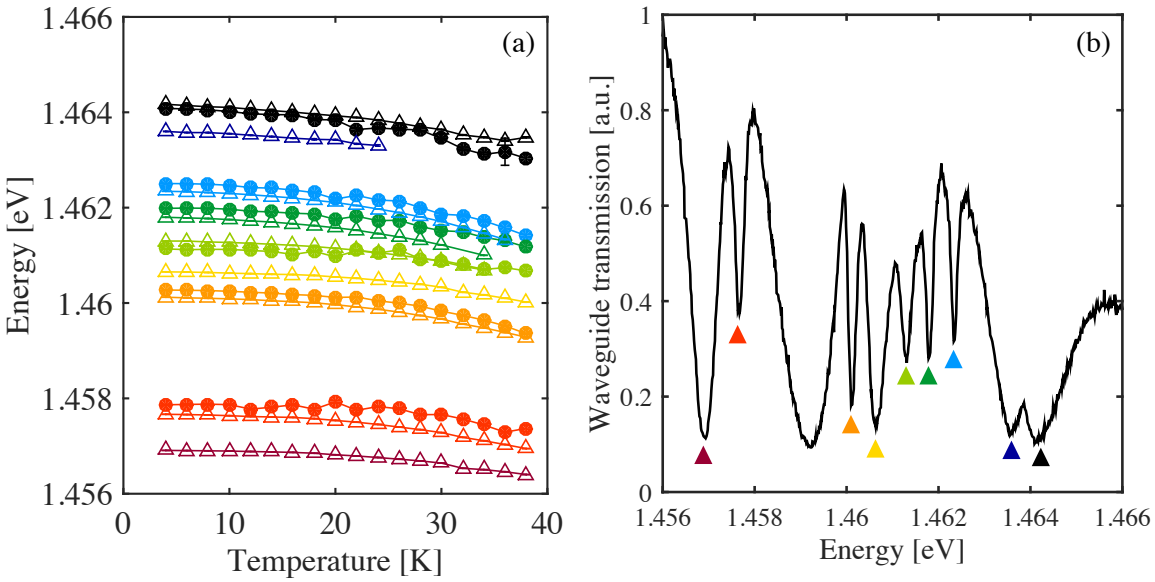

Figure 4.11 – (a) Energy variation of eight LP branches as function of temperature, for a disk with $R = 1.984\ \mu m$ and the 5-QW structure. Circles : Measured through PL emission using the second experimental configuration (section 3.1). Triangles : Measured resonant laser spectroscopy using the third experimental configuration (section 3.1). Black: exciton. Each color signal corresponds to a different LP. The thin solid lines are guides to the eyes. (b) Waveguide optical transmission spectrum at 4 K for the same disk. The triangle markers highlight the exciton and LPs, the colors used correspond to the ones in (a).

4.3 Polariton lasing

Here we address another particular feature of the polaritonic regime, the phenomenon of polariton lasing. When exciting non resonantly the semiconductor microcavity at higher energy, polaritons can exhibit peculiar kinetics. Generated electron-holes lose their coherence and start to populate the exciton reservoir. Polaritons will finally populate the lowest energy states by overcoming the bottleneck effect (a moment where phonon scattering is no more efficient, but other mechanisms such as polariton/free-carrier interaction or polariton/polariton interaction take over. [277–281]): the density of polaritons in the lowest states therefore increases. If this density remains below the saturation density $n_{sat} \simeq a_{B,2D}^{-2}$, polaritons behave almost as bosons. For a high enough pump power, the population in the lowest states can be macroscopic and polaritons start to condensate: this is the regime of polariton lasing, also dubbed non-equilibrium polariton condensate [282, 283].

A polariton condensate can emit coherent light very much like a laser. The corresponding threshold is however not given by a population inversion condition, and can be significantly lower than the one required for conventional photon lasing. In semiconductors, evidence of polariton lasing is accompanied by the appearance of a second threshold, at higher excitation power, corresponding to the occurrence of conventional photon lasing [76, 284]. This transition happens for high density, where excitons are dissociated into an electron-hole

plasma (bleaching). The mechanisms responsible for such dissociation are multiple [285]: *Phase-space filling*: electron and hole states out of which excitons are created are all filled, excitons cannot be created; *Screening*: degradation of the electron-hole interaction due to the presence of other carriers; *Exchange interaction*: carriers with the same spin avoid each other.

4.3.1 Bose-Einstein condensation of polaritons

The pioneering works of Einstein [286] and Bose [287] on a dilute gas of bosons has put forward the existence of a critical temperature below which bosonic stimulation and condensation occurs (quantum phase transition) [288] :

$$T_c = \Big(\frac{n}{2.612L^3}\Big)^{2/3}\frac{2\pi\hbar^2}{mk_B} \tag{4.28}$$

in a three-dimensional system, with L the typical dimension of the system. This temperature is inversely proportional to the mass m of the bosonic particles. Famous experimental demonstration of this Bose-Einstein Condensate (BEC) was realized on alkali atoms [289] at extremely low temperature $\simeq$ 200 nK. The condensation temperature can be increased by using bosons of lower mass. Due to their partial photonic nature, polaritons inherit a really low effective mass, 10^9 times smaller than the rubidium atoms [290], making them suitable candidates for the observation of BEC at regular cryogenic temperature or even room temperature.

The historical BEC models consist in noninteracting bosons albeit the Boson gas must adopt a well define temperature T. In true experiments bosons do interact: in the case of polaritons, the interaction comes from exciton-exciton interaction (charge interaction), since photons themselves do not interact with one another. The exciton/photon Hamiltonian taking into account excitonic interactions is given by [72, 291]:

$$\begin{aligned}\hat{H}_{cx}^{int} + = \hbar\omega_x\hat{d}^\dagger\hat{d} + \hbar\omega_c\hat{a}^\dagger\hat{a} + \hbar g_{cx}(\hat{a}^\dagger\hat{d} + \hat{a}\hat{d}^\dagger)\\ + \frac{\hbar g_{exh}}{2}\hat{d}^\dagger\hat{d}^\dagger\hat{d}\hat{d} - g_{pae}(\hat{a}\hat{d}^\dagger\hat{d}^\dagger\hat{d} + \hat{a}^\dagger\hat{d}^\dagger\hat{d}\hat{d})\end{aligned} \tag{4.29}$$

The first term of the second line corresponds to the Coulomb exchange interaction between excitons, while the second term is called photon-assisted exchange scattering, or phase-space filling. It represents the annihilation/creation of two excitons accompanied by the creation/annihilation of a pair of exciton and photon: this last term reduces the Rabi splitting, and leads to a blue-shift of the LP and a red-shift of the UP [292]. From that Hamiltonian one can derive the Heisenberg equations of motion in the exciton/photon basis, and reach the Gross-Pitaevskii set of equations similar to those employed in atomic condensates [288, 290]. Despite all these similarities, polariton condensation differs from atomic BEC notably. Indeed, polariton lifetimes are usually very short, continuous pumping is required to maintain polariton condensates steadily alive for a time longer than decay times of the system.

4.3.2 Experimental observation

Figure 4.12 groups the emission energy and intensity of all LP modes of a disk, as a function of the pump power P, measured in the confocal excitation path just before impinging on the disk. Different regimes can be observed: For $P < 100\ \mu W$, as the power increases we observe a slight increase in the PL signal, with relatively constant emission energies. For $100\ \mu W < P < 800\ \mu W$ (gray shaded area in figure 4.12), we observe sharp nonlinear increase of the different PL signals, together with a pronounced blueshift on the energies. This behavior is consistent with a signature of polariton lasing, where the blueshift is the consequence of the polariton-polariton interactions. In this regime, we observe a rise in the signal intensity of LP modes when decreasing energy: this effect was were not visible in the prior spectra at lower excitation power. This is consistent with the idea that as polaritons become more numerous, they will tend to populate lower energy states, involving some scattering mechanisms. This regime seems only prevail for a certain range of excitation power, and for $P > 800\ \mu W$, the signal intensity starts to decrease and the energies come back to their initial value. It is our understanding that it is due to an overpumping of the sample (experiments are performed under continuous pumping), which would deteriorate the polaritons through heating or generation of an electron-hole plasma. One way out would then be to chop our pump signal: it may mitigate heating and stabilize the polariton lasing regime at higher power. In our present set of experiments, we observed an increase of emitted signal by one order of magnitude before losing the regime.

How to be sure that what we observe is actually polariton lasing? It has been an open question for many years in the polariton community [293–295]. As a matter of fact, an emission blueshift is not enough to prove the persistence of the strong coupling regime, at variance with the observation of a second threshold at higher excitation density. The fact that we do not observe this second threshold is questioning. In a MQW case bleaching (transition to a plasma) is expected to appear at higher power compared to a single QW, since the exciton density is distributed over several QWs, still we should be able to observe it.

In order to gain understanding, we also performed power-dependent experiments on another type of sample with embedding a single QW with a higher fraction of indium (13%). We do believe that this sample always operates in the weak coupling regime: we do not observe emission branches at low excitation power and energy lower than the exciton, and we observe a lasing behavior at high excitation power, which is understood as a regular photonic lasing. The results of this experiment, performed at varying temperatures are presented in figure 4.13. The observed observed is typical of a regular photon laser: above a certain power threshold, the intensity rises sharply (figure 4.13 (a)) and the linewidth decreases (figure 4.13 (c)). We notice that the power lasing threshold, which slightly increases when we increase the temperature, is almost an order of magnitude higher than in the strong-coupling case with the 5-QW structure, consistent with the fact that polariton lasing occurs at lower excitation. However, we still observe a blueshift of the emission (figure 4.13 (b)), indicating that exciton-exciton interactions still take place. Note that we are not losing this regime even at higher power, up to $10^4\ \mu$W..

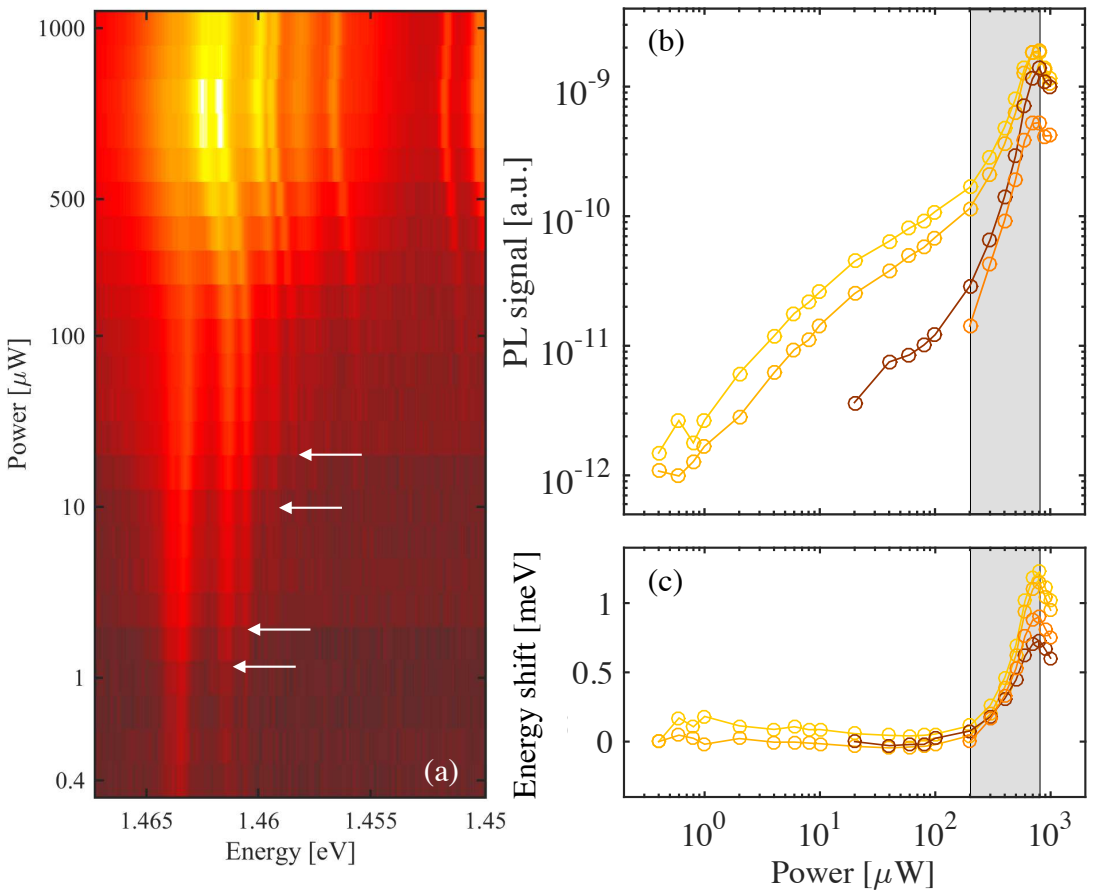

Figure 4.12 – (a) Map of emission spectra of a GaAs disk embedding a 5-QW heterostructure (same as before) as function of pump power. (b) Emission signal intensity (log-log scale) and (c) emission energy of different LP modes as function of the excitation power, extracted from the map (a) and indicated by the white arrows. The colors brown to yellow indicate LP modes with an increasing energy, i.e. with an increasing excitonic fraction

This series of experiments does enable us able to be perfectly conclusive. On one hand, we observe a lower lasing threshold and a stronger blueshift in the strong coupling sample embedding 5 QWs, but we do not observe a second threshold. On the other hand, a single QW sample showing photon lasing also exhibits a blueshift in the emission. To advance in understanding and confidence on polariton lasing, we should estimate and model the polariton density in our device and compare it to the saturation density. A conclusion can be drawn from this information. The discussion of the different lasing regimes is illustrated in figure (d). A further study on the lasing regime at different cavity-exciton detuning will also bring us more information.

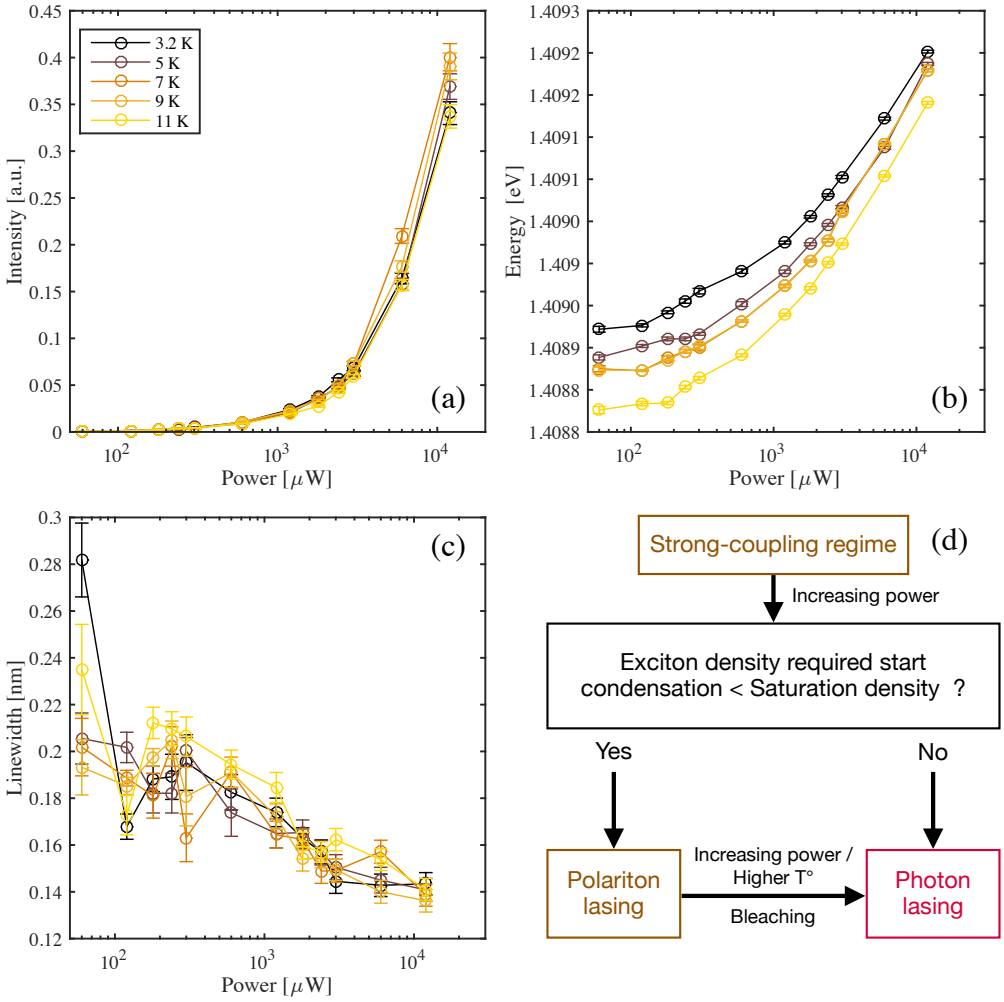

Figure 4.13 – Lasing of a disk containing a single QW. Emission signal intensity (a), energy (b) and linewidth as function of the excitation power and temperature inside the cryostat. (d) Polariton versus Photon lasing

Chapter 5

Optomechanical measurements in a hybrid quantum-well disk resonator

Summary : We present in this chapter the first optomechanical experiments we carried out in hybrid quantum-well WGM resonators. We notably report experiments involving the self-oscillation regime and highlight peculiar visible features that were hardly visible in a mere optomechanical resonator. We present the first steps towards perspective experiments to be carried out in the exciton band and in a two-color telecom/exciton band configuration.

5.1 Optomechanical self-oscillation regime

Now that we demonstrated that our resonator hosts polaritons resonances (chapter 4), we need to confirm that the presence of the QW hetero-structure does not perturb the optomechanical properties of resonators. In our case, this can be investigated by running usual

optomechanical experiments in the telecom band, where we usually operate bare GaAs resonators. One of the most common optomechanical experiments is that of the self-oscillation regime [296–298]. This regime was introduced in chapter 1: under blue detuned conditions, mechanical fluctuations are optomechanically amplified and grow exponentially if the amplification overcomes the natural mechanical damping. Non-linear effects provoke saturation of this exponential amplification, and the mechanical resonator stabilizes on a trajectory where coherent harmonic oscillations are sustained by optical forces. This situation resembles that of laser (or more precisely that of an Optical Parametric Oscillator), hence the name of *mechanical lasing* or *phonon lasing* sometimes encountered in the literature. This regime has potential applications notably in sensing [299]. In this section, we focus on experiments run at telecom wavelength on hybrid QW-disks and highlight similarities and differences in the self-oscillating regime, compared to the case of a bare GaAs optomechanical disk.

5.1.1 Experimental observation

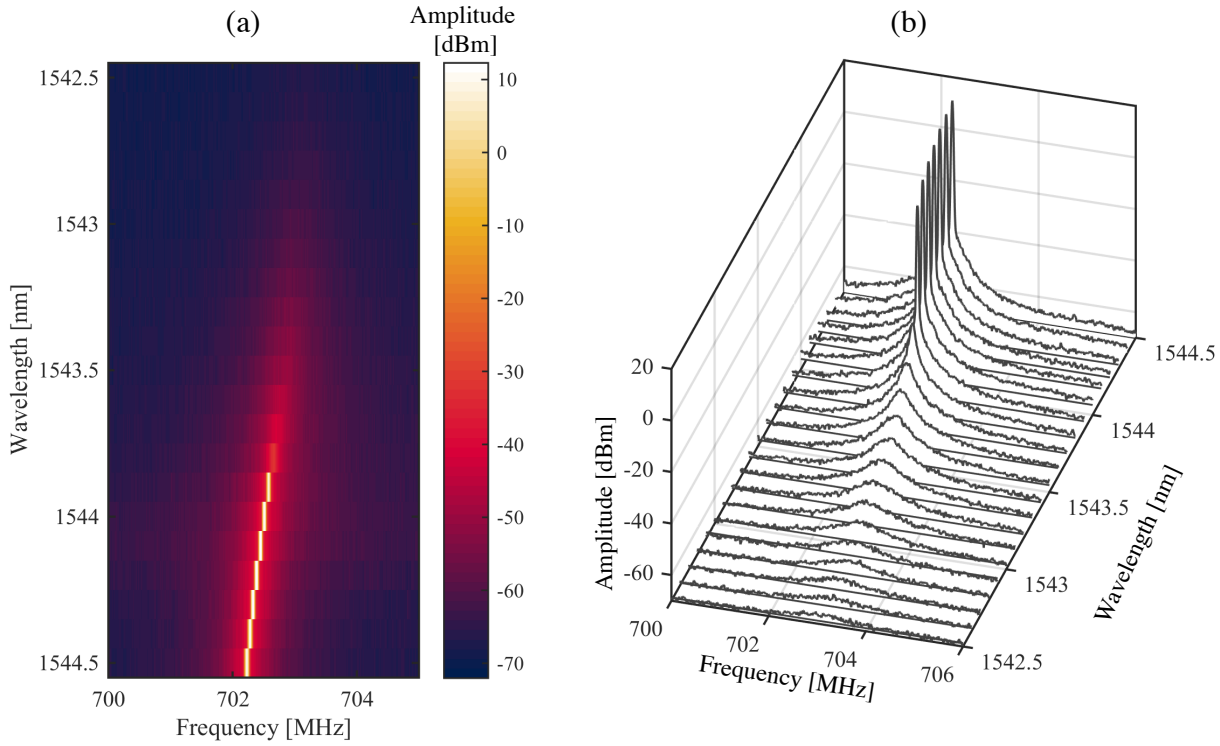

Figure 5.1 – Evolution of mechanical spectra as a function of the laser wavelength, measured at cryogenic temperature (T$\sim$ 3.5 K). (a) Two dimensional map (b) 3D complementary view. RBW = 1 kHz, $\omega_m = 2\pi \cdot 702.6$ MHz, $Q_m \simeq 10^3$, $R = 1.998\mu$m.

Figure 5.1 presents the evolution of measured mechanical spectra as a function of the laser wavelength, as the latter varies on the blue flank of a WGM resonance. For sufficiently high optical power, the optical resonance adopts a characteristic triangular shape as a consequence of the thermo-optic effect (see section 3.2.1.2 for a discussion). In this regime,

the in-cavity power is approximatively linear with wavelength. In figure 5.1, we see that the mechanical signal is red-shifted and amplified when the wavelength is increased. The considered mechanical mode is the first RBM, calculated analytically and numerically on section 2.2, it possesses an eigenfrequency around 700 MHz.

Let us describe the data of figure 5.1 more progressively. We start the experiment by setting the laser wavelength on the blue side of the optical resonance, out of the resonance ($\lambda = 1542.5$ nm). By gradually increasing the wavelength, we progressively enter the optical resonance: the circulating optical power in the WGM increases, increasing the amplitude of optically induced forces acting on the disk motion. The optomechanical dynamical back-action mechanism described in section 1.2.3 provokes a parametric amplification of the disk movement (Γ'_m decreases since $\Gamma_{om} < 0$, see figure 1.3 (a)). In consequence, the linewidth of the mechanical signal decreases as seen in figure 5.1 from $\lambda = 1542.5$ to 1543.7 nm.At some point, when the circulating power inside the disk reaches a certain threshold P_{th} proportional to $Q_m^{-1}Q_{opt}^{-3}$ [296], the amplification of the motion compensates the mechanical damping (at this point $\Gamma'_m = 0$). This happens close to $\lambda = 1543.8$ nm. The movement of the resonator is self-sustained and the amplitude motion is high, orders of magnitude higher than the Brownian motion. At the same time, the mechanical linewidth strongly narrows, which is a marker of the oscillator threshold.

In parallel with this evolution towards self-oscillation, the mechanical frequency is progressively reduced with wavelength. This is in contrast with the optical spring effect introduced in section 1.2.3, and will be explained below as a consequence of thermal effects associated with the increase of circulating power.

Figure 5.2 presents radio-frequency spectra of the photo-detected light similar to 5.1, but taken at different central frequency and different frequency span. On a large span (several GHz) like in figure 5.2 (d), several peaks appear. They correspond to the fundamental ($\simeq$ 700 MHz) and harmonics of the periodic signal coming from the mechanical RBM1. At large amplitude of motion reached in self-oscillation, the linearized picture introduced in eq. (1.20) is no longer valid: multiple harmonics do appear in the output signal, even if the mechanical motion is predominantly sinusoidal. These harmonics also follow a linear variation with the laser wavelength, as shown in figure 5.2 (a), (b) and (c) but with different slopes, the ratios of these slopes correspond to an expected factor 1, 2, and 3 for the harmonics 1, 2 and 3.

When reducing the span and decreasing the resolution bandwidth (figure 5.2 (e)), symmetric lateral sidebands appear on the spectrum, located at $\pm$ 7 MHz around the main peak at 702 MHz. These features were observed in the past in our group in GaAs disks, and in a few other systems [297, 300].

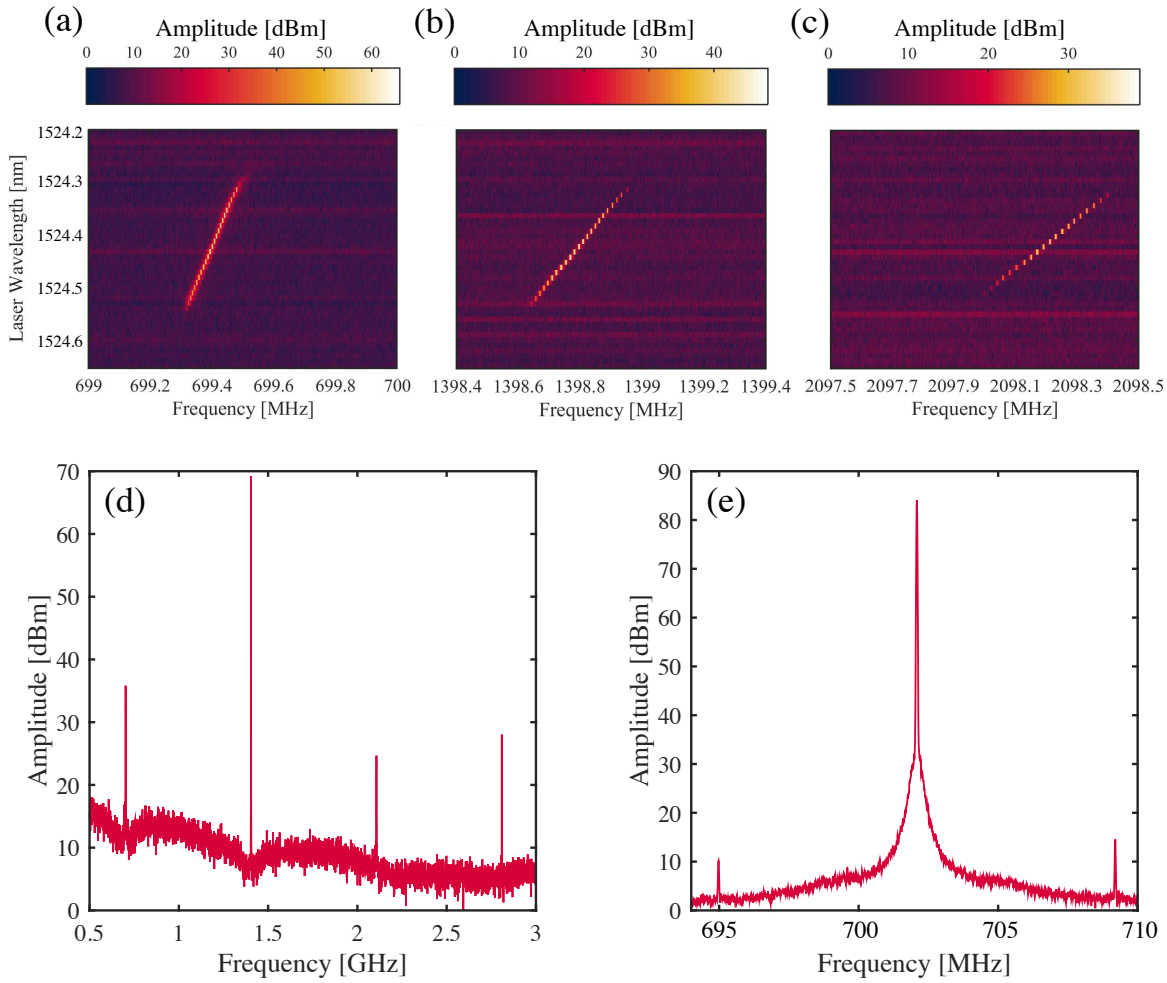

Figure 5.2 – Evolution of the "mechanical" radio-frequency spectrum of the output light as a function of laser wavelength. Two dimensional map (a) Fundamental RBM1 mode (b) Second harmonic (c) Third harmonic. Radio-frequency spectrum of a self oscillating disk (d) Large-span exhibiting the fundamental as well as the next three harmonics. RBW = 100 kHz, $\omega_m = 2\pi \cdot 699.4$ MHz, $Q_m \simeq 10^3$, $R = 2.008\mu$m, thickness $h = 200$ nm (e) Small-span centered around the fundamental RBM1, displaying side-bands at ± 7 MHz. RBW = 1 kHz, $\omega_m = 2\pi \cdot 702.6$ MHz, $Q_m \simeq 10^3$, $R = 1.998\mu$m, thickness $h = 200$ nm.

5.1.2 Absorption and thermal effects

5.1.2.1 Evolution of the temperature inside the microdisk

As introduced on section 3.2.1.2, optical absorption is present on our semiconductor disks. This absorption is a consequence of linear or non-linear mechanisms, resulting in an elevation of the temperature. The evolution of the temperature is governed by [301, 302]:

$$\frac{d\Delta T}{dt} = -\frac{\Delta T}{\tau_{\text{th}}} + \frac{R_{\text{th}}\hbar\omega_l\kappa_{\text{abs}}}{\tau_{\text{th}}}|a(t)|^2 = -\frac{\Delta T}{\tau_{\text{th}}} + \frac{\Gamma_{pth}}{\tau_{\text{th}}}|a(t)|^2 \tag{5.1}$$

where τ_{th} is the disk thermal response time, R_{th} the thermal resistance linking the temper-

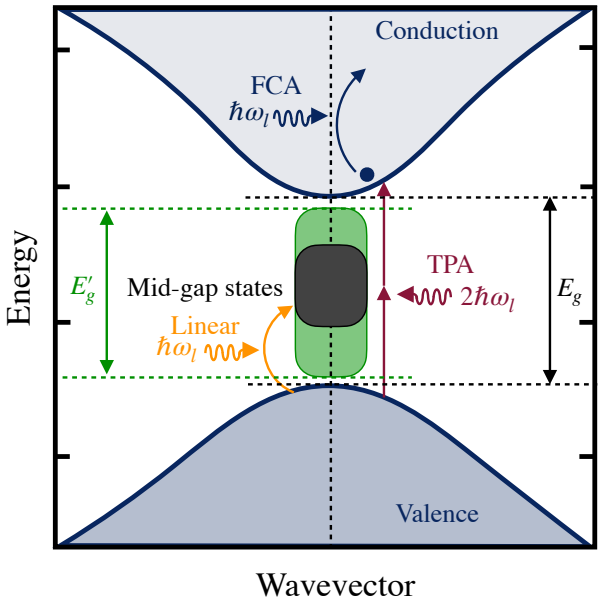

Figure 5.3 – Schematic representation of the three mechanisms responsible for the optical absorption. The telecom linear absorption (represented in orange) involves mid-gap states present either at the surface or in the bulk of the disk. TPA (represented in dark red) promotes an electron from the valence to the conduction band. The free carriers generated this way in the conduction band give rise to FCA (represented in blue). The GaAs band gap, E_g is designated by the black double arrow, while the MQW fundamental transition E'_g is indicated by a green double arrow.

ature increase to the intra-cavity absorbed power, and κ_{abs} the total intra-cavity absorption rate. This latter parameter accounts for several contributions schematized in figure 5.5 and listed below $\kappa_{\text{abs}} = \kappa_{\text{lin}} + \kappa_{\text{TPA}} + \kappa_{\text{FCA}}$:

- **Linear absorption (κ_{lin}):** Even if working with telecom photons ($\hbar\omega \simeq 0.8$ eV) of energy well below the band gap (1.42 eV at room temperature - 1.52 eV at cryogenic temperature), the presence of impurities and defects, notably at surface [121], generates mid-gap states, creating available absorption transitions. This linear absorption is a fraction ϵ of intrinsic losses $\kappa_{\text{lin}} = \epsilon\kappa_{\text{in}}$

- **Two-Photon absorption (TPA) (κ_{TPA}):** TPA describes the simultaneous absorption of two sub-bandgap photons, promoting one electron from the valence band to the conduction band. The two-photon absorption rate κ_{TPA} is given by [303] :

$$\kappa_{\text{TPA}} = \frac{\beta c^2}{n^2 V_{\text{TPA}}} \hbar\omega_l |a(t)|^2 \tag{5.2}$$

  with n the refractive index of the material, β the two-photon absoption coefficient (eq. (3.13)), and V_{TPA} the effective volume of two-photon absorption defined by [303,304]:

$$V_{\mathrm{TPA}} = \frac{\left(n^2(\boldsymbol{r})|\boldsymbol{E}(\boldsymbol{r})|^2\right)^2 d\boldsymbol{r}}{n^4(\boldsymbol{r})|\boldsymbol{E}(\boldsymbol{r})|^4 d\boldsymbol{r}} \tag{5.3}$$

that can be computed by FEM simulations.

- **Free-Carrier Absorption (FCA) (κ_{FCA}):** It is the absorption of one or several photons that promotes one free carrier (electron or hole) to a higher energy free-carrier level. The absorption rate, κ_{FCA} takes the form [303]:

$$\kappa_{\mathrm{FCA}} = \frac{\sigma_{\mathrm{FCA}} c}{n} N_c \tag{5.4}$$

where N_c is the density of free carriers and σ_{FCA} the free-carrier cross section in m^2

Since the GaAs bandgap energy is higher than the energy of telecom photons, the only possibility to generate free carriers is via TPA. The number of free carriers therefore obeys the equation :

$$\begin{aligned} \frac{dN_c}{dt} &= -\frac{N_c}{\tau_{fc}} + \frac{V_{\mathrm{TPA}}}{2V_{\mathrm{FCA}}^2}\kappa_{\mathrm{TPA}}|a(t)|^2 \\ &= -\frac{N_c}{\tau_{fc}} + \frac{\beta c^2 \hbar\omega_l}{2n^2 V_{\mathrm{FCA}}^2}\kappa_{\mathrm{TPA}}|a(t)|^4 \end{aligned} \tag{5.5}$$

where τ_{fc} is the free carrier relaxation time and V_{FCA} the effective volume of free-carrier absorption [303]:

$$V_{\mathrm{FCA}} = \frac{\left(n^2(\boldsymbol{r})|\boldsymbol{E}(\boldsymbol{r})|^2\right)^3 d\boldsymbol{r}}{n^6(\boldsymbol{r})|\boldsymbol{E}(\boldsymbol{r})|^6 d\boldsymbol{r}} \tag{5.6}$$

that can also be computed by FEM simulations.

5.1.2.2 Changes in optical cavity resonance

An important consequence of these absorption effects is the modification of the refractive index of the material upon heating on one hand, and upon changes in the density in free carriers on the other hand. The optical cavity eigenfrequency changes accordingly:

$$\omega_c \longrightarrow \omega_c - \left(\frac{\omega_c}{n}\frac{dn}{dT}\Delta T\right) - \left(\frac{\omega_c}{n}\frac{dn}{dN_c}N_c\right) \tag{5.7}$$

with dn/dT the thermo-optic coefficient [305], ΔT the increase of the system's temperature, dn/dN_c the free-carrier dispersion coefficient [306] and N_c the density of free carriers. Consequently the classical Langevin equation given in (1.17) is modified according to :

$$\dot{\alpha} = -\frac{\kappa_{\mathrm{ext}} + \epsilon\kappa_{\mathrm{in}} + \kappa_{\mathrm{TPA}} + \kappa_{\mathrm{FCA}}}{2}\alpha + j\left(\Delta + g_{om}x\frac{\omega_c}{n}\frac{dn}{dT}\Delta T + \frac{\omega_c}{n}\frac{dn}{dN_c}N_c\right)\alpha + \sqrt{\kappa_{\mathrm{ext}}}\alpha_{\mathrm{ext}} \tag{5.8}$$

with $x = x_{\mathrm{ZPF}}(\beta + \beta^*)$.

5.1.2.3 Photothermal forces and coupled optomechanical equations with thermal effects

We write down an extension of standard optomechanics equations in the classical regime (1.15), which describes the evolution of the mean value of operators $\hat{a}$ and $\hat{b}$. We wish to now include the effects of absorption described above. In order to do so, we need to add a supplementary optically-induced force: the photothermal force, resulting from thermal distortion and movement of the mechanical system upon heating. The photothermal force can be derived from the thermal-induced stress σ^{th} (eq. (2.141)) [125, 301, 302]:

$$F_{\mathrm{th}} = \int_V dV \sigma_{ij}^{th} S_{ij} = \alpha_{\mathrm{th}} \Delta T \tag{5.9}$$

with α the thermal expansion coefficient and S the modal strain profile for the considered mechanical mode. With all absorptive effects now included (eq. (5.1), (5.5) and (5.8)), we obtain the generalized equations [301]:

$$\begin{aligned}\dot{\alpha} = &-\frac{\kappa_{\mathrm{ext}} + \kappa_{\mathrm{in}} + \kappa_{\mathrm{TPA}} + \kappa_{\mathrm{FCA}}}{2}\alpha + \sqrt{\kappa_{\mathrm{ext}}}\alpha_{\mathrm{ext}} \\ &+ j\left(\Delta + g_{om}x\frac{\omega_c}{n}\frac{dn}{dT}\Delta T + \frac{\omega_c}{n}\frac{dn}{dN}N\right)\alpha\end{aligned} \tag{5.10}$$

$$m_{\mathrm{eff}}\left[\ddot{x} + \Gamma_m\dot{x} + \omega_m^2 x\right] = F_{opt} + F_{\mathrm{th}} \tag{5.11}$$

$$\frac{d\Delta T}{dt} = -\frac{\Delta T}{\tau_{\mathrm{th}}} + \frac{R_{\mathrm{th}}\hbar\omega_l}{\tau_{\mathrm{th}}}(\epsilon\kappa_{\mathrm{in}} + \kappa_{\mathrm{TPA}} + \kappa_{\mathrm{FCA}})|a(t)|^2 \tag{5.12}$$

$$\frac{dN}{dt} = -\frac{N_c}{\tau_{fc}} + \frac{\beta c^2\hbar\omega_l}{2n^2V_{\mathrm{FCA}}^2}\kappa_{\mathrm{TPA}}|a(t)|^4 \tag{5.13}$$

This set of four coupled equations is far more complete than the two coupled equations of standard optomechanics. It grasps all the complexity of the dynamics that can settle in semiconductor optomechanical systems [1]. Taking the Fourier transform of these equations, after linearization as done in chapter 1 for the standard case leads to a modified mechanical frequency and damping. The evolution of these parameters will greatly differ from the one plotted in figure 1.3. This generalized model enables retrieving the behavior of evolution towards optomechanical self-oscillation [121, 299, 307]. Ignoring the influence of the free carriers, linearizing equations (5.10), (5.11), and (5.12), and moving in the Fourier space, we derive an effective mechanical frequency ω_m'' and an effective mechanical damping Γ_m':

1. At cryogenic temperature and low excitation power we should nevertheless come closer to the standard behavior, as thermal expansion and thermal effects approach zero

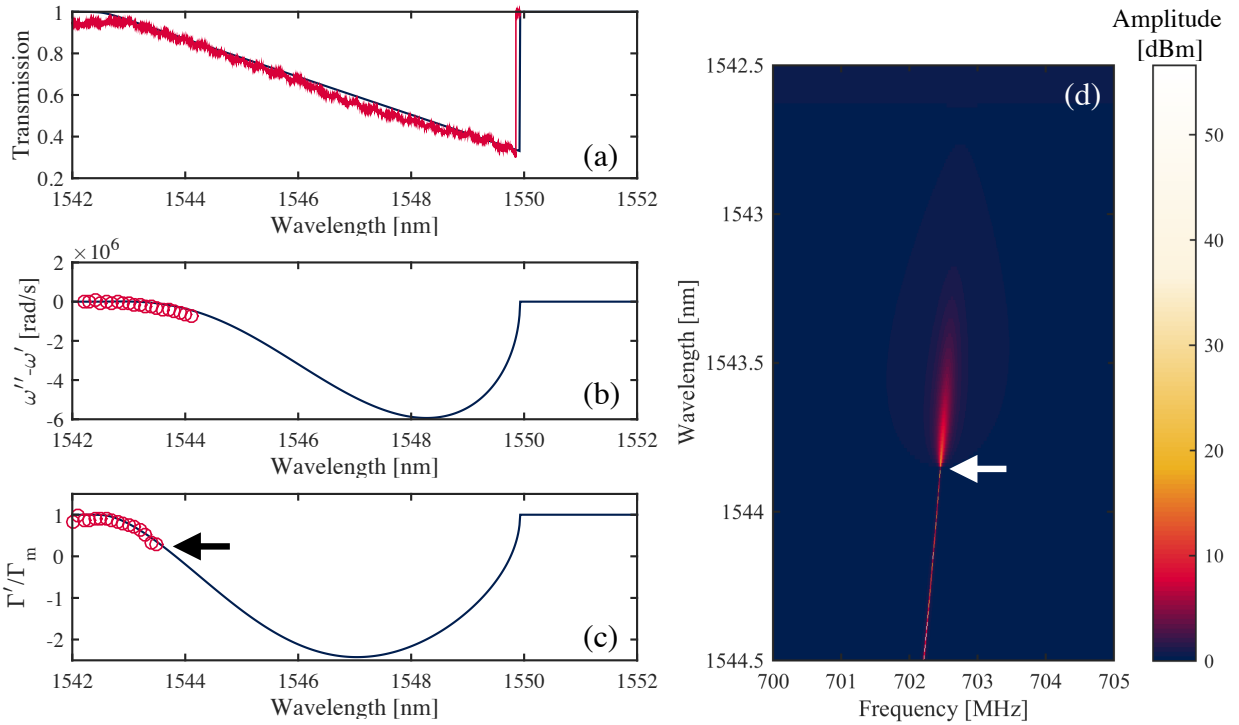

Figure 5.4 – Optomechanical fitting model, experimental data are extracted from the self-oscillation spectra series of figure 5.1 (a) Optical waveguide transmission spectrum, Injected laser power in the waveguide $\simeq$ 1 mW. Red curve: Experimental data. Dark blue curve: thermo-optic model. Mechanical frequency (b) and linewidth (c) as a function of the laser wavelength. The open symbols are experimental data, while the solid lines are fits with equations (5.14) and (5.15). (d) Modelled evolution of the mechanical radio-frequency spectrum as function of the telecom laser wavelength. The arrows in (c) and (d) mark the transition to the mechanical lasing regime.

$$\omega_m'' = \omega_m' \left\{ 1 + \frac{\hbar g_{om}^2 |\alpha|^2}{2 m_{\text{eff}} \omega_m'^2} \left[\frac{(\omega_m + \Delta')}{(\omega_m + \Delta')^2 + \left(\frac{\kappa_c}{2}\right)^2} + \frac{-(\omega_m - \Delta')}{(\omega_m - \Delta')^2 + \left(\frac{\kappa_c}{2}\right)^2} \right] \right.$$
$$\left. \frac{g_{om} |\alpha|^2 \alpha_{\text{th}} \Gamma_{pth}}{2 m_{\text{eff}} \omega_m'^2 (1 + (\omega_m \tau_{\text{th}})^2)} \left[\frac{(\omega_m + \Delta') + \omega_m \tau_{\text{th}} \kappa_c/2}{(\omega_m + \Delta')^2 + \left(\frac{\kappa_c}{2}\right)^2} + \frac{-(\omega_m - \Delta') - \omega_m \tau_{\text{th}} \kappa_c/2}{(\omega_m - \Delta')^2 + \left(\frac{\kappa_c}{2}\right)^2} \right] \right\} \tag{5.14}$$

$$\Gamma_m' = \Gamma_m \left\{ 1 + \frac{\hbar g_{om}^2 |\alpha|^2}{\Gamma_m m_{\text{eff}} \omega_m} \left[\frac{\frac{\kappa_c}{2}}{(\omega_m + \Delta')^2 + \left(\frac{\kappa_c}{2}\right)^2} + \frac{-\frac{\kappa_c}{2}}{(\omega_m - \Delta')^2 + \left(\frac{\kappa_c}{2}\right)^2} \right] \right.$$
$$\left. + \frac{g_{om} |\alpha|^2 \alpha_{\text{th}} \Gamma_{pth}}{\Gamma_m m_{\text{eff}} \omega_m (1 + (\omega_m \tau_{\text{th}})^2)} \left[\frac{\frac{\kappa_c}{2} - (\omega_m + \Delta') \omega_m \tau_{\text{th}}}{(\omega_m + \Delta')^2 + \left(\frac{\kappa_c}{2}\right)^2} + \frac{-\frac{\kappa_c}{2} + (\omega_m - \Delta') \omega_m \tau_{\text{th}}}{(\omega_m - \Delta')^2 + \left(\frac{\kappa_c}{2}\right)^2} \right] \right\} \tag{5.15}$$

with $\omega' = \omega_m + \frac{\partial \omega_m}{\partial T} \Delta T_{eq}$. These expressions are used to predict optomechanical frequency shifts and self-oscillations thresholds, as represented in figure 5.4.

5.1.3 Miscellaneous observations

We report different experimental observations that differ from usual behaviors experienced in our group with bare GaAs disk resonators that do not embed QW heterostructure. Among other things, it seems that free carriers play a more important role: the MQW, whose energy gap is below the GaAs bandgap (see figure 5.5), can trap generated carriers and give rise to light emission. The data presented below are taken at cryogenic temperatures (3 to 4 K).

5.1.3.1 TPA induced photo-luminescence

A first marked observation is the emission of light at the energy of the MQW transitions, i.e. photo-luminescence, as the system is optically injected with telecom light at 1.5 μm: it is represented in figure 5.5 (a) and (b).

The quantity of signal emitted depends on the position of the laser wavelength inside the optical mode of the disk: it seems to be proportional to the number of photons injected in the mode. The evolution of the PL signal, plotted in figure 5.5 (c), follows almost perfectly the shape of the optical resonance distorted by the thermo-optic effect (figure 5.5 (a)).

Photons in the telecom range do not have sufficient energy to promote an electron from the MQW valence band to the conduction band. This PL is enabled by the action of the TPA mechanism. Electrons from the GaAs or MQW valence band are promoted to the GaAs conduction band via TPA, once there, they cascade to the bottom of the well conduction band via non-radiative mechanisms and relax by emitting a photon.

If TPA is responsible for the emitted PL signal, we naively expect a quadratic evolution of the quantity of this PLsignal (P_{PL}) with respect to the power dropped by the waveguide to the disk resonator (P_{drop}). It is not what we observe here, the amount of PL signal is rather linear in the power injected in the waveguide (and therefore in the power dropped in the resonator), as illustrated in figure 5.6 (a) and implied by the shape of the signal in 5.5 (c). To explain this variation, we start by establishing a relation between the dropped and the circulating power inside the disk P_{circ}. In the linear regime, this relation is: $P_{\text{circ}} = (Q_{opt}/2\pi m) \cdot P_{\text{drop}}$, with m the azimuthal number of the WGM, and Q_{opt} the optical quality factor. Using the expression introduced in the prior section 5.1.2 we have:

$$\begin{aligned} P_{\text{circ}} &= \frac{1}{2\pi m} \frac{\omega_c}{\kappa_{\text{ext}} + \epsilon\kappa_{\text{in}} + \kappa_{\text{TPA}} + \kappa_{\text{FCA}}} P_{\text{drop}} \\ &= \frac{1}{2\pi m} \frac{\omega_c}{\kappa_{\text{ext}} + \epsilon\kappa_{\text{in}} + \kappa_{\text{FCA}} + \frac{\beta c^2 \hbar\omega_l}{n^2 V_{\text{TPA}}} P_{\text{circ}} \tau_{rt}} P_{\text{drop}} \end{aligned} \tag{5.16}$$

with $\tau_{rt} \simeq 2\pi m/\omega_c$ the cavity round trip time. P_{circ} answers therefore to the following equation :

$$\left[\kappa_{\text{ext}} + \epsilon\kappa_{\text{in}} + \kappa_{\text{FCA}}\right] P_{\text{circ}} + \frac{\beta c^2 \hbar\omega_l}{n^2 V_{\text{TPA}}} \tau_{rt} P_{\text{circ}}^2 = \frac{\omega_c}{2\pi m} P_{\text{drop}} \tag{5.17}$$

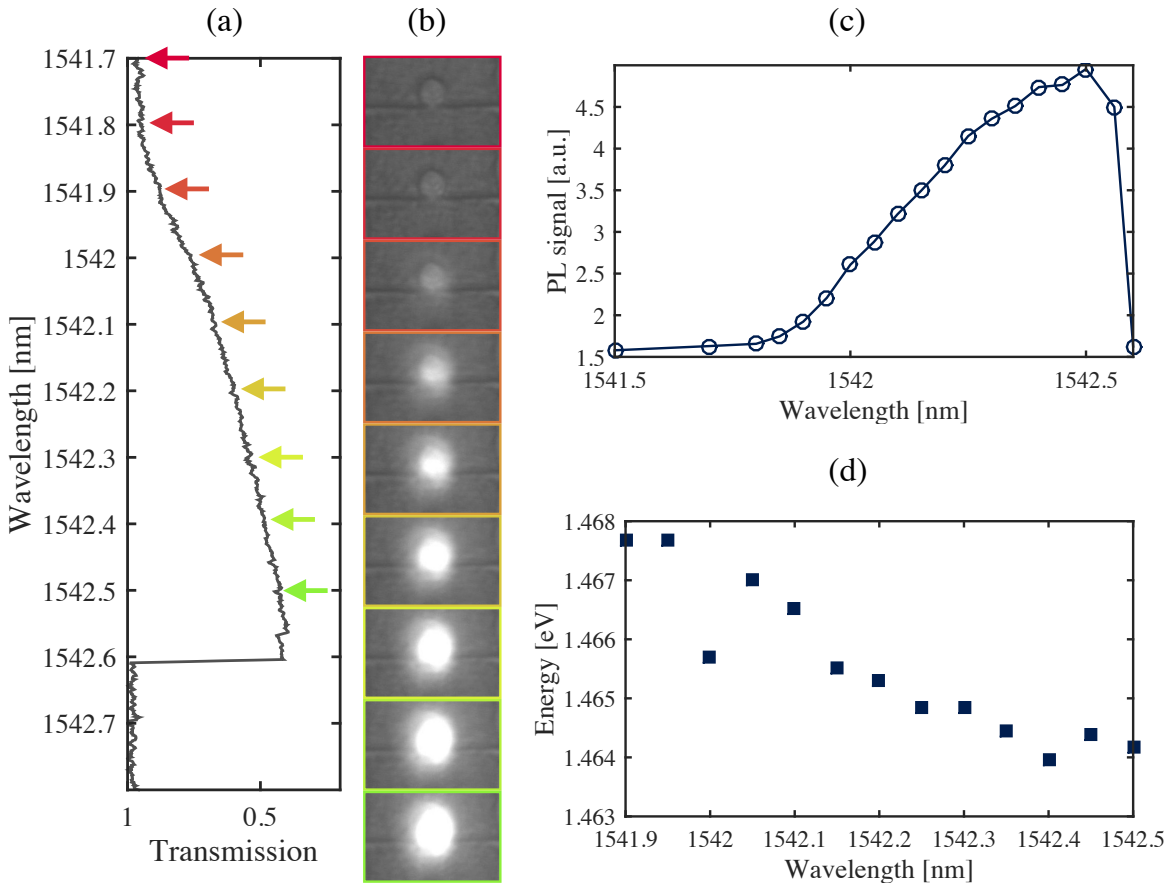

Figure 5.5 – (a) Optical waveguide transmission spectrum showing a WGM resonance with a thermo-optic distortion. (b) CCD camera pictures of the disk imaged from the top with the confocal microscope, for different telecom laser wavelengths inside the WGM resonance. The CCD camera is silicon-based and can only detect photons of wavelength $\lesssim 1\mu$m: it does not respond to the laser photons at 1.5 μm. The color of the picture frame corresponds to the arrow in (a). (c)-(d) Evolution of the PL signal and energy as a function of the telecom laser wavelength, collected from the top with the confocal cold objective. Injected telecom laser power in the waveguide 188 μW

In the regime of high powers, the first term in the previous equation can be neglected, we thus obtain :

$$P_{\text{circ}} \simeq \sqrt{\frac{\omega_c}{2\pi m}\frac{n^2 V_{\text{TPA}}\tau_{rt}}{\beta c^2 \hbar\omega_l}P_{\text{drop}}} \tag{5.18}$$

As P_{PL} is proportional to P_{circ}^2, we recover the behavior observed in figure 5.6 (a).

In addition to that, one interesting of this TPA activated PL is the evolution of the energy of the emitted signal. Since the energy depends on the temperature, we can deduce the shift in disk temperature between out-of-resonance and in-resonance conditions for the telecom input laser, making use of the calibration curve represented in figure 4.5 (a).

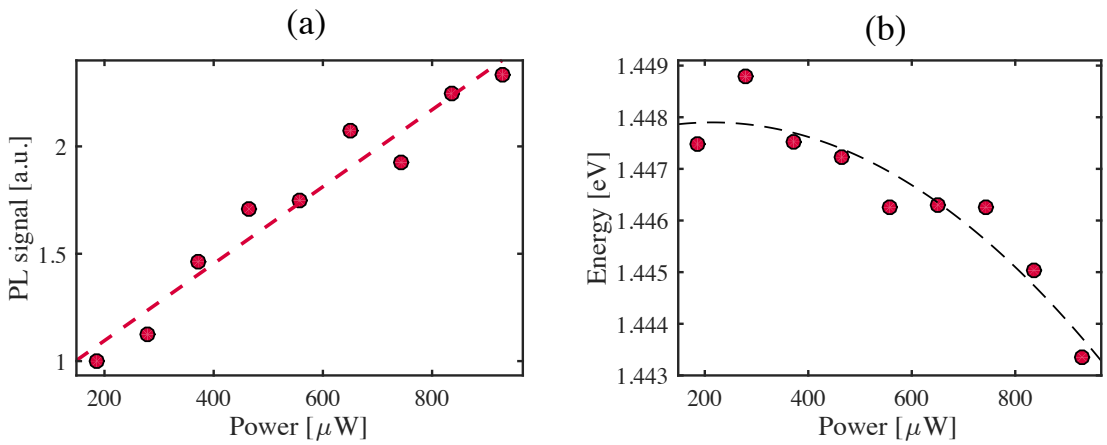

Figure 5.6 – Evolution of the PL signal (a) and energy (b) as a function of the estimated telecom laser power injected in the waveguide. PL is collected from the top with the cold confocal objective. The emitted signal is always measured at the bottom of the telecom distorted optical resonance. The red dashed line in (a) is a linear fit ($r^2 > 0.9$). The black dashed line in (b) is a guide to the eye.

This temperature elevation ΔT_{eq} is proportional to the number of photons inside the cavity $\Delta T_{eq} = R_{\text{th}}\hbar\omega_l\kappa_{\text{abs}}|a(t)|^2$. Taking data of figure 5.5 (d), we deduce this way that this temperature increase is of 50 K when the telecom laser is at the optical resonance. This value is consistent with FEM simulations, as represented in figure 5.7.

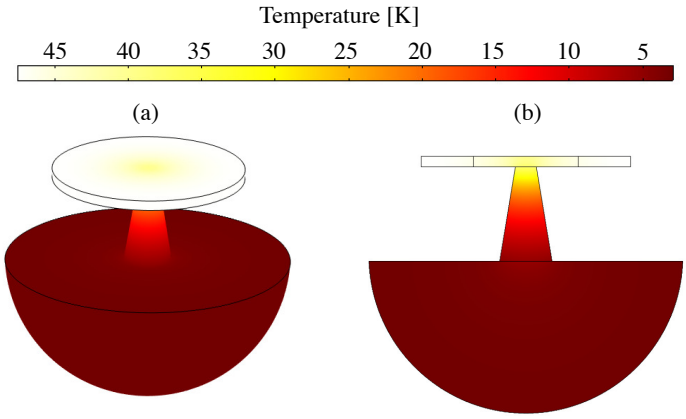

Figure 5.7 – Temperature profile (steady-state) inside the disk. The geometry of disk reproduces the micrograph 3.34-(b). (a) 3D view. (b) Cross-section in 2D view. Injected telecom laser power in the waveguide 188 μW.

5.1.3.2 Self-pulsing regime of the optical cavity

As already mentioned the strong optical confinement inside our tiny disk resonators modifies the local free-carrier density and temperature, in particular through the TPA mecha-

nism. Strong thermo-optic and free-carrier effects are this way appearing: the interplay of all these mechanisms can possibly activate a self-induced modulation of the cavity field, usually referred as self-pulsing. [308–312]. The experimental manifestation of this phenomenon in our case is illustrated in figure 5.8.

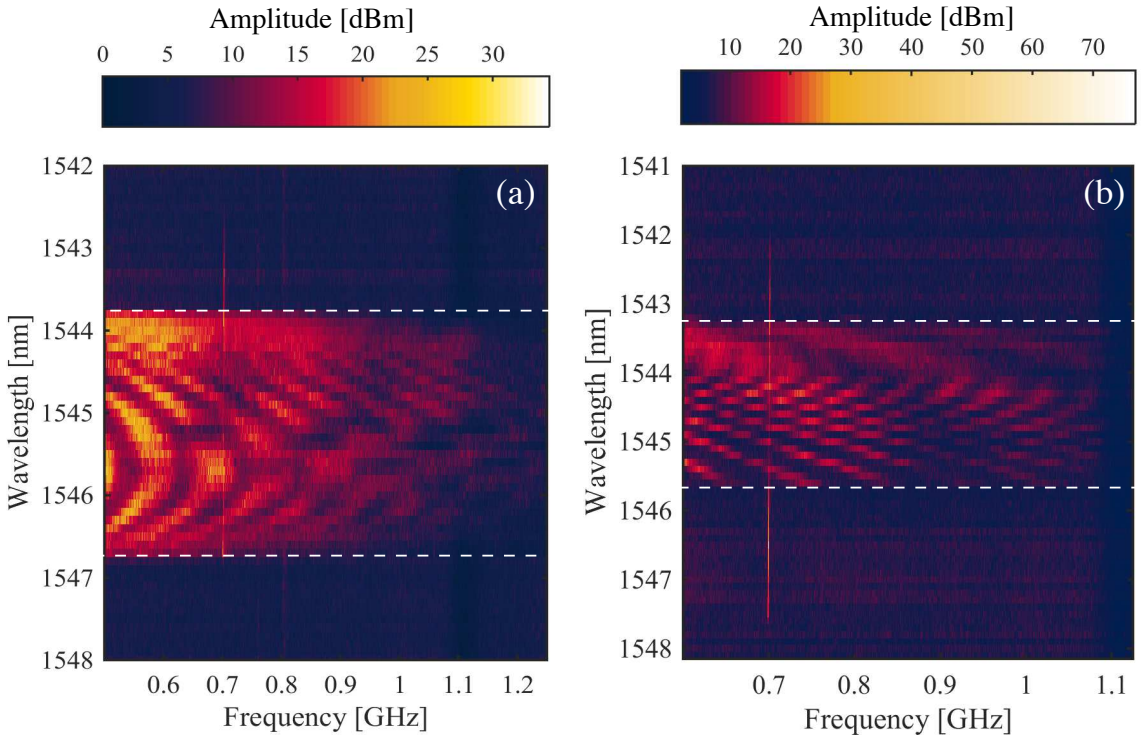

Figure 5.8 – (a)-(b) Two dimensional map of radio-frequency power spectral densities as a function of the laser wavelength, showing a self-pulsing regime (delineated by the white dashed lines) and mechanical self-oscillation thin vertical line at ~ 0.7 GHz. Data collected on two different disks with identical radius $R = 1.998$ μm.

Again, the laser wavelength is tuned to the blue flank of a WGM resonance, at sufficient power to show a strong thermo-optic distortion. By scanning the laser wavelength progressively towards the mode, two phenomena start-off in consequence. The first is the optomechanical self-oscillation discussed above, appearing above$P_{\rm th}$. The second is the self-pulsing, where harmonics of the self-pulsing oscillation appear (between the white dashed lines in figure 5.8). The power threshold for this self-pulsing P_{sp}, scales as $V_{\rm eff}Q_{opt}^{-2}$ [313], with $V_{\rm eff}$ the effective mode volume of the cavity. In our common experiments, optomechanical self-oscillation occurs before self pulsing, which means that $P_{\rm th} < P_{sp}$.

One can also notice in figure 5.8 that the frequency of the self-pulsing oscillation varies with the laser wavelength. The frequency of this oscillation is given by [314] :

$$\Omega_{sp} \simeq \sqrt[5]{\frac{\tau_{fc}\,\mathrm{Im}\{\kappa_{\rm TPA}\}\kappa_{\rm FCA}}{2(\hbar\omega_c)^2 V_{\rm eff}} \cdot T_{max}\left(\frac{P_{\rm in}\omega_c}{2Q_{opt}}\right)^2} - \frac{\Delta}{5} \tag{5.19}$$

where T_{max} is the maximum waveguide transmission at low input power, Δ the laser-cavity detuning, and where κ_{TPA} is a complex number to represents the effect of both free-carrier induced absorption and dispersion. Since these parameters evolve with the circulating power inside the microdisk, the frequency of the self-pulsing oscillation naturally changes with the laser wavelength.

This self-pulsing oscillation also has a signature in the time domain. The output telecom signal alternates between transmission close to unity and transmission close to zero. This situation can evolve chaotically or periodically for a few minutes. In this situation, the disk appears to be "blinking" when we observe it with the CCD camera. The QW emission reproduced the apparent dynamic of the cavity.

5.1.3.3 Anti-crossing in "mechanical" radio-frequency spectrum

The last phenomenon presented in this section is not attributed to the free-carriers dynamics but is worth mentioning in complement.

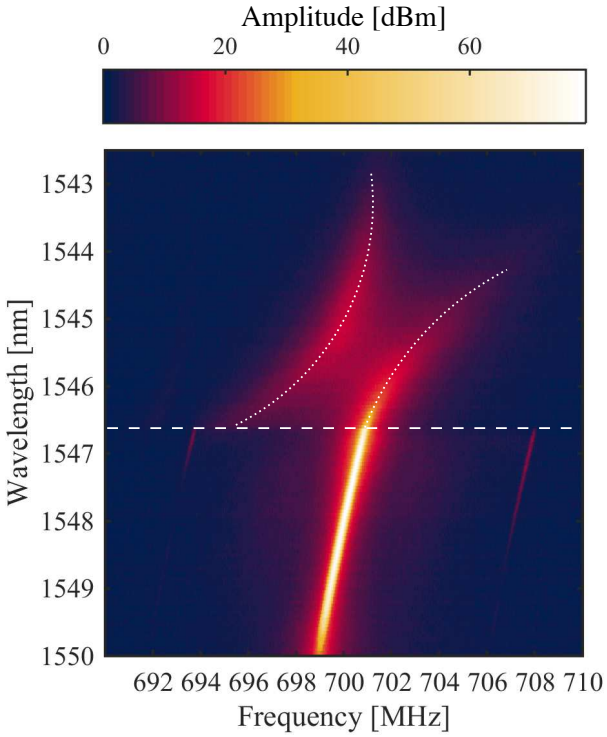

Figure 5.9 – Two-dimensional map of "mechanical" radio-frequency power spectral densities of the output signal, as a function of the laser wavelength. Two regimes (separated by the white dashed line) are present: a regime of mechanical hybridization and a regime of self-oscillating regime. The white dotted curves are guides to the eye.

On a few disks, we have observed an anti-crossing phenomenon in the "mechanical" radio-frequency spectrum of the output signal. By varying the laser wavelength, we witnessed the appearance of a mechanical doublet instead of a unique Lorentzian, as presented

in figure 5.9. When the circulating power inside the cavity reaches the self-oscillating threshold (white dashed line in figure 5.9), we lose this doublet regime and we recover the usual self-oscillating signal with its sidebands. This anti-crossing should not be mistaken for optomechanical strong coupling [10, 315], which should appear for a red detuning, at variance with what we observe here. The most plausible scenario for this anti-crossing is a hybridization of two mechanical modes that are sufficiently close in energy. If the coupling between these two modes is stronger than their dissipation, we can observe a doublet. As the temperature is evolving when we change the laser wavelength, the detuning between these two mechanical modes can change, generating an anti-crossing behavior. The fact that two modes of a disk hybridize is surprising since these modes are supposedly orthogonal. This said, we observed in the past that a mode of the disk, mostly confined in the disk can couple to modes of the pedestal [316], leading to such hybridization.

This phenomenon was observed sporadically. We will keep it in mind as a nonideality of our resonators.

5.2 Perspectives for future experiments

We review now the perspectives for hybrid optomechanics addressable by our experimental platform. We also present the first characterization steps towards these.

5.2.1 Optomechanical experiments in the exciton band

So far in section 5.1.1 and 5.1.3, we reported optomechanical experiments with the drive laser in the telecom band. The most wanted experiment would consist in switching the wavelength range toward the exciton band and exploring exciton-assisted optomechanical effects. The last months of this Ph.D. were dedicated to this task, however, working in the exciton band to observe optomechanical signatures presents several difficulties:

- The laser source we use in this band is not as user-friendly as the technology we use for telecom wavelength. Taking laser scans with the M-squared laser is very long, and measuring an optical spectrum can demand several hours of alignment especially if we are working at room temperature, where the PL signal cannot help for this purpose.

- A stronger linear absorption is present in this wavelength range, in comparison to telecom, which means that the optical power we collect at the output of the set-up is weak, typically below a few μW even when working at high laser power. This absorption mostly happens occurs in the suspended waveguide (by construction the waveguide also contains the MQW structure), which is thermally isolated from the rest of the sample and hence very sensitive to the thermo-optic effect. When the temperature inside the waveguide rises, QW absorption band-edges are red-shifted, causing even more absorption for a fixed laser wavelength. The local temperature of

the disk and waveguide become distinct: the waveguide absorbs photons at energy smaller than the disk, preventing us to resolve optical resonances coming from the disk, especially for modes that are close to the exciton energy, i.e. potential polaritonic modes. Figure 5.10 illustrates this effect: we see that the spectral position of the WGMs or WGM polaritons is merely affected by the increase of input power, while marked absorption is visible for the waveguide QW heterostructure. If the input power is increased the absorption edge is red-shifted (figure 5.10). The signal at energy higher than the edge is not transmitted by the waveguide: it is absorbed and lost for the output light. If we want to optically address the exciton and disk polariton modes spectrally close to it, we are doomed to work with low power, posing severe constraints on achievable optomechanics experiments.

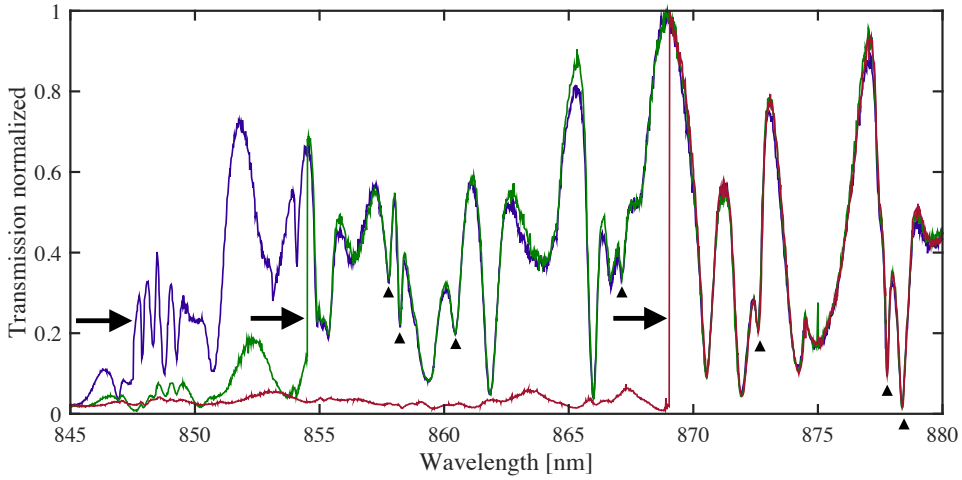

Figure 5.10 – Evolution of the waveguide/disk transmission spectrum measured at different input powers. Blue trace P, green trace $\simeq 3.8 \cdot P$, red trace $7.5 \cdot P$. The black arrow indicates the absorption edge below which the waveguide ceases to absorb. The black triangles highlights some of the WGMs or polaritons present in the spectrum.

- In addition to working with low optical power, the exciton band lacks proper optical amplification technologies. For the telecom range, Erbium-Doped Fiber Amplifier (EDFA) enables amplification of signal with very low added noise, an advantage that we lose in the exciton band.

Despite these issues and the consequences of working with low power, we have carefully analyzed and optimized the different stages of our chain of detection: measuring the Brownian motion in this exciton band should be possible. The last months before writing this thesis have been dedicated to this task, and experiments are currently underway.

The first experiment will be to measure in a calibrated manner the optomechanical coupling parameter g_0. By varying different cavity-exciton detuning we can tune the value of g_0 and obtain a controllable optomechanical coupling. Our model predicts a value above that measured in the telecom range. A strong boost in the g_0 paves the way to regimes such as

single-photon optomechanics, which has up to now remained impossible to explore with the current state of technology. The "quantumness" factor g_0/κ_c [91] discriminates the entrance into this regime, where photon blockade is for instance expected. This ultimate optomechanical regime is completely unprecedented in the field of meso/nanoscopic optomechanical devices and was only demonstrated in a formally-equivalent ultracold gas experiment [317]. In addition to that, boosting g_0 is tantamount to improving the optomechanical cooperativity, of great importance in nowadays quantum optomechanics applications.

5.2.2 Two-color experiments

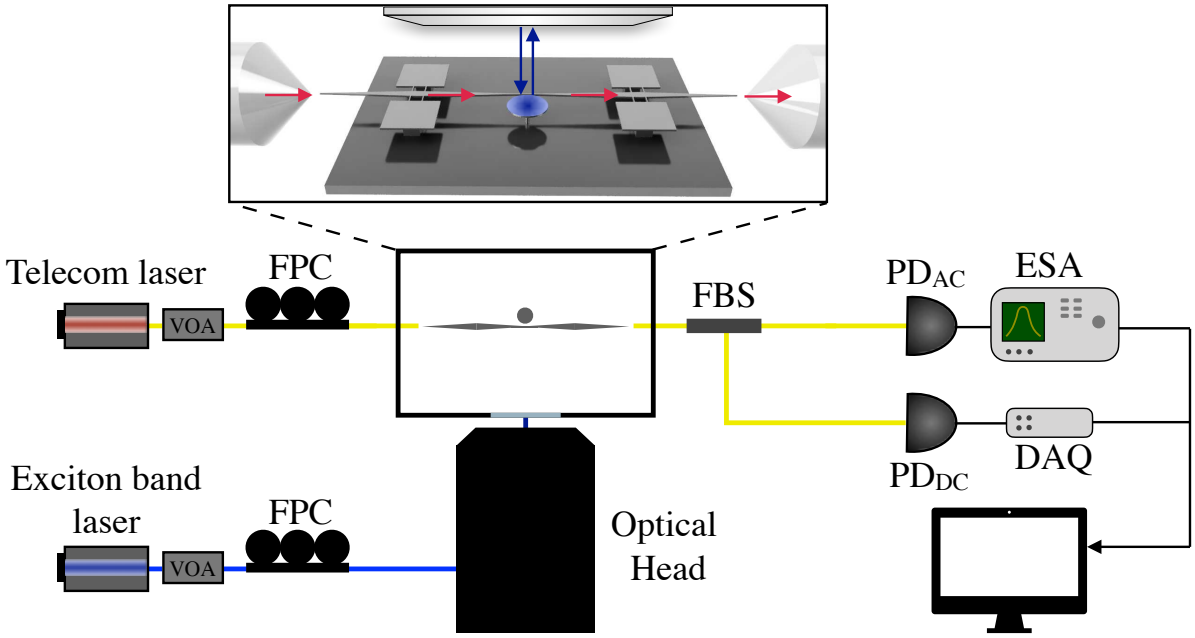

Figure 5.11 – Two-color experiment set-up. The yellow lines represent single mode telecom fiber, blue lines single mode exciton band fibers ,and the black lines electric cables. The inset represents a close-up of the sample located inside the cryostat chamber.

Another perspective for the future is to fully exploit the potential of our original optical set-up by performing two-color experiments: combining optomechanical techniques in the telecom band with traditional polariton spectroscopy in the exciton band. Our sample can be excited either from the top, in confocal configuration, to generate polaritons for instance, or with the suspended waveguide in the plane of the disk. By exploiting these two possibilities, we can simultaneously actuate and detect the mechanical motion of the disk with telecom light and create polaritons by either quasi-resonant or non-resonant excitation in the exciton band, as represented in figure 5.12.

Under peculiar conditions, quantum-well exciton-polaritons in a cavity can form a Bose-Einstein condensate. The two-color scheme would allow studying the interaction between a mechanical resonator and such a condensate [81,318,319], or inversely to impact this condensate with a well defined mechanical motion. The superfluid behavior of polariton gas [77,320]

could be probed optomechanically with high resolution enabled by telecom technologies.

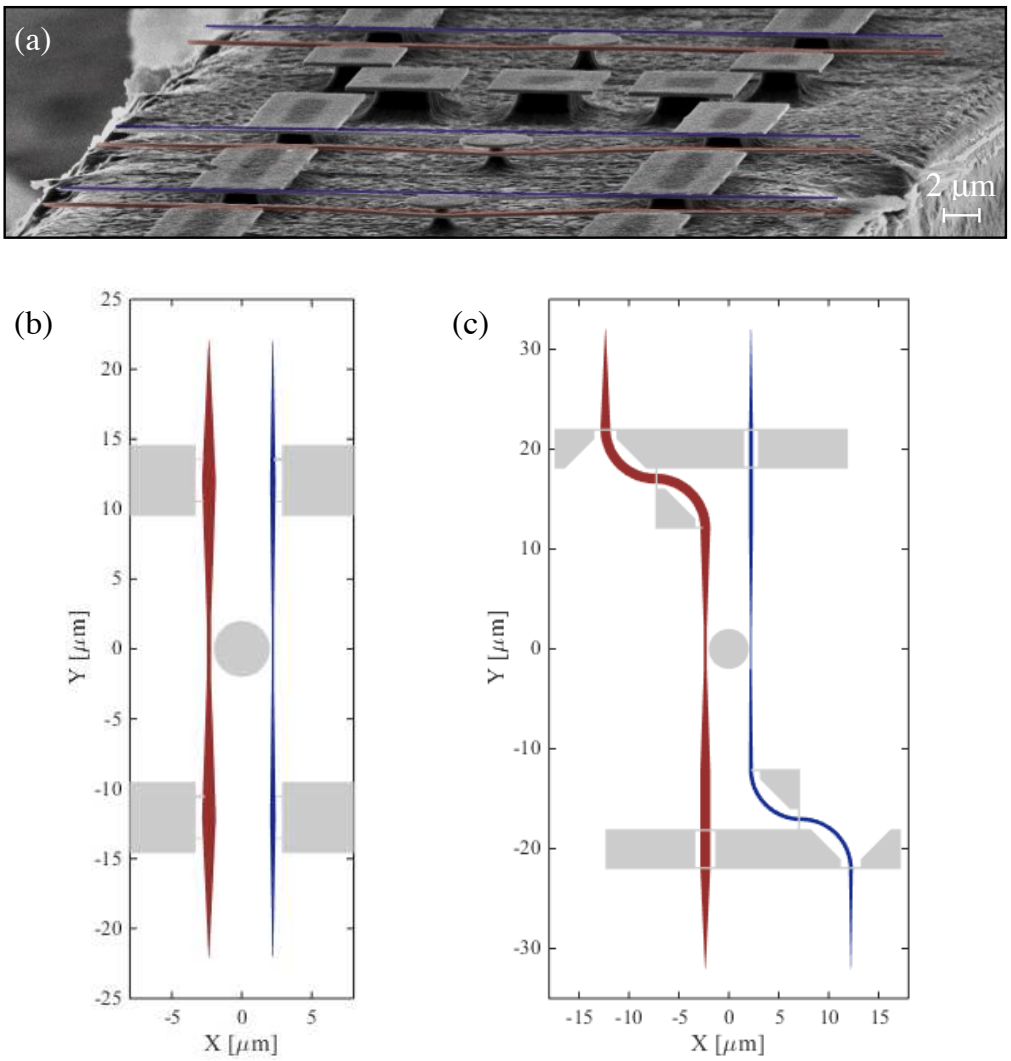

Figure 5.12 – (a) SEM micrograph of a sample with a double-waveguide structure, Magnification $\sim$ 1.6K. (b) Schematic representation of the double-waveguide structure corresponding to (a). (c) Schematic representation of a more complex double-waveguide structure, the space between the tips of each waveguide is increased to avoid a simultaneous injection on both waveguides. The color red/blue corresponds to the waveguide optimized for telecom/exciton band.

This hybrid configuration, combining a confocal and in-plane approach is ready, and experiments will be carried out very soon. Now, if we want to make a complete in-plane approach for the two-color experiments several dedicated features need to be brought. This concern notably the design of our waveguide/resonator units. The simplest option to operate a resonator with two colors is to employ a single waveguide and make it compliant with both photon-bands (exciton and telecom). With this mindset, we tried several combinations of taper width w_t, and gap distance g_{dw}. Unfortunately, as already illustrated in

figure 3.17, the range of waveguide geometric parameters required for optimized operation in the two photon-bands is very different. For instance, using the geometric parameters of the exciton band waveguide (small g_{dw}, small w_t), lead to an over-coupled regime for photons in the telecom band. Another approach is to use two waveguides, one for each band, as represented in figure 5.12. This four-port photonic chip approach was used in our group to demonstrate Second Harmonic Generation and Spontaneous Parametric Down Conversion in an AlGaAs platform [63]. This type of architecture is, however, less compact (especially structures with the architecture illustrated in figure 5.12 (c)) and increases the length of the light path inside the waveguide, which is problematic when having linear absorption in the material. Another issue is that in our set-up, we can only address two ports, one on each side of the chip, meaning that if we use the two μ-lensed fibers to inject both telecom and exciton band photons in the two respective waveguides, the only possible solution to collect the signal is to use the confocal configuration, which is not efficient to collect signal coming from WGMs.

In the current state of our chip design, we choose to keep a single waveguide approach. The sample possesses both waveguide/resonator units optimized for telecom and exciton band wavelength.

5.2.3 Phonoritons

As the effective optomechanical coupling strength increases with the number of polariton inside the cavity, it can at some point exceed both the polariton decay rate $\kappa_{l/u}$ and mechanical damping rate Γ_m. In that scenario, the energy exchange between mechanical motion and polaritons is strong, and the normal modes of the system become hybrid. These are so-called phonoritons, a superposition of photons, excitons, and phonons (see figure 5.13 (b)).

Historically the notion of phonoritons was introduced in reference [321]. In terms of second quantization operators $\hat{a}_k$,$\hat{d}_k$,$\hat{b}_k$ for photons, excitons and phonons, the Hamiltonian describing the system reads [322]:

$$\begin{aligned}\hat{H} = &\sum_k \hbar \left[\omega_c(k)\hat{a}_k^\dagger\hat{a}_k + \omega_x(k)\hat{d}_k^\dagger\hat{d}_k + \frac{\Omega_R}{2}(\hat{a}_k^\dagger\hat{d} + \hat{a}_k\hat{d}_k^\dagger)\right] \\ &+ \sum_q \hbar\omega_m(q)\hat{b}_q^\dagger\hat{b}_q + \sum_{k,q}\left[M(k-q)\hat{d}_k^\dagger\hat{d}_q(\hat{b}_{k-q} + \hat{b}_{q-k}^\dagger) + c.c.\right]\end{aligned} \tag{5.20}$$

This Hamiltonian can be rewritten in the polariton basis :

$$\hat{H} = \sum_k \hbar\omega_\eta(k)\hat{p}_{\eta,k}^\dagger\hat{p}_{\eta,k} + \sum_k \hbar\omega_m(k)\hat{b}_k^\dagger\hat{b}_k + \sum_{k,q}\left[M'(k-q)\hat{p}_{\eta,k}^\dagger\hat{p}_{\eta,q}(\hat{b}_{k-q} + \hat{b}_{q-k}^\dagger) + c.c.\right] \tag{5.21}$$

An expression that recalls the Hamiltonians of eqs. (1.39), where η represents a polariton that sits either in the upper or lower branch. Considering now a strong pumping close to

the resonance of the polariton mode k_0, one can diagonalize the Hamiltonianto obtain a new energy dispersion :

$$\omega_{\pm} = \frac{1}{2}\left(\omega(k) - \omega(k_0) \ {}^{+}\!/_{-} \ \omega_m(k_0 - k)\right) \pm \frac{1}{2}\left[\left[\omega(k) - \omega(k_0) - \omega_m(k_0 - k)\right]^2 + XQ\right]^{1/2} \quad (5.22)$$

with X the excitonic fraction of the polariton and $Q = \sqrt{VN_0}M(k - k_0)$, where V is the volume of the crystal, and N_0 the occupation number of the incident polariton. The sign $\pm$ stands for the two phonoriton branch (+: upper phonoriton - UPho, −: lower phonoriton - LPho), while ${}^{+}\!/_{-}$ is for the Stokes/Anti-stokes scattering process, i.e. for $\omega = \omega_0 \pm \omega_m(k_0 - k)$. This dispersion results in the appearance of a new gap and a new anti-crossing behavior as illustrated in figure 5.13 (a).

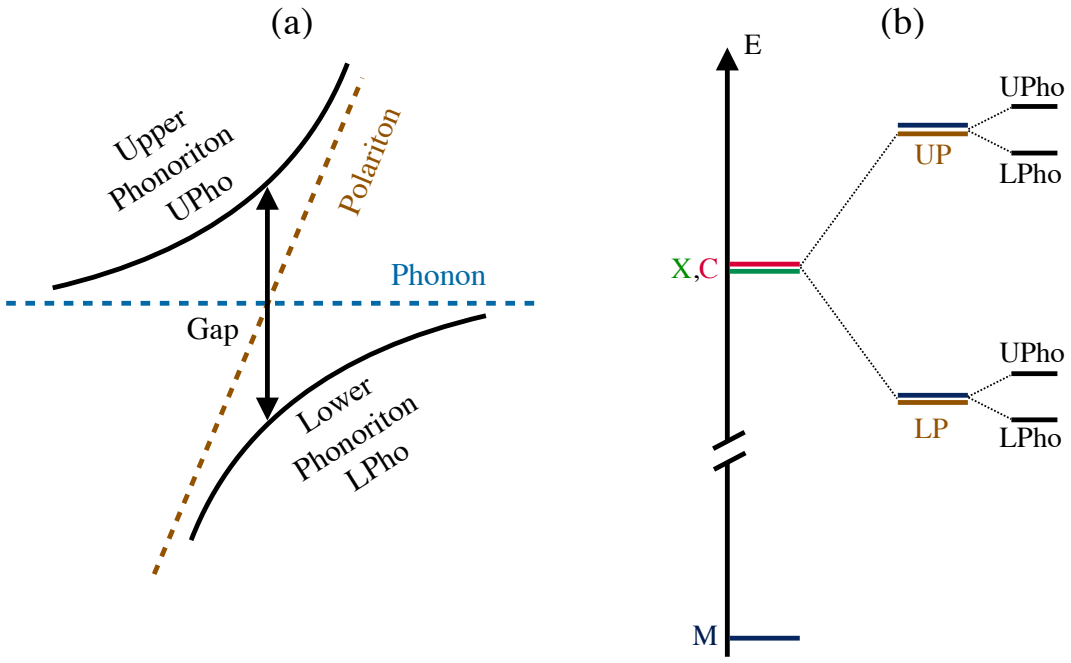

Figure 5.13 – (a) Dispersion of the phonoriton close to the Stokes frequency (b) Energy diagram of the phonoritons coupling. UPho: upper phonoritons. LPho: lower phonoritons

There has been little experimental evidence of the existence of phonoritons phenomena. Our system is a potential candidate to reach this regime.

Conclusion

This doctoral work has been focused on the conceptual development, design, fabrication, and testing of hybrid GaAs disk optomechanical resonators embedding MQW structures. We developed a minimal quantum model to describe this tripartite system involving photons, excitons, and phonons. This led us to establish which phenomena could be expected to occur in such a platform. Thorough modeling of the optical, mechanical, and excitonic modes in the geometry of a disk resonator was then carried out, as well as analytic expressions to quantitatively predict their mutual coupling. We then went through the challenges in terms of design, experiments, and fabrication, induced by such a hybrid structure. Great efforts were devoted to enabling the optic l operation of the devices in the wavelength range of the MQW exciton, but also in the telecom range traditionally used by the group until now. Despite our first success, further improvement in the technology will involve a reduction of the exciton linewidth and an improvement in the injection/collection efficiency of suspended waveguides (particularly working in the exciton range).

We experimentally demonstrated the existence of polaritons, half-matter half-light particles, in our GaAs disks. Strong coupling signatures, such as anti-crossing, were obtained by tuning optical modes and excitonic resonances, varying both the temperature and cavity size. To our knowledge, it is the first observation of quantum-well exciton-polaritons in a whispering gallery mode resonator. This observation was enabled by the peculiarities of our experimental set-up, which allows different configurations of signal excitation/collection combining confocal microscopy with resonant near-field laser spectroscopy. The control of polaritons in such a disk resonator establishes this platform for polaritonic optomechanical experiments.

Concomitantly, we checked that the presence of this MQW does not disturb optomechanical operations at telecom wavelength. Optomechanical self-oscillation was for example achieved at both room temperature and cryogenic temperature. We highlighted specific features in the behavior of our structure that arises from modified free carriers dynamics imputable to the presence of the active MQW structure. In a near future, efforts will be pursued to perform optomechanical experiments in the exciton wavelength range. In such a regime, polaritons are generated and enhancement of the optomechanical coupling is expected. A second step will be to combine telecom optomechanical experiments with the generation of a polariton condensate and use this disk platform to study the condensate interacting with mechanical vibrations.

List of publications

The work done during this thesis resulted in three poster presentations in national conferences/summer schools and three papers (one accepted and two in preparation) listed below:

- N. Carlon Zambon, Z. Denis, R. De Oliveira, S. Ravets, C. Ciuti, I. Favero and J. Bloch, " Enhanced cavity optomechanics via quantum-well exciton polariton", *submitted* [113].

- R. De Oliveira, M. Colombano, A. Lemaître, and I. Favero, "Quantum well exciton-polaritons in a whispering gallery mode semiconductor microcavity", *in preparation* [276].

- I. Roland, A. Borne, M. Ravaro, R. De Oliveira, S. Suffit, P. Filloux, and A. Lemaître, and I. Favero, and G.Leo,"Frequency doubling and parametric fluorescence in a four-port aluminum gallium arsenide photonic chip", *Opt Lett.* **45** (10), 2878-2881 (2020) [63].

Glossary

$Q_{\mathbf{m}}$ Mechanical quality factor. 67, 73

$Q_{\mathbf{opt}}$ Optical quality factor. 71, 73, 76, 78, 80, 81

μ-lensed fiber Micro-Lensed fiber. vi, vii, ix, 66–69, 82, 87–89, 107, 108, 123, 155

AFM Atomic Force Microscope. 1

AlAs Aluminium Arsenide. 43, 177

ALD Atomic Layer Deposition. 80, 112

AlGaAs Aluminium Gallium Arsenide. iv, ix, 4, 94, 104–106, 155

BCK chemical etchant solution made with an isovolumic mixing of hydrobromic acid (H**B**r), acetic acid (**C**H_3COOH) and potassium dichromate ($\mathbf{K}_2Cr_2O_7$) aqueous solutions. 99, 109

BEC Bose-Einstein Condensate. 134

BRF BiRefringent Filter. 71, 72

C-μPL Confoncal Micro-Photo-Luminescence. vi, 69, 70

C-μPL Micro Confocal Photo-Luminescence. viii, 94

CMT Coupled Modes Theory. vi, 75, 76

CW-CCW ClockWise-CounterClockWise coupling. vii, 77, 81

EBL Electron Beam Lithography. 99, 101–103

ECDL External Cavity Diode Laser. 73

EDFA Erbium Doped Fiber Amplifier. 71, 152

ESA Electrical Spectrum Analyzer. 66

FCA Free Carrier Absorption. xii, 142, 143

FDTD Finite Difference Time Domain. viii, 26, 87–90

FEM Finite Element Method. v–vii, x, xiv, 26, 34, 35, 41–43, 55, 79, 83, 84, 86, 87, 94, 126, 143, 148

FPC Fiber Polarization Controller. 66

FSR Free Spectral Range. 71

FWHM Full Width at Half Maximum . viii, 73, 97, 116

GaAs Gallium Arsenide. iv, v, vii, viii, x–xii, xiv, xv, 3–5, 24, 39, 42–44, 52–55, 70, 75, 79–83, 90, 91, 94, 95, 99, 104, 106, 107, 109, 119, 124, 136, 139, 140, 142, 143, 146, 157, 177, 179

H_2 dihydrogen. 106

H_3PO_4/H_2O_2 chemical etchant solution made with an isovolumic mixing of phosporic acid (H_3PO_4), hydrogen peroxide (H_2O_2) and water (H_2O). ix, 99, 109, 110

HF hydrofluoric acid. ix, 99, 105–107, 110

HH Heavy Holes. 91, 93, 94, 114, 179

ICP Inductively Coupled Plasma. ix, 99, 102, 104–107, 118

ICT Information and Communication Technology. 1

InAs Indium Arsenide. 43, 95, 177

InGaAs Indium Gallium Arsenide. viii, xv, xvi, 90, 95, 99

IPA Isopropanol $CH_3CHOHCH_3$. 101, 105–107

KOH Potassium hydroxyde. 106

LH Light Holes. 114, 179

LP Lower Polariton. iv, v, viii–xi, 17–22, 97, 98, 121–123, 128, 129, 131, 134–136

MEMS Micro-ElectroMechanical Systems. 1

MQW multiple quantum well. viii, xii, 3, 5, 24, 61, 90, 91, 95, 99, 122, 123, 125, 131, 135, 142, 146, 151, 157

MST Maxwell Stress Tensor. 52

N_2 dinitrogen. 101

O_2 dioxygen. 103, 106

OSA Optical Spectrum Analyzer. 66, 121

PD_{AC} Fast Photo-Diode. 66

PD_{DC} quasi-DC Photo-Diode. 66

PL Photo-Luminescence. x–xii, xiv, 66, 67, 69, 112, 114, 117, 119–123, 125–132, 135, 146–148, 151

PML Perfectly Matched layer. 79

PZT PieZoelectric Translator. 71

QW quantum well. v, vi, viii, xi, 5, 20, 24, 47, 49, 56, 59, 61, 80, 90, 92, 95, 96, 99, 114, 124, 126, 130, 133, 135–139, 146, 150, 152

RBM Radial Breathing Mode . iv–vi, xii–xiv, 3, 4, 40–43, 54, 55, 62–64, 74, 140, 141, 164

RIE Reactive Ion Etching. ix, 99, 103, 104

SEM Scanning Electron Microscope. iv, ix, xiii, 4, 103, 105–107, 110, 111, 154

TE Transverse Electric. v–viii, x, 26–35, 55, 57, 66, 74, 79, 82–90, 119, 126, 176

TEM Transmission Electron Microscopy. 79

Ti:S Titanium Sapphire. 71

TM Transverse Magnetic. v, vii, viii, 26–29, 31, 32, 39, 66, 83–85, 88, 119, 176

TPA Two Photons Absorption. vii, xii, 78, 80, 81, 138, 142, 143, 146, 148, 149

UP Upper Polariton. iv, v, viii–xi, 17–22, 97, 98, 120–122, 128, 129, 134

UV ultra violet. 102, 107, 108

VOA Variable Optical Attenuator. 66

WGM Whispering Gallery Mode. ii, iv–vii, x, xii–xv, 3–5, 24–26, 32–35, 38, 39, 51, 54, 55, 60, 66, 70, 71, 75–77, 79–82, 85, 86, 113, 114, 117, 119–131, 138–140, 146, 147, 149, 152, 155

Appendix A

Input-Output Formalism: application to hybrid optomechanics

A.1 Mathematical definitions

Throughout this section, we use the following definition for the Fourier transform of a random signal $u(t)$.

$$u[\omega] = \frac{1}{\sqrt{2\pi}} \int_{-\infty}^{+\infty} u(t) e^{-j\omega t} dt \tag{A.1}$$

$$u(t) = \frac{1}{\sqrt{2\pi}} \int_{-\infty}^{+\infty} u[\omega] e^{j\omega t} d\omega \tag{A.2}$$

For operators $\hat{U}(t)$ the definitions are similar :

$$\hat{U}[\omega] = \frac{1}{\sqrt{2\pi}} \int_{-\infty}^{+\infty} \hat{U}(t) e^{-j\omega t} dt \tag{A.3}$$

$$\hat{U}(t) = \frac{1}{\sqrt{2\pi}} \int_{-\infty}^{+\infty} \hat{U}[\omega] e^{j\omega t} d\omega \tag{A.4}$$

$$\hat{U}^\dagger[\omega] = \frac{1}{\sqrt{2\pi}} \int_{-\infty}^{+\infty} \hat{U}^\dagger(t) e^{-j\omega t} dt \tag{A.5}$$

$$\tag{A.6}$$

Note the same definition is used for taking the Fourier transform of the conjugate, meaning that $\hat{U}^\dagger[\omega] = \left(\hat{U}[-\omega]\right)^\dagger$.

The power spectrum $S_{uu}(\omega)$ of a real random signal $u(t)$ is a function describing how the total power of this signal is distributed over the different frequencies constituting the signal. If the process corresponding to this signal is stationary and the two time-correlation function $g(\tau) \equiv \langle u(t)u(t+\tau)\rangle$ only depends on the time difference τ then the power spectrum is linked to $u(t)$ and to its Fourier transform $U[\omega]$ via :

$$S_{uu}(\omega) = \int_{-\infty}^{+\infty} \langle u(t)u(t+\tau)\rangle e^{j\omega\tau} d\tau \tag{A.7}$$

$$= \int_{-\infty}^{+\infty} \langle u(\omega)u(\omega')\rangle d\omega' \tag{A.8}$$

The first relation is a direct result of the Wiener-Kinchin theorem, the second one comes from Fourier transforms properties. The above definitions can be applied to operators [88, 323].

A.2 Introduction to the formalism

A.2.0.1 Example : Single optical cavity

In this section, we follow the method described in [90] to obtain the quantum stochastic Langevin equation of a system coupled to an external bath. We consider here the case of a single optical cavity (harmonic oscillator) coupled to a thermal environment. The cavity is described by the following Hamiltonian :

$$\hat{H}_{sys} = \hbar\omega_c \hat{a}^\dagger \hat{a} \tag{A.9}$$

with ω_c the resonance frequency and $\hat{a}^\dagger$ ($\hat{a}$) the creation (annihilation) operator. The thermal bath is described by a continuum of independent harmonic oscillators represented by the Hamiltonian,

$$\hat{H}_{bath} = \hbar \int \omega \hat{A}^\dagger(\omega)\hat{A}(\omega) d\omega \tag{A.10}$$

where the bath creation $\hat{A}^\dagger(\omega)$ and annihilation $\hat{A}(\omega)$ operators obey the commutation relation $\left[\hat{A}(\omega'), \hat{A}^\dagger(\omega)\right] = \delta(\omega - \omega')$. The coupling Hamiltonian describing the interaction between the system and the bath is given by :

$$\hat{H}_{coupling} = -j\hbar \int d\omega \sqrt{\kappa(\omega)} \left[\hat{a}^\dagger \hat{A}(\omega) - \hat{A}^\dagger(\omega)\hat{a}\right] \tag{A.11}$$

where $\sqrt{\kappa(\omega)}$ represents the strength of the interaction. The actual frequency limits are $(0, \infty)$ but for high-frequency optical systems we can shift the integration to the cavity resonance frequency, the limits become then $(-\omega_c, +\infty)$, but as ω_c is large, set the lower limit to $-\infty$ is a good approximation.

The Heisenberg equation of motion for $\hat{A}(\omega)$ at any given pulsation ω is :

$$\dot{\hat{A}}(\omega) = -j\omega\hat{A}(\omega) + \sqrt{\kappa(\omega)}\hat{a} \tag{A.12}$$

There is two different ways of solving this equation either we integrate with an initial condition $t_0 < t$ (*input*), or we integrate with a final condition $t_1 > t$ (*output*). t_0 corresponds

physically to the initial time when the cavity and the bath are not in interaction and t_1 the duration of the interaction. The two solutions are respectively :

$$\hat{A}(\omega) = e^{-j\omega(t-t_0)}\hat{A}_0(\omega) + \int_{t_0}^{t} \sqrt{\kappa(\omega)} e^{j\omega(t-t')}\hat{a}(t')dt' \tag{A.13}$$

with $\hat{A}_0(\omega)$ the value of $\hat{A}(\omega)$ at $t = t_0$ and,

$$\hat{A}(\omega) = e^{-j\omega(t-t_1)}\hat{A}_1(\omega) - \int_{t}^{t_1} \sqrt{\kappa(\omega)} e^{-j\omega(t-t')}\hat{a}(t')dt' \tag{A.14}$$

where $\hat{A}_1(\omega)$ the value of $\hat{A}(\omega)$ at $t = t_1$. The first term in both solutions corresponds to the evolution of the bath isolated, while the second term represents the evolution of the optical mode leaking into the bath.

The system annihilation operator obeys to the following Heisenberg equation of motion :

$$\dot{\hat{a}} = -j\omega_c\hat{a} - \int_{-\infty}^{+\infty} d\omega \sqrt{\kappa(\omega)}\hat{A}(\omega) \tag{A.15}$$

In terms of the initial condition we have the following equation :

$$\dot{\hat{a}} = -j\omega_c\hat{a} - \int_{-\infty}^{+\infty} d\omega \sqrt{\kappa(\omega)} e^{-j\omega(t-t_0)}\hat{A}_0(\omega) - \int_{-\infty}^{+\infty} d\omega\kappa(\omega) \int_{t_0}^{t} e^{-j\omega(t-t')}\hat{a}(t')dt' \tag{A.16}$$

We proceed now to a new assumption, we take $\kappa(\omega)$ nearly constant (frequency independent) over the bandwidth of the external modes, this approximation is also know as the first *Markov approximation* [90]. Thus we set :

$$\sqrt{\kappa(\omega)} = \sqrt{\frac{\kappa_c}{2\pi}} \tag{A.17}$$

where κ_c corresponds to the cavity decay rate which determines the out-coupling of the cavity modes with the external modes. We also define an *input field* operator as :

$$\hat{a}_{in} = \frac{-1}{\sqrt{2\pi}} \int_{-\infty}^{+\infty} d\omega e^{-j\omega(t-t_0)}\hat{A}_0(\omega) \tag{A.18}$$

Given the fact that,

$$\int_{-\infty}^{+\infty} d\omega e^{-j\omega(t-t_0)} = 2\pi\delta(t-t_0) \tag{A.19}$$

we can demonstrate that the input field satisfy the following relation $\left[\hat{a}_{in}(t), \hat{a}_{in}^{\dagger}(t')\right] = \delta(t-t')$. A quick analysis of the previous equations shows that $\hat{a}_{in}$ and $\hat{A}_0(\omega)$ have different units, the system is interacting at each time t with a delta-bath like function independent

of other bath modes at earlier or other times.

With the Markovian approximation we get :

$$\begin{aligned}\int_{-\infty}^{+\infty} d\omega\kappa(\omega)\int_{t_0}^{t} e^{-i\omega(t-t')}\hat{a}(t')dt' &\simeq \frac{\kappa_c}{2\pi}\int_{-\infty}^{+\infty} d\omega\int_{t_0}^{t} e^{-i\omega(t-t')}\hat{a}(t')dt' \\ &= \frac{\kappa_c}{2\pi}2\pi\int_{t_0}^{t}\delta(t-t')\hat{a}(t')dt' = \frac{\kappa_c}{2}\hat{a}(t)\end{aligned} \tag{A.20}$$

where we have used the following relation :

$$\int_{t_0}^{t}\delta(t-t')f(t')dt' = \int_{t}^{t_1}\delta(t-t')f(t')dt' = \frac{1}{2}f(t), \qquad (t_0 < t < t_1) \tag{A.21}$$

The system creation operator thus obeys the following quantum Langevin equation :

$$\begin{aligned}\dot{\hat{a}}(t) &= -j\omega_c\hat{a} - \int_{-\infty}^{+\infty} d\omega\sqrt{\kappa(\omega)}e^{-i\omega(t-t_0)}\hat{A}_0(\omega) - \int_{-\infty}^{+\infty} d\omega\kappa(\omega)\int_{t_0}^{t} e^{-i\omega(t-t')}\hat{a}(t')dt' \\ &= -j\omega_c\hat{a} - \frac{\kappa_c}{2}\hat{a}(t) + \sqrt{\kappa_c}\hat{a}_{in}(t) \\ &= -(j\omega_c + \frac{\kappa_c}{2})\hat{a}(t) + \sqrt{\kappa_c}\hat{a}_{in}(t)\end{aligned} \tag{A.22}$$

This quantum stochastic differential equation (QSDE) for the intra-cavity field indicates that the amplitude is damped at a rate $\kappa_c/2$ due to energy radiation to the bath, and that the quantum noise entering the cavity appears explicitly as the input operator $\hat{a}_{in}(t)$.

In a similar fashion, if we use the final condition (eq. (A.14)), we define an *output field* and obtain the QSDE for the output modes :

$$\dot{\hat{a}}(t) = -(j\omega_c - \frac{\kappa}{2})\hat{a}(t) - \sqrt{\kappa_c}\hat{a}_{out}(t) \tag{A.23}$$

where the output field is defined as,

$$\hat{a}_{out} = \frac{-1}{\sqrt{2\pi}}\int_{-\infty}^{+\infty} d\omega e^{-j\omega(t-t_1)}\hat{A}_1(\omega) \tag{A.24}$$

By using the equations (A.22) and (A.23) we finally obtain the input-output boundary condition :

$$\hat{a}_{out}(t) = \sqrt{\kappa}\hat{a}(t) - \hat{a}_{in}(t) \tag{A.25}$$

To include an external laser driving of the cavity, we can either admit that the input field $\hat{a}_{in}(t)$ has an average value or add an explicit linear driving term of the form :

$$\hat{H}_{drive} = -j\left(\alpha_{ext}e^{-j\omega_l t}\hat{a}^{\dagger} + h.c.\right) \tag{A.26}$$

A.2.0.2 Quantum Stochastic Differential Equations for phonons and excitons

Provided that the thermal bath and the coupling Hamiltonian possess the same form, this formalism can be applied to any bosonic operator. For the phonon ($\hat{b}$ and the exciton ($\hat{d}$) we have similar relations :

$$\frac{d}{dt}\hat{b}(t) = -(j\omega_m + \frac{\Gamma_m}{2})\hat{b}(t) + \sqrt{\Gamma_m}\hat{b}_{in}(t) \tag{A.27}$$

$$\frac{d}{dt}\hat{d}(t) = -(j\omega_x + \frac{\kappa_x}{2})\hat{d}(t) + \sqrt{\kappa_x}\hat{d}_{in}(t) \tag{A.28}$$

where Γ_m/κ_x represents the damping and $\hat{b}_{in}/\hat{d}_{in}$ the input-operator for the phonon/exciton.

A.3 Bath correlation functions

Photons, phonons and excitons are bosons described by the Hamiltonian of a quantum harmonic oscillator, their occupancy probability for an certain energy level $p(n)$ is given by the Bose-Einstein statistics :

$$p(n) = \exp\left(\frac{n\hbar\omega}{k_B T}\right)(1 - \exp\left(\frac{\hbar\omega}{k_B T}\right)) \tag{A.29}$$

The mean occupation of the oscillator is :

$$\overline{n}_{th} = \langle\hat{n}\rangle = \sum_{n=0}^{\infty} np(n) = \left[\exp\left(\frac{\hbar\omega}{k_B T}\right) - 1\right]^{-1} \tag{A.30}$$

In this way, if we suppose that the external bath is initially in a thermal state, i.e. every bath modes exist at a temperature T and a time t, we get the following correlations for the input operators :

$$\begin{aligned}
&\left\langle \hat{e}_{in}(t), \hat{e}^{\dagger}_{in}(t') \right\rangle = (\overline{n}_{th} + 1)\delta(t - t') \\
&\left\langle \hat{e}^{\dagger}_{in}(t'), \hat{e}_{in}(t) \right\rangle = \overline{n}_{th}\delta(t - t') \\
&\langle \hat{e}_{in}(t), \hat{e}_{in}(t') \rangle = \left\langle \hat{e}^{\dagger}_{in}(t'), \hat{e}^{\dagger}_{in}(t') \right\rangle = 0
\end{aligned} \tag{A.31}$$

where $\hat{e}_{in}(t)$ is a generic input operator. In the case of optical systems and exitonic resonances, the range of frequency is sufficiently high ($\hbar\omega_l, \hbar\omega_c, \hbar\omega_x \gg k_B T$) to approximate the bath as a zero temperature (vacuum, $\overline{n}^{cav}_{th} \simeq 0$), thus for the photon and the exciton the previous noise correlation functions become :

$$\begin{aligned}
&\left\langle \hat{a}_{in}(t), \hat{a}^{\dagger}_{in}(t') \right\rangle = \delta(t - t') && \left\langle \hat{d}_{in}(t), \hat{d}^{\dagger}_{in}(t') \right\rangle = \delta(t - t') \\
&\left\langle \hat{a}^{\dagger}_{in}(t'), \hat{a}_{in}(t) \right\rangle = 0 && \left\langle \hat{d}^{\dagger}_{in}(t'), \hat{d}_{in}(t) \right\rangle = 0 \\
&\langle \hat{a}_{in}(t), \hat{a}_{in}(t') \rangle = \left\langle \hat{a}^{\dagger}_{in}(t'), \hat{a}^{\dagger}_{in}(t') \right\rangle = 0 && \left\langle \hat{d}_{in}(t), \hat{d}_{in}(t') \right\rangle = \left\langle \hat{d}^{\dagger}_{in}(t'), \hat{d}^{\dagger}_{in}(t') \right\rangle = 0
\end{aligned} \tag{A.32}$$

Regarding the mechanical noise operator, the noise correlations are then given by :

$$\begin{aligned}\left\langle \hat{b}_{in}(t), \hat{b}_{in}^{\dagger}(t') \right\rangle &= (\overline{n}_{th}^{mec} + 1)\delta(t - t') \\ \left\langle \hat{b}_{in}^{\dagger}(t'), \hat{b}_{in}(t) \right\rangle &= \overline{n}_{th}^{mec}\delta(t - t') \\ \left\langle \hat{b}_{in}(t), \hat{b}_{in}(t') \right\rangle &= \left\langle \hat{b}_{in}^{\dagger}(t'), \hat{b}_{in}^{\dagger}(t') \right\rangle = 0\end{aligned} \tag{A.33}$$

The lowest temperature T_{min} being accessed in our cryostat is 3K (accentuated by the black dashed line on figure A.1), at this temperature the phonon occupancy for the first three RBMs is well above 1. For $T \geq T_{min}$, and for the mechanical frequencies relevant here, the approximation $\bar{n}_{th}^{mec} = k_B T/\hbar\omega$ is valid.

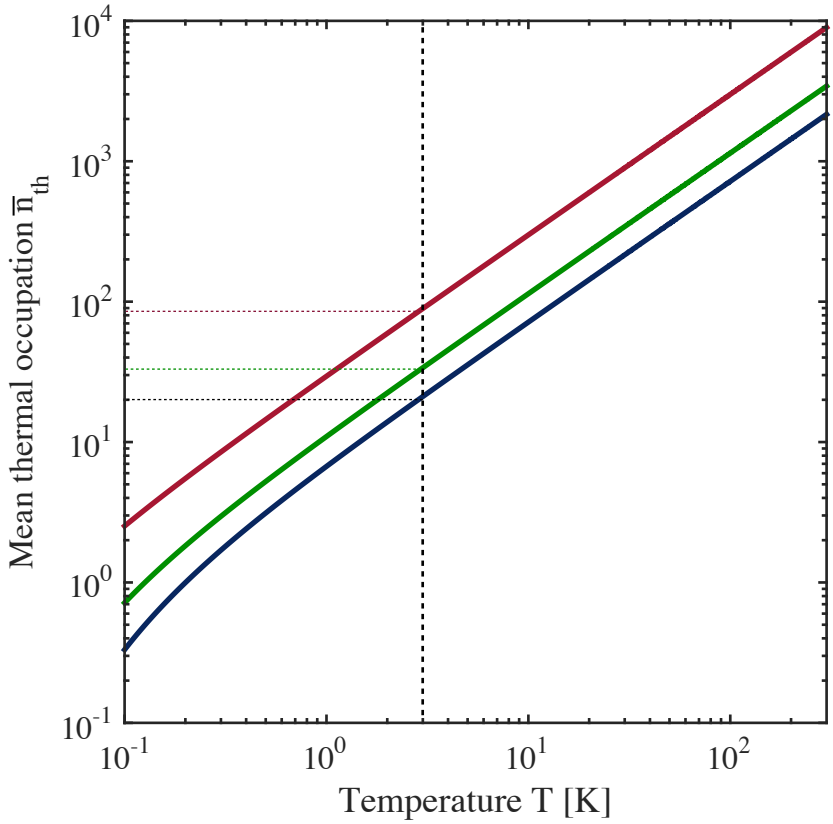

Figure A.1 – Thermal phonon population as a function of temperature for the first three RBMs (see Table 2.1)

A.4 Limitation of cooling via dynamical back-action

We compute here the quantum noise spectrum of the linearized radiation pressure derived from the hamiltonian (1.20) :

$$\hat{F} = \frac{\hbar G}{x_{ZPF}}(\delta\hat{a}^\dagger + \delta\hat{a}) \tag{A.34}$$

In the absence of the optomechanical coupling the spectral density of this force is given by [1] [96]:

$$S_{FF}[\omega_m] = \left(\frac{\hbar G}{x_{ZPF}}\right)^2 \frac{\kappa_c}{(\Delta + \omega_m)^2 + \left(\frac{\kappa_c}{2}\right)^2} \tag{A.35}$$

evaluated here for $\omega = \omega_m$. We introduce the coefficients A_+ and A_- proportional respectively to the Stokes and anti-Stokes scattering rates (illustrated respectively by red and blue double arrows on figure 1.2) of cavity photons and defined by :

$$A_\pm = \frac{x_{ZPF}^2 S_{FF}[\mp\omega_m]}{\hbar^2} = \frac{G^2\kappa_c}{(\Delta \mp \omega_m)^2 + \left(\frac{\kappa_c}{2}\right)^2} \tag{A.36}$$

The cooling process then occurs when $A_- > A_+$ and amplification in the opposite situation. These two factors can be directly derived from Fermi's Golden Rule applied to the optomechanical interaction Hamiltonian $\hat{H}_{int}$ [88]. Hence they logically appear in the expression of the optical damping, $\Gamma_{om} = A_- - A_+$. The steady-state phonon occupancy $\langle n\rangle$ in terms of the frequency domain fluctuation operators is :

$$\begin{aligned}\langle n\rangle &= \langle\delta\hat{b}^\dagger(t)\delta\hat{b}(t)\rangle = \frac{1}{2\pi}\int_{-\infty}^{+\infty} d\omega \int_{-\infty}^{+\infty} e^{j(\omega+\omega')}\langle\delta\hat{b}^\dagger[\omega]\delta\hat{b}[\omega]\rangle \\ &= \int_{-\infty}^{+\infty} d\omega \underbrace{\frac{\Gamma'_m/2\pi}{(\omega_m-\omega)^2 + (\Gamma'_m/2)^2}}_{L[\omega]} \left[\frac{\Gamma_m\bar{n}_{th}^{mec}}{\Gamma'_m} + \frac{G^2\kappa}{\Gamma'_m}\frac{1}{(\Delta \mp \omega_m)^2 + (\kappa_c/2)^2}\right]\end{aligned} \tag{A.37}$$

In the expression (A.37) the Lorentzian function $L[\omega]$ is peaked around $\omega = \omega_m$, we assume that the bracketed term in (A.37) is approximately constant over the bandwidth of the expression, the phonon occupancy is therefore given by :

$$\langle n\rangle = \underbrace{\frac{\Gamma_m\bar{n}_{th}^{mec}}{\Gamma'_m}}_{\bar{n}_{th}} + \underbrace{\frac{A_+}{\Gamma'_m}}_{\bar{n}_{ba}} \tag{A.38}$$

where $\bar{n}_{th}^{mec}$ is the thermal occupation of the mechanical mode (see appendix A.3), $\bar{n}_{th}$ the classical cooling limit and $\bar{n}_{ba}$ the fundamental quantum limit originating from the back-action. For significant cooling $\Gamma'_m \gg \bar{n}_{th}^{mec}\Gamma_m$, this fundamental limit can be simplified to :

$$\bar{n}_{ba} \simeq \frac{A_+}{A_- - A_+} = \frac{4(\Delta + \omega_m)^2 + \kappa_c^2}{-16\omega_m\Delta} \tag{A.39}$$

which leads to a minimum phonon occupancy of

1. see the definition of the quantum power spectral density provided on section A.1

$$\min(\bar{n}_{ba}) = \frac{1}{2}\left(\sqrt{1+\frac{\kappa_c^2}{4\omega_m^2}}-1\right) \tag{A.40}$$

Obtained for an optimal laser detuning of $\Delta = -\sqrt{\omega_m^2 + \kappa_c^2/4}$ and exhibited in figure A.2. In the unresolved sideband regime ($\omega_m \ll \kappa_c$), the quantum limit is $\min(\bar{n}_{ba}) = \kappa_c/(4\omega_m)$ ($\Delta = -\kappa_c/2$), the minimum phonon number cannot reach 1, which precludes the ground state cooling of the mechanical resonator. On the other hand, in the resolved sideband regime ($\omega_m \gg \kappa_c$), the quantum limit is simplified into $\min(\bar{n}_{ba}) = \kappa_c^2/(16\omega_m^2)$ ($\Delta = -\omega_m$) which makes the ground-state cooling possible [95, 96, 324–326]. In this last regime the minimum thermal phonon occupancy is given by $\min(\bar{n}_{th}) \simeq \frac{\bar{n}_{th}^{mec}}{1+C}$, where C corresponds to the optomechanical cooperativity of the system defined by :

$$C = \frac{\Gamma_{om}}{\Gamma_m}|_{\Delta=-\omega_m} = N_{ph}C_0 \qquad C_0 = \frac{4g_0^2}{\kappa_c\Gamma_m} \tag{A.41}$$

C_0 represents the single-photon cooperativity which quantifies the coupling strength of the mechanical resonator to the optical noise bath compared to the mechanical thermal bath.

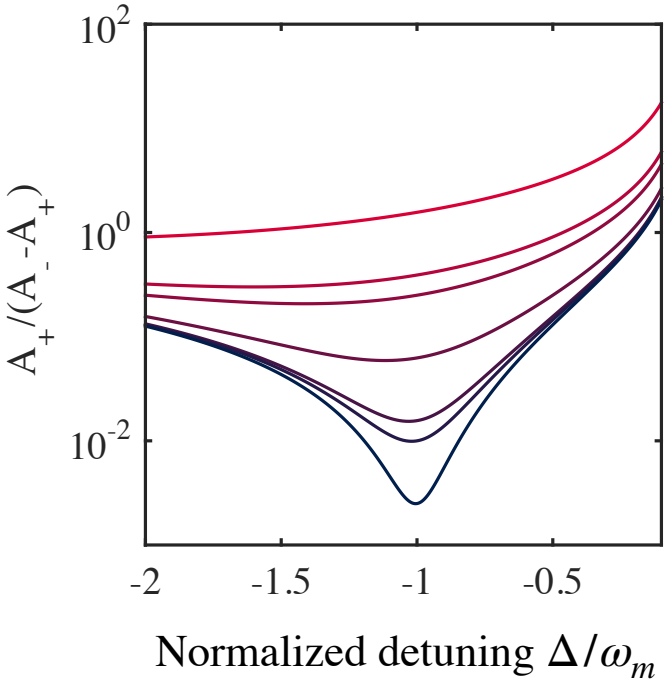

Figure A.2 – Phonon population fundamental quantum limit around the anti-Stokes sideband. The color code corresponds to different value of the ω_m/κ_c ratio. From red to blue this ratio is equal to [0.2, 0.4, 0.5, 1, 2, 2.5, 5]

The cooperativity can be artificially enhanced for a higher number of photons in the cavity, however when the injected power is increased some parasite thermal effect usually comes into play. Maximizing C_0 represents a safer way to reach the ground state. In the

light of this, one question is whether new phenomena can emerge by reaching the regime of large single-photon cooperativity $C_0 > 1$. Very few system have reached this condition [93] but some recent works already beat this criterion [327–331]. These last remarkable results are the product of extensive design improvements and optimization.

Appendix B

Quantum-well and excitons: supplements

B.1 Derivation of the effective mass equation in bulk semiconductor

In this section we derive the effective mass equation in bulk semiconductor. The derivation starts with the many body Hamiltonian (2.90):

$$\begin{aligned}\hat{H}_{ex} &= \hat{H}_0 + \hat{H}_I \\ &= \underbrace{\sum_{\boldsymbol{k}_1}\left(E_g + \frac{\hbar^2\boldsymbol{k}_1^2}{2m_c^*}\right)\hat{c}^\dagger_{c\boldsymbol{k}_1}\hat{c}_{c\boldsymbol{k}_1}}_{\boxed{1}} + \underbrace{\sum_{\boldsymbol{k}_1}\left(-\frac{\hbar^2\boldsymbol{k}_1^2}{2m_v^*}\right)\hat{c}^\dagger_{v\boldsymbol{k}_1}\hat{c}_{v\boldsymbol{k}_1}}_{\boxed{2}} \\ &+ \underbrace{\sum_{\boldsymbol{k}_1\boldsymbol{k}_2\boldsymbol{k}_3\boldsymbol{k}_4}^{\boldsymbol{k}_1\neq\boldsymbol{k}_4} \frac{e^2}{4\pi\varepsilon_0\varepsilon_r V}\frac{1}{|\boldsymbol{k}_1-\boldsymbol{k}_4|^2}\hat{c}^\dagger_{v\boldsymbol{k}_1}\hat{c}^\dagger_{c\boldsymbol{k}_2}\hat{c}_{c\boldsymbol{k}_3}\hat{c}_{v\boldsymbol{k}_4}\delta_{\boldsymbol{k}_1-\boldsymbol{k}_4,\boldsymbol{k}_3-\boldsymbol{k}_2}}_{\boxed{3}}\end{aligned} \tag{B.1}$$

We need to find an equation for the coefficients $O(\boldsymbol{k},\boldsymbol{k'})$ in order to make $|\Psi\rangle = \sum_{\boldsymbol{k},\boldsymbol{k'}} O(\boldsymbol{k},\boldsymbol{k'})\,|\Psi_0\rangle$ an eigenstate of $\hat{H}_{ex}$ i.e. :

$$\hat{H}_{ex}\,|\Psi\rangle = E\,|\Psi\rangle \tag{B.2}$$

We are going to examine the action of $\hat{H}_{ex}$ on the exciton state, starting with the part related to the conduction electrons:

$$\boxed{1}\,|\Psi\rangle = \sum_{\boldsymbol{k}_1}\sum_{\boldsymbol{k},\boldsymbol{k'}}\left(E_g + \frac{\hbar^2\boldsymbol{k}_1^2}{2m_c^*}\right)\hat{c}^\dagger_{c\boldsymbol{k}_1}\hat{c}_{c\boldsymbol{k}_1}\hat{c}^\dagger_{c\boldsymbol{k}}\hat{c}_{v\boldsymbol{k'}}O(\boldsymbol{k},\boldsymbol{k'})\,|\Psi_0\rangle \tag{B.3}$$

To simplify the product of creation and annihilation operators we apply the fermionic commutation relations:

$$\begin{aligned}\left\{\hat{c}_{\sigma\boldsymbol{k}}, \hat{c}^{\dagger}_{\sigma'\boldsymbol{k}'}\right\} &= \hat{c}_{\sigma\boldsymbol{k}}\hat{c}^{\dagger}_{\sigma'\boldsymbol{k}'} + \hat{c}^{\dagger}_{\sigma'\boldsymbol{k}'}\hat{c}_{\sigma\boldsymbol{k}} = \delta_{\boldsymbol{k},\boldsymbol{k}'}\delta_{\sigma,\sigma'} \\ \{\hat{c}_{\sigma\boldsymbol{k}}, \hat{c}_{\sigma'\boldsymbol{k}'}\} &= \left\{\hat{c}^{\dagger}_{\sigma\boldsymbol{k}}, \hat{c}^{\dagger}_{\sigma'\boldsymbol{k}'}\right\} = 0 \quad \forall \boldsymbol{k}, \boldsymbol{k'}, \sigma, \sigma'\end{aligned} \tag{B.4}$$

Using these rules we find:

$$\begin{aligned}\hat{c}^{\dagger}_{c\boldsymbol{k}_1}\hat{c}_{c\boldsymbol{k}_1}\hat{c}^{\dagger}_{c\boldsymbol{k}}\hat{c}_{v\boldsymbol{k'}} &= \delta_{\boldsymbol{k}_1,\boldsymbol{k}}\hat{c}^{\dagger}_{c\boldsymbol{k}_1}\hat{c}_{v\boldsymbol{k'}} - \hat{c}^{\dagger}_{c\boldsymbol{k}_1}\hat{c}^{\dagger}_{c\boldsymbol{k}}\hat{c}_{c\boldsymbol{k}_1}\hat{c}_{v\boldsymbol{k'}} \\ &= \delta_{\boldsymbol{k}_1,\boldsymbol{k}}\hat{c}^{\dagger}_{c\boldsymbol{k}_1}\hat{c}_{v\boldsymbol{k'}} + \hat{c}^{\dagger}_{c\boldsymbol{k}_1}\hat{c}^{\dagger}_{c\boldsymbol{k}}\hat{c}_{v\boldsymbol{k'}}\hat{c}_{c\boldsymbol{k}_1}\end{aligned} \tag{B.5}$$

Acting on the ground state $|\Psi_0\rangle$:

$$\hat{c}^{\dagger}_{c\boldsymbol{k}_1}\hat{c}_{c\boldsymbol{k}_1}\hat{c}^{\dagger}_{c\boldsymbol{k}}\hat{c}_{v\boldsymbol{k'}}|\Psi_0\rangle = \delta_{\boldsymbol{k}_1,\boldsymbol{k}}\hat{c}^{\dagger}_{c\boldsymbol{k}_1}\hat{c}_{v\boldsymbol{k'}}|\Psi_0\rangle + \hat{c}^{\dagger}_{c\boldsymbol{k}_1}\hat{c}^{\dagger}_{c\boldsymbol{k}}\hat{c}_{v\boldsymbol{k'}}\underbrace{\hat{c}_{c\boldsymbol{k}_1}|\Psi_0\rangle}_{=0} \tag{B.6}$$

The last term on the right hand side vanishes, since the conduction band is empty in the ground state. In the end the term $\boxed{1}$ acting on $|\Psi\rangle$ becomes:

$$\boxed{1}|\Psi\rangle = \sum_{\boldsymbol{k},\boldsymbol{k'}}\left[\left(E_g + \frac{\hbar^2\boldsymbol{k}^2}{2m_c^*}\right)O(\boldsymbol{k},\boldsymbol{k'})\right]\hat{c}^{\dagger}_{c\boldsymbol{k}}\hat{c}_{v\boldsymbol{k'}}|\Psi_0\rangle \tag{B.7}$$

Similarly, the part associated with the valence electrons gives the following term:

$$\boxed{2}|\Psi\rangle = \sum_{\boldsymbol{k}_1}\sum_{\boldsymbol{k},\boldsymbol{k'}}\left(-\frac{\hbar^2\boldsymbol{k}_1^2}{2m_v^*}\right)\hat{c}^{\dagger}_{v\boldsymbol{k}_1}\hat{c}_{v\boldsymbol{k}_1}\hat{c}^{\dagger}_{c\boldsymbol{k}}\hat{c}_{v\boldsymbol{k'}}O(\boldsymbol{k},\boldsymbol{k'})|\Psi_0\rangle \tag{B.8}$$

As a result, we should simplify the following product of operators:

$$\begin{aligned}\hat{c}^{\dagger}_{v\boldsymbol{k}_1}\hat{c}_{v\boldsymbol{k}_1}\hat{c}^{\dagger}_{c\boldsymbol{k}}\hat{c}_{v\boldsymbol{k'}} &= \hat{c}^{\dagger}_{c\boldsymbol{k}}\hat{c}_{v\boldsymbol{k'}} - \hat{c}_{v\boldsymbol{k}_1}\hat{c}^{\dagger}_{v\boldsymbol{k}_1}\hat{c}^{\dagger}_{c\boldsymbol{k}}\hat{c}_{v\boldsymbol{k'}} \\ &= \hat{c}^{\dagger}_{c\boldsymbol{k}}\hat{c}_{v\boldsymbol{k'}} + \hat{c}_{v\boldsymbol{k}_1}\hat{c}^{\dagger}_{c\boldsymbol{k}}\hat{c}^{\dagger}_{v\boldsymbol{k}_1}\hat{c}_{v\boldsymbol{k'}} \\ &= \hat{c}^{\dagger}_{c\boldsymbol{k}}\hat{c}_{v\boldsymbol{k'}} + \delta_{\boldsymbol{k}_1,\boldsymbol{k'}}\hat{c}_{v\boldsymbol{k}_1}\hat{c}^{\dagger}_{c\boldsymbol{k}} - \hat{c}_{v\boldsymbol{k}_1}\hat{c}^{\dagger}_{c\boldsymbol{k}}\hat{c}_{v\boldsymbol{k'}}\hat{c}^{\dagger}_{v\boldsymbol{k}_1}\end{aligned} \tag{B.9}$$

Again acting on the ground state $|\Psi_0\rangle$:

$$\hat{c}^{\dagger}_{v\boldsymbol{k}_1}\hat{c}_{v\boldsymbol{k}_1}\hat{c}^{\dagger}_{c\boldsymbol{k}}\hat{c}_{v\boldsymbol{k'}}|\Psi_0\rangle = \hat{c}^{\dagger}_{c\boldsymbol{k}}\hat{c}_{v\boldsymbol{k'}}|\Psi_0\rangle + \delta_{\boldsymbol{k}_1,\boldsymbol{k'}}\hat{c}_{v\boldsymbol{k}_1}\hat{c}^{\dagger}_{c\boldsymbol{k}}|\Psi_0\rangle - \hat{c}_{v\boldsymbol{k}_1}\hat{c}^{\dagger}_{c\boldsymbol{k}}\hat{c}_{v\boldsymbol{k'}}\underbrace{\hat{c}^{\dagger}_{v\boldsymbol{k}_1}|\Psi_0\rangle}_{=0} \tag{B.10}$$

The last term on the right hand side vanishes because in the ground state the valence band is full, no extra electron can be created. The term $\boxed{2}$ acting on $|\Psi\rangle$ becomes:

$$\boxed{2}|\Psi\rangle = \sum_{\boldsymbol{k},\boldsymbol{k'}}\left[\left(\underbrace{\sum_{\boldsymbol{k}_1}\frac{\hbar^2\boldsymbol{k}_1^2}{2m_v^*}}_{=E_0} + \frac{\hbar^2\boldsymbol{k'}^2}{2m_v^*}\right)O(\boldsymbol{k},\boldsymbol{k'})\right]\hat{c}^{\dagger}_{c\boldsymbol{k}}\hat{c}_{v\boldsymbol{k'}}|\Psi_0\rangle \tag{B.11}$$

Last but not least, we now study the part linked to the Coulomb interaction:

$$\boxed{3}\,|\Psi\rangle = \sum_{\boldsymbol{k},\boldsymbol{k'}} \sum_{\boldsymbol{k}_1\boldsymbol{k}_2\boldsymbol{k}_3\boldsymbol{k}_4}^{\boldsymbol{k}_1\neq\boldsymbol{k}_4} \frac{e^2}{4\pi\varepsilon_0\varepsilon_r V}\frac{1}{|\boldsymbol{k}_1-\boldsymbol{k}_4|^2}\delta_{\boldsymbol{k}_1-\boldsymbol{k}_4,\boldsymbol{k}_3-\boldsymbol{k}_2}\hat{c}^\dagger_{v\boldsymbol{k}_1}\hat{c}^\dagger_{c\boldsymbol{k}_2}\hat{c}_{c\boldsymbol{k}_3}\hat{c}_{v\boldsymbol{k}_4}\hat{c}^\dagger_{c\boldsymbol{k}}\hat{c}_{v\boldsymbol{k'}}O(\boldsymbol{k},\boldsymbol{k'})\,|\Psi_0\rangle \tag{B.12}$$

Simplify this last expression is a bit more complicated, we have to study a product of six fermionic operators:

$$\begin{aligned}\hat{c}^\dagger_{v\boldsymbol{k}_1}\hat{c}^\dagger_{c\boldsymbol{k}_2}\hat{c}_{c\boldsymbol{k}_3}\hat{c}_{v\boldsymbol{k}_4}\hat{c}^\dagger_{c\boldsymbol{k}}\hat{c}_{v\boldsymbol{k'}} &= -\hat{c}^\dagger_{v\boldsymbol{k}_1}\hat{c}^\dagger_{c\boldsymbol{k}_2}\hat{c}_{v\boldsymbol{k}_4}\hat{c}_{c\boldsymbol{k}_3}\hat{c}^\dagger_{c\boldsymbol{k}}\hat{c}_{v\boldsymbol{k'}} \\ &= -\hat{c}^\dagger_{v\boldsymbol{k}_1}\hat{c}^\dagger_{c\boldsymbol{k}_2}\hat{c}_{v\boldsymbol{k}_4}\hat{c}_{v\boldsymbol{k'}}\hat{c}_{c\boldsymbol{k}_3}\hat{c}^\dagger_{c\boldsymbol{k}} \\ &= -\delta_{\boldsymbol{k}_3,\boldsymbol{k}}\hat{c}^\dagger_{v\boldsymbol{k}_1}\hat{c}^\dagger_{c\boldsymbol{k}_2}\hat{c}_{v\boldsymbol{k}_4}\hat{c}_{v\boldsymbol{k'}} + \hat{c}^\dagger_{v\boldsymbol{k}_1}\hat{c}^\dagger_{c\boldsymbol{k}_2}\hat{c}_{v\boldsymbol{k}_4}\hat{c}_{v\boldsymbol{k'}}\hat{c}^\dagger_{c\boldsymbol{k}}\hat{c}_{c\boldsymbol{k}_3}\end{aligned} \tag{B.13}$$

Acting on the ground state, the last term on the right-hand sight vanishes using the same argument as for eq. (B.6). The problem is therefore reduced to the following product of four operators:

$$\begin{aligned}-\delta_{\boldsymbol{k}_3,\boldsymbol{k}}\hat{c}^\dagger_{v\boldsymbol{k}_1}\hat{c}^\dagger_{c\boldsymbol{k}_2}\hat{c}_{v\boldsymbol{k}_4}\hat{c}_{v\boldsymbol{k'}} &= \delta_{\boldsymbol{k}_3,\boldsymbol{k}}\hat{c}^\dagger_{v\boldsymbol{k}_1}\hat{c}_{v\boldsymbol{k}_4}\hat{c}^\dagger_{c\boldsymbol{k}_2}\hat{c}_{v\boldsymbol{k'}} \\ &= \delta_{\boldsymbol{k}_3,\boldsymbol{k}}\delta_{\boldsymbol{k}_1,\boldsymbol{k}_4}\hat{c}^\dagger_{c\boldsymbol{k}_2}\hat{c}_{v\boldsymbol{k'}} - \delta_{\boldsymbol{k}_3,\boldsymbol{k}}\hat{c}_{v\boldsymbol{k}_4}\hat{c}^\dagger_{v\boldsymbol{k}_1}\hat{c}^\dagger_{c\boldsymbol{k}_2}\hat{c}_{v\boldsymbol{k'}} \\ &= \delta_{\boldsymbol{k}_3,\boldsymbol{k}}\delta_{\boldsymbol{k}_1,\boldsymbol{k}_4}\hat{c}^\dagger_{c\boldsymbol{k}_2}\hat{c}_{v\boldsymbol{k'}} + \delta_{\boldsymbol{k}_3,\boldsymbol{k}}\hat{c}_{v\boldsymbol{k}_4}\hat{c}^\dagger_{c\boldsymbol{k}_2}\hat{c}^\dagger_{v\boldsymbol{k}_1}\hat{c}_{v\boldsymbol{k'}} \\ &= \delta_{\boldsymbol{k}_3,\boldsymbol{k}}\delta_{\boldsymbol{k}_1,\boldsymbol{k}_4}\hat{c}^\dagger_{c\boldsymbol{k}_2}\hat{c}_{v\boldsymbol{k'}} + \delta_{\boldsymbol{k}_3,\boldsymbol{k}}\delta_{\boldsymbol{k}_1,\boldsymbol{k'}}\hat{c}_{v\boldsymbol{k}_4}\hat{c}^\dagger_{c\boldsymbol{k}_2} - \delta_{\boldsymbol{k}_3,\boldsymbol{k}}\hat{c}_{v\boldsymbol{k}_4}\hat{c}^\dagger_{c\boldsymbol{k}_2}\hat{c}_{v\boldsymbol{k'}}\hat{c}^\dagger_{v\boldsymbol{k}_1}\end{aligned} \tag{B.14}$$

Again the last term on the right hand side vanishes using the same argument as for eq. (B.10). As a consequence, the term $\boxed{3}$ acting on $|\Psi_{ex}\rangle$ takes the following form:

$$\begin{aligned}\boxed{3}\,|\Psi\rangle = &\underbrace{\sum_{\boldsymbol{k},\boldsymbol{k'}} \sum_{\boldsymbol{k}_1\boldsymbol{k}_2\boldsymbol{k}_3\boldsymbol{k}_4}^{\boldsymbol{k}_1\neq\boldsymbol{k}_4} \frac{e^2}{4\pi\varepsilon_0\varepsilon_r V}\frac{1}{|\boldsymbol{k}_1-\boldsymbol{k}_4|^2}\delta_{\boldsymbol{k}_1-\boldsymbol{k}_4,\boldsymbol{k}_3-\boldsymbol{k}_2}O(\boldsymbol{k},\boldsymbol{k'})\left\{\delta_{\boldsymbol{k}_3,\boldsymbol{k}}\delta_{\boldsymbol{k}_1,\boldsymbol{k}_4}\hat{c}^\dagger_{c\boldsymbol{k}_2}\hat{c}_{v\boldsymbol{k'}}\,|\Psi_0\rangle\right\}}_{\boxed{A}} \\ &+\underbrace{\sum_{\boldsymbol{k},\boldsymbol{k'}} \sum_{\boldsymbol{k}_1\boldsymbol{k}_2\boldsymbol{k}_3\boldsymbol{k}_4}^{\boldsymbol{k}_1\neq\boldsymbol{k}_4} \frac{e^2}{4\pi\varepsilon_0\varepsilon_r V}\frac{1}{|\boldsymbol{k}_1-\boldsymbol{k}_4|^2}\delta_{\boldsymbol{k}_1-\boldsymbol{k}_4,\boldsymbol{k}_3-\boldsymbol{k}_2}O(\boldsymbol{k},\boldsymbol{k'})\left\{-\delta_{\boldsymbol{k}_3,\boldsymbol{k}}\delta_{\boldsymbol{k}_1,\boldsymbol{k'}}\hat{c}^\dagger_{c\boldsymbol{k}_2}\hat{c}_{v\boldsymbol{k}_4}\,|\Psi_0\rangle\right\}}_{\boxed{B}}\end{aligned} \tag{B.15}$$

Given the existing condition on the wavevectors $\boldsymbol{k}_1 \neq \boldsymbol{k}_4$ the Kronecker symbol $\delta_{\boldsymbol{k}_1,\boldsymbol{k}_4}$ in the term $\boxed{A}$ implies that this term is null. Regarding the term $\boxed{B}$ we have $\boldsymbol{k}_1 = \boldsymbol{k'}$ and $\boldsymbol{k}_3 = \boldsymbol{k}$, it can be rewritten as:

$$\boxed{B} \Longrightarrow -\sum_{\boldsymbol{k},\boldsymbol{k'}}\sum_{\boldsymbol{k}_2\boldsymbol{k}_4}\frac{e^2}{4\pi\varepsilon_0\varepsilon_r V}\frac{1}{|\boldsymbol{k'}-\boldsymbol{k}_4|^2}\delta_{\boldsymbol{k'}-\boldsymbol{k}_4,\boldsymbol{k}-\boldsymbol{k}_2}O(\boldsymbol{k},\boldsymbol{k'})\hat{c}^\dagger_{c\boldsymbol{k}_2}\hat{c}_{v\boldsymbol{k}_4}\,|\Psi_0\rangle \tag{B.16}$$

The way the wave-vectors are labeled is completely arbitrary, there is no consequence in changing the indexes, we choose to operate the following change in two times, first $\boldsymbol{k}_2 \longleftrightarrow \boldsymbol{k}, \boldsymbol{k}_4 \longleftrightarrow \boldsymbol{k'}$ and then $\boldsymbol{k}_4 \longleftrightarrow \boldsymbol{k}_1, \boldsymbol{k}_2 \longleftrightarrow \boldsymbol{k}_1$. As the result the term $\boxed{B}$ take the following form:

$$\boxed{B} \Longrightarrow -\sum_{\boldsymbol{k},\boldsymbol{k'}} \sum_{\boldsymbol{k}_1 \boldsymbol{k}_2} \frac{e^2}{4\pi\varepsilon_0\varepsilon_r V} \frac{1}{|\boldsymbol{k}_2 - \boldsymbol{k'}|^2} \delta_{\boldsymbol{k}_2 - \boldsymbol{k'}, \boldsymbol{k}_1 - \boldsymbol{k}} O(\boldsymbol{k}_1, \boldsymbol{k}_2) \hat{c}^{\dagger}_{c\boldsymbol{k}} \hat{c}_{v\boldsymbol{k'}} |\Psi_0\rangle \tag{B.17}$$

If we choose to call $\boldsymbol{k}_2 - \boldsymbol{k'} = -\boldsymbol{q'}$ and put the parts $\boxed{1}$, $\boxed{2}$ and $\boxed{3}$ together we have:

$$\begin{aligned} \boxed{1}|\Psi\rangle + \boxed{2}|\Psi\rangle + \boxed{3}|\Psi\rangle &= E|\Psi\rangle \\ \sum_{\boldsymbol{k},\boldsymbol{k'}} \left[E_g + \frac{\hbar^2 \boldsymbol{k}^2}{2m_c^*} + E_0 + \frac{\hbar^2 \boldsymbol{k'}^2}{2m_v^*} \right] O(\boldsymbol{k}, \boldsymbol{k'}) \hat{c}^{\dagger}_{c\boldsymbol{k}} \hat{c}_{v\boldsymbol{k'}} |\Psi_0\rangle & \\ + \sum_{\boldsymbol{k},\boldsymbol{k'}} \sum_{\boldsymbol{q'}} \frac{-e^2}{4\pi\varepsilon_0\varepsilon_r V} \frac{1}{|\boldsymbol{q'}|^2} O(\boldsymbol{k} - \boldsymbol{q'}, \boldsymbol{k'} - \boldsymbol{q'}) \hat{c}^{\dagger}_{c\boldsymbol{k}} \hat{c}_{v\boldsymbol{k'}} |\Psi_0\rangle &= E|\Psi\rangle \end{aligned} \tag{B.18}$$

Closing (B.18) with the bra $\langle \boldsymbol{k}_{\boldsymbol{\alpha}}, \boldsymbol{k}_{\boldsymbol{\beta}}| = \langle \Psi_0| \hat{c}^{\dagger}_{v,\boldsymbol{k}_{\boldsymbol{\beta}}} \hat{c}_{c,\boldsymbol{k}_{\boldsymbol{\alpha}}}$ gives:

$$(E - E_g - E_0) O(\boldsymbol{k}_{\boldsymbol{\alpha}}, \boldsymbol{k}_{\boldsymbol{\beta}}) = \left(\frac{\hbar^2 \boldsymbol{k}_{\boldsymbol{\alpha}}^2}{2m_c^*} + \frac{\hbar^2 \boldsymbol{k}_{\boldsymbol{\beta}}^2}{2m_v^*} \right) O(\boldsymbol{k}_{\boldsymbol{\alpha}}, \boldsymbol{k}_{\boldsymbol{\beta}}) - \sum_{\boldsymbol{q'}} \frac{e^2}{4\pi\varepsilon_0\varepsilon_r V} \frac{1}{|\boldsymbol{q'}|^2} O(\boldsymbol{k}_{\boldsymbol{\alpha}} - \boldsymbol{q'}, \boldsymbol{k}_{\boldsymbol{\beta}} - \boldsymbol{q'}) \tag{B.19}$$

where we have used the following relation:

$$\begin{aligned} \langle \Psi_0| \hat{c}^{\dagger}_{v,\boldsymbol{k}_{\boldsymbol{\beta}}} \hat{c}_{c,\boldsymbol{k}_{\boldsymbol{\alpha}}} \hat{c}^{\dagger}_{c,\boldsymbol{k}} \hat{c}_{v,\boldsymbol{k'}} |\Psi_0\rangle &= \langle \Psi_0| \delta_{\boldsymbol{k}_{\boldsymbol{\alpha}},\boldsymbol{k}} \delta_{\boldsymbol{k}_{\boldsymbol{\beta}},\boldsymbol{k'}} - \hat{c}_{v,\boldsymbol{k'}} \hat{c}^{\dagger}_{v,\boldsymbol{k}_{\boldsymbol{\beta}}} + \hat{c}^{\dagger}_{v,\boldsymbol{k}_{\boldsymbol{\beta}}} \hat{c}^{\dagger}_{c,\boldsymbol{k}} \hat{c}_{v,\boldsymbol{k'}} \hat{c}_{c,\boldsymbol{k}_{\boldsymbol{\alpha}}} |\Psi_0\rangle \\ &= \delta_{\boldsymbol{k}_{\boldsymbol{\alpha}},\boldsymbol{k}} \delta_{\boldsymbol{k}_{\boldsymbol{\beta}},\boldsymbol{k'}} \end{aligned} \tag{B.20}$$

By changing the variables to the center of mass frame (eq. (2.95) and eq. (2.96)) we get:

$$\frac{\hbar^2 \boldsymbol{k}_{\boldsymbol{\alpha}}^2}{2m_c^*} \Longrightarrow \frac{\hbar^2}{2m_c^*} \left(\boldsymbol{K} + \frac{m_c^*}{M} \boldsymbol{q} \right)^2 = \frac{\hbar^2}{2m_c^*} \left(\boldsymbol{K}^2 + \frac{2m_c^* \boldsymbol{q}\boldsymbol{K}}{M} + \frac{m_c^{*2} \boldsymbol{q}^2}{M^2} \right) \tag{B.21}$$

$$\frac{\hbar^2 \boldsymbol{k}_{\boldsymbol{\beta}}^2}{2m_v^*} \Longrightarrow \frac{\hbar^2}{2m_v^*} \left(\boldsymbol{K} - \frac{m_v^*}{M} \boldsymbol{q} \right)^2 = \frac{\hbar^2}{2m_v^*} \left(\boldsymbol{K}^2 - \frac{2m_v^* \boldsymbol{q}\boldsymbol{K}}{M} + \frac{m_v^{*2} \boldsymbol{q}^2}{M^2} \right) \tag{B.22}$$

$$\begin{aligned} O(\boldsymbol{k}_{\boldsymbol{\alpha}} - \boldsymbol{q'}, \boldsymbol{k}_{\boldsymbol{\beta}} - \boldsymbol{q'}) &\Longrightarrow O\left(\boldsymbol{K} + \frac{m_c^*}{M} \boldsymbol{q} - \boldsymbol{q'}, \boldsymbol{K} - \frac{m_v^*}{M} \boldsymbol{q} - \boldsymbol{q'} \right) \\ &\equiv O\left(\frac{m_c^*}{M} \boldsymbol{q} + \boldsymbol{K'}, -\frac{m_v^*}{M} \boldsymbol{q} + \boldsymbol{K'} \right) \equiv O_{\boldsymbol{q}}(\boldsymbol{K'}) \end{aligned} \tag{B.23}$$

Consequently, we obtain eq. (2.98).

B.2 Exciton operators commutator :

- Exciton creation operator $\hat{d}^{\dagger}_{0,n} = \sum_{\boldsymbol{K}} O^{n}_{0}(\boldsymbol{K})\hat{c}^{\dagger}_{c,\boldsymbol{K}}\hat{c}_{v,\boldsymbol{K}}$
- Exciton annihilation operator $\hat{d}_{0,n} = \sum_{\boldsymbol{K'}} O^{n*}_{0}(\boldsymbol{K'})\hat{c}_{c,\boldsymbol{K'}}\hat{c}^{\dagger}_{v,\boldsymbol{K'}}$

$$\left[\hat{d}_{0,n}, \hat{d}^{\dagger}_{0,n}\right] = \underbrace{\hat{d}_{0,n}\hat{d}^{\dagger}_{0,n}}_{\boxed{1}} \underbrace{-\hat{d}^{\dagger}_{0,n}\hat{d}_{0,n}}_{\boxed{2}} \tag{B.24}$$

$$\begin{aligned}
\boxed{1} &= \sum_{\boldsymbol{K}}\sum_{\boldsymbol{K'}} O^{n*}_{0}(\boldsymbol{K'})O^{n}_{0}(\boldsymbol{K})\hat{c}_{c,\boldsymbol{K'}}\hat{c}^{\dagger}_{v,\boldsymbol{K'}}\hat{c}^{\dagger}_{c,\boldsymbol{K}}\hat{c}_{v,\boldsymbol{K}} \\
&= -\sum_{\boldsymbol{K}}\sum_{\boldsymbol{K'}} O^{n*}_{0}(\boldsymbol{K'})O^{n}_{0}(\boldsymbol{K})\hat{c}^{\dagger}_{c,\boldsymbol{K}}\hat{c}_{c,\boldsymbol{K'}} \underbrace{\hat{c}_{v,\boldsymbol{K}}\hat{c}^{\dagger}_{v,\boldsymbol{K'}}}_{\delta_{\boldsymbol{K},\boldsymbol{K'}} - \hat{c}^{\dagger}_{v,\boldsymbol{K'}}\hat{c}_{v,\boldsymbol{K}}} \\
&= -\sum_{\boldsymbol{K}} |O^{n}_{0}(\boldsymbol{K})|^{2}\hat{c}^{\dagger}_{c,\boldsymbol{K}}\hat{c}_{c,\boldsymbol{K'}} + \sum_{\boldsymbol{K}}\sum_{\boldsymbol{K'}} O^{n*}_{0}(\boldsymbol{K'})O^{n}_{0}(\boldsymbol{K})\hat{c}^{\dagger}_{c,\boldsymbol{K}}\hat{c}_{c,\boldsymbol{K'}}\hat{c}^{\dagger}_{v,\boldsymbol{K'}}\hat{c}_{v,\boldsymbol{K}}
\end{aligned} \tag{B.25}$$

$$\begin{aligned}
\boxed{2} &= -\sum_{\boldsymbol{K}}\sum_{\boldsymbol{K'}} O^{n*}_{0}(\boldsymbol{K'})O^{n}_{0}(\boldsymbol{K})\hat{c}^{\dagger}_{c,\boldsymbol{K}}\hat{c}_{v,\boldsymbol{K}}\hat{c}_{c,\boldsymbol{K'}}\hat{c}^{\dagger}_{v,\boldsymbol{K'}} \\
&= \sum_{\boldsymbol{K}}\sum_{\boldsymbol{K'}} O^{n*}_{0}(\boldsymbol{K'})O^{n}_{0}(\boldsymbol{K})\hat{c}^{\dagger}_{v,\boldsymbol{K'}}\hat{c}_{v,\boldsymbol{K}} \underbrace{\hat{c}_{c,\boldsymbol{K'}}\hat{c}^{\dagger}_{c,\boldsymbol{K}}}_{\delta_{\boldsymbol{K},\boldsymbol{K'}} - \hat{c}^{\dagger}_{c,\boldsymbol{K}}\hat{c}_{c,\boldsymbol{K'}}} \\
&= \sum_{\boldsymbol{K}} |O^{n}_{0}(\boldsymbol{K})|^{2}\hat{c}^{\dagger}_{v,\boldsymbol{K}}\hat{c}_{v,\boldsymbol{K'}} - \sum_{\boldsymbol{K}}\sum_{\boldsymbol{K'}} O^{n*}_{0}(\boldsymbol{K'})O^{n}_{0}(\boldsymbol{K})\hat{c}^{\dagger}_{v,\boldsymbol{K'}}\hat{c}_{v,\boldsymbol{K}}\hat{c}^{\dagger}_{c,\boldsymbol{K}}\hat{c}_{c,\boldsymbol{K'}} \\
&= \sum_{\boldsymbol{K}} |O^{n}_{0}(\boldsymbol{K})|^{2}\hat{c}^{\dagger}_{v,\boldsymbol{K}}\hat{c}_{v,\boldsymbol{K'}} - \sum_{\boldsymbol{K}}\sum_{\boldsymbol{K'}} O^{n*}_{0}(\boldsymbol{K'})O^{n}_{0}(\boldsymbol{K})\hat{c}^{\dagger}_{c,\boldsymbol{K}}\hat{c}_{c,\boldsymbol{K'}}\hat{c}^{\dagger}_{v,\boldsymbol{K'}}\hat{c}_{v,\boldsymbol{K}}
\end{aligned} \tag{B.26}$$

$$\begin{aligned}
\left[\hat{d}_{0,n}, \hat{d}^{\dagger}_{0,n}\right] &= \boxed{1} + \boxed{2} \\
&= \sum_{\boldsymbol{K}} |O^{n}_{0}(\boldsymbol{K})|^{2}\left[\hat{c}^{\dagger}_{v,\boldsymbol{K'}}\hat{c}_{v,\boldsymbol{K}} - \hat{c}^{\dagger}_{c,\boldsymbol{K}}\hat{c}_{c,\boldsymbol{K'}}\right] \\
&= \sum_{\boldsymbol{K}} |O^{n}_{0}(\boldsymbol{K})|^{2}\left[1 - \hat{c}^{\dagger}_{c,\boldsymbol{K}}\hat{c}_{c,\boldsymbol{K'}} - \hat{c}_{v,\boldsymbol{K}}\hat{c}^{\dagger}_{v,\boldsymbol{K'}}\right]
\end{aligned} \tag{B.27}$$

B.3 Momentum matrix element

We start this section with the commonly used parabolic band model derived in the Kane model and also used in the more complete Luttinger-Kohn model (Table : B.1).

For a wave vector $\boldsymbol{k}$ not along the z-direction as supposed in the Kane model we need to use a unitary transformation to find the basis functions in the general coordinate system. If the electron wave vector $\boldsymbol{k}$ has a general direction specified by (k, θ, φ) in spherical coordinates:

Table B.1 – Periodic parts of the band-edge Bloch functions of a tetrahedral point group symmetry - Kane Model

Symmetry	$\|J, m_J\rangle$	Ψ_{J,m_J}
Γ_6	$\left\|\frac{1}{2}, \frac{1}{2}\right\rangle$	$S\uparrow$
Γ_6	$\left\|\frac{1}{2}, -\frac{1}{2}\right\rangle$	$S\downarrow$
Γ_8	$\left\|\frac{3}{2}, -\frac{3}{2}\right\rangle$	$\frac{1}{\sqrt{2}}(X - jY)\downarrow$
Γ_8	$\left\|\frac{3}{2}, -\frac{1}{2}\right\rangle$	$\frac{1}{\sqrt{6}}\left[(X - jY)\uparrow + \sqrt{\frac{2}{3}}Z\downarrow\right]$
Γ_8	$\left\|\frac{3}{2}, \frac{1}{2}\right\rangle$	$-\frac{1}{\sqrt{6}}\left[(X + jY)\downarrow + \sqrt{\frac{2}{3}}Z\uparrow\right]$
Γ_8	$\left\|\frac{3}{2}, \frac{3}{2}\right\rangle$	$-\frac{1}{\sqrt{2}}(X + jY)\uparrow$
Γ_7	$\left\|\frac{1}{2}, -\frac{1}{2}\right\rangle$	$\frac{1}{\sqrt{3}}\left[(X - jY)\uparrow - Z\downarrow\right]$
Γ_7	$\left\|\frac{1}{2}, \frac{1}{2}\right\rangle$	$-\frac{1}{\sqrt{3}}\left[(X + jY)\downarrow + Z\uparrow\right]$

$$\boldsymbol{k} = k\sin\theta\cos\varphi\boldsymbol{x} + k\sin\theta\sin\varphi\boldsymbol{y} + k\cos\theta\boldsymbol{z} \tag{B.28}$$

the following transformation may be employed:

$$\begin{aligned}
\begin{bmatrix}\uparrow' \\ \downarrow'\end{bmatrix} &= \begin{pmatrix} e^{-j\frac{\varphi}{2}}\cos\left(\frac{\theta}{2}\right) & e^{j\frac{\varphi}{2}}\sin\left(\frac{\theta}{2}\right) \\ e^{-j\frac{\varphi}{2}}\sin\left(\frac{\theta}{2}\right) & e^{j\frac{\varphi}{2}}\cos\left(\frac{\theta}{2}\right)\end{pmatrix}\begin{bmatrix}\uparrow \\ \downarrow\end{bmatrix} \\
\begin{bmatrix}X' \\ Y' \\ Z'\end{bmatrix} &= \begin{pmatrix}\cos\theta\cos\varphi & \cos\theta\sin\varphi & -\sin\theta \\ -\sin\varphi & \cos\varphi & 0 \\ \sin\theta\cos\varphi & \cos\theta\sin\varphi & \cos\theta\end{pmatrix}\begin{bmatrix}X \\ Y \\ Z\end{bmatrix}
\end{aligned} \tag{B.29}$$

The spherical symmetrical functions maintains its symmetry $S(r') = S(r)$ since unitary transformation preserve length. Here the superscript prime ($\prime$) means that the new z-axis is set along the k-direction. Using the previous unitary transformation the band edges wave functions are as follows:

Conduction bands :

$$|jS\uparrow'\rangle \quad \text{and} \quad |jS\downarrow'\rangle \tag{B.30}$$

Heavy-Hole bands :

$$\begin{aligned}\left|\frac{3}{2},\frac{3}{2}\right\rangle' &= -\frac{1}{\sqrt{2}}\left|(X'+jY')\uparrow'\right\rangle \\ &= -\frac{1}{\sqrt{2}}\left|(\cos\theta\cos\varphi - j\sin\varphi)X + (\cos\theta\sin\varphi + j\cos\varphi)Y - \sin\theta Z\right\rangle\left|\uparrow'\right\rangle\end{aligned} \tag{B.31}$$

$$\begin{aligned}\left|\frac{3}{2},-\frac{3}{2}\right\rangle' &= \frac{1}{\sqrt{2}}\left|(X'-jY')\downarrow'\right\rangle \\ &= \frac{1}{\sqrt{2}}\left|(\cos\theta\cos\varphi + j\sin\varphi)X + (\cos\theta\sin\varphi - j\cos\varphi)Y - \sin\theta Z\right\rangle\left|\downarrow'\right\rangle\end{aligned} \tag{B.32}$$

Light-Hole bands :

$$\begin{aligned}\left|\frac{3}{2},\frac{1}{2}\right\rangle' &= -\frac{1}{\sqrt{6}}\left|(X'+jY')\downarrow'\right\rangle + \sqrt{\frac{2}{3}}\left|Z'\uparrow'\right\rangle \\ &= \frac{1}{\sqrt{6}}\left|(\cos\theta\cos\varphi - j\sin\varphi)X + (\cos\theta\sin\varphi + j\cos\varphi)Y - \sin\theta Z\right\rangle\left|\downarrow'\right\rangle \\ &+ \sqrt{\frac{2}{3}}\left|\sin\theta\cos\varphi X + \sin\theta\sin\varphi Y + \cos\theta Z\right\rangle\left|\uparrow'\right\rangle\end{aligned} \tag{B.33}$$

$$\begin{aligned}\left|\frac{3}{2},-\frac{1}{2}\right\rangle' &= \frac{1}{\sqrt{6}}\left|(X'-jY')\uparrow'\right\rangle + \sqrt{\frac{2}{3}}\left|Z'\downarrow'\right\rangle \\ &= -\frac{1}{\sqrt{6}}\left|(\cos\theta\cos\varphi + j\sin\varphi)X + (\cos\theta\sin\varphi - j\cos\varphi)Y - \sin\theta Z\right\rangle\left|\uparrow'\right\rangle \\ &+ \sqrt{\frac{2}{3}}\left|\sin\theta\cos\varphi X + \sin\theta\sin\varphi Y + \cos\theta Z\right\rangle\left|\downarrow'\right\rangle\end{aligned} \tag{B.34}$$

Spin-orbit split-off bands :

$$\begin{aligned}\left|\frac{1}{2},\frac{1}{2}\right\rangle' &= \frac{1}{\sqrt{3}}\left|(X'+jY')\downarrow'\right\rangle + \frac{1}{\sqrt{3}}\left|Z'\uparrow'\right\rangle \\ &= \frac{1}{\sqrt{3}}\left|(\cos\theta\cos\varphi - j\sin\varphi)X + (\cos\theta\sin\varphi + j\cos\varphi)Y - \sin\theta Z\right\rangle\left|\downarrow'\right\rangle \\ &+ \frac{1}{\sqrt{3}}\left|\sin\theta\cos\varphi X + \sin\theta\sin\varphi Y + \cos\theta Z\right\rangle\left|\uparrow'\right\rangle\end{aligned} \tag{B.35}$$

$$\begin{aligned}\left|\frac{1}{2},-\frac{1}{2}\right\rangle' &= \frac{1}{\sqrt{3}}\left|(X'-jY')\uparrow'\right\rangle - \frac{1}{\sqrt{3}}\left|Z'\downarrow'\right\rangle \\ &= \frac{1}{\sqrt{3}}\left|(\cos\theta\cos\varphi + j\sin\varphi)X + (\cos\theta\sin\varphi - j\cos\varphi)Y - \sin\theta Z\right\rangle\left|\uparrow'\right\rangle \\ &- \frac{1}{\sqrt{3}}\left|\sin\theta\cos\varphi X + \sin\theta\sin\varphi Y + \cos\theta Z\right\rangle\left|\downarrow'\right\rangle\end{aligned} \tag{B.36}$$

We compute now the optical momentum matrix element:

$$\begin{aligned}\boldsymbol{p_{cv}} &= \langle u_c|\boldsymbol{p}|u_v\rangle = \boldsymbol{M} \\ &= \langle u_c|\frac{\hbar}{j}\frac{\partial}{\partial x}|u_v\rangle\,\boldsymbol{x} + \langle u_c|\frac{\hbar}{j}\frac{\partial}{\partial y}|u_v\rangle\,\boldsymbol{y} + \langle u_c|\frac{\hbar}{j}\frac{\partial}{\partial z}|u_v\rangle\,\boldsymbol{z}\end{aligned} \tag{B.37}$$

For conduction to heavy-hole transitions we obtain $\boldsymbol{M_{c-hh}}$ as:

$$\begin{aligned}\left\langle jS\uparrow'\middle|\boldsymbol{p}\middle|\frac{3}{2},\frac{3}{2}\right\rangle' &= -\left[(\cos\theta\cos\varphi - j\sin\varphi)\boldsymbol{x} + (\cos\theta\sin\varphi + j\cos\varphi)\boldsymbol{y} - \sin\theta\boldsymbol{z}\right] \\ &\quad\times\frac{P_x}{\sqrt{2}} \\ \left\langle jS\downarrow'\middle|\boldsymbol{p}\middle|\frac{3}{2},-\frac{3}{2}\right\rangle' &= \left[(\cos\theta\cos\varphi + j\sin\varphi)\boldsymbol{x} + (\cos\theta\sin\varphi - j\cos\varphi)\boldsymbol{y} - \sin\theta\boldsymbol{z}\right] \\ &\quad\times\frac{P_x}{\sqrt{2}} \\ \left\langle jS\uparrow'\middle|\boldsymbol{p}\middle|\frac{3}{2},-\frac{3}{2}\right\rangle' &= \boldsymbol{0} \\ \left\langle jS\downarrow'\middle|\boldsymbol{p}\middle|\frac{3}{2},\frac{3}{2}\right\rangle' &= \boldsymbol{0}\end{aligned} \tag{B.38}$$

Similarly for conduction to light-hole transitions we obtain $\boldsymbol{M_{l-hh}}$ as:

$$\begin{aligned}\left\langle iS\uparrow'\middle|\boldsymbol{p}\middle|\frac{3}{2},\frac{1}{2}\right\rangle' &= \sqrt{\frac{2}{3}}\left[\sin\theta\cos\varphi\boldsymbol{x} + \sin\theta\sin\varphi\boldsymbol{y} + \cos\theta\boldsymbol{z}\right]P_x \\ \left\langle iS\downarrow'\middle|\boldsymbol{p}\middle|\frac{3}{2},-\frac{1}{2}\right\rangle' &= \sqrt{\frac{2}{3}}\left[\sin\theta\cos\varphi\boldsymbol{x} + \sin\theta\sin\varphi\boldsymbol{y} + \cos\theta\boldsymbol{z}\right]P_x \\ \left\langle iS\uparrow'\middle|\boldsymbol{p}\middle|\frac{3}{2},-\frac{1}{2}\right\rangle' &= \frac{1}{\sqrt{6}}\left[(\cos\theta\cos\varphi + j\sin\varphi)\boldsymbol{x} + (\cos\theta\sin\varphi - j\cos\varphi)\boldsymbol{y} - \sin\theta\boldsymbol{z}\right] \\ &\quad\times P_x \\ \left\langle iS\downarrow'\middle|\boldsymbol{p}\middle|\frac{3}{2},\frac{1}{2}\right\rangle' &= -\frac{1}{\sqrt{6}}\left[(\cos\theta\cos\varphi - j\sin\varphi)\boldsymbol{x} + (\cos\theta\sin\varphi + j\cos\varphi)\boldsymbol{y} - \sin\theta\boldsymbol{z}\right] \\ &\quad\times P_x\end{aligned} \tag{B.39}$$

In those last equations we have defined the Kane parameter P and a momentum matrix parameter P_x as:

$$\begin{aligned}P &= \frac{\hbar}{m_0}\langle jS|p_z|Z\rangle = \frac{\hbar}{m_0}P_x \\ P_x &= \langle jS|p_x|X\rangle = \langle jS|p_y|Y\rangle = \langle jS|p_z|Z\rangle\end{aligned} \tag{B.40}$$

To compute this momentum matrix element in the case of bulk or in the case of a quantum well we need to take an average value for it. For a bulk semiconductor, we take the average of the momentum matrix element with respect to the solid angle $d\Omega$. For example with a TE polarization (i.e. the polarization vector of the electric field, $\boldsymbol{e}$ is taken as $\boldsymbol{x}$) and for a conduction to heavy hole transition we have :

$$\begin{aligned}
|\boldsymbol{e}\cdot\boldsymbol{p_{cv}}|^2 = \left\langle|\boldsymbol{e}\cdot\boldsymbol{M_{c-hh}}|^2\right\rangle &= \frac{1}{4\pi}\int_{\theta=0}^{\pi}\int_{\varphi=0}^{2\pi}|\boldsymbol{x}\cdot\boldsymbol{M_{c-hh}}|^2\sin\theta d\theta d\varphi \\
&= \frac{1}{4\pi}\int_{\theta=0}^{\pi}\sin\theta d\theta\int_{\varphi=0}^{2\pi}d\varphi(\cos^2\theta\cos^2\varphi+\sin^2\varphi)\frac{{P_x}^2}{2} \\
&= \frac{1}{3}{P_x}^2
\end{aligned} \tag{B.41}$$

We obtain the same result for another direction for the electric field ($\boldsymbol{e}=\boldsymbol{y}$ or $\boldsymbol{z}$) since bulk crystal is isotropic.

In the case of quantum well, the momentum matrix element is averaged along the azimuthal angle φ in the plane and will become polarization dependent. We consider a quantum-well structure with the growth axis along the z-direction. For a TE-polarization ($\boldsymbol{e}=\boldsymbol{x}$) and a conduction to heavy hole transition the following momentum matrix element:

$$\begin{aligned}
|\boldsymbol{e}\cdot\boldsymbol{p_{cv}}|^2 = \left\langle|\boldsymbol{e}\cdot\boldsymbol{M_{c-hh}}|^2\right\rangle &= \frac{1}{2\pi}\int_{\varphi=0}^{2\pi}|\boldsymbol{x}\cdot\boldsymbol{M_{c-hh}}|^2 d\varphi \\
&= \frac{1}{2\pi}\int_{\varphi=0}^{2\pi}d\varphi(\cos^2\theta\cos^2\varphi+\sin^2\varphi)\frac{{P_x}^2}{2} \\
&= \frac{1}{4}(1+\cos^2\theta){P_x}^2
\end{aligned} \tag{B.42}$$

The result for the TE-polarization would be the same if we had chosen $\boldsymbol{e}=\boldsymbol{y}$. In the case of TM-polarization ($\boldsymbol{e}=\boldsymbol{z}$) we have:

$$\begin{aligned}
|\boldsymbol{e}\cdot\boldsymbol{p_{cv}}|^2 = \left\langle|\boldsymbol{e}\cdot\boldsymbol{M_{c-hh}}|^2\right\rangle &= \frac{1}{2\pi}\int_{\varphi=0}^{2\pi}|\boldsymbol{z}\cdot\boldsymbol{M_{c-hh}}|^2 d\varphi \\
&= \frac{1}{2}\sin^2\theta{P_x}^2
\end{aligned} \tag{B.43}$$

The angular factor $\cos\theta$ can be related to the electron or hole wavevector, but at the band edge, we have $\theta=0$ which gives according to the previous equations a momentum matrix element null for the TM polarization. This last result is nothing else than the quantum well selection rule.

B.4 Evalutation of the scalar product p.E

We aim in this section to evaluate the scalar product $[\boldsymbol{p}_{vc} \cdot \boldsymbol{e}^*(r,\theta)]$ for an electronic transitions involving conduction band electrons and heavy holes. We start the calculation by expressing $\boldsymbol{p_{cv}}$ at the band edge (eq. (B.38)) [1]

$$\begin{aligned}
\left\langle jS\uparrow' \middle| \boldsymbol{p} \middle| \frac{3}{2},\frac{3}{2} \right\rangle' &= -\frac{P_x}{\sqrt{2}}\left[(\cos\theta - j\sin\theta)\boldsymbol{x} + (\sin\theta + j\cos\theta)\boldsymbol{y}\right] \\
&= \frac{P_x}{\sqrt{2}}\left[-e^{-j\theta}\boldsymbol{x} - je^{-j\theta}\boldsymbol{y}\right] \\
\left\langle jS\downarrow' \middle| \boldsymbol{p} \middle| \frac{3}{2},-\frac{3}{2} \right\rangle' &= \frac{P_x}{\sqrt{2}}\left[(\cos\theta + j\sin\theta)\boldsymbol{x} + (\sin\theta - j\cos\theta)\boldsymbol{y}\right] \\
&= \frac{P_x}{\sqrt{2}}\left[e^{j\theta}\boldsymbol{x} - je^{j\theta}\boldsymbol{y}\right]
\end{aligned} \tag{B.44}$$

We write now the expression of the 2D electric field $\tilde{\boldsymbol{E}}_{m,p}(r,\theta)$ (in the plane of the QW) in cartesian coordinates using equations (2.40) and (2.49):

$$\begin{aligned}
\tilde{\boldsymbol{E}}_{m,p}(r,\theta) =& E_{0-m,p}\frac{\boldsymbol{x}}{\sqrt{2}}\left[J_{m-1}(\beta_{m,p}r)e^{-j(m-1)\theta} + J_{m+1}(\beta_{m,p}r)e^{-j(m+1)\theta}\right] \\
&+ E_{0-m,p}\frac{j\boldsymbol{y}}{\sqrt{2}}\left[J_{m+1}(\beta_{m,p}r)e^{-j(m+1)\theta} - J_{m-1}(\beta_{m,p}r)e^{-j(m-1)\theta}\right]
\end{aligned} \tag{B.45}$$

Using $\boldsymbol{p_{vc}} = \boldsymbol{p}^*_{\boldsymbol{cv}}$, we can express the scalar product for the case involving the band $|\frac{3}{2},\frac{3}{2}\rangle$:

$$\begin{aligned}
\boldsymbol{p_{vc}} \cdot \tilde{\boldsymbol{E}}^*_{m,p}(r,\theta) =& \frac{P_x}{\sqrt{2}}E_{0-m,p}\frac{-e^{j\theta}}{\sqrt{2}}\left[J_{m-1}(\beta_{m,p}r)e^{j(m-1)\theta} + J_{m+1}(\beta_{m,p}r)e^{j(m+1)\theta}\right] \\
&+ \frac{P_x}{\sqrt{2}}E_{0-m,p}\frac{e^{j\theta}}{\sqrt{2}}\left[J_{m+1}(\beta_{m,p}r)e^{j(m+1)\theta} - J_{m-1}(\beta_{m,p}r)e^{j(m-1)\theta}\right] \\
=& -\frac{P_x}{2}E_{0-m,p}\left[J_{m-1}(\beta_{m,p}r)e^{jm\theta} + J_{m+1}(\beta_{m,p}r)e^{j(m+2)\theta}\right] \\
&+ \frac{P_x}{2}E_{0-m,p}\left[J_{m+1}(\beta_{m,p}r)e^{j(m+2)\theta} - J_{m-1}(\beta_{m,p}r)e^{jm\theta}\right] \\
=& -P_xE_{0-m,p}J_{m-1}(\beta_{m,p}r)e^{jm\theta} = -P_x\tilde{E}^*_{m,p,+}e^{j\theta}
\end{aligned} \tag{B.46}$$

Similarly, we found for the case involving the band $|\frac{3}{2},-\frac{3}{2}\rangle$:

$$\boldsymbol{p_{vc}} \cdot \tilde{\boldsymbol{E}}^*_{m,p}(r,\theta) = P_xE_{0-m,p}J_{m+1}(\beta_{m,p}r)e^{jm\theta} = P_x\tilde{E}^*_{m,p,-}e^{-j\theta} \tag{B.47}$$

A priori, the electron participating in the transition can be in the two valence bands (having a different orbital momumtum), we construct a general state as follows:

1. Note that in this section we change the name of the angle φ, commonly use in spherical coordinates by θ, its counterpart in cylindrical coordinates.

$$\frac{\pm\left(|\frac{3}{2},-\frac{3}{2}\rangle - |\frac{3}{2},\frac{3}{2}\rangle\right)}{\sqrt{2}} \tag{B.48}$$

The wavefunction should be anti-symmetric, hence the "-" between the states. For the conduction band the electron has only one choice an will be in the $|S\rangle$ state. The scalar product $[\boldsymbol{p}_{vc}\cdot\boldsymbol{e}^*(r,\theta)]$ is therefore given by:

$$\boldsymbol{p_{vc}}\cdot\tilde{\boldsymbol{E}}^*_{m,p}(r,\theta) = \pm\frac{P_x}{\sqrt{2}}(\tilde{E}^*_{m,p,+}e^{j\theta} + \tilde{E}^*_{m,p,-}e^{-j\theta}) \tag{B.49}$$

By injecting this last expression into (2.167) we obtain equation (2.170).

B.5 Optoelectronical coupling in the MQW case

In this section, we present a simple demonstration of the optoelectronical coupling in the case of a MQW structure, with N_{QW} the number of QW, and where each individual QW possesses a different coupling to the electromagnetic field. For the sake of clarity we consider here the case where $N_{QW}=3$. The demonstration remains valid for an arbitrary number of QW. The interaction Hamiltonian of a such system is given by:

$$\hat{H}_{int} = g_1\left(\hat{a}^\dagger\hat{d}_1 + \hat{a}\hat{d}_1^\dagger\right) + g_2\left(\hat{a}^\dagger\hat{d}_2 + \hat{a}\hat{d}_2^\dagger\right) + g_3\left(\hat{a}^\dagger\hat{d}_3 + \hat{a}\hat{d}_3^\dagger\right) \tag{B.50}$$

where $\hat{a}/\hat{a}^\dagger$ are the bosonic operator for the electromagnetic field and $\hat{d}_i/\hat{d}_i^\dagger$ the bosonic operators for the exciton in the i$^{\text{th}}$ QW with a coupling to the electromagnetic field parametrized by g_i. We consider the first QW to have an optimized coupling to the electromagnetic field, and serve us as a reference ($g_1 > g_2, g_3$). We define a new operator for the bright mode involving the 3 different QW:

$$\hat{D} = \frac{1}{\sqrt{1+\frac{g_2^2}{g_1^2}+\frac{g_3^2}{g_1^2}}}\left(\hat{d}_1 + \frac{g_2}{g_1}\hat{d}_2 + \frac{g_3}{g_1}\hat{d}_3\right) \tag{B.51}$$

This last operator obeys to the usual bosonic commutation relation $\left[\hat{D},\hat{D}^\dagger\right]=1$. Consequently the interaction Hamiltonian of the system now reads:

$$\begin{aligned}\hat{H}_{int} &= g_1\hat{a}^\dagger\left(\hat{d}_1 + \frac{g_2}{g_1}\hat{d}_2 + \frac{g_3}{g_1}\hat{d}_3\right) + g_1\hat{a}\left(\hat{d}_1^\dagger + \frac{g_2}{g_1}\hat{d}_2^\dagger + \frac{g_3}{g_1}\hat{d}_3^\dagger\right)\\ \hat{H}_{int} &= g_1\sqrt{1+\frac{g_2^2}{g_1^2}+\frac{g_3^2}{g_1^2}}\left(\hat{a}^\dagger\hat{D} + \hat{a}\hat{D}^\dagger\right) = G\left(\hat{a}^\dagger\hat{D} + \hat{a}\hat{D}^\dagger\right)\end{aligned} \tag{B.52}$$

The system behaves like in the single QW case, but with a new coupling characterized by the coupling factor G.

Appendix C

Material properties and Bir Pikus Hamiltonian

C.1 Binary alloys material properties

	GaAs	AlAs	InAs
Structural properties			
a (Å)	5.6532	5.6611	6.0583
ρ (kg.m^{-3})	5317	3730	5667
Electronic Properties			
E_g^Γ (eV)	1.42 (1.516)	2.163 (2.239)	0.360 (0.42)
m_c^*/m_0	0.067	0.15	0.026
m_{hh}^*/m_0	0.5	0.47	0.42
m_{lh}^*/m_0	0.081	0.185	0.026
Elastic Properties			
E (GPa)	85.9	82.2	51.4
σ	0.312	0.324	0.352
C_{11} (GPa)	122.1	125.0	83.29
C_{12} (GPa)	56.6	53.4	45.26
C_{44} (GPa)	60	54.2	39.59
Deformation Potential			
a_c (eV)	-7.17	-5.64	-5.08
a_v (eV)	1.16	2.47	1.00
b (eV)	-2.0	-2.3	-1.8
d (eV)	-4.8	-3.4	-3.6

Table C.1 – Binary alloys parameters at room temperature. The parameters are taken from [201, 332–338] or from COMSOL material library. For the energy gap E_g^Γ, the values between parenthesis are taken at 3K

C.2 Ternary alloys material properties

To compute the parameters for ternary alloys we use Vegard's law in a quadratic form with bowing parameter :

$$K(\mathrm{A}_{1-x}\mathrm{B}_x\mathrm{C}) = (1-x)K(\mathrm{AC}) + xK(\mathrm{BC}) - x(1-x)K_{bow} \tag{C.1}$$

where K represents a physical parameter and K_{bow} a bowing parameter that arises from the increasing disorder generated by the alloying.

	$Al_{0.8}Ga_{0.2}As$	$Al_{0.2}Ga_{0.8}As$	$In_{0.05}Ga_{0.95}As$	$In_{0.13}Ga_{0.87}As$
Structural properties				
a (Å)	5.6585	5.6548	5.6735	5.7059
ρ (kg.m^{-3})	4047	4999	5345	5362
Electronic properties				
E_g^Γ (eV)	1.87	1.54	1.34	1.23
m_c^*/m_0	0.13	0.08	0.064	0.061
m_{hh}^*/m_0	0.476	0.49	0.503	0.506
m_{lh}^*/m_0	0.16	0.10	0.077	0.071
Elastic properties				
E (GPa)	82.9	85.2	84.2	81.4
σ	0.322	0.314	0.314	0.317
C_{11} (GPa)	124.4	122.7	120.2	117.1
C_{12} (GPa)	54.04	55.96	56.03	55.12
C_{44} (GPa)	55.36	58.84	58.98	57.35
Deformation potential				
a_c (eV)	−5.95	−6.86	−7.19	−7.19
a_v (eV)	2.21	1.42	1.15	−1.14
b (eV)	−2.24	−2.06	−1.99	−1.83
d (eV)	−3.68	−4.52	−4.74	−4.64

Table C.2 – Ternary alloys band parameters, computed with Vegard's law, bowing parameters are from [334]

C.3 Bir-Pikus Hamiltonian

Bir-Pikus Hamiltonian [79] is an extension of the Luttinger-Kohn Hamiltonian taking into account the effect of strain on the electronic band structure, its expression is given below :

$$\begin{bmatrix} P+Q & -S & R & 0 & -\frac{1}{\sqrt{2}}S & \sqrt{2}S \\ -S^* & P-Q & 0 & R & -\sqrt{2}Q & \sqrt{\frac{3}{2}}S \\ R^* & 0 & P-Q & S & \sqrt{\frac{3}{2}}S^* & -\frac{1}{\sqrt{2}}S^* \\ 0 & R^* & S^* & P+Q & -\sqrt{2}R^* & -\frac{1}{\sqrt{2}}S^* \\ -\frac{1}{\sqrt{2}}S^* & -\sqrt{2}Q^* & \sqrt{\frac{3}{2}}S & -\sqrt{2}R & P+\Delta & 0 \\ \sqrt{2}S^* & \sqrt{\frac{3}{2}}S^* & -\frac{1}{\sqrt{2}}S & -\frac{1}{\sqrt{2}}S & 0 & P+\Delta \end{bmatrix} \tag{C.2}$$

where the various parameters are defined by :

$$\begin{array}{lll} P = P_k + P_\varepsilon & P_k = \left(\frac{\hbar^2}{2m_0}\right)\gamma_1\left(k_x^2+k_y^2+k_z^2\right) & P_\varepsilon = -a_v\left(\varepsilon_{xx}+\varepsilon_{yy}+\varepsilon_{zz}\right) \\ Q = Q_k + Q_\varepsilon & Q_k = \left(\frac{\hbar^2}{2m_0}\right)\gamma_2\left(k_x^2+k_y^2-2k_z^2\right) & Q_\varepsilon = \frac{b}{2}\left(\varepsilon_{xx}+\varepsilon_{yy}-2\varepsilon_{zz}\right) \\ R = R_k + R_\varepsilon & R_k = \left(\frac{\sqrt{3}\hbar^2}{2m_0}\right)\left[-\gamma_2\left(k_x^2-k_y^2\right)+2j\gamma_3 k_x k_y\right] & R_\varepsilon = \frac{\sqrt{3}b}{2}\left(\varepsilon_{xx}-\varepsilon_{yy}\right)-jd\varepsilon_{xy} \\ S = S_k + S_\varepsilon & S_k = \left(\frac{\hbar^2}{2m_0}\right)2\sqrt{3}\gamma_3\left(k_x^2-jk_y^2\right)k_z & S_\varepsilon = d\left(\varepsilon_{xz}-j\varepsilon_{yz}\right) \end{array} \tag{C.3}$$

γ_1, γ_2 and γ_3 are the Luttinger parameters derived from matrix elements between various bands and experimentally measured [199]. They notably take into account the influence of other electronic bands (remote bands) that are not represented in the theory. This last Hamiltonian only represents the valence bands, by including the conduction band, another similar Hamiltonian (8×8) can be derived [126]. A more complex model that takes into consideration strain effect on the conduction band with respect to the valence band can be derived [339], but in the limit of large band gaps like in GaAs, the Bir-Pikus Hamiltonian grasps all the relevant subtleties.

To that extent the evolution of the transition (C-HH) and (C-LH) for a biaxial strain are given by:

$$\begin{aligned} E_{C-HH}(k=0) &= E_g + (a_c-a_v)(\varepsilon_{xx}+\varepsilon_{yy}+\varepsilon_{zz}) - \frac{b}{2}(\varepsilon_{xx}+\varepsilon_{yy}-2\varepsilon_{zz}) \\ E_{C-HH}(k=0) &= E_g + (\delta E^c_{hyd}+\delta E^v_{hyd}) + \frac{1}{2}\delta E_{sh} \end{aligned} \tag{C.4}$$

$$\begin{aligned} E_{C-LH}(k=0) &= E_g + (a_c-a_v)(\varepsilon_{xx}+\varepsilon_{yy}+\varepsilon_{zz}) + \frac{b}{2}(\varepsilon_{xx}+\varepsilon_{yy}-2\varepsilon_{zz}) \\ E_{C-LH}(k=0) &= E_g + (\delta E^c_{hyd}+\delta E^v_{hyd}) - \frac{1}{2}\delta E_{sh} \end{aligned} \tag{C.5}$$

where we have defined $\delta E^{c/v}_{hyd} = \pm(a_{c/v})(\varepsilon_{xx}+\varepsilon_{yy}+\varepsilon_{zz})$ the hydro-static energy shift and $\frac{1}{2}\delta E_{sh} = -\frac{b}{2}(\varepsilon_{xx}+\varepsilon_{yy}-2\varepsilon_{zz})$ the shear energy shift. These last energy shifts are illustrated in figure C.1.

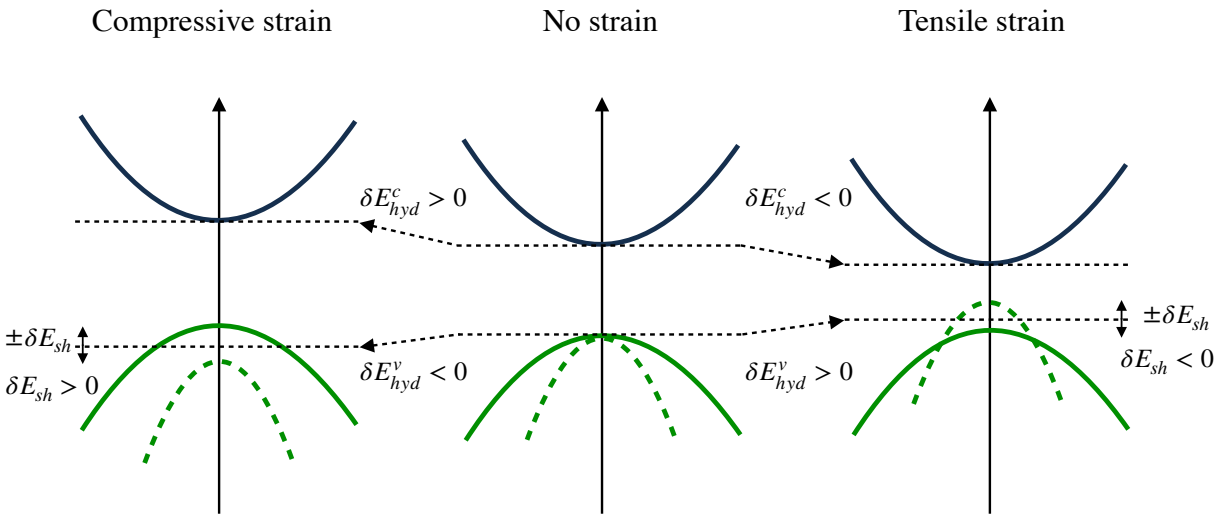

Figure C.1 – Sketch representing the impact of the built-in strain on the electronic bands when an over-layer is built on top of a substrate with a different lattice parameters. Biaxial strain case : the wafer is grown along the (001) direction. Blue curve: Conduction band - Green curve: Heavy holes band - Green dashed curve: Light holes band.

Bibliography

[1] Qiang Zhang, Feihu Xu, Li Li, Nai-Le Liu, and Jian-Wei Pan. Quantum information research in China. *Quantum Science and Technology*, 4(4):040503, 2019. 1

[2] AK Fedorov, AV Akimov, JD Biamonte, AV Kavokin, F Ya Khalili, EO Kiktenko, NN Kolachevsky, Yu V Kurochkin, AI Lvovsky, AN Rubtsov, et al. Quantum technologies in Russia. *Quantum Science and Technology*, 4(4):040501, 2019. 1

[3] Peter Knight and Ian Walmsley. UK national quantum technology programme. *Quantum Science and Technology*, 4(4):040502, 2019. 1

[4] Ben Sussman, Paul Corkum, Alexandre Blais, David Cory, and Andrea Damascelli. Quantum Canada. *Quantum Science and Technology*, 4(2):020503, 2019. 1

[5] Yoshihisa Yamamoto, Masahide Sasaki, and Hiroki Takesue. Quantum information science and technology in Japan. *Quantum Science and Technology*, 4(2):020502, 2019. 1

[6] TM Roberson and Andrew G White. Charting the Australian quantum landscape. *Quantum Science and Technology*, 4(2):020505, 2019. 1

[7] Max Riedel, Matyas Kovacs, Peter Zoller, Jürgen Mlynek, and Tommaso Calarco. Europe's quantum flagship initiative. *Quantum Science and Technology*, 4(2):020501, 2019. 1

[8] Michael G Raymer and Christopher Monroe. The US national quantum initiative. *Quantum Science and Technology*, 4(2):020504, 2019. 1

[9] AFP. Emmanuel macron veut mettre la france dans le trio de tête mondial des technologies quantiques, Jan. 21, 2021 [Online]. 1

[10] Markus Aspelmeyer, Tobias J Kippenberg, and Florian Marquardt. *Cavity optomechanics: nano-and micromechanical resonators interacting with light*. Springer, 2014. 1, 3, 7, 12, 15, 54, 152

[11] Ivan Favero and Khaled Karrai. Optomechanics of deformable optical cavities. *Nature Photonics*, 3(4):201–205, 2009. 1, 7

[12] Gershon Kurizki, Patrice Bertet, Yuimaru Kubo, Klaus Mølmer, David Petrosyan, Peter Rabl, and Jörg Schmiedmayer. Quantum technologies with hybrid systems. *Proceedings of the National Academy of Sciences*, 112(13):3866–3873, 2015. 1

[13] Ze-Liang Xiang, Sahel Ashhab, JQ You, and Franco Nori. Hybrid quantum circuits: Superconducting circuits interacting with other quantum systems. *Reviews of Modern Physics*, 85(2):623, 2013. 1, 16

[14] Margareta Wallquist, Klemens Hammerer, Peter Rabl, Mikhail Lukin, and Peter Zoller. Hybrid quantum devices and quantum engineering. *Physica Scripta*, 2009(T137):014001, 2009. 1

[15] Marc Sansa, Martial Defoort, Ariel Brenac, Maxime Hermouet, Louise Banniard, Alexandre Fafin, Marc Gely, Christophe Masselon, Ivan Favero, Guillaume Jourdan, et al. Optomechanical mass spectrometry. *Nature Communications*, 11(1):1–7, 2020. 1

[16] Fenfei Liu, Seyedhamidreza Alaie, Zayd C Leseman, and Mani Hossein-Zadeh. Sub-pg mass sensing and measurement with an optomechanical oscillator. *Optics express*, 21(17):19555–19567, 2013. 1

[17] Kartik Srinivasan, Houxun Miao, Matthew T Rakher, Marcelo Davanco, and Vladimir Aksyuk. Optomechanical transduction of an integrated silicon cantilever probe using a microdisk resonator. *Nano letters*, 11(2):791–797, 2011. 1

[18] Pierre Etienne Allain, Lucien Schwab, Colin Mismer, Marc Gely, Estelle Mairiaux, Maxime Hermouet, Benjamin Walter, Giuseppe Leo, Sébastien Hentz, Marc Faucher, et al. Optomechanical resonating probe for very high-frequency sensing of atomic forces. *Nanoscale*, 12(5):2939–2945, 2020. 1, 2

[19] Wenyan Yu, Wei C Jiang, Qiang Lin, and Tao Lu. Cavity optomechanical spring sensing of single molecules. *Nature communications*, 7(1):1–9, 2016. 1

[20] Eduardo Gil-Santos, Jose J Ruz, Oscar Malvar, Ivan Favero, Aristide Lemaître, Priscila Kosaka, Sergio García-López, Montserrat Calleja, Javier Tamayo, et al. Optomechanical detection of vibration modes of a single bacterium. *Nature Nanotechnology*, 15(6):469–474, 2020. 1

[21] Samantha Sbarra, Louis Waquier, Stephan Suffit, Aristide Lemaître, and Ivan Favero. Multimode optomechanical weighting of a single nanoparticle. *arXiv preprint arXiv:2111.10121*, 2021. 1

[22] Aaron D O'Connell, Max Hofheinz, Markus Ansmann, Radoslaw C Bialczak, Mike Lenander, Erik Lucero, Matthew Neeley, Daniel Sank, H Wang, Ms Weides, et al. Quantum ground state and single-phonon control of a mechanical resonator. *Nature*, 464(7289):697–703, 2010. 1

[23] John D Teufel, Tobias Donner, Dale Li, Jennifer W Harlow, MS Allman, Katarina Cicak, Adam J Sirois, Jed D Whittaker, Konrad W Lehnert, and Raymond W Simmonds. Sideband cooling of micromechanical motion to the quantum ground state. *Nature*, 475(7356):359–363, 2011. 1

[24] K Børkje, A Nunnenkamp, and SM Girvin. Proposal for entangling remote micromechanical oscillators via optical measurements. *Physical review letters*, 107(12):123601, 2011. 1

[25] Claudiu Genes, A Mari, P Tombesi, and D Vitali. Robust entanglement of a micromechanical resonator with output optical fields. *Physical Review A*, 78(3):032316, 2008. 1

[26] Dustin Kleckner, Igor Pikovski, Evan Jeffrey, Luuk Ament, Eric Eliel, Jeroen Van Den Brink, and Dirk Bouwmeester. Creating and verifying a quantum superposition in a micro-optomechanical system. *New Journal of Physics*, 10(9):095020, 2008. 1

[27] Samuel Pautrel, Zakari Denis, Jérémy Bon, Adrien Borne, and Ivan Favero. Optomechanical discrete-variable quantum teleportation scheme. *Physical Review A*, 101(6):063820, 2020. 1

[28] Chunhua Dong, Victor Fiore, Mark C Kuzyk, Lin Tian, and Hailin Wang. Optical wavelength conversion via optomechanical coupling in a silica resonator. *Annalen der Physik*, 527(1-2):100–106, 2015. 1

[29] Amir H Safavi-Naeini, TP Mayer Alegre, Jasper Chan, Matt Eichenfield, Martin Winger, Qiang Lin, Jeff T Hill, Darrick E Chang, and Oskar Painter. Electromagnetically induced transparency and slow light with optomechanics. *Nature*, 472(7341):69–73, 2011. 1

[30] Benjamin P Abbott, Richard Abbott, TD Abbott, MR Abernathy, Fausto Acernese, Kendall Ackley, Carl Adams, Thomas Adams, Paolo Addesso, RX Adhikari, et al. Observation of gravitational waves from a binary black hole merger. *Physical review letters*, 116(6):061102, 2016. 1

[31] Carlton M Caves. Quantum-mechanical radiation-pressure fluctuations in an interferometer. *Physical Review Letters*, 45(2):75, 1980. 1

[32] Thomas Corbitt, Yanbei Chen, Edith Innerhofer, Helge Müller-Ebhardt, David Ottaway, Henning Rehbein, Daniel Sigg, Stanley Whitcomb, Christopher Wipf, and Nergis Mavalvala. An all-optical trap for a gram-scale mirror. *Physical review letters*, 98(15):150802, 2007. 2

[33] S Anguiano, Axel Emerico Bruchhausen, B Jusserand, I Favero, FR Lamberti, L Lanco, I Sagnes, A Lemaître, Norberto Daniel Lanzillotti-Kimura, P Senellart, et al. Micropillar resonators for optomechanics in the extremely high 19-95 Ghz frequency range. *Physical review letters*, 118(26):263901, 2017. 2

[34] Dustin Kleckner, Brian Pepper, Evan Jeffrey, Petro Sonin, Susanna M Thon, and Dirk Bouwmeester. Optomechanical trampoline resonators. *Optics express*, 19(20):19708–19716, 2011. 2

[35] JD Thompson, BM Zwickl, AM Jayich, Florian Marquardt, SM Girvin, and JGE Harris. Strong dispersive coupling of a high-finesse cavity to a micromechanical membrane. *Nature*, 452(7183):72–75, 2008. 2, 3

[36] Ewold Verhagen, Samuel Deléglise, Stefan Weis, Albert Schliesser, and Tobias J Kippenberg. Quantum-coherent coupling of a mechanical oscillator to an optical cavity mode. *Nature*, 482(7383):63–67, 2012. 2, 16

[37] Lu Ding, Christophe Baker, Pascale Senellart, Aristide Lemaitre, Sara Ducci, Giuseppe Leo, and Ivan Favero. High frequency GaAs nano-optomechanical disk resonator. *Physical review letters*, 105(26):263903, 2010. 2, 3, 54

[38] Inah Yeo, Pierre-Louis de Assis, Arnaud Gloppe, Eva Dupont-Ferrier, Pierre Verlot, Nitin S Malik, Emmanuel Dupuy, Julien Claudon, Jean-Michel Gérard, Alexia Auffèves, et al. Strain-mediated coupling in a quantum dot–mechanical oscillator hybrid system. *Nature nanotechnology*, 9(2):106–110, 2014. 2, 3, 16

[39] Mo Li, WHP Pernice, C Xiong, T Baehr-Jones, M Hochberg, and HX Tang. Harnessing optical forces in integrated photonic circuits. *Nature*, 456(7221):480–484, 2008. 2

[40] Yiwen Chu, Prashanta Kharel, William H Renninger, Luke D Burkhart, Luigi Frunzio, Peter T Rakich, and Robert J Schoelkopf. Quantum acoustics with superconducting qubits. *Science*, 358(6360):199–202, 2017. 2

[41] John D Teufel, Tobias Donner, Dale Li, Jennifer W Harlow, MS Allman, Katarina Cicak, Adam J Sirois, Jed D Whittaker, Konrad W Lehnert, and Raymond W Simmonds. Sideband cooling of micromechanical motion to the quantum ground state. *Nature*, 475(7356):359–363, 2011. 2

[42] Thiago P Mayer Alegre, Raviv Perahia, and Oskar Painter. Optomechanical zipper cavity lasers: theoretical analysis of tuning range and stability. *Optics express*, 18(8):7872–7885, 2010. 2

[43] Ivan Favero, Sebastian Stapfner, David Hunger, Philipp Paulitschke, Jakob Reichel, Heribert Lorenz, Eva M Weig, and Khaled Karrai. Fluctuating nanomechanical system in a high finesse optical microcavity. *Optics express*, 17(15):12813–12820, 2009. 2

[44] Tom P Purdy, DWC Brooks, Thierry Botter, Nathan Brahms, Z-Y Ma, and Dan M Stamper-Kurn. Tunable cavity optomechanics with ultracold atoms. *Physical review letters*, 105(13):133602, 2010. 2

[45] Kater W Murch, Kevin L Moore, Subhadeep Gupta, and Dan M Stamper-Kurn. Observation of quantum-measurement backaction with an ultracold atomic gas. *Nature Physics*, 4(7):561–564, 2008. 3, 16

[46] Jasper Chan, TP Mayer Alegre, Amir H Safavi-Naeini, Jeff T Hill, Alex Krause, Simon Gröblacher, Markus Aspelmeyer, and Oskar Painter. Laser cooling of a nanomechanical oscillator into its quantum ground state. *Nature*, 478(7367):89–92, 2011. 3

[47] BD Cuthbertson, ME Tobar, EN Ivanov, and DG Blair. Parametric back-action effects in a high-Q cyrogenic sapphire transducer. *Review of Scientific Instruments*, 67(7):2435–2442, 1996. 3

[48] Benjamin Rogers, N Lo Gullo, Gabriele De Chiara, G Massimo Palma, and Mauro Paternostro. Hybrid optomechanics for quantum technologies. *Quantum Measurements and Quantum Metrology*, 2(1), 2014. 3, 16

[49] Juan Restrepo, Cristiano Ciuti, and Ivan Favero. Single-polariton optomechanics. *Physical review letters*, 112(1):013601, 2014. 3, 16

[50] Juan Restrepo, Ivan Favero, and Cristiano Ciuti. Fully coupled hybrid cavity optomechanics: quantum interferences and correlations. *Physical Review A*, 95(2):023832, 2017. 3, 16

[51] Sh Barzanjeh, MH Naderi, and M Soltanolkotabi. Steady-state entanglement and normal-mode splitting in an atom-assisted optomechanical system with intensity-dependent coupling. *Physical Review A*, 84(6):063850, 2011. 16

[52] Gabriele De Chiara, Mauro Paternostro, and G Massimo Palma. Entanglement detection in hybrid optomechanical systems. *Physical Review A*, 83(5):052324, 2011. 3, 16

[53] S Singh, H Jing, EM Wright, and P Meystre. Quantum-state transfer between a bose-einstein condensate and an optomechanical mirror. *Physical Review A*, 86(2):021801, 2012. 3, 16

[54] B Rogers, M Paternostro, GM Palma, and G De Chiara. Entanglement control in hybrid optomechanical systems. *Physical Review A*, 86(4):042323, 2012. 3, 16

[55] Ville Bergholm, Witlef Wieczorek, Thomas Schulte-Herbrüggen, and Michael Keyl. Optimal control of hybrid optomechanical systems for generating non-classical states of mechanical motion. *Quantum Science and Technology*, 4(3):034001, 2019. 3, 16

[56] Olivier Arcizet, Vincent Jacques, Alessandro Siria, Philippe Poncharal, Pascal Vincent, and Signe Seidelin. A single nitrogen-vacancy defect coupled to a nanomechanical oscillator. *Nature Physics*, 7(11):879–883, 2011. 3, 16

[57] KV Kepesidis, SD Bennett, S Portolan, Mikhail D Lukin, and P Rabl. Phonon cooling and lasing with nitrogen-vacancy centers in diamond. *Physical Review B*, 88(6):064105, 2013. 3, 16

[58] I Wilson-Rae, P Zoller, and A Imamoglu. Laser cooling of a nanomechanical resonator mode to its quantum ground state. *Physical Review Letters*, 92(7):075507, 2004. 3, 16

[59] Eyob A Sete and Hichem Eleuch. Controllable nonlinear effects in an optomechanical resonator containing a quantum well. *Physical Review A*, 85(4):043824, 2012. 3, 16

[60] SL McCall, AFJ Levi, RE Slusher, SJ Pearton, and RA Logan. Whispering-gallery mode microdisk lasers. *Applied physics letters*, 60(3):289–291, 1992. 3

[61] Jiangang Zhu, Sahin Kaya Ozdemir, Yun-Feng Xiao, Lin Li, Lina He, Da-Ren Chen, and Lan Yang. On-chip single nanoparticle detection and sizing by mode splitting in an ultrahigh-q microresonator. *Nature photonics*, 4(1):46–49, 2010. 3

[62] F Vollmer, S Arnold, and D Keng. Single virus detection from the reactive shift of a whispering-gallery mode. *Proceedings of the National Academy of Sciences*, 105(52):20701–20704, 2008. 3

[63] Iännis Roland, ADRIEN Borne, MARCO Ravaro, ROMAIN De Oliveira, Stéphan Suffit, Pascal Filloux, ARISTIDE Lemaître, Ivan Favero, and GIUSEPPE Leo. Frequency doubling and parametric fluorescence in a four-port aluminum gallium arsenide photonic chip. *Optics letters*, 45(10):2878–2881, 2020. 3, 156, 159

[64] Dmitry V Strekalov, Abijith S Kowligy, Yu-Ping Huang, and Prem Kumar. Optical sum-frequency generation in a whispering-gallery-mode resonator. *New Journal of Physics*, 16(5):053025, 2014. 3

[65] DW Vernooy, A Furusawa, N Ph Georgiades, VS Ilchenko, and HJ Kimble. Cavity qed with high-q whispering gallery modes. *Physical Review A*, 57(4):R2293, 1998. 3

[66] A Schliesser and TJ Kippenberg. Cavity optomechanics with whispering-gallery-mode microresonators. In *Cavity Optomechanics*, pages 121–148. Springer, 2014. 3

[67] Christopher Baker, William Hease, Dac-Trung Nguyen, Alessio Andronico, Sara Ducci, Giuseppe Leo, and Ivan Favero. Photoelastic coupling in gallium arsenide optomechanical disk resonators. *Optics express*, 22(12):14072–14086, 2014. 3

[68] C Weisbuch, R Dingle, AC Gossard, and W Wiegmann. Optical characterization of interface disorder in GaAs-$Ga_{1-x}Al_x$As multi-quantum well structures. *Solid State Communications*, 38(8):709–712, 1981. 3, 97

[69] JJ Hopfield. Theory of the contribution of excitons to the complex dielectric constant of crystals. *Physical Review*, 112(5):1555, 1958. 3, 16, 17

[70] E Wertz, A Amo, DD Solnyshkov, L Ferrier, Timothy Chi Hin Liew, D Sanvitto, P Senellart, I Sagnes, A Lemaître, AV Kavokin, et al. Propagation and amplification dynamics of 1d polariton condensates. *Physical review letters*, 109(21):216404, 2012. 3

[71] Kartik Srinivasan and Oskar Painter. Linear and nonlinear optical spectroscopy of a strongly coupled microdisk–quantum dot system. *Nature*, 450(7171):862–865, 2007. 3

[72] C Ciuti, P Schwendimann, and A Quattropani. Theory of polariton parametric interactions in semiconductor microcavities. *Semiconductor science and technology*, 18(10):S279, 2003. 4, 135

[73] Lydie Ferrier, Simon Pigeon, Esther Wertz, Motoaki Bamba, Pascale Senellart, Isabelle Sagnes, Aristide Lemaitre, Cristiano Ciuti, and Jacqueline Bloch. Polariton parametric oscillation in a single micropillar cavity. *Applied Physics Letters*, 97(3):031105, 2010. 4, 122

[74] Jacek Kasprzak, Murielle Richard, S Kundermann, A Baas, P Jeambrun, Jonathan Mark James Keeling, FM Marchetti, MH Szymańska, R André, JL Staehli, et al. Bose-einstein condensation of exciton polaritons. *Nature*, 443(7110):409–414, 2006. 4

[75] R Balili, V Hartwell, D Snoke, L Pfeiffer, and K West. Bose-einstein condensation of microcavity polaritons in a trap. *Science*, 316(5827):1007–1010, 2007. 4

[76] Daniele Bajoni, Pascale Senellart, Esther Wertz, Isabelle Sagnes, Audrey Miard, Aristide Lemaître, and Jacqueline Bloch. Polariton laser using single micropillar GaAs-GaAlAs semiconductor cavities. *Physical review letters*, 100(4):047401, 2008. 4, 115, 122, 134

[77] A Amo, D Sanvitto, FP Laussy, D Ballarini, E Del Valle, MD Martin, A Lemaitre, J Bloch, DN Krizhanovskii, MS Skolnick, et al. Collective fluid dynamics of a polariton condensate in a semiconductor microcavity. *Nature*, 457(7227):291–295, 2009. 4, 154

[78] Konstantinos G Lagoudakis, Michiel Wouters, Maxime Richard, Augustin Baas, Iacopo Carusotto, Regis André, Le Si Dang, and B Deveaud-Plédran. Quantized vortices in an exciton–polariton condensate. *Nature physics*, 4(9):706–710, 2008. 4

[79] Gennadiui Levikovich Bir, Grigoriui Ezekielevich Pikus, et al. *Symmetry and strain-induced effects in semiconductors*, volume 484. Wiley New York, 1974. 5, 63, 92, 184

[80] J Bardeen and W Shockley. Deformation potentials and mobilities in non-polar crystals. *Physical review*, 80(1):72, 1950. 5, 63

[81] Dimitri Lisandro Chafatinos, AS Kuznetsov, Sebastian Anguiano, Axel Emerico Bruchhausen, Andres Alejandro Reynoso, Klaus Biermann, PV Santos, and Alejandro Fainstein. Polariton-driven phonon laser. *Nature communications*, 11(1):1–8, 2020. 5, 154

[82] Alexander S Kuznetsov, Diego HO Machado, Klaus Biermann, and Paulo V Santos. Electrically driven microcavity exciton-polariton optomechanics at 20 ghz. *Physical Review X*, 11(2):021020, 2021. 5

[83] CK Law. Interaction between a moving mirror and radiation pressure: A Hamiltonian formulation. *Physical Review A*, 51(3):2537, 1995. 8

[84] Warwick P Bowen and Gerard J Milburn. *Quantum optomechanics*. CRC Press, 2015. 8

[85] Kurt Jacobs. *Quantum measurement theory and its applications*. Cambridge University Press, 2014. 8

[86] Pierre Meystre and Murray Sargent. *Elements of quantum optics*. Springer Science & Business Media, 2013. 8, 56

[87] DF Walls and GJ Milburn. *Quantum Optics (Springer Study Edition)*. Springer, 1995. 8

[88] Aashish A Clerk, Michel H Devoret, Steven M Girvin, Florian Marquardt, and Robert J Schoelkopf. Introduction to quantum noise, measurement, and amplification. *Reviews of Modern Physics*, 82(2):1155, 2010. 8, 164, 169

[89] Claude Cohen-Tannoudji, Franck Laloe, and Bernard Diu. *Mécanique quantique*, volume 3. EDP Sciences, 2017. 9, 58

[90] CW Gardiner and MJ Collett. Input and output in damped quantum systems: Quantum stochastic differential equations and the master equation. *Physical Review A*, 31(6):3761, 1985. 10, 164, 165

[91] Max Ludwig, Björn Kubala, and Florian Marquardt. The optomechanical instability in the quantum regime. *New Journal of Physics*, 10(9):095013, 2008. 11, 154

[92] Aashish A Clerk. Optomechanics and quantum measurement. *Les Houches*, 2015. 12

[93] Markus Aspelmeyer, Tobias J Kippenberg, and Florian Marquardt. Cavity optomechanics. *Reviews of Modern Physics*, 86(4):1391, 2014. 12, 171

[94] Tobias J Kippenberg and Kerry J Vahala. Cavity optomechanics: back-action at the mesoscale. *science*, 321(5893):1172–1176, 2008. 12

[95] Ignacio Wilson-Rae, Nima Nooshi, W Zwerger, and Tobias J Kippenberg. Theory of ground state cooling of a mechanical oscillator using dynamical backaction. *Physical review letters*, 99(9):093901, 2007. 12, 170

[96] Florian Marquardt, Joe P Chen, Aashish A Clerk, and SM Girvin. Quantum theory of cavity-assisted sideband cooling of mechanical motion. *Physical review letters*, 99(9):093902, 2007. 12, 169, 170

[97] Constanze Metzger, Ivan Favero, Alexander Ortlieb, and Khaled Karrai. Optical self cooling of a deformable fabry-perot cavity in the classical limit. *Physical Review B*, 78(3):035309, 2008. 12, 54

[98] SC Burd, R Srinivas, JJ Bollinger, AC Wilson, DJ Wineland, D Leibfried, DH Slichter, and DTC Allcock. Quantum amplification of mechanical oscillator motion. *Science*, 364(6446):1163–1165, 2019. 12

[99] Girish S Agarwal and Sumei Huang. Electromagnetically induced transparency in mechanical effects of light. *Physical Review A*, 81(4):041803, 2010. 15

[100] Stefan Weis, Rémi Rivière, Samuel Deléglise, Emanuel Gavartin, Olivier Arcizet, Albert Schliesser, and Tobias J Kippenberg. Optomechanically induced transparency. *Science*, 330(6010):1520–1523, 2010. 15

[101] Mehdi Hamoumi, Pierre Etienne Allain, William Hease, E Gil-Santos, L Morgenroth, B Gérard, A Lemaître, G Leo, and I Favero. Microscopic nanomechanical dissipation in gallium arsenide resonators. *Physical review letters*, 120(22):223601, 2018. 15, 113

[102] Simon Gröblacher, Klemens Hammerer, Michael R Vanner, and Markus Aspelmeyer. Observation of strong coupling between a micromechanical resonator and an optical cavity field. *Nature*, 460(7256):724–727, 2009. 16

[103] John D Teufel, Dale Li, MS Allman, K Cicak, AJ Sirois, JD Whittaker, and RW Simmonds. Circuit cavity electromechanics in the strong-coupling regime. *Nature*, 471(7337):204–208, 2011. 16

[104] GA Peterson, S Kotler, F Lecocq, K Cicak, XY Jin, RW Simmonds, J Aumentado, and JD Teufel. Ultrastrong parametric coupling between a superconducting cavity and a mechanical resonator. *Physical review letters*, 123(24):247701, 2019. 16

[105] Biswarup Guha, Felix Marsault, Fabian Cadiz, Laurence Morgenroth, Vladimir Ulin, Vladimir Berkovitz, Aristide Lemaître, Carmen Gomez, Alberto Amo, Sylvain Combrié, et al. Surface-enhanced gallium arsenide photonic resonator with quality factor of 6×10^6. *Optica*, 4(2):218–221, 2017. 16, 81, 113

[106] Dac Trung Nguyen, Christophe Baker, William Hease, Selsabil Sejil, Pascale Senellart, Aristide Lemaitre, Sara Ducci, Giuseppe Leo, and Ivan Favero. Ultrahigh Q-frequency product for optomechanical disk resonators with a mechanical shield. *Applied Physics Letters*, 103(24):241112, 2013. 16

[107] Oleksandr Kyriienko, Timothy Chi Hin Liew, and Ivan A Shelykh. Optomechanics with cavity polaritons: dissipative coupling and unconventional bistability. *Physical review letters*, 112(7):076402, 2014. 16

[108] Guillermo Rozas, Axel Emerico Bruchhausen, Alejandro Fainstein, Bernard Jusserand, and A Lemaître. Polariton path to fully resonant dispersive coupling in optomechanical resonators. *Physical Review B*, 90(20):201302, 2014. 16

[109] Edward Mills Purcell. Spontaneous emission probabilities at radio frequencies. In *Confined Electrons and Photons*, pages 839–839. Springer, 1995. 16

[110] C Genes, D Vitali, and P Tombesi. Emergence of atom-light-mirror entanglement inside an optical cavity. *Physical Review A*, 77(5):050307, 2008. 17

[111] Vincenzo Savona, LC Andreani, P Schwendimann, and A Quattropani. Quantum well excitons in semiconductor microcavities: Unified treatment of weak and strong coupling regimes. *Solid State Communications*, 93(9):733–739, 1995. 18

[112] Said Rahimzadeh-Kalaleh Rodriguez. Classical and quantum distinctions between weak and strong coupling. *European Journal of Physics*, 37(2):025802, 2016. 18

[113] N. Carlon Zambon Z. Denis C. Ciuti I. Favero R. De Oliveira, S. Ravets and J. Bloch. Enhanced cavity optomechanics via quantum-well exciton polariton. *arXiv preprint arXiv:2202.12094*, 2022. 20, 40, 63, 159

[114] Lord Rayleigh. Theory of sound. *Ed*, 1:93, 1877. 25

[115] Philip Trøst Kristensen, Cole Van Vlack, and Stephen Hughes. Generalized effective mode volume for leaky optical cavities. *Optics letters*, 37(10):1649–1651, 2012. 29

[116] Tobias Jan August Kippenberg. *Nonlinear optics in ultra-high-Q whispering-gallery optical microcavities*. PhD thesis, California Institute of Technology, 2004. 30

[117] Kartik Srinivasan, Matthew Borselli, Oskar Painter, Andreas Stintz, and Sanjay Krishna. Cavity Q, mode volume, and lasing threshold in small diameter algaas microdisks with embedded quantum dots. *Optics Express*, 14(3):1094–1105, 2006. 35

[118] Marina Radulaski, Thomas M Babinec, Kai Muller, Konstantinos G Lagoudakis, Jingyuan Linda Zhang, Sonia Buckley, Yousif A Kelaita, Kassem Alassaad, Gabriel Ferro, and Jelena Vucković. Visible photoluminescence from cubic (3C) silicon carbide microdisks coupled to high-quality whispering gallery modes. *ACS photonics*, 2(1):14–19, 2015. 35

[119] Claude Cohen-Tannoudji, Jacques Dupont-Roc, and Gilbert Grynberg. *Processus d'interaction entre photons et atomes*. Edp Sciences, 2012. 36

[120] Arthur W Leissa. Vibration of plates. Technical report, OHIO STATE UNIV COLUMBUS, 1969. 40

[121] David Parrain. *Optomécanique fibrée des disques GaAs: dissipation, amplification et non-linéarités*. PhD thesis, Paris 7, 2014. 40, 76, 78, 80, 81, 82, 104, 106, 143, 145

[122] Christopher Baker. *On-chip nano-optomechanical whispering gallery resonators*. PhD thesis, Paris 7, 2013. 40, 52, 53, 75, 76

[123] Morio Onoe. Contour vibrations of isotropic circular plates. *the Journal of the Acoustical Society of America*, 28(6):1158–1162, 1956. 40

[124] Augustus Edward Hough Love. *A treatise on the mathematical theory of elasticity*. Cambridge university press, 2013. 40

[125] Ivan Favero. *Quantum Optomechanics and Nanomechanics: Lecture Notes of the Les Houches Summer School: Volume 105, August 2015*, volume 105. Oxford University Press, 2020. 43, 53, 54, 145

[126] Guy Fishman. *Semi-conducteurs: les bases de la théorie kp*. Editions Ecole Polytechnique, 2010. 44, 92, 185

[127] U Rössler. Nonparabolicity and warping in the conduction band of GaAs. *Solid state communications*, 49(10):943–947, 1984. 44

[128] Gerald Bastard. Wave mechanics applied to semiconductor heterostructures. 1990. 44, 46, 48, 97

[129] Henrik Bruus and Karsten Flensberg. *Many-body quantum theory in condensed matter physics: an introduction*. Oxford university press, 2004. 45

[130] Wolfgang Nolting. *Fundamentals of Many-body Physics*. Springer, 2008. 45

[131] Vincenzo Savona, Carlo Piermarocchi, Antonio Quattropani, Paolo Schwendimann, and Francesco Tassone. Optical properties of microcavity polaritons. *Phase transitions*, 68(1):169–279, 1999. 45

[132] Michael P Marder. *Condensed matter physics*. John Wiley & Sons, 2010. 47

[133] Monique Combescot and Christian Tanguy. New criteria for bosonic behavior of excitons. *EPL (Europhysics Letters)*, 55(3):390, 2001. 47

[134] Hartmut Haug and Stephan W Koch. *Quantum theory of the optical and electronic properties of semiconductors: fifth edition*. World Scientific Publishing Company, 2009. 47

[135] Mitsuru Sugawara. Theory of spontaneous-emission lifetime of Wannier excitons in mesoscopic semiconductor quantum disks. *Physical Review B*, 51(16):10743, 1995. 48

[136] Yoshimasa Murayama. *Mesoscopic systems: fundamentals and applications*. John Wiley & Sons, 2008. 49

[137] C Ciuti, P Schwendimann, and A Quattropani. Theory of polariton parametric interactions in semiconductor microcavities. *Semiconductor science and technology*, 18(10):S279, 2003. 50

[138] Jolyon K Bloomfield, Stephen HP Face, and Zander Moss. Indefinite integrals of spherical bessel functions. *arXiv preprint arXiv:1703.06428*, 2017. 51

[139] John David Jackson. Classical electrodynamics, 1999. 52

[140] Albert Feldman. Relations between electrostriction and the stress-optical effect. *Physical Review B*, 11(12):5112, 1975. 53

[141] Peter T Rakich, Paul Davids, and Zheng Wang. Tailoring optical forces in waveguides through radiation pressure and electrostrictive forces. *Optics express*, 18(14):14439–14453, 2010. 53

[142] Tamma Satya Narasimhamurty. *Photoelastic and electro-optic properties of crystals*. Springer Science & Business Media, 2012. 53

[143] Y Itoh, S Adachi, and C Hamaguchi. Analysis of resonant brillouin scattering in GaAs. *physica status solidi (b)*, 93(1):381–389, 1979. 53

[144] B Jusserand, AN Poddubny, AV Poshakinskiy, Alejandro Fainstein, and A Lemaitre. Polariton resonances for ultrastrong coupling cavity optomechanics in GaAs/AlAs multiple quantum wells. *Physical review letters*, 115(26):267402, 2015. 53

[145] Albert Feldman and Deane Horowitz. Dispersion of the piezobirefringence of GaAs. *Journal of Applied Physics*, 39(12):5597–5599, 1968. 53

[146] P Renosi, J Sapriel, and B Djafari-Rouhani. Resonant acousto-optic effects in InP and GaAs and related devices. In *1993 (5th) International Conference on Indium Phosphide and Related Materials*, pages 592–595. IEEE, 1993. 53

[147] P Renosi and JS Apriel. Acousto-optics of semiconductor crystals and superlattices in resonance conditions. *Ultrasonics*, 31(5):327–332, 1993. 53

[148] Norberto Daniel Lanzillotti-Kimura, Alejandro Fainstein, and Bernard Jusserand. Towards GHz-THz cavity optomechanics in DBR-based semiconductor resonators. *Ultrasonics*, 56:80–89, 2015. 53

[149] V Villafañe, P Sesin, P Soubelet, S Anguiano, AE Bruchhausen, G Rozas, A Lemaître, and A Fainstein. Optoelectronic forces with quantum wells for cavity optomechanics in gaas/alas semiconductor microcavities. *arXiv preprint arXiv:1709.08987*, 2017. 54, 55

[150] Constanze Metzger, Max Ludwig, Clemens Neuenhahn, Alexander Ortlieb, Ivan Favero, Khaled Karrai, and Florian Marquardt. Self-induced oscillations in an optomechanical system driven by bolometric backaction. *Physical review letters*, 101(13):133903, 2008. 54

[151] Michel Pinard and Aurélien Dantan. Quantum limits of photothermal and radiation pressure cooling of a movable mirror. *New Journal of Physics*, 10(9):095012, 2008. 54

[152] Juan Restrepo, Julien Gabelli, Cristiano Ciuti, and Ivan Favero. Classical and quantum theory of photothermal cavity cooling of a mechanical oscillator. *Comptes Rendus Physique*, 12(9-10):860–870, 2011. 54

[153] JS Blakemore. Semiconducting and other major properties of gallium arsenide. *Journal of Applied Physics*, 53(10):R123–R181, 1982. 54

[154] Robert A Barton, Isaac R Storch, Vivekananda P Adiga, Reyu Sakakibara, Benjamin R Cipriany, B Ilic, Si Ping Wang, Peijie Ong, Paul L McEuen, Jeevak M Parpia, et al. Photothermal self-oscillation and laser cooling of graphene optomechanical systems. *Nano letters*, 12(9):4681–4686, 2012. 54

[155] Constanze Höhberger Metzger and Khaled Karrai. Cavity cooling of a microlever. *Nature*, 432(7020):1002, 2004. 54

[156] Steven G Johnson, Mihai Ibanescu, MA Skorobogatiy, Ori Weisberg, JD Joannopoulos, and Yoel Fink. Perturbation theory for Maxwell's equations with shifting material boundaries. *Physical review E*, 65(6):066611, 2002. 54

[157] Matt Eichenfield, Jasper Chan, Amir H Safavi-Naeini, Kerry J Vahala, and Oskar Painter. Modeling dispersive coupling and losses of localized optical and mechanical modes in optomechanical crystals. *Optics express*, 17(22):20078–20098, 2009. 54

[158] Jasper Chan, Amir H Safavi-Naeini, Jeff T Hill, Seán Meenehan, and Oskar Painter. Optimized optomechanical crystal cavity with acoustic radiation shield. *Applied Physics Letters*, 101(8):081115, 2012. 55

[159] Krishna C Balram, Marcelo Davanço, Ju Young Lim, Jin Dong Song, and Kartik Srinivasan. Moving boundary and photoelastic coupling in GaAs optomechanical resonators. *Optica*, 1(6):414–420, 2014. 55

[160] Vincenzo Savona. Linear optical properties of semiconductor microcavities with embedded quantum wells. In *Confined photon systems*, pages 173–242. Springer, 1999. 56, 97

[161] Giovanna Panzarini and Lucio Claudio Andreani. Quantum theory of exciton polaritons in cylindrical semiconductor microcavities. *Physical Review B*, 60(24):16799, 1999. 56

[162] F Bassani, F Ruggiero, and A Quattropani. Microscopic quantum theory of exciton polaritons with spatial dispersion. *Il Nuovo Cimento D*, 7(5):700–716, 1986. 56

[163] Mauro Nisoli. *Semiconductor photonics. Principles and Applications*. Società Editrice Esculapio, 2016. 60

[164] Emmanuel Rosencher and Borge Vinter. *Optoelectronics*. Cambridge University Press, 2002. 60

[165] WH Kleiner and LM Roth. Deformation potential in germanium from optical absorption lines for exciton formation. *Physical Review Letters*, 2(8):334, 1959. 63

[166] W Shockley and J Bardeen. Energy bands and mobilities in monatomic semiconductors. *Physical Review*, 77(3):407, 1950. 63

[167] SL Chuang and CS Chang. k.p method for strained wurtzite semiconductors. *Physical Review B*, 54(4):2491, 1996. 63

[168] Manuel Cardona and Y Yu Peter. *Fundamentals of semiconductors*, volume 619. Springer, 2005. 63

[169] C Piermarocchi, F Tassone, V Savona, A Quattropani, and P Schwendimann. Nonequilibrium dynamics of free quantum-well excitons in time-resolved photoluminescence. *Physical Review B*, 53(23):15834, 1996. 63, 97

[170] A Cantarero, C Trallero-Giner, and M Cardona. Excitons in one-phonon resonant raman scattering: Deformation-potential interaction. *Physical Review B*, 39(12):8388, 1989. 63

[171] Katharina Rojan, Yoan Léger, Giovanna Morigi, Maxime Richard, and Anna Minguzzi. Enhanced second-order nonlinearity for Thz generation by resonant interaction of exciton-polariton rabi oscillations with optical phonons. *Physical review letters*, 119(12):127401, 2017. 63

[172] Achintya K Ganguly and Joseph L Birman. Theory of lattice raman scattering in insulators. *Physical Review*, 162(3):806, 1967. 63

[173] Zakari Denis. *Contrôle et apprentissage induits par réservoir dans des systèmes quantiques et classiques*. PhD thesis, Université de Paris, 2021. 63

[174] *attoMicroscopy*, 2018 (accessed May 20, 2021). `https://www.attocube.com/en/products/cryostats/closed-cycle-cryostats/attodry800/vacuum-shrouds/photonic-probe-station`. 68

[175] Ray Radebaugh. A review of pulse tube refrigeration. In *Advances in cryogenic engineering*, pages 1191–1205. Springer, 1990. 69

[176] *attoMotion*, 2018 (accessed May 20, 2021). `http://www.attocube.com/attomotion/premium-line/key-features/#tab-2`. 69

[177] A Davila, JM Huntley, C Pallikarakis, PD Ruiz, and JM Coupland. Wavelength scanning interferometry using a Ti: Sapphire laser with wide tuning range. *Optics and Lasers in Engineering*, 50(8):1089–1096, 2012. 72

[178] RWP Drever, John L Hall, FV Kowalski, J_ Hough, GM Ford, AJ Munley, and H Ward. Laser phase and frequency stabilization using an optical resonator. *Applied Physics B*, 31(2):97–105, 1983. 72

[179] William Hease. *Gallium arsenide optomechnaical disks approaching the quantum regime*. PhD thesis, Paris 7, 2016. 74, 87, 106, 111

[180] Mehdi Hamoumi. *Vers l'optomécanique quantique en arséniure de gallium: dissipation nanomécanique et opération pulsée*. PhD thesis, Université Sorbonne Paris Cité, 2018. 75, 87, 106

[181] Hermann A Haus and Weiping Huang. Coupled-mode theory. *Proceedings of the IEEE*, 79(10):1505–1518, 1991. 76

[182] JCL Ding, Christophe Baker, Alessio Andronico, David Parrain, P Senellart, A Lemaître, S Ducci, G Leo, and I Favero. Gallium arsenide disk optomechanical resonators. *Handbook of Optical Microcavities*, page 381, 2014. 76, 80

[183] Hermann A Haus. *Waves and fields in optoelectronics*. Prentice-Hall,, 1984. 76

[184] Matthew Borselli, Thomas J Johnson, and Oskar Painter. Beyond the rayleigh scattering limit in high-Q silicon microdisks: theory and experiment. *Optics express*, 13(5):1515–1530, 2005. 78, 81

[185] David Parrain, Christophe Baker, Guillaume Wang, Biswarup Guha, Eduardo Gil Santos, Aristide Lemaitre, Pascale Senellart, Giuseppe Leo, Sara Ducci, and Ivan Favero. Origin of optical losses in gallium arsenide disk whispering gallery resonators. *Optics Express*, 23(15):19656–19672, 2015. 80, 81, 82

[186] Srini Krishnamurthy, Zhi Gang Yu, Leonel P Gonzalez, and Shekhar Guha. Temperature- and wavelength-dependent two-photon and free-carrier absorption in GaAs, InP, GaInAs, and InAsP. *Journal of Applied Physics*, 109(3):033102, 2011. 81

[187] Eric W Van Stryland, MA Woodall, H Vanherzeele, and MJ Soileau. Energy band-gap dependence of two-photon absorption. *Optics letters*, 10(10):490–492, 1985. 81, 94

[188] Brent E Little and Sai T Chu. Estimating surface-roughness loss and output coupling in microdisk resonators. *Optics letters*, 21(17):1390–1392, 1996. 83

[189] Sadao Adachi. Optical dispersion relations for GaP, GaAs, GaSb, InP, InAs, InSb, $Al_xGa_{1-x}As$, and $In_{1-x}Ga_xAs_yP_{1-y}$. *Journal of Applied Physics*, 66(12):6030–6040, 1989. 84

[190] Konstantinos Papatryfonos, Todora Angelova, Antoine Brimont, Barry Reid, Stefan Guldin, Peter Raymond Smith, Mingchu Tang, Keshuang Li, Alwyn J Seeds, Huiyun Liu, et al. Refractive indices of MBE-grown $Al_xGa_{(1-x)}As$ ternary alloys in the transparent wavelength region. *AIP Advances*, 11(2):025327, 2021. 84

[191] Enrique AJ Marcatili. Dielectric rectangular waveguide and directional coupler for integrated optics. *Bell System Technical Journal*, 48(7):2071–2102, 1969. 83

[192] Wouter J Westerveld, Suzanne M Leinders, Koen WA van Dongen, H Paul Urbach, and Mirvais Yousefi. Extension of marcatili's analytical approach for rectangular silicon optical waveguides. *Journal of Lightwave Technology*, 30(14):2388–2401, 2012. 83, 84

[193] Alessio Andronico. *Etude électromagnétique d'émetteurs intégrés infrarouges et Thz en AlGaAs*. PhD thesis, Paris 7, 2008. 84

[194] Thomas Kamalakis and Thomas Sphicopoulos. Frequency dependence of the coupling coefficients and resonant frequency detuning in a nanophotonic waveguide-cavity system. *IEEE journal of quantum electronics*, 42(8):827–837, 2006. 85

[195] Ehsan Shah Hosseini, Siva Yegnanarayanan, Amir Hossein Atabaki, Mohammad Soltani, and Ali Adibi. Systematic design and fabrication of high-Q single-mode pulley-coupled planar silicon nitride microdisk resonators at visible wavelengths. *Optics express*, 18(3):2127–2136, 2010. 87

[196] Vilson R Almeida, Roberto R Panepucci, and Michal Lipson. Nanotaper for compact mode conversion. *Optics letters*, 28(15):1302–1304, 2003. 88

[197] RJ Black, S Lacroix, F Gonthier, and JD Love. Tapered single-mode fibres and devices. *IEE Proceedings J-Optoelectronics*, 138(5):355–364, 1991. 89

[198] EO Kane. The k.p method. In *Semiconductors and semimetals*, volume 1, pages 75–100. Elsevier, 1966. 92

[199] J Mi Luttinger. Quantum theory of cyclotron resonance in semiconductors: General theory. *Physical review*, 102(4):1030, 1956. 92, 185

[200] YP Varshni. *Physica (Utrecht)*, 34:149, 1967. 92, 124

[201] Jasprit Singh. *Physics of Semiconductors and their Heterostructures*. McGraw-Hill College, 1993. 94, 183

[202] R People and JC Bean. Calculation of critical layer thickness versus lattice mismatch for Ge_xSi_{1-x}/Si strained-layer heterostructures. *Applied Physics Letters*, 47(3):322–324, 1985. 94

[203] R People and JC Bean. Erratum: Calculation of critical layer thickness versus lattice mismatch for Ge_xSi_{1-x}/Si strained-layer heterostructures [appl. phys. lett. 4 7, 322 (1985)]. *Applied Physics Letters*, 49(4):229–229, 1986. 94

[204] JW Matthews and AE Blakeslee. Defects in epitaxial multilayers: I. misfit dislocations. *Journal of Crystal growth*, 27:118–125, 1974. 94

[205] Shun Lien Chuang. Efficient band-structure calculations of strained quantum wells. *Physical Review B*, 43(12):9649, 1991. 94

[206] Calvin Yi-Ping Chao and Shun Lien Chuang. Spin-orbit-coupling effects on the valence-band structure of strained semiconductor quantum wells. *Physical Review B*, 46(7):4110, 1992. 94

[207] Daniela Stange, Stephan Wirths, Richard Geiger, Christian Schulte-Braucks, Bahareh Marzban, Nils von den Driesch, Gregor Mussler, Thomas Zabel, Toma Stoica, Jean-Michel Hartmann, et al. Optically pumped GeSn microdisk lasers on Si. *ACS photonics*, 3(7):1279–1285, 2016. 95

[208] Quang Minh Thai, Nicolas Pauc, Joris Aubin, Mathieu Bertrand, Jérémie Chrétien, Vincent Delaye, Alexei Chelnokov, Jean-Michel Hartmann, Vincent Reboud, and Vincent Calvo. Gesn heterostructure micro-disk laser operating at 230 k. *Optics express*, 26(25):32500–32508, 2018. 95

[209] Karen J Moore, Geoffrey Duggan, Karl Woodbridge, and Christine Roberts. Observations and calculations of the exciton binding energy in (In, Ga) As/GaAs strained-quantum-well heterostructures. *Physical Review B*, 41(2):1090, 1990. 96

[210] Ronald L Greene, Krishan K Bajaj, and Dwight E Phelps. Energy levels of wannier excitons in GaAs-$Ga_{1-x}Al_x$As quantum-well structures. *Physical Review B*, 29(4):1807, 1984. 96

[211] Lucio Claudio Andreani, Francesco Tassone, and Franco Bassani. Radiative lifetime of free excitons in quantum wells. *Solid state communications*, 77(9):641–645, 1991. 97

[212] Baoping Zhang, SS Kano, R Ito, and Y Shiraki. Oscillator strength of higher-subband excitons in InGaAs/GaAs quantum wells. *Semiconductor science and technology*, 10(4):443, 1995. 97

[213] Lucio Claudio Andreani and Alfredo Pasquarello. Accurate theory of excitons in GaAs-$Ga_{1-x}Al_xAs$ quantum wells. *Physical Review B*, 42(14):8928, 1990. 97

[214] Alan D Bristow, Tianhao Zhang, Mark E Siemens, Steven T Cundiff, and RP Mirin. Separating homogeneous and inhomogeneous line widths of heavy-and light-hole excitons in weakly disordered semiconductor quantum wells. *The Journal of Physical Chemistry B*, 115(18):5365–5371, 2011. 97

[215] Roland Zimmermann. Theory of resonant rayleigh scattering of excitons in semiconductor quantum wells. *Il Nuovo Cimento D*, 17(11):1801–1805, 1995. 97

[216] Vincenzo Savona. Effect of interface disorder on quantum well excitons and microcavity polaritons. *Journal of Physics: Condensed Matter*, 19(29):295208, 2007. 97

[217] F Tassone and Y Yamamoto. Exciton-exciton scattering dynamics in a semiconductor microcavity and stimulated scattering into polaritons. *Physical Review B*, 59(16):10830, 1999. 97

[218] C Ciuti, V Savona, C Piermarocchi, A Quattropani, and P Schwendimann. Role of the exchange of carriers in elastic exciton-exciton scattering in quantum wells. *Physical Review B*, 58(12):7926, 1998. 97

[219] C Ciuti, V Savona, C Piermarocchi, A Quattropani, and P Schwendimann. Threshold behavior in the collision broadening of microcavity polaritons. *Physical Review B*, 58(16):R10123, 1998. 97

[220] R Houdré, RP Stanley, and M Ilegems. Vacuum-field Rabi splitting in the presence of inhomogeneous broadening: Resolution of a homogeneous linewidth in an inhomogeneously broadened system. *Physical Review A*, 53(4):2711, 1996. 97

[221] Stanley Pau, Gunnar Björk, H Cao, Eiichi Hanamura, and Yoshihisa Yamamoto. Theory of inhomogeneous microcavity polariton splitting. *Solid state communications*, 98(9):781–784, 1996. 97

[222] I Diniz, S Portolan, R Ferreira, JM Gérard, Patrice Bertet, and A Auffeves. Strongly coupling a cavity to inhomogeneous ensembles of emitters: Potential for long-lived solid-state quantum memories. *Physical Review A*, 84(6):063810, 2011. 97

[223] Aymeric Delteil, Thomas Fink, Anne Schade, Sven Höfling, Christian Schneider, and Ataç İmamoğlu. Towards polariton blockade of confined exciton-polaritons. *Nature materials*, 18(3):219–222, 2019. 98

[224] Nicola Carlon Zambon. *Chirality and nonlinear dynamics in polariton microresonators*. PhD thesis, Université Paris-Saclay, 2020. 98

[225] Benjamin Besga, Cyril Vaneph, Jakob Reichel, Jérôme Estève, Andreas Reinhard, Javier Miguel-Sánchez, Ataç Imamoğlu, and Thomas Volz. Polariton boxes in a tunable fiber cavity. *Physical Review Applied*, 3(1):014008, 2015. 98, 123

[226] DM Whittaker. What determines inhomogeneous linewidths in semiconductor microcavities? *Physical review letters*, 80(21):4791, 1998. 98

[227] Paola Borri, W Langbein, U Woggon, Jacob Riis Jensen, and Jørn Märcher Hvam. Microcavity polariton linewidths in the weak-disorder regime. *Physical Review B*, 63(3):035307, 2000. 98

[228] JW Lee, MW Devre, BH Reelfs, D Johnson, JN Sasserath, F Clayton, D Hays, and SJ Pearton. Advanced selective dry etching of GaAs/AlGaAs in high density inductively coupled plasmas. *Journal of Vacuum Science & Technology A: Vacuum, Surfaces, and Films*, 18(4):1220–1224, 2000. 106

[229] Michael Huff. Recent advances in Reactive Ion Etching and applications of high-aspect-ratio microfabrication. *Micromachines*, 12(8):991, 2021. 106

[230] Katherine Booker, Yahuitl Osorio Mayon, Christopher Jones, Matthew Stocks, and Andrew Blakers. Deep, vertical etching for GaAs using inductively coupled plasma/reactive ion etching. *Journal of Vacuum Science & Technology B, Nanotechnology and Microelectronics: Materials, Processing, Measurement, and Phenomena*, 38(1):012206, 2020. 106

[231] Eli Yablonovitch, T Gmitter, JP Harbison, and R Bhat. Extreme selectivity in the lift-off of epitaxial GaAs films. *Applied Physics Letters*, 51(26):2222–2224, 1987. 107

[232] Klas Hjort. Sacrificial etching of iii-v compounds for micromechanical devices. *Journal of Micromechanics and Microengineering*, 6(4):370, 1996. 107

[233] J Sweet, BC Richards, JD Olitzky, J Hendrickson, G Khitrova, HM Gibbs, D Litvinov, D Gerthsen, DZ Hu, DM Schaadt, et al. GaAs photonic crystal slab nanocavities: Growth, fabrication, and quality factor. *Photonics and Nanostructures-Fundamentals and Applications*, 8(1):1–6, 2010. 107

[234] M Rei Vilar, J El Beghdadi, F Debontridder, R Artzi, R Naaman, AM Ferraria, and AM Botelho do Rego. Characterization of wet-etched GaAs (100) surfaces. *Surface and Interface Analysis: An International Journal devoted to the development and application of techniques for the analysis of surfaces, interfaces and thin films*, 37(8):673–682, 2005. 110

[235] Sadao Adachi and Kunishige Oe. Chemical etching characteristics of (001) GaAs. *Journal of The Electrochemical Society*, 130(12):2427, 1983. 110

[236] Sadao Adachi. Chemical etching of InP and InGaAsP/InP. *Journal of The Electrochemical Society*, 129(3):609, 1982. 110

[237] V Cambel, D Gregušová, and R Kúdela. Formation of GaAs three-dimensional objects using AlAs "facet-forming" sacrificial layer and H_3PO_4, H_2O_2, H_2o based solution. *Journal of applied physics*, 94(7):4643–4648, 2003. 110

[238] Eun-A Moon, Jong-Lam Lee, and Hyung Mo Yoo. Selective wet etching of GaAs on Al_xGa_{1-x}as for AlGaAs/InGaAs/AlGaAs pseudomorphic high electron mobility transistor. *Journal of applied physics*, 84(7):3933–3938, 1998. 110

[239] David Parrain, Christophe Baker, Guillaume Wang, Biswarup Guha, Eduardo Gil Santos, Aristide Lemaitre, Pascale Senellart, Giuseppe Leo, Sara Ducci, and Ivan Favero. Origin of optical losses in gallium arsenide disk whispering gallery resonators. *Optics express*, 23(15):19656–19672, 2015. 113

[240] Gregory Moille, Sylvain Combrié, Laurence Morgenroth, Gaëlle Lehoucq, François Neuilly, Bowen Hu, Didier Decoster, and Alfredo de Rossi. Integrated all-optical switch with 10 ps time resolution enabled by ALD. *Laser & Photonics Reviews*, 10(3):409–419, 2016. 113

[241] Claude Weisbuch, Mr Nishioka, A Ishikawa, and Y Arakawa. Observation of the coupled exciton-photon mode splitting in a semiconductor quantum microcavity. *Physical Review Letters*, 69(23):3314, 1992. 115

[242] Kartik Srinivasan and Oskar Painter. Optical fiber taper coupling and high-resolution wavelength tuning of microdisk resonators at cryogenic temperatures. *Applied Physics Letters*, 90(3):031114, 2007. 115

[243] Kartik Srinivasan and Oskar Painter. Linear and nonlinear optical spectroscopy of a strongly coupled microdisk-quantum dot system. *Nature*, 450(7171):862–865, 2007. 115

[244] S Mosor, J Hendrickson, BC Richards, J Sweet, G Khitrova, HM Gibbs, Tomoyuki Yoshie, Axel Scherer, OB Shchekin, and DG Deppe. Scanning a photonic crystal slab nanocavity by condensation of xenon. *Applied Physics Letters*, 87(14):141105, 2005. 115

[245] F Ding, R Singh, f JD Plumhof, T Zander, V Křápek, YH Chen, M Benyoucef, V Zwiller, K Dörr, G Bester, et al. Tuning the exciton binding energies in single self-assembled InGaAs/GaAs quantum dots by piezoelectric-induced biaxial stress. *Physical review letters*, 104(6):067405, 2010. 115

[246] Ozgur Burak Aslan, Minda Deng, and Tony F Heinz. Strain tuning of excitons in monolayer wse 2. *Physical Review B*, 98(11):115308, 2018. 115

[247] J Pelal Reithmaier, G Skek, A Löffler, C Hofmann, S Kuhn, S Reitzenstein, LV Keldysh, VD Kulakovskii, TL Reinecke, and A Forchel. Strong coupling in a single quantum dot-semiconductor microcavity system. *Nature*, 432(7014):197–200, 2004. 115

[248] Tomoyuki Yoshie, Axel Scherer, J Hendrickson, Galina Khitrova, HM Gibbs, G Rupper, C Ell, OB Shchekin, and DG Deppe. Vacuum rabi splitting with a single quantum dot in a photonic crystal nanocavity. *Nature*, 432(7014):200–203, 2004. 115

[249] Emmanuelle Peter, Pascale Senellart, David Martrou, Aristide Lemaître, J Hours, JM Gérard, and Jacqueline Bloch. Exciton-photon strong-coupling regime for a single quantum dot embedded in a microcavity. *Physical review letters*, 95(6):067401, 2005. 115

[250] S Reitzenstein, C Hofmann, A Gorbunov, M Strauß, SH Kwon, C Schneider, A Löffler, S Höfling, M Kamp, and A Forchel. AlAs/GaAs micropillar cavities with quality factors exceeding 150.000. *Applied Physics Letters*, 90(25):251109, 2007. 115

[251] TB Norris, J-K Rhee, C-Y Sung, Y Arakawa, M Nishioka, and C Weisbuch. Time-resolved vacuum rabi oscillations in a semiconductor quantum microcavity. *Physical Review B*, 50(19):14663, 1994. 115

[252] R Houdré, C Weisbuch, RP Stanley, U Oesterle, P Pellandini, and M Ilegems. Measurement of cavity-polariton dispersion curve from angle-resolved photoluminescence experiments. *Physical Review Letters*, 73(15):2043, 1994. 115

[253] HJ Carmichael, RJ Brecha, MG Raizen, HJ Kimble, and PR Rice. Subnatural linewidth averaging for coupled atomic and cavity-mode oscillators. *Physical Review A*, 40(10):5516, 1989. 116

[254] Lucio Claudio Andreani, Giovanna Panzarini, and Jean-Michel Gérard. Strong-coupling regime for quantum boxes in pillar microcavities: Theory. *Physical Review B*, 60(19):13276, 1999. 116

[255] V Savona and C Weisbuch. Theory of time-resolved light emission from polaritons in a semiconductor microcavity under resonant excitation. *Physical Review B*, 54(15):10835, 1996. 117

[256] T-D Lee, P-H Cheng, J-S Pan, R-S Tsai, Y Lai, and K Tai. Far-field emission narrowing effect of microdisk lasers. *Applied physics letters*, 72(18):2223–2225, 1998. 119

[257] M Balasubrahmaniyam, Cyriaque Genet, and Tal Schwartz. Coupling and decoupling of polaritonic states in multimode cavities. *Physical Review B*, 103(24):L241407, 2021. 121, 122

[258] Steffen Richter, Tom Michalsky, Lennart Fricke, Chris Sturm, Helena Franke, Marius Grundmann, and Rüdiger Schmidt-Grund. Maxwell consideration of polaritonic quasiparticle hamiltonians in multi-level systems. *Applied Physics Letters*, 107(23):231104, 2015. 121, 122

[259] Rüdiger Schmidt-Grund, Helena Hilmer, Annekatrin Hinkel, Chris Sturm, Bernd Rheinlaender, Volker Gottschalch, Martin Lange, Jesus Zúñiga-Pérez, and Marius Grundmann. Two-dimensional confined photonic wire resonators-strong light-matter coupling. *physica status solidi (b)*, 247(6):1351–1364, 2010. 122

[260] Laurent Orosz, Francois Reveret, Sophie Bouchoule, Jésus Zúñiga-Pérez, François Médard, Joël Leymarie, Pierre Disseix, Martine Mihailovic, Eric Frayssinet, Fabrice Semond, et al. Fabrication and optical properties of a fully-hybrid epitaxial ZnO-based microcavity in the strong-coupling regime. *Applied physics express*, 4(7):072001, 2011. 122

[261] F Réveret, P Disseix, J Leymarie, A Vasson, F Semond, and M Leroux. Influence of optical confinement and excitonic absorption on strong coupling in a bulk GaN microcavity grown on silicon. *Superlattices and Microstructures*, 52(3):541–551, 2012. 122

[262] Jacqueline Bloch, R Planel, V Thierry-Mieg, JM Gérard, D Barrier, JY Marzin, and E Costard. Strong-coupling regime in pillar semiconductor microcavities. *Superlattices and microstructures*, 22(3):371–374, 1997. 122

[263] Aurélien Trichet, Liaoxin Sun, Goran Pavlovic, Nikolay A Gippius, Guillaume Malpuech, Wei Xie, Zhanghai Chen, Maxime Richard, and Le Si Dang. One-dimensional ZnO exciton polaritons with negligible thermal broadening at room temperature. *Physical Review B*, 83(4):041302, 2011. 122

[264] J Bloch, F Boeuf, JM Gérard, B Legrand, JY Marzin, R Planel, V Thierry-Mieg, and E Costard. Strong and weak coupling regime in pillar semiconductor microcavities. *Physica E: Low-dimensional Systems and Nanostructures*, 2(1-4):915–919, 1998. 122

[265] G Dasbach, M Schwab, M Bayer, and A Forchel. Parametric polariton scattering in microresonators with three-dimensional optical confinement. *Physical Review B*, 64(20):201309, 2001. 122

[266] Guillermo Muñoz-Matutano, Andrew Wood, Mattias Johnsson, Xavier Vidal, Ben Q Baragiola, Andreas Reinhard, Aristide Lemaître, Jacqueline Bloch, Alberto Amo, Gilles Nogues, et al. Emergence of quantum correlations from interacting fibre-cavity polaritons. *Nature materials*, 18(3):213–218, 2019. 123

[267] Walter Koechner. *Solid-state laser engineering*, volume 1. Springer, 2013. 124

[268] L Vina, S Logothetidis, and M Cardona. Temperature dependence of the dielectric function of germanium. *Physical Review B*, 30(4):1979, 1984. 124

[269] R Pässler. Alternative analytical descriptions of the temperature dependence of the energy gap in cadmium sulfide. *physica status solidi (b)*, 193(1):135–144, 1996. 124

[270] JS Rojas-Ramírez, R Goldhahn, P Moser, J Huerta-Ruelas, Juan Hernandez-Rosas, and M López-López. Temperature dependence of the photoluminescence emission from $In_xGa_{1-x}As$ quantum wells on GaAs (311) substrates. *Journal of Applied Physics*, 104(12):124304, 2008. 125

[271] Jean Wei, Joel M Murray, Jacob O Barnes, Douglas M Krein, Peter G Schunemann, and Shekhar Guha. Temperature dependent sellmeier equation for the refractive index of GaP. *Optical Materials Express*, 8(2):485–490, 2018. 125

[272] Mario Bertolotti, Victor Bogdanov, Aldo Ferrari, Andrei Jascow, Natalia Nazorova, Alexander Pikhtin, and Luigi Schirone. Temperature dependence of the refractive index in semiconductors. *JOSA B*, 7(6):918–922, 1990. 125

[273] SR Kisting, PW Bohn, E Andideh, I Adesida, BT Cunningham, GE Stillman, and TD Harris. High precision temperature-and energy-dependent refractive index of GaAs determined from excitation of optical waveguide eigenmodes. *Applied physics letters*, 57(13):1328–1330, 1990. 125

[274] T Skauli, PS Kuo, KL Vodopyanov, TJ Pinguet, O Levi, LA Eyres, JS Harris, MM Fejer, B Gerard, L Becouarn, et al. Improved dispersion relations for GaAs and applications to nonlinear optics. *Journal of Applied Physics*, 94(10):6447–6455, 2003. 125

[275] Christian Tanguy. Temperature dependence of the refractive index of direct band gap semiconductors near the absorption threshold: Application to GaAs. *Journal of applied physics*, 80(8):4626–4631, 1996. 125

[276] A. Lemaître R. De Oliveira, M. Colombano and I. Favero. Quantum well exciton-polaritons in a whispering gallery mode semiconductor microcavity. *in prepraration*. 128, 129, 159

[277] F. Tassone, C. Piermarocchi, V. Savona, A. Quattropani, and P. Schwendimann. Bottleneck effects in the relaxation and photoluminescence of microcavity polaritons. *Phys. Rev. B*, 56:7554–7563, Sep 1997. 134

[278] F Tassone and Y Yamamoto. Exciton-exciton scattering dynamics in a semiconductor microcavity and stimulated scattering into polaritons. *Physical Review B*, 59(16):10830, 1999. 134

[279] Alexey Kavokin and Guillaume Malpuech. *Cavity polaritons*. Elsevier, 2003. 134

[280] AI Tartakovskii, M Emam-Ismail, RM Stevenson, MS Skolnick, VN Astratov, DM Whittaker, Jeremy J Baumberg, and JS Roberts. Relaxation bottleneck and its suppression in semiconductor microcavities. *Physical Review B*, 62(4):R2283, 2000. 134

[281] Markus Müller, Joël Bleuse, and Régis André. Dynamics of the cavity polariton in cdte-based semiconductor microcavities: Evidence for a relaxation edge. *Physical Review B*, 62(24):16886, 2000. 134

[282] A Imamog, RJ Ram, S Pau, Y Yamamoto, et al. Nonequilibrium condensates and lasers without inversion: Exciton-polariton lasers. *Physical Review A*, 53(6):4250, 1996. 134

[283] G Malpuech, A Kavokin, A Di Carlo, and JJ Baumberg. Polariton lasing by exciton-electron scattering in semiconductor microcavities. *Physical Review B*, 65(15):153310, 2002. 134

[284] Hui Deng, Gregor Weihs, David Snoke, Jacqueline Bloch, and Yoshihisa Yamamoto. Polariton lasing vs. photon lasing in a semiconductor microcavity. *Proceedings of the National Academy of Sciences*, 100(26):15318–15323, 2003. 134

[285] Ss Schmitt-Rink, DS Chemla, and DAB Miller. Linear and nonlinear optical properties of semiconductor quantum wells. *Advances in Physics*, 38(2):89–188, 1989. 135

[286] Albert Einstein. Quantentheorie des einatomigen idealen gases. zweite abhandlung. *Albert Einstein: Akademie-Vorträge: Sitzungsberichte der Preußischen Akademie der Wissenschaften 1914–1932*, pages 245–257, 2005. 135

[287] Satyendra Nath Bose. Plancks gesetz und lichtquantenhypothese. 1924. 135

[288] Allan Griffin, David W Snoke, and Sandro Stringari. *Bose-einstein condensation*. Cambridge University Press, 1996. 135

[289] Mike H Anderson, Jason R Ensher, Michael R Matthews, Carl E Wieman, and Eric A Cornell. Observation of Bose-Einstein condensation in a dilute atomic vapor. *science*, 269(5221):198–201, 1995. 135

[290] Hui Deng, Hartmut Haug, and Yoshihisa Yamamoto. Exciton-polariton bose-einstein condensation. *Reviews of modern physics*, 82(2):1489, 2010. 135

[291] G Rochat, C Ciuti, V Savona, C Piermarocchi, A Quattropani, and P Schwendimann. Excitonic Bloch equations for a two-dimensional system of interacting excitons. *Physical Review B*, 61(20):13856, 2000. 135

[292] FM Marchetti, J Keeling, MH Szymańska, and PB Littlewood. Absorption, photoluminescence, and resonant rayleigh scattering probes of condensed microcavity polaritons. *Physical Review B*, 76(11):115326, 2007. 135

[293] R Butté, G Delalleau, AI Tartakovskii, MS Skolnick, VN Astratov, JJ Baumberg, G Malpuech, A Di Carlo, AV Kavokin, and JS Roberts. Transition from strong to weak coupling and the onset of lasing in semiconductor microcavities. *Physical Review B*, 65(20):205310, 2002. 136

[294] Daniele Bajoni, Pascale Senellart, Aristide Lemaître, and Jacqueline Bloch. Photon lasing in GaAs microcavity: Similarities with a polariton condensate. *Physical Review B*, 76(20):201305, 2007. 136

[295] Elena Kammann, Hamid Ohadi, Maria Maragkou, Alexey V Kavokin, and Pavlos G Lagoudakis. Crossover from photon to exciton-polariton lasing. *New Journal of Physics*, 14(10):105003, 2012. 136

[296] TJ Kippenberg, H Rokhsari, T Carmon, Axel Scherer, and KJ Vahala. Analysis of radiation-pressure induced mechanical oscillation of an optical microcavity. *Physical Review Letters*, 95(3):033901, 2005. 140, 141

[297] Olivier Arcizet, P-F Cohadon, Tristan Briant, Michel Pinard, and Antoine Heidmann. Radiation-pressure cooling and optomechanical instability of a micromirror. *Nature*, 444(7115):71–74, 2006. 140, 141

[298] Constanze Metzger, Max Ludwig, Clemens Neuenhahn, Alexander Ortlieb, Ivan Favero, Khaled Karrai, and Florian Marquardt. Self-induced oscillations in an optomechanical system driven by bolometric backaction. *Physical review letters*, 101(13):133903, 2008. 140

[299] Biswarup Guha, Pierre Etienne Allain, Aristide Lemaitre, Giuseppe Leo, and Ivan Favero. Force sensing with an optomechanical self-oscillator. *Physical Review Applied*, 14(2):024079, 2020. 140, 145

[300] Daniel Navarro-Urrios, Jordi Gomis-Bresco, Said El-Jallal, Mourad Oudich, A Pitanti, N Capuj, Alessandro Tredicucci, Francesc Alzina, Amadeu Griol, Yan Pennec, et al. Dynamical back-action at 5.5 ghz in a corrugated optomechanical beam. *AIP advances*, 4(12):124601, 2014. 141

[301] Pierre Etienne Allain, Biswarup Guha, Christophe Baker, David Parrain, Aristide Lemaître, Giuseppe Leo, and Ivan Favero. Electro-optomechanical modulation instability in a semiconductor resonator. *Physical Review Letters*, 126(24):243901, 2021. 142, 145

[302] S Sbarra, PE Allain, S Suffit, A Lemaître, and I Favero. A multiphysics model for ultra-high frequency optomechanical resonators optically actuated and detected in the oscillating mode. *APL Photonics*, 6(8):086111, 2021. 142, 145

[303] Paul E Barclay, Kartik Srinivasan, and Oskar Painter. Nonlinear response of silicon photonic crystal microresonators excited via an integrated waveguide and fiber taper. *Optics express*, 13(3):801–820, 2005. 143, 144

[304] Alfredo de Rossi, Michele Lauritano, Sylvain Combrié, Quynh Vy Tran, and Chad Husko. Interplay of plasma-induced and fast thermal nonlinearities in a GaAs-based photonic crystal nanocavity. *Physical Review A*, 79(4):043818, 2009. 143

[305] Francesco G Della Corte, Giuseppe Cocorullo, Mario Iodice, and Ivo Rendina. Temperature dependence of the thermo-optic coefficient of InP, GaAs, and SiC from room temperature to 600 k at the wavelength of 1.5 μm. *Applied Physics Letters*, 77(11):1614–1616, 2000. 144

[306] Brian R Bennett, Richard A Soref, and Jesus A Del Alamo. Carrier-induced change in refractive index of InP, GaAs and InGaAsP. *IEEE Journal of Quantum Electronics*, 26(1):113–122, 1990. 144

[307] Biswarup Guha, Silvia Mariani, Aristide Lemaître, Sylvain Combrié, Giuseppe Leo, and Ivan Favero. High frequency optomechanical disk resonators in iii–v ternary semiconductors. *Optics express*, 25(20):24639–24649, 2017. 145

[308] Yongjun Huang, Jaime Gonzalo Flor Flores, Ziqiang Cai, Jiagui Wu, Mingbin Yu, Dim-Lee Kwong, Guangjun Wen, Layne Churchill, and Chee Wei Wong. Controllable optomechanical coupling and drude self-pulsation plasma locking in chip-scale optomechanical cavities. *Optics express*, 25(6):6851–6859, 2017. 150

[309] Daniel Navarro-Urrios, Nestor E Capuj, Jordi Gomis-Bresco, Francesc Alzina, Alessandro Pitanti, Amadeu Griol, Alejandro Martínez, and CM Sotomayor Torres. A self-stabilized coherent phonon source driven by optical forces. *Scientific reports*, 5(1):1–7, 2015. 150

[310] Daniel Navarro-Urrios, Néstor E Capuj, Martín F Colombano, P David García, Marianna Sledzinska, Francesc Alzina, Amadeu Griol, Alejandro Martínez, and Clivia M Sotomayor-Torres. Nonlinear dynamics and chaos in an optomechanical beam. *Nature communications*, 8(1):1–10, 2017. 150

[311] Christophe Baker, Sebastian Stapfner, David Parrain, Sara Ducci, Giuseppe Leo, Eva M Weig, and Ivan Favero. Optical instability and self-pulsing in silicon nitride whispering gallery resonators. *Optics express*, 20(27):29076–29089, 2012. 150

[312] Thomas J Johnson, Matthew Borselli, and Oskar Painter. Self-induced optical modulation of the transmission through a high-q silicon microdisk resonator. *Optics express*, 14(2):817–831, 2006. 150

[313] Maia Brunstein, Alejandro M Yacomotti, Isabel Sagnes, Fabrice Raineri, Laurent Bigot, and Ariel Levenson. Excitability and self-pulsing in a photonic crystal nanocavity. *Physical Review A*, 85(3):031803, 2012. 150

[314] Nicolas Cazier, Xavier Checoury, Laurent-Daniel Haret, and Philippe Boucaud. High-frequency self-induced oscillations in a silicon nanocavity. *Optics express*, 21(11):13626–13638, 2013. 150

[315] Simon Gröblacher, Klemens Hammerer, Michael R Vanner, and Markus Aspelmeyer. Observation of strong coupling between a micromechanical resonator and an optical cavity field. *Nature*, 460(7256):724–727, 2009. 152

[316] Dac Trung Nguyen, William Hease, Christopher Baker, Eduardo Gil-Santos, Pascale Senellart, Aristide Lemaître, Sara Ducci, Giuseppe Leo, and Ivan Favero. Improved optomechanical disk resonator sitting on a pedestal mechanical shield. *New Journal of Physics*, 17(2):023016, 2015. 152

[317] Monika H Schleier-Smith, Ian D Leroux, Hao Zhang, Mackenzie A Van Camp, and Vladan Vuletić. Optomechanical cavity cooling of an atomic ensemble. *Physical review letters*, 107(14):143005, 2011. 154

[318] David Hunger, Stephan Camerer, Theodor W Hänsch, Daniel König, Jörg P Kotthaus, Jakob Reichel, and Philipp Treutlein. Resonant coupling of a bose-einstein condensate to a micromechanical oscillator. *Physical review letters*, 104(14):143002, 2010. 154

[319] Ferdinand Brennecke, Stephan Ritter, Tobias Donner, and Tilman Esslinger. Cavity optomechanics with a bose-einstein condensate. *Science*, 322(5899):235–238, 2008. 154

[320] Konstantinos G Lagoudakis, Francesco Manni, Barbara Pietka, Michiel Wouters, Timothy Chi Hin Liew, Vincenzo Savona, Alexey V Kavokin, Régis André, and Benoit Deveaud-Plédran. Probing the dynamics of spontaneous quantum vortices in polariton superfluids. *Physical review letters*, 106(11):115301, 2011. 154

[321] AL Ivanov and LV Keldysh. Restructuring of polariton and phonon spectra of a semiconductor in the presence of a strong electromagnetic wave. *Soviet Journal of Experimental and Theoretical Physics*, 57(1):234, 1983. 156

[322] Joseph L Birman, Maurizio Artoni, and Bing Shen Wang. Some properties of families of excitonic quasiparticles. In *AIP Conference Proceedings*, volume 213, pages 140–148. American Institute of Physics, 1990. 156

[323] BD Hauer, J Maciejko, and JP Davis. Nonlinear power spectral densities for the harmonic oscillator. *Annals of Physics*, 361:148–183, 2015. 164

[324] Jeremy B Clark, Florent Lecocq, Raymond W Simmonds, José Aumentado, and John D Teufel. Sideband cooling beyond the quantum backaction limit with squeezed light. *Nature*, 541(7636):191–195, 2017. 170

[325] Claudiu Genes, David Vitali, Paolo Tombesi, Sylvain Gigan, and Markus Aspelmeyer. Ground-state cooling of a micromechanical oscillator: Comparing cold damping and cavity-assisted cooling schemes. *Physical Review A*, 77(3):033804, 2008. 170

[326] GJ Milburn. 5. an introduction to quantum optomechanics. *acta physica slovaca*, 61(1), 2011. 170

[327] Dalziel J Wilson, Vivishek Sudhir, Nicolas Piro, Ryan Schilling, Amir Ghadimi, and Tobias J Kippenberg. Measurement-based control of a mechanical oscillator at its thermal decoherence rate. *Nature*, 524(7565):325–329, 2015. 171

[328] Rick Leijssen, Giada R La Gala, Lars Freisem, Juha T Muhonen, and Ewold Verhagen. Nonlinear cavity optomechanics with nanomechanical thermal fluctuations. *Nature communications*, 8(1):1–10, 2017. 171

[329] Jingkun Guo, Richard Norte, and Simon Gröblacher. Feedback cooling of a room temperature mechanical oscillator close to its motional ground state. *Physical review letters*, 123(22):223602, 2019. 171

[330] Francesco Fogliano, Benjamin Besga, Antoine Reigue, Philip Heringlake, Laure Mercier de Lépinay, Cyril Vaneph, Jakob Reichel, Benjamin Pigeau, and Olivier Arcizet. Cavity nano-optomechanics in the ultrastrong coupling regime with ultrasensitive force sensors. *arXiv preprint arXiv:1904.01140*, 2019. 171

[331] Christoph Reinhardt, Tina Müller, Alexandre Bourassa, and Jack C Sankey. Ultralownoise sin trampoline resonators for sensing and optomechanics. *Physical Review X*, 6(2):021001, 2016. 171

[332] VA Wilkinson and AR Adams. The effect of temperature and pressure on InGaAs band structure. *Properties of Lattice-matched and Strained Indium Gallium Arsenide (EMIS Data Reviews Series vol 8)*, pages 70–5, 1993. 183

[333] V Gottschalch. Properties of lattice-matched and strained indium gallium arsenide, 1994. 183

[334] I Vurgaftman, J áR Meyer, and L áR Ram-Mohan. Band parameters for III-V compound semiconductors and their alloys. *Journal of applied physics*, 89(11):5815–5875, 2001. 183, 184

[335] Newton Cesario Frateschi. *Optoelectronic devices based on low threshold strained InGaAs/GaAs quantum well lasers grown on structured substrates*. PhD thesis, University of Southern California, 1993. 183

[336] Sadao Adachi. Gaas, alas, and al x ga1- x as: Material parameters for use in research and device applications. *Journal of Applied Physics*, 58(3):R1–R29, 1985. 183

[337] Adachi Sadao. Properties of group-IV, III-V and II-VI semiconductors. *Hoboken (USA) Wiley&Sons*, 2005. 183

[338] Shun Lien Chuang. *Physics of photonic devices*, volume 80. John Wiley & Sons, 2012. 183

[339] Thomas B Bahder. Eight-band k·p model of strained zinc-blende crystals. *Physical Review B*, 41(17):11992, 1990. 185

Résumé détaillé en français

Ce manuscrit de thèse présente les différents résultats de notre travail théorique et experimental portant sur les systèmes d'optomécanique quantiques hybrides. L'optomécanique hybride représente une sous-branche de l'optomécanique, où vient s'ajouter en complément d'un système optique et mécanique, un troisième objet quantique, représentant de nouveaux degrés de liberté supplémentaires. Nous nous sommes tout particulièrement intéressés ici au couplage d'une structure de type puit quantique à un système optomécanique constitué d'un disque en Arséniure de Gallium (GaAs), un système optomécanique de cavité dont la fabrication et la technologie sont maitrisées dans notre groupe depuis plusieurs années.

Une nouvelle phénoménologie émerge de ce couplage, notamment avec l'apparition d'un nouveau type de boson : l'exciton. Ce dernier est le résultat d'une excitation élémentaire du puit quantique et vient se coupler aux photons et phonons déjà présents en optomécanique traditionnelle. Le modèle théorique associé à ce nouveau système à trois pôles, prévoit dans un régime de couplage fort entre les photons et les excitons, la création d'un nouveau type de quasi-particule : les polaritons. Ces polaritons possédant une nature à la fois photonique et électronique, se couplent aux phonons créant ainsi un système optomécanique hybride.

Les trois premiers chapitres de ce manuscrit définissent le cadre théorique, les différents paramètres physiques propres à notre système ainsi que les méthodes expérimentales utilisées pendant cette thèse. Les deux derniers chapitres présentent les principaux résultats expérimentaux originaux obtenus pendant ce doctorat.

Nous introduisons dans le **chapitre 1** les systèmes optomécaniques hybrides à puit quantique. Nous commençons par présenter un système optomécanique traditionnel ainsi que le cadre théorique nécessaire pour décrire la physique en jeu. L'Hamiltonien général d'une cavité optomécanique de type Fabry-Pérot, composée d'un résonateur optique avec un miroir mobile est décrit. Afin de tenir compte de la dissipation, autrement dit, des différentes inéluctables pertes optiques et mécaniques dues au couplage du système avec son environnement, nous présentons des Hamiltoniens de couplage du système à des bains thermiques.

En écrivant les équations de Langevin quantiques en régime linéarisé, nous exposons deux applications potentielles du couplage optomécanique : le refroidissement et l'amplification du mouvement mécanique. Nous en profitons pour introduire une grandeur phare en optomécanique : la coopérativité, un paramètre sans dimension, definit par le ratio entre la valeur du couplage optomécanique au carré et les le produits des taux de dissipations du système (optique et mécanique). Ce paramètre traduit la capacité du système à transférer

une énergie optique en énergie mécanique (et inversement), avant que les phénomènes de dissipation prennent l'avantage. En d'autres termes la coopérativité représente le niveau de contrôle que l'on possède sur le résonateur optomécanique.

Nous passons brièvement en revue l'ensemble des paramètres impliqués dans les résonateurs optomécanique. En particulier, il est toujours interessant de maximiser la valeur du couplage optomécanique et de minimiser la valuers des différentes source de dissipation du système, et par conséquent augmenter la valeur de la coopérativité. La stratégie retenue dans ce manuscrit consiste principalement à augmenter la valeur du couplage optomécanique, en utilisant une approche hybride.

Avant d'introduire l'Hamiltonien d'un système optomécanique hybride, nous traitons tout d'abord le régime de couplage fort entre exciton et photon, grâce au modèle de Hopfield. Nous décrivons les nouveaux états propres du système dans ce régime, ainsi que les énergies propres qui y sont associées. Nous définissons aussi la notion de fraction excitonique et fraction photonique qui décrivent le comportement du polariton. Enfin, nous présentons une formulation théorique du système hybride complet où, photons, phonons et excitons sont tous en interaction. L'Hamiltonien de ce triple système peut être ré-exprimé dans la base des polaritons. On obtient alors un système d'équation pour les opérateurs polaritoniques qui prend la même forme que l'Hamiltonien optomécanique usuel. Le couplage des polaritons à la mécanique est alors pondéré par les fractions excitonique et photonique. Le couplage des excitons à la mécanique pouvant être jusqu'à trois ordres de grandeur supérieur à celui des photons, l'interaction des polaritons avec les phonons est en conséquence accrue par rapport à l'optomécanique standard. Une situation où les valeurs de la coopérativité peuvent s'envoler avec des effets bénéfiques pour certaines applications de l'optomécanique.

Le **chapitre 2** présente de façon plus détaillée tous les paramètres physiques relatifs à notre système optomécanique hybride : un disque en GaAs avec une structure comportant plusieurs puits quantiques à base d'Arséniure d'Indium-Gallium (InGaAs). Nous commençons ce chapitre par la description des modes optiques de notre cavité : des modes "chuchotements de galerie" (*Whispering Gallery Modes* - WGMs en anglais). Nous présentons une méthode analytique qui permet d'obtenir la distribution spatiale ainsi que l'énergie des différents modes électromagnétiques. Nous comparons ces résultats à ceux obtenus par simulation numérique sur un logiciel d'analyse par éléments finis (COMSOL).

Dans un second temps nous traitons les modes mécaniques de notre système et plus particulièrement nous nous intéressons à la famille des modes radiaux de respiration (*Radial Breathing Modes* - RBMs en anglais). Nous procédons de la même façon, nous introduisons un modèle analytique et nous comparons les résultats obtenus grâce au logiciel COMSOL.

Nous nous occupons ensuite du dernier type de bosons présents dans le système : les excitons. Nous débutons par le cas des semi-conducteurs massifs (*bulk* en anglais) et nous traitons le cas d'un puit quantique dans un second temps. Le cas d'un puit quantique à symétrie cylindrique présent par construction dans notre résonateur, vient clore cette partie. La fonction d'onde de l'exciton arbore alors une géométrie similaire à celle des modes de galerie optiques.

Une fois que les modes photoniques, phononiques et excitoniques ont été proprement introduits nous calculons leurs couplages respectifs. En ce qui concerne le couplage optomécanique nous employons une méthode purement numérique (logiciel COMSOL). Pour

les deux autres couplages (opto-éléctronique et electro-mécanique) restants nous présentons des modèles analytiques reposant sur des descriptions Hamiltoniennes. Ces deux dernières quantités prennent la forme d'une intégrale de recouvrement entre la fonction d'onde et le profil de déformation/le champs électrique pour le couplage electro-mécanique/opto-éléctronique. Nous calculons ces deux facteurs de couplage en fonction des différent paramètre du système.

Le **chapitre 3** passe en revue les différentes techniques expérimentales utilisées lors de cette thèse. Nous présentons tout d'abord brièvement le montage expérimental comprenant notamment un cryostat à tube pulsé, différentes sources laser, ainsi qu'une station photonique permettant de sonder avec plusieurs configurations notre système.

En second lieu, nous expliquons les différents points clefs du design de l'échantillon. Nous insistons notamment sur la lecture des modes optiques et le couplage évanescent du disque à des guides suspendus. Ces guides, par l'intermédiaire de fibres optiques microlentillées nous permettront d'extraire l'information optique. Cette optimisation du couplage et du guide d'onde est présentée pour deux gammes de longueur d'onde différentes : la gamme des longueurs d'onde telecom (1500 -1630 nm) traditionnellement utilisée pour les technologies à base de GaAs et une gamme de longeur d'onde proche de l'énergie de transition du puit quantique et donc de l'exciton (800-900 nm). Nous listons également les différentes sources de pertes optiques propres à notre système. Concernant le design des puits quantiques plusieurs caractéristiques sont à prendre en compte notamment la composition et la taille. La présence de matériaux possédant des paramètres de maille légèrement différents entraîne l'apparition de contrainte mécanique sur la structure du résonateur. Nous terminons cette discussion par un commentaire sur la largeur inhomogène de l'exciton. Un phénomène qui augmente la dissipation des excitons et par extension des polaritons. Cet élargissement a pour conséquence de limiter le boost de coopérativité obtenu par l'intervention des polaritons.

Dans un dernier temps, nous énumérons les diverses techniques de nano-fabrication de l'échantillon en salle blanche, nous mettons l'accent sur la minutie et la précision dont on doit faire preuve à chacune des étapes de fabrication.

Le **chapitre 4** traite principalement de l'observation expérimentale du régime de couplage fort exciton-photon dans notre système. Nous parcourons d'abord les différentes attentes en terme de spectres optiques et de resultats que l'on peut obtenir pour l'observation des polaritons dans notre système. En particulier, notre système possède plusieurs modes optiques capables de se coupler aux excitons ce qui raisonnablement nous conduit à l'existence de plusieurs branches polaritoniques. De plus, nous constatons dans notre système une absence de signaux provenant des branches dites "hautes" (*Upper Polariton* - UP en anglais), un phénomène qui peut s'expliquer par de diverses raisons. En conséquence, nous observons uniquement des signaux provenant de l'exciton et des branches dites "basses" (*Lower Polariton* - LP en anglais).

Afin de prouver la nature polaritonique des signaux observés, nous devons reconstruire la courbe de dispersion de ces derniers en fonction de la différence d'énergie entre modes de cavité et excitons. Pour modifier cette quantité, nous utilisons la température, une élévation en température provoquant un double décalage en énergie des modes de galerie et de l'exciton. L'évolution de l'énergie des différents signaux observés est comparée au modèle théorique

d'Hopfield et nous permet de conclure sur le caractère polaritonique. Grâce à cette procédure, nous pouvons extraire la valeur du couplage entre exciton et photon, que nous comparons à notre modèle théorique. Une discussion sur les phénomènes observés à haut pompage optique vient clore ce chapitre. Pour un pompage à haute puissance optique des régimes de laser à polaritons ou à photon apparaissent.

Le dernier chapitre (**chapitre 5**) porte sur les premières expériences d'optomécanique réalisées sur ce type de résonateur. Nous présentons notamment des résultats d'auto-oscillation dans la gamme des longueurs d'onde télécom. Les observations que nous faisons sont cohérentes avec celles effectuées sur un système composé d'un simple disque en GaAs (système non hybride) à quelques différences près. À savoir que le rôle des porteurs de charges libres diffère dans notre système principalement à cause de la présence du puit quantique. Des phénomènes de photo-luminescence liés à l'absorption à deux photons de la matrice GaAs sont observés ainsi que des signatures d'instabilité optique. Nous présentons dans un second temps, les différentes perspectives pour notre système comme la réalisation d'experience d'optomécanique avec des polaritons, la réalisation d'expérience à deux longueurs d'onde différent ou encore la génération d'une particule hybride polariton-phonon : les phonoritons.

Mots-clefs : Optomécanique, polariton de cavité, couplage fort, mode de galerie, cavité optique, mode de respiration, puit quantique, exciton, potentiel de déformation, cryogénie, couplage evanescent, guide d'onde, photonique intégrée, GaAs, AlGaAs, InGaAs, nanofabrication, auto-oscillation.